



**HAL**  
open science

# Numerical Modelling of transcritical turbulent jets using a tabulated real-fluid approach

Sajad Jafari

► **To cite this version:**

Sajad Jafari. Numerical Modelling of transcritical turbulent jets using a tabulated real-fluid approach. Fluids mechanics [physics.class-ph]. Université Paris-Saclay, 2022. English. NNT : 2022UPAST038 . tel-03783607

**HAL Id: tel-03783607**

**<https://theses.hal.science/tel-03783607>**

Submitted on 22 Sep 2022

**HAL** is a multi-disciplinary open access archive for the deposit and dissemination of scientific research documents, whether they are published or not. The documents may come from teaching and research institutions in France or abroad, or from public or private research centers.

L'archive ouverte pluridisciplinaire **HAL**, est destinée au dépôt et à la diffusion de documents scientifiques de niveau recherche, publiés ou non, émanant des établissements d'enseignement et de recherche français ou étrangers, des laboratoires publics ou privés.

# Numerical modeling of transcritical turbulent jets using a tabulated real-fluid approach

*Modélisation numérique des jets turbulents transcritiques à l'aide d'une  
approche tabulaire des fluides réels*

## Thèse de doctorat de l'université Paris-Saclay

École doctorale n° 579 : sciences mécaniques et énergétiques, matériaux et  
géosciences (SMEMaG)  
Spécialité de doctorat : mécanique des fluides  
Graduate School : Sciences de l'ingénierie et des systèmes. Référent : CentraleSupélec

Thèse préparée à l'**IFP Énergies Nouvelles**, sous la direction de **Chaouki HABCHI**,  
chercheur

Thèse soutenue à Rueil-Malmaison, le 28 Mars 2022, par

**Sajad JAFARI**

## Composition du Jury

<b>Grégoire ALLAIRE</b> Professeur, École Polytechnique	Président
<b>Jean-Noël JAUBERT</b> Professeur, Université de Lorraine	Rapporteur & Examineur
<b>Michele BATTISTONI</b> Associate Professor, University of Perugia	Rapporteur & Examineur
<b>Sébastien DUCRUIX</b> Directeur de recherche, CentraleSupélec EM2C	Examineur
<b>Vincent MOUREAU</b> Docteur, Université de Rouen CORIA	Examineur
<b>Peter Kelly SENEAL</b> Docteur, Convergent Science	Examineur
<b>Chaouki HABCHI</b> Chercheur HDR, IFP Énergies Nouvelles	Directeur de thèse



THÈSE DE DOCTORAT DE L'UNIVERSITÉ PARIS-SACLAY

PRÉPARÉE À IFP ENERGIES NOUVELLES

---

---

**Numerical modeling of transcritical turbulent  
jets using a tabulated real-fluid approach**

---

---

**Doctorant**

SAJAD JAFARI

**Date**

March 28, 2022

Dr. Pascal MOUGIN    Supervisor    IFPEN (FR)

Dr. Chaouki HABCHI    Directeur de thèse    IFPEN (FR)

**Titre :** Modélisation numérique des jets turbulents transcritiques à l'aide d'une approche tabulaire des fluides réels

**Mots clés :** Modèle de fluide réel; Équilibre vapeur-liquide; Tabulation; Condensation; Évaporation; Injection

**Résumé :** Dans cette thèse, un modèle de fluide réel entièrement compressible a été développé, dans lequel les caractéristiques diphasiques sont obtenues en utilisant une approche tabulée d'équilibre vapeur-liquide (VLE). Ce modèle de fluide réel multicomposant tabulé (RFM) est proposé pour surmonter la plupart des limitations et rendre les simulations de fluide réel abordables. Fondamentalement, le modèle RFM se compose de quatre équations d'équilibre : densité de masse, densité partielle des espèces, quantité de mouvement et énergie. Les propriétés thermodynamiques du mélange sont calculées en fonction de la température (T), de la pression (P) et des compositions (Y) sur la base de différentes équations d'état (EoS). Ce calcul est effectué à l'aide de la bibliothèque thermodynamique IFPEN-Carnot qui génère une table 3D avec (T,P,Y) comme entrées. Cette table de consultation est générée à l'aide d'un flash isotherme-isobarique (TPn) efficace sur le plan informatique, évitant ainsi le flash itératif isochore-isoénergétique (UVn) plus coûteux utilisé dans les travaux précédents. Il inclut spécifiquement différentes sorties thermodynamiques telles que la vitesse du son, la capacité thermique et les propriétés de transport. Le modèle RFM, ainsi que la méthode de tabulation 3D, a été implémenté dans le solveur CFD de CONVERGE. Toutes les propriétés thermiques et de transport sont interpolées linéairement à l'aide de la mise à jour (T,P,Y) pendant la simulation.

Tout d'abord, diverses études ont été réalisées pour le raffinement et la dépendance à la grille des tableaux thermodynamiques, en particulier près de la limite de la phase thermodynamique en utilisant des grilles uniformes et non uniformes. Ces études ont démontré que les grilles non uniformes, comme octree et quadtree, sont coûteuses par rapport à l'approche uniforme. Par conséquent, la tabulation uniforme couplée à la technique de mémoire partagée d'IFPEN s'est avérée être l'approche la plus appropriée pour la tabulation, pour les études industrielles ciblées.

Ensuite, le présent travail a également étudié la robustesse et la précision du modèle RFM proposé et des méthodologies de tabulation en conjonction avec deux schémas numériques modifiés différents, un algorithme PISO modifié et un algorithme SIMPLE modifié, adaptés à l'approche actuelle de modélisation des fluides réels. Ensuite, le modèle RFM proposé a été appliqué avec succès à différentes applications universitaires et industrielles pour étudier les caractéristiques de l'évaporation/condensation classique sous-critique et du mélange transcritique. Parmi elles, deux cas d'essai importants sur le plan industriel pour lesquels des résultats expérimentaux récents sont disponibles ont été simulés et analysés afin de valider le modèle RFM.

- 1- La simulation d'une injection cryogénique conventionnelle d'azote liquide coaxiale à un jet d'hydrogène chaud a été réalisée à l'aide de tables thermodynamiques générées par deux équations d'état différentes : Peng-Robinson (PR) et Soave-Redlich-Kwong (SRK).
- 2- Simulation de l'interaction entre la transition de phase et la dynamique des fluides turbulents pour des jets multi-espèces sous-critiques et supercritiques à l'aide de différents modèles de turbulence, y compris des modèles de simulation de grands tourbillons (LES Sigma et Smagorinsky) ainsi qu'un modèle Navier-Stokes à moyenne de Reynolds (RANS K- $\epsilon$ )

Enfin, les résultats numériques ont montré que la méthode de tabulation améliore l'efficacité de l'équilibre liquide-vapeur (VLE) pour la modélisation des fluides réels et fournit un moyen d'étudier et de comprendre la structure des interfaces liquide-gaz sous-critiques et transcritiques révélant les caractéristiques hydro-thermodynamiques du mélange de jets multicomposants.

**Title :** Numerical modeling of transcritical turbulent jets using a tabulated real-fluid approach

**Keywords :** Real fluid model; Vapor-liquid equilibrium; Tabulation; Condensation; Evaporation; Injection.

**Abstract :** In this thesis, a fully compressible real-fluid model has been developed, in which the two-phase characteristics are obtained using a tabulated vapor-liquid equilibrium (VLE) approach. This tabulated multicomponent real-fluid model (RFM) is proposed to overcome most limitations and make real-fluid simulations affordable. Basically, the RFM model consists of four balance equations: mass density, partial species density, momentum, and energy. The thermodynamic properties of the mixture are calculated as a function of temperature (T), pressure (P), and compositions (Y) based on different equations of state (EoS). This is carried out using the IFPEN-Carnot thermodynamic library which generates a 3D-table with (T,P,Y) as inputs. This look-up table is generated using a computationally efficient isothermal-isobaric (TPn)-flash, thereby avoiding the costlier iterative isochoric-isoenergetic (UVn)-flash employed in previous works. It specifically includes different thermodynamic outputs such as sound speed, heat capacity, and transport properties. The RFM model, along with the 3D tabulation method, has been implemented in the CONVERGE CFD solver. All thermal and transport properties are linearly interpolated using the updated (T,P,Y) during the simulation.

First, various studies have been done for the refinement, and grid in-dependency of the thermodynamic tables, especially near the thermodynamic phase boundary using uniform and nonuniform grids. These studies have demonstrated that nonuniform grids, like octree and quadtree, is costly compared to the uniform approach. Therefore, uniform tabulation coupled with IFPEN's shared memory technique proved to be the most appropriate approach for tabulation, for the targeted industrial studies. Next, the present work has also investigated the robustness and accuracy of the proposed RFM model and the tabulation methodologies in conjunction with two different modified numerical schemes, a modified PISO and modified SIMPLE algorithms, adapted for the current real fluid modeling approach.

Then, the proposed RFM model has been successfully applied to different academic and industrial applications to investigate subcritical classical evaporation/condensation and transcritical mixing characteristics. Among them, two industrially important test cases for which recent experimental results are available have been simulated and analyzed to validate the RFM model.

- 1- Simulation of a conventional cryogenic injection of liquid nitrogen coaxially with a hot hydrogen jet was performed using thermodynamic tables generated by two different equations of state: Peng-Robinson (PR) and Soave-Redlich-Kwong (SRK).
- 2- Simulation of the interaction between phase transition and turbulent fluid dynamics for subcritical and supercritical multi-species jets using different turbulence models including large-eddy simulations (LES Sigma and Smagorinsky) models as well as a Reynolds Averaged Navier-Stokes (RANS K- $\epsilon$ ).

The numerical results were found to be in good agreement with the available experimental data and published numerical studies, which also showed the relevance of the LES approach associated with the Sigma model for these very complex two-phase flows. Finally, numerical results showed that the tabulation method improves the liquid-vapor equilibrium (VLE) efficiency for real fluid modeling and provides a means to study and understand the structure of subcritical and transcritical liquid-gas interfaces revealing the hydro-thermodynamic characteristics of the multicomponent jet mixture.

# Contents

<b>1</b>	<b>General introduction</b>	<b>3</b>
1.1	Background and Motivation . . . . .	3
1.1.1	High pressure engines employing renewable fuels as a solution to achieve carbon-neutrality . . . . .	5
1.1.2	Real fluid jet mixing under subcritical and supercritical conditions . . . . .	6
1.1.3	Transcritical and supercritical injection regimes . . . . .	9
1.1.4	Effect of nozzle geometry in high pressure injections . . . . .	10
1.2	Objectives of the thesis . . . . .	11
1.3	Outline of the thesis . . . . .	12
<b>2</b>	<b>Physical concept and classical models of two phase flows</b>	<b>14</b>
2.1	Physical concepts . . . . .	16
2.1.1	Introduction . . . . .	16
2.1.2	Review on transcritical and supercritical injection . . . . .	16
2.2	Classical models of two phase flows . . . . .	20
2.2.1	Review on numerical and thermodynamic models for two-phase flows . . . . .	20
2.2.2	DIM for two-phase flow modeling . . . . .	23
2.2.3	How to select a thermodynamic model . . . . .	26
2.2.4	Equations of state . . . . .	27
2.2.5	Vapor Liquid Equilibrium . . . . .	29
2.3	Conclusion . . . . .	35
<b>3</b>	<b>High performance simulation using tabulated real fluid EOS considering VLE</b>	<b>36</b>
3.1	Real fluid model (RFM) . . . . .	36
3.1.1	Governing equations of the flow solver . . . . .	37

3.1.2	Equilibrium thermodynamic closure of the flow solver, and the tabulation look-up . . . . .	38
3.1.3	Validation of the VLE solver . . . . .	41
3.1.4	Coupling the flow solver with the thermodynamic solver . . . . .	42
<b>4</b>	<b>Thermodynamic table refinement approaches</b>	<b>47</b>
4.1	Review on the VLE Tabulation Approaches . . . . .	48
4.2	Preliminary Remarks on VLE Tabulation . . . . .	49
4.3	Introduction to data structuring . . . . .	54
4.3.1	Uniform Tabulation . . . . .	54
4.3.2	Non-Uniform Tabulation: Quadtree and Octree . . . . .	59
4.3.3	IFPEN Shared Memory for refined Uniform Table storage and access . . . . .	71
4.4	Preliminary highly resolved RFM simulations . . . . .	72
4.5	Conclusion . . . . .	78
<b>5</b>	<b>Application to “ High-pressure modeling of multi-component two phase flow with phase change”</b>	<b>80</b>
5.1	Towards understanding the structure of subcritical and transcritical multi-species liquid-gas interfaces . . . . .	82
5.1.1	Transcritical mixing and evaporation study . . . . .	85
5.1.2	Transcritical single-component Cryogenic injection . . . . .	89
5.1.3	Binary coaxial injection of $LN_2$ with hot $GH_2$ . . . . .	93
5.1.4	Conclusion . . . . .	104
5.2	Exploring the interaction between phase separation and turbulent fluid dynamics in multi-species supercritical flow jets . . . . .	106
5.2.1	Introduction . . . . .	106
5.2.2	Equilibrium thermodynamic closure of the flow solver, and the tabulation look-up . . . . .	109
5.2.3	Analytical study of condensing supercritical jet . . . . .	111
5.2.4	Results and discussion . . . . .	113
5.2.5	Quantitative validation . . . . .	126
5.2.6	Conclusion . . . . .	130
<b>6</b>	<b>Summary, conclusion, and future work</b>	<b>132</b>
6.1	Summary and conclusions . . . . .	132

6.2	Future work . . . . .	136
6.2.1	Cavitation simulation . . . . .	136
6.2.2	Real fluid simulations by machine learning . . . . .	137
6.3	Sommaire et conclusions . . . . .	139
<b>Appendix</b>		
A	One dimensional validation of shock tube test case	144
B	Mixing layer study of Methane-Oxygen using different EOS	146
C	Cavitation	148
	<b>Bibliography</b>	<b>150</b>

# List of Figures

1.1 Global warming: Land and ocean temperature departure in January 2021 from the average temperature since 1981 up to 2010 worldwide. (Credit: national centers for environmental information: [1]) . . . . . 4

1.2 Effect of varying the ambient pressure on the injection of a supercritical fuel. ( $p_{inj} = 200$  bar,  $T_{inj} = 554K$ ,  $T_{ch} = 957K$ ,  $T_r = \frac{T}{T_c} = 1.09$  where  $T_c = 507.6K$  is n-hexane critical temperature.) [11] . . . . . 6

1.3 Regime diagram for n-dodecane injected at a temperature  $TF = 363$  K into gaseous nitrogen at varying ambient pressures and temperatures. Regimes of classical sprays and diffusion-dominated mixing are found based on the Knudsen number criterion, studies by [12, 13]. Classical spray phenomena are exhibited at the low-temperature condition (b), while diffusion-dominated mixing dynamics are observed at the high-temperature condition (c). . . . . 7

1.4 Interfacial density profiles and thicknesses for the low-temperature (a) and high-temperature (b) interface states, calculated using Linear Gradient Theory studied by [12]. Regimes of classical sprays and diffusion-dominated mixing are found based on the Knudsen number criterion (1.1-1.2) studies by [12, 13]. Notice that Gradient Theory is entirely valid to calculate the physical mean density profile of molecular vapor-liquid interfaces. . . . . 7

1.5 Overview of morphology and mixing in supercritical jets [25]. The reservoir conditions are always supercritical, both in pressure and temperature. While the chamber pressure was varied from subcritical to supercritical values.  $\bar{P}$  is the reduced pressure, and  $\bar{s}$  is the reduced entropy. For the sake of simplicity, the paths indicated for the highlighted four jet behaviours in the  $\bar{P} - \bar{s}$  diagram assume isentropic flows. . . . . 10

1.6 The variation of saturation pressure for n-dodecane-N<sub>2</sub> system at a temperature range of 300 K-600 K with different N<sub>2</sub> concentrations [27](left), along with the experimental study of cavitation for n-dodecane-N<sub>2</sub> system inside nozzle (right) [26]. . . . . 11

2.1 Fluid state planes at subcritical and supercritical regimes. (a) The traditional perspective about the supercritical fluid behavior was that the distinction between the liquid and gas phases vanishes above the critical point (CP). (b) With the new perspective, the supercritical fluid states are not homogeneously distributed but, it can be differentiated into two distinct regions with gas-like and liquid-like regions. It is revealed that these two regions could be separated by a virtual line, the so-called Widom line or pseudo-boiling line( [20,24,34]). . . . . 17

2.2 Experimental images (adapted from [23]) of pure liquid N<sub>2</sub> injection from subcritical to supercritical pressure conditions (a-c). A schematic showing the three (subcritical (a), transcritical (b), and supercritical (c)) isobaric paths for a single component (a-c). Figure (d) denotes different modelling regimes with regards to the variation of  $T_r$  and  $P_r$ , schematically. The variations of the density, and isobaric heat capacity of pure nitrogen at transcritical condition calculated in this study, using PR EoS, are shown in the Figure (e) where liquid-like properties are colored in blue and gas-like properties are colored in red. . . . . 19

2.3 Comparison and validation of the thermodynamic model calculated in this study with the data of NIST [66] for different EoS for density, isobaric heat capacity, sound speed, and viscosity, respectively, for pure N<sub>2</sub>. PR, and SRK refer to the Peng Robinson, and Soave-Redlich-Kwong equation of states. The viscosity is calculated by the Chung correlation [68]. . . . . 23

2.4 A proposal for thermodynamic model selection for property calculations, has been suggested by [71]. The black area is two phase domain, vapour-liquid equilibrium. 27

2.5 Flow chart of the thermodynamic solver for generating the properties table . . . 31

2.6 Phase diagram for a single component of n-dodecane, plotted in PT diagram colored by density value, and calculated by Peng Robinson equation of states, PR EoS. . . . . 32

2.7 Schematic of a phase diagram for a multicomponent system with two components, binary system. The variation of mixture density for a binary system consists of 80% $C_{12}H_{26}$  – 20% $N_2$  at a temperature range of 50 K-1050 K and pressure range up to 20 MPa. . . . . 33

2.8 Phase diagram for a ternary system consists of n-dodecane-ethanol-nitrogen colored with mixture gas volume fraction and mixture density . . . . . 34

2.9 Comparison of mixture critical point for  $C_{12}H_{26}$  –  $N_2$  system, computed by commercial software Simulis based on Peng-Robinson EoS with experimental data [5] 35

3.1 Schematic of the thermodynamic table, and the properties calculated, and stored at each cell. P1:P8 are the 8 points of the thermodynamic cell surrounding the unknown point (X). Interpolation approach is based on the inverse distance weighting method. . . . . 40

3.2 Vapor-Liquid equilibrium of  $H_2$ - $N_2$  calculated in this study using SRK-EoS compared to the experimental data [82]. . . . . 41

3.3 Different properties variations as a function of temperature and  $H_2$  mass fraction for binary mixture of  $H_2$ - $N_2$  at P=4 MPa . . . . . 42

3.4 (a) Flow chart of the decoupled flow solver and thermodynamic solver used in [17] for the SIMPLE algorithm and (b) the proposed flow chart of the fully coupled flow solver and thermodynamic solver applied in the SIMPLE algorithm. . . . . 43

3.5 Flow chart of the RFM PISO algorithm. . . . . 44

4.1 (a) Pressure-Temperature diagram for pure n-dodecane, and nitrogen, and (b) Pressure-Molar composition diagram for binary mixture of n-dodecane-nitrogen ( $C_{12}H_{26}$  –  $N_2$ ) at different temperatures. . . . . 49

4.2 Effects of the refinement of the table on the data distributions: (a) The mixture density ( $\rho_{Mix}$ ) variations of n-dodecane-nitrogen ( $C_{12}H_{26} - N_2$ ) as a function of n-dodecane mass fraction at different pressures of P=1 bar, and P=10bar at  $T = 291K$  for grids refined with 500 points in mass fraction axis. (b) The mixture density variations of n-dodecane-nitrogen ( $C_{12}H_{26} - N_2$ ) as a function of n-dodecane mass fraction at P=1 bar at  $T = 291K$  for coarse grids with 100 points in mass fraction axis. (c) The mixture sound speed ( $C_s$ ) variations, using Wood formula [93] for two phase region, of n-dodecane-nitrogen ( $C_{12}H_{26} - N_2$ ) as a function of mixture gas volume fraction at P=1 bar at  $T = 291K$  for refined table-grids with 500 points in mass fraction axis. (d) The mixture sound speed variations, using Wood formula [93] for two phase region, of n-dodecane-nitrogen ( $C_{12}H_{26} - N_2$ ) as a function of mixture gas volume fraction at P=1 bar at  $T = 291K$  for table-grids refined with 100 points in mass fraction axis . . . . . 50

4.3 Variations of n-dodecane density as a function of pressure at constant temperature T=300 K. Coarse and medium grids generation, the non-refined tables, with red and green colors with different numbers of points on the pressure axis, lead to the appearance of virtual saturation points. The profile with the refined table is shown with blue color as "True profile". The locus of virtual saturation points have been marked with the red and green color for two different non-refined tables. These nonphysical saturation points lead to movement of the phase transition position, which is a function of the number of grid points, and it commences to various phase change nonlinearities and behaviors for the flow. . . . . 51

4.4 Variations of mixture density for the binary mixture of n-dodecane-nitrogen ( $C_{12}H_{26} - N_2$ ) as a function of pressure at different n-dodecane mass fractions at  $T = 291K$ . Since the variation of density due to pressure changes is negligible for incompressible and is considerable for compressible flow, by changing the saturation points, the compressibility or  $\frac{dP}{d\rho}$  of the flow will be changed. . . . . 52

4.5 2D refinements near the phase boundary for pure oxygen colored with density at PT diagram [92] . . . . . 53

4.6 P-T diagram for pure n-dodecane colored by density. . . . . 54

4.7 (a) Contour plots of mixture density, (b) Mixture gas volume fraction, (c) Mixture sound speed, for a typical n-dodecane-nitrogen mixture (80% of  $C_{12}H_{26}$  and 20% of  $N_2$ ). The results as well indicate different nonlinearities at dissimilar conditions for the properties. . . . . 55

4.8 Distribution of pure n-dodecane density as a function of pressure at T=293 K using 1000 points the normal space (a), and logarithmic space (b). The pressure axis is in the range [0, 1 MPa] in the normal space which corresponds to the range [0, 6] in the logarithmic space. The zoom in (a) shows the phase transition jump of density at the saturation pressure ( $P_{sat} \approx 140Pa$ ). Note that  $\log_{10}140 \approx 2.2$  in (b). This figure shows that uniform table with a  $\log_{10}P$  axis can be helpful for better discretize the pressure axis. As it demonstrates, there are lots of points before and after the saturation point at  $P_{sat} = 140Pa$ . Hence, it designates more points for low pressures, and less points for high pressures using logarithmic distribution with the base value more than Neper( $e=2.7182$ ) value. . . . . 58

4.9 Schematic of linear (a) and logarithmic distribution (b) of density contour in pressure axis in PT, and  $\log_{10}P - T$  spaces . . . . . 58

4.10 Typical schematics for (a) the one-dimensional (1D) refinement, (b) the Quadtree 2D refinement (usually used for the tabulation a single component in P-T space), and (c) the Octree 3D refinement (usually used for the tabulation of binary mixtures in P-T-Y space). . . . . 59

4.11 Snapshot of the implemented Octree code . . . . . 62

4.12 Two different algorithms for space-filling curve as BFS, which stands for Breadth-First Search (a), and DFS stands for Deep First Search (b). As shown, BFS and DFS generate different neighbors, affecting the searching algorithm mechanism and interpolation approach. . . . . 63

4.13 Different types of searching algorithms, and CPU time complexity . . . . . 65

4.14 Binary, Interpolation, and two other hybrid searches models run time variations for different array sizes for an indeterminate uniform data distribution (a), a normal data distribution (b), an exponential data distribution (c) studied by [100]. Adaptive search and IBS approaches (interpolated binary searches; hybrid model) have been developed by [100]. As the figures demonstrate, the costs will differ for various distributions for different algorithms, and there is no best approach for unknown distributions. . . . . 66

4.15 Schematics of BFS or level by level (a) and DFS, or sorted (b) arrays in addition with the schematic of P-Y diagram for unstructured framework(c). . . . . 67

4.16 Double expansion test case results at  $t = 3.5ms$ . Numerical comparisons between the RFM model using a uniform tabulation method, and the results of the IFP-C3D solver [5, 17, 22, 27], which employs an online (UV)-flash calculations for the physical properties of  $C_{12}H_{26} - N_2$  mixture for various specified initial mass fractions. . . . . 69

4.17 Different physical properties of  $C_{12}H_{26} - N_2$  mixture in shock tube test case for various mass fraction along 1m long tube . . . . . 70

4.18 Geometry setup, boundary conditions and working parameters used in the case of n-dodecane liquid injection into supercritical nitrogen. . . . . 73

4.19 Instantaneous contour plots at  $t = 60\mu s$  obtained from simulations of n-dodecane injected at  $T_{inj} = 600K$  and inflow velocity of 200 m/s into nitrogen at  $T_{ch} = 972K$ , for two different chamber pressures: first column  $P_{ch} = 6MPa$ , and left column  $P_{ch} = 11MPa$ . Phase indicator, PHI = 0 designates a liquid state with blue color, PHI = 1 designates a gas state with red color, and PHI = 2 refers to two phase state with black color. . . . . 74

4.20 Instantaneous contour plots at  $t = 60\mu s$  obtained from simulations of n-dodecane injected at  $T_{inj} = 658K$  and inflow velocity of 200 m/s into nitrogen at  $T_{ch} = 972K$ , for two different chamber pressures: first column  $P_{ch} = 6MPa$ , and left column  $P_{ch} = 11MPa$ . Phase indicator, PHI = 0 designates a liquid state with blue color, PHI = 1 designates a gas state with red color, and PHI = 2 refers to two phase state with black color. . . . . 76

4.21 Temperature-nitrogen mole fraction diagram colorized with mixture density at two different pressures  $P_{ch} = 6 MPa$ , and  $P_{ch} = 11 MPa$  . . . . . 77

4.22 Temperature-nitrogen mole fraction diagram colorized with phase indicator, phase state contour, at two different pressure  $P_{ch} = 6 MPa$ , and  $P_{ch} = 11 MPa$ . The yellow cross shows the locus of mixture critical points at the two different pressures. Also, AMT, which denotes adiabatic mixing temperature, demonstrates the locus of mixture temperature at adiabatic conditions for two different conditions with inflow temperatures of  $T_{inj} = 600K$  colorized with gray, and  $T_{inj} = 658K$  colorized with orange in Temperature-nitrogen mole fraction diagram at  $P_{ch} = 6 MPa$ . . . . . 77

4.23 Instantaneous contour plots at  $t = 60\mu s$  obtained from the present tabulated simulation (a) of n-dodecane injected at  $T_{inj} = 658K$  and inflow velocity of 200 m/s into nitrogen at  $T_{ch} = 972K$ ,  $P_{ch} = 6$ , compared to the study of [38] using direct evaluation of real fluid equations of state (b), for different properties, as mixture isobaric heat capacity, mixture viscosity using Chung correlation in both studies [68], and pressure, from top to down, respectively. . . . . 78

5.1 (a) Schematic for a liquid-like  $LN_2$  main stream injected in the center, and a secondary hot supercritical gaseous  $H_2$  injected co-axially into a combustor at a pressure higher than the critical pressures of the two non premixed components. This figure sketches the case in which the liquid core is partially covered by  $GH_2$  jet. The liquid core interface is divided into two parts. The leading interface part 1 is a transcritical interface (see the dashed line colored in red). A subcritical interface is formed upstream between the main  $LN_2$  flow and the secondary  $GH_2$  flow (see the dashed line colored in blue). (b) The gas volume fraction contour plot in a temperature and  $H_2$  composition diagram shows the locus and the thermodynamic states for subcritical ( $N_2 - H_2$ ) interface. (c) The isobaric heat capacity of  $N_2$ , has a peak value, on the widom line, at the transcritical interface between  $LN_2$  and  $GN_2$ . . . . . 83

5.2 Phase envelope movements and critical point variations for different compositions for  $N_2 - H_2$  mixture. . . . . 84

5.3 Case 1, comparison of different results for the density, temperature, pressure, velocity, heat capacity, and gas volume fraction, respectively, using PR-EoS, for the transcritical shock tube between the presented model in this study named the RFM and Ma et al. [34] at  $500\mu s$ .  $CFL = 0.1$  for the RFM model and  $CFL=0.8$  for the Ma model. The thin dashed lines are the initial conditions. . . . . 86

5.4 The impacts of pressure variations on the properties evolution for the transcritical shock tube test case, defined as case 1:3 in table 5.1, using PR-EoS, on (a) Pressure profile, (b) Temperature profile, (c) density profile, (d) Isobaric heat capacity, using SIMPLE numerical scheme, at  $t=500\mu s$ . Also, a comparison between SIMPLE and PISO schemes for cases (3-4) shows a good agreement between them at this condition. . . . . 87

5.5 Setup of transcritical jet simulation . . . . . 89

5.6 Case 5 instantaneous contour plots of density, heat capacity, and phase indicator (PHI); PHI=0 designates a liquid state and PHI=1 designates a gas state. . . . . 91

5.7 Case 5 instantaneous contour plots of temperature and vorticity fields at trans-critical condition at t=5 ms. The position of interface between the liquid like and gas like at Pseudo boiling line, at temperature contour, is determined by  $C_{p,max}$  iso-line, colored by white. The  $C_{p,max}$  at the interface acts like a thermal shield for the jet. . . . . 92

5.8 Case 6, instantaneous contour plots of temperature and isobaric heat for super-critical nitrogen injection at T=150K and P= 6 MPa after t=5 ms. . . . . 92

5.9 Case 7, instantaneous contour plots of density, temperature, and isobaric heat capacity for supercritical nitrogen injection at T=135K and P= 4 MPa after t=5 ms. Isobaric heat capacity (Cp) reduces continuously from liquid jet to the chamber, and there is no peak at Cp, no thermal shield at the interface, no thermal shield, and it has a symmetrical distribution. Hence, there is no crossing of Widom line, which proves that the jet is in supercritical regime. . . . . 92

5.10 Case 8: (Left) Schematic of the injector experimental configuration: blue and red color indicate  $LN_2$  and  $GH_2$  canals, respectively. (Right) Computational domain in the central cut-section of the simulated 3D geometry. AMR is used based on the criterion of the minimum velocity of 0.1 m/s. . . . . 94

5.11 Distribution of mixture density (Left), and  $H_2$  mass fraction (Right) . . . . . 96

5.12 Distribution of  $H_2$  density, temperature, and phase indicator (in the central cut-section) using the two different EoS at t = 4.5 ms. PHI=0, 1, 2 denotes liquid, gas, and two-phase states. . . . . 97

5.13 Temperature  $H_2$ -composition phase diagram for binary mixture of  $N_2$ - $H_2$  at P= 4 MPa, calculated by PR-EoS, compared with [28], used PR-EoS, along with the adiabatic mixing temperature (AMT) . . . . . 98

5.14 Distribution of mixture heat capacity (Left), and reduced temperature.  $T_r = T/T_{c,mix}$  (Right) where  $T_{c,mix}$  is the mixture critical temperature. The subcritical region for the mixture where  $T_r < 1$  is colored by white colour. . . . . 99

5.15 Radial reduced temperature and gas volume fraction profiles at X=3 mm after t=3 ms. The radial axis is displayed in Figure 5.14(b). . . . . 100

5.16 Different properties contours plotted at t=4 ms as (a) Mixture gas volume fraction, (b) Mixture compressibility factor, and (c) Mixture sound speed. . . . . 101

5.17 Axial and radial density profiles compared to the experimental [29] and the LES study Matheis et al. [28].  $D_i = 1.9mm$  . . . . . 102

5.18 Pressure oscillations of the flow field in the chamber at the central cut section. The initial ambient pressure in the chamber is  $P = 4$  MPa. . . . . 103

5.19 Illustration of the phase transition in subcritical states (i.e., evaporation and condensation processes) when the coexistence line is crossed, and gradual phase change processes in the transcritical regime (i.e., pseudo-boiling and pseudo-condensation) when crossing the Widom line. Pressure-Temperature diagram: (a) Density contour mapped by coexistence and Widom lines, and (b) Heat capacity contour for  $C_6H_{14}$ . Nonlinear behavior is present along the Widom line but also along the liquid-vapor coexistence line. . . . . 107

5.20 Comparison of PR-EoS and ideal gas EoS with reference data obtained from NIST [66] for n-hexane at  $P = 5MPa$  showing a) Density, and b) Isobaric heat capacity profiles. The results, using PR-EoS, Peng Robinson equation of state, are in a good agreement with NIST data [66], however the fluid properties specially for isobaric heat capacity (outside the range) significantly differ from an ideal gas at this high pressure  $P = 5MPa$ . . . . . 110

5.21 Vapor-Liquid equilibrium of  $C_6H_{14} - N_2$  calculated in this study using PR-EoS compared to the experimental data [110] . . . . . 110

5.22 Contour plots of mixture density(a), and mixture heat capacity(b) for  $C_6H_{14} - N_2$  at  $P_{ch} = 5MPa$ . As the plots show, due to the different non-linearity for various properties, the grid independency for having a refined thermodynamic table is mandatory. . . . . 111

5.23 Condensing and non-condensing supercritical regime (a) at different pressures, (b) at different temperatures. AMT denotes adiabatic mixing temperature, plotted by dash lines, and by crossing the phase boundary(dew points line), the droplet nucleation, and the condensation begins and develops at the periphery of the jet. If the AMT doesn't cross the two-phase dome, it will remain at supercritical regime without any nucleation process, non-condensing supercritical regime (pure supercritical regime). . . . . 112

5.24 Schematic of the injector setup as (a) Geometry setup, and (b) Computational domain grid discretization. Fixed embedding has been used to refine the grid at specific locations in the domain. (Local grid size = (Base grid size) /  $2^{embed_{scale}}$ ). The base grid size was set to  $30\mu m$  so that the minimum grid size near the nozzle exit has been specified to be  $7.5\mu m$  using an  $embed_{scale} = 2$ . . . . . 114

5.25 Temperature  $N_2$ -composition phase diagram for binary mixture of  $C_6H_{14} - N_2$  at  $P = 5$  MPa, calculated by PR-EoS along with the adiabatic mixing temperature (AMT). (a) includes the comparison with [30] along with the three scatter plots of the numerical LES mixing temperature results. The low scattering of the LES mixing temperatures indicate almost adiabatic injection flows. The graphical insert shows that the LES mixing temperature scatterplots for the T560 case do intersect the dew line and enter the two-phase region. (b) includes the theoretical AMT for the three cases and show the same behavior as the RFM model for case T560. The two-phase region background is colorized by the gas volume fraction values. . . . . 115

5.26 Comparison of experimental (left(1)) and numerical snapshots (right(2)) for the three test cases (T480, T560, and T600). The ELS image superimposed onto the corresponding shadowgraph are used to visualize both the flow structure as well as the thermodynamic state (adapted from [30]) in quasi-steady state condition.  $\alpha_{Gas}$  is the gas volume fraction . . . . . 116

5.27 Temporal evolution of (temperature +gas volume fraction( $\alpha_{Gas}$ )) contours using Sigma turbulence model for case T=480. . . . . 117

5.28 Temporal evolution of (temperature +gas volume fraction ( $\alpha_{Gas}$ )) contours using Sigma turbulence model for case 560 (see table 5.3). . . . . 118

5.29 T560 case results: contour plot of (a) Temperature, (b)  $C_6H_{14}$  mass fraction, (c) Phase indicator in which PHI= 1, 2 denotes single phase and two-phase states, respectively, and (d)  $C_6H_{14}$  liquid mass fraction. This mass fraction ( $Y_{C_6H_{14},l}$ ) is defined as the ratio of  $C_6H_{14}$  density in the liquid phase (index  $l$ ) with respect to the liquid density ( $\rho_l$ ), as  $Y_{C_6H_{14},l} = \alpha_l \rho_{C_6H_{14},l} / \rho_l$ . . . . . 120

5.30 Impacts of turbulence modellings of the jet structure for various properties for two phase flows using ( $k - \epsilon$ ) RANS, LES-Smagorinsky, and LES-Sigma models, respectively, from top to down, at  $t=2.5$  ms. . . . . 123

5.31 Impacts of turbulence modellings on different turbulent properties using different  $(k-\epsilon)$  RANS, LES-Smagorinsky, and LES-Sigma models, respectively, from top to down, at  $t=2.5$  ms at  $X/D = 10$ . Due to the much higher values from the  $(k-\epsilon)$  model for the different turbulent properties, they have been divided by 100, 100, and 20 for turbulent viscosity, TKE, and turbulent conductivity, respectively, to be in the same range as LES data. . . . . 124

5.32 Impacts of density gradient on the turbulent properties, at  $t=2.5$  ms at  $X/D = 10$ , using LES-Sigma model. . . . . 124

5.33 (a) Density gradient, (b) Pressure gradient and (c) Vorticity contours at the interface at  $t=2.5$  ms. The misalignment of spatial pressure and density gradients is at the origin of the baroclinic torque source term. . . . . 125

5.34 (a) Mean velocity field ( $\bar{U}$ ), (b) The resolved velocity ( $U$ ) at 3 ms, and (c) The velocity profile plotted along the jet axis where the resolved velocity is at 3 ms and the mean velocity is computed using the LES results in the time interval between 2 and 3 ms after the start of injection. For this case, a fluctuating boundary condition has been superimposed on the inflow velocity profile using Fourier method with 5% intensity. . . . . 127

5.35 Temperature- $N_2$  mole fraction diagram for binary mixture of  $N_2-C_6H_{14}$ , colorized with the mixture sound speed, using Wood formula for two phase region [93] at  $P= 5$  MPa, using PR-EoS, along with the phase boundary (in black). The scatter plots (white points) show the locus of the mixing temperature obtained by the RFM-LES model for the case with  $T_e = 627K$  simulation. . . . . 128

5.36 The top LES results at  $t = 3ms$  are: (a) Instantaneous contours of the mixture temperature, (b) n-hexane mass fraction at  $Z=0$  cut section. The bottom LES results (c) at  $t = 3ms$  are the mixture sound speed at  $z = 0$  (left), and at  $x/D_i = 35$  cut sections (right). The sound speed in the chamber, filled initially with the  $N_2$  at  $T_{ch} = 296K$ , is  $C_{s,ch} \approx 360m/s$  (orange color). At the nozzle exit where  $T_e = 627K$ , the sound speed is  $C_{s,exit} \approx 197m/s$  (blue color). . . . . 129

5.37 Validations of mixture sound speed with experimental data of Baab et al. [31],  
 (a) Along the jet axis, and (b) At radial direction at  $x/D_i = 35$  determined and  
 plotted at Figure 5.36. LES results colorized with gray thin line denotes the  
 LES-sigma results for some instantaneous times in the range of  $t=2-3$  ms. LES  
 simulation @  $t=3$  ms shows the variations of the mixture sound speed at  $t=3$  ms,  
 as shown in Figure 5.36. . . . . 129

5.38 Instantaneous contours of (a) n-hexane mole fraction, at  $Z=0$  cut-section at  $t =$   
 $3ms$ , and (b) Validations of LES n-hexane mole fraction, along the jet axis, with  
 the analytical self-similar solutions calculated by Gerber et al. [25]. They hired PR  
 EoS, and REFPROP data to analytically calculate fuel mole fraction at different  
 distances from the nozzle exit. LES results colorized with gray thin line denotes  
 the LES-sigma results for some instantaneous times in the range of  $t=2-3$  ms. LES  
 simulation @  $t=3$  ms, with blue color shows the variations of the n-hexane mole  
 fraction, shown in contour plot in (a). . . . . 130

6.1 (a) X-ray tomography of a Spray C nozzle [132]; (b) Computational domain grids.  
 Fixed embedding has been used to refine the grid in the nozzle orifice and the  
 needle seat, as shown in the different inserts. . . . . 136

6.2 Illustration of cavitation appearance inside the orifice by gas volume fraction con-  
 tour at a condition with no needle movement (fully open sac). . . . . 137

A.1 Schematic representation of  $H_2O - N_2$  mixture along 1m long shock tube test case. 144

A.2 Comparison between the presented numerical model using PISO, and SIMPLE  
 algorithm with [5, 53] for  $Y_{H_2O} = 0.3$  for the binary mixture of  $H_2O - N_2$  along  
 1m long tube at  $t = 1ms$ . . . . . 145

A.3 Comparison between the presented numerical model using PISO, and SIMPLE  
 algorithm with [5, 53] for  $Y_{H_2O} = 0.98$  for the binary mixture of  $H_2O - N_2$  along  
 1m long tube at  $t = 1ms$ . . . . . 145

B.1 Mixing layer configuration of methane-oxygen and computational domain. (left)  
 Typical coaxial injector of a liquid rocket engine. (right) Computational domain  
 dimensions and boundary conditions [109, 138]. . . . . 146

B.2 Comparison of instantaneous methane mass fraction (left) and Temperature (right)  
 using different equations of state, at 0.125 ms ( half flow-through-time). . . . . 147

B.3 Comparison of instantaneous sound speed (left) and isobaric heat capacity (right) using different equations of state, at 0.125 ms (half flow-through-time).  $C_{p,mix}$  has the maximum value at the interface. . . . . 147

C.1 (a) Schematic of a cavitation injector setup (geometry setup), (b) In addition with the experimental X-ray tomography of Winklhofer cavitation nozzle [139] . . . . . 148

C.2 Gas volume fraction contours for different percentages of nitrogen dissolved gas added to the n-dodecane fuel, as 0%  $N_2$  (a), 0.1%  $N_2$  (b), and 1%  $N_2$  (c). The cavitation intensity increases by adding more nitrogen dissolved gas due to the changing saturation pressure with  $N_2$  concentration, as thermodynamic demonstrates in figure 1.6. . . . . 149

C.3 Gas volume fraction contours for different chamber pressures (various pressure differences between the chamber and the injector), as  $\Delta P = 40MPa$ (a),  $\Delta P = 60MPa$ ,  $\Delta P = 70MPa$ , from top to down, respectively. The cavitation intensity enhances by increasing the pressure differences between the chamber and the injector. Besides, Figure (b) demonstrates the cavitation region experimentally studied by [139]. . . . . 149

# List of Tables

2.1	Parameters for cubic equations of state (index c stands for critical value) . . . . .	28
4.1	Operating conditions for the transcritical n-dodecane- $N_2$ injection similar to the the study performed by Prof. Battistoni group [38] and Prof. Gavaises group [104].	72
5.1	Initial conditions for pure $N_2$ transcritical shock tube test cases for different pressures	85
5.2	Operating conditions for the transcritical cryogenic $N_2$ injection similar to the Mayer's experimental study [21]. . . . .	89
5.3	Operating conditions used for the current numerical study similar to the experi- mental study of [30]. . . . .	114
5.4	Operating conditions used for the current numerical study taken from Baab et al [31] experimental study. The nozzle exit temperature $T_e$ was estimated based on the assumption of an isentropic flow inside the injector calculated by [31]. . .	126
6.1	Injection and ambient conditions of ECN cavitation spray C . . . . .	136

# Nomenclature

$\alpha_g$	Gas volume fraction
$\Delta t$	Time step
$\Delta x$	Grid size
$\lambda$	Thermal conductivity
$\lambda_t$	Turbulent thermal conductivity
$\mu$	Dynamic viscosity
$\omega$	Accent factor
$\psi_g$	Gas vapor fraction
$\rho$	Density
$\tau$	Viscous stress tensor
$P_c$	Critical pressure
$T_c$	Critical temperature
$T_r$	Reduced temperature: $T/T_c$
<b>g</b> <sub>l</sub>	Gas-like
<b>g</b>	Gas
<b>l</b> <sub>l</sub>	Liquid-like
<b>l</b>	Liquid
<b>mix</b>	Mixture
a,b	Coefficients in PR EoS

BIP/ $k_{i,j}$	Binary interaction factor
BWR	Benedict–Webb Rubin
$C_p$	Isobaric specific heat capacity
$C_s$	Sound speed
CFL	Courant number: $U * \Delta t / \Delta x$
D	Diffusion coefficient
DIM	Diffused interface model
e	Specific internal energy
ECN	Engine Combustion Network
EoS	Equation of State
$K_i$	Equilibrium constant
LES	Large-Eddy simulation
$P_r$	Reduced pressure: $P/P_c$
PR	Peng Robinson
Pr	Prandtl number
$Pr_t$	Turbulent Prandtl number
RANS	Reynolds-averaged Navier–Stokes equations
Sc	Schmidt number
SRK	Soave-Redlich-Kwong
TP flash	Isothermal-isobaric flash
UV flash	Isoenergetic-Isochoric flash
VLE	Vapour liquid equilibrium
VOF	Volume of fluid
Y	Mass fraction
Z	Compressibility factor
$Z_i$	Mole fraction of component(feed)

## Acknowledgements

Firstly, I would like to convey my gratitude and thanks to my supervisor, Dr. Chaouki HABCHI for his considerable, valuable, continuous guidance and encouragement during my Ph.D. study. He has greatly influenced my growth as a critical thinker and researcher throughout my Ph.D. I believe all these traits will positively affect my future career.

Besides, I would like to convey my thanks to my advisors Dr. Pascal MOUGIN, and Dr. Jean-Charles DE HEMPTINNE for their guidance during writing my papers and manuscript.

I would also like to thank Dr. Angela DI LELLA for her support and providing the thermodynamic library, IFPEN-CARNOT. I also convey my thanks to my colleague Hesham GABALLA for his helps during my thesis. Besides, I would like to thank the colleagues in IFPEN, to name but a few, Kumar RAJESH. I also express my sincere thanks to Dr. Christian ANGELBERGER, Dr. Julien BOHBOT, Carole GUENAUD, and especially Dr. Gilles BRUNEAUX for their guidance and helps during the thesis. Furthermore, I would like to acknowledge Mr. Bruno DELHOM for his supporters in solving technical problems in CFD solver.

Furthermore, I would like to acknowledge the Ph.D. defense committee for their guidance and advice for reviewing the manuscripts and their valuable viewpoints during the defense meeting.

I also convey my sincere thanks to Dr. Mehdi SADEGHI for his encouragement and guidance during my PH.D. period in France.

I would also like to sincerely thank all my friends and families in IRAN who have constantly inspired me to be a better version of myself in all aspects. I am forever thankful to my parents and siblings for their unwavering support and love. The Ph.D. will never have been achieved without their continuous encouragement and support.

ALBERT EINSTEIN

**"IT IS NOT THAT I'M SO SMART. IT IS JUST THAT I STAY WITH PROBLEMS LONGER"**

## List of Publications

1. S. Jafari\*, H. Gaballa , C. Habchi, J.Ch. de Hemptinne, and P. Mougin, Exploring the interaction between phase separation and turbulent fluid dynamics in multi-species supercritical flow jets using a tabulated real-fluid model, J. Supercrit. Fluids, 2022  
<https://doi.org/10.1016/j.supflu.2022.105557>
2. H. Gaballa, S Jafari, C. Habchi, and J.Ch. de Hemptinne, Numerical investigation of droplet evaporation in high-pressure dual-fuel conditions using a tabulated real-fluid model, Int J. Heat. Mass Transf., 2022.  
<https://doi.org/10.1016/j.ijheatmasstransfer.2022.122671>
3. H. Gaballa , S Jafari, C. Habchi, and J.Ch. de Hemptinne, LES of high-pressure injection and mixing in a dual-fuel configuration using a tabulated real-fluid modeling approach, Submitted, proceedings of the Combustion Institute.
4. S Jafari\*, H. Gaballa , C. Habchi , and J.Ch. de Hemptinne, Towards Understanding the Structure of Subcritical and Transcritical Liquid–Gas Interfaces Using a Tabulated Real Fluid Modeling Approach. Energies. 2021; 14(18):5621.  
<https://doi.org/10.3390/en14185621>
5. S Jafari\*, H. Gaballa , C. Habchi , and J.Ch. de Hemptinne, A tabulated real-fluid modeling approach applied to cryogenic LN2-H2 jets evaporation and mixing at transcritical regime, ICLASS, 2021.  
[http://journals.ed.ac.uk/ICLASS\\_Edinburgh/article/view/5988](http://journals.ed.ac.uk/ICLASS_Edinburgh/article/view/5988)
6. H. Gaballa , S Jafari, C. Habchi, and J.Ch. de Hemptinne, A tabulated real fluid modeling approach applied to renewable dual-fuel evaporation and mixing, ICLASS, 2021. [http://journals.ed.ac.uk/ICLASS\\_Edinburgh/article/view/5952](http://journals.ed.ac.uk/ICLASS_Edinburgh/article/view/5952)
7. P. Yip, S. Jafari, S. Yang, C. Habchi, Numerical analysis of subcritical vaporization and transcritical mixing of droplet using a tabulated multicomponent vapor-liquid equilibrium model, ILASS, 2019.  
<https://ilass19.sciencesconf.org/browse/author?authorid=654508>

# Chapter 1

## General introduction

### Contents

---

<b>1.1</b>	<b>Background and Motivation</b> . . . . .	<b>3</b>
1.1.1	High pressure engines employing renewable fuels as a solution to achieve carbon-neutrality . . . . .	5
1.1.2	Real fluid jet mixing under subcritical and supercritical conditions . . . . .	6
1.1.3	Transcritical and supercritical injection regimes . . . . .	9
1.1.4	Effect of nozzle geometry in high pressure injections . . . . .	10
<b>1.2</b>	<b>Objectives of the thesis</b> . . . . .	<b>11</b>
<b>1.3</b>	<b>Outline of the thesis</b> . . . . .	<b>12</b>

---

### 1.1 Background and Motivation

Although global warming may bring some localized benefits, such as fewer winter deaths and increased food production in some regions, the overall impacts of climate-changing change are overwhelmingly negative. World health organization (WHO) has predicted that climate change will cause approximately 250,000 additional deaths per year between 2030 and 2050 from malnutrition, malaria, diarrhea, and heat stress due to the direct and indirect impacts of global warming in nature. Figure 1.1 shows the global warming: land and ocean temperature departure in January 2021 from the average temperature since 1981 up to 2010 around the world (Credit: national centers for environmental information [1]). As it demonstrates, climate change affects all regions around the world. Arctic ice shields are melting, the sea is rising, and extreme weather events and rainfall are becoming more common in some regions, while others are experiencing more extreme heat waves and droughts. Combining these changes is causing sea levels

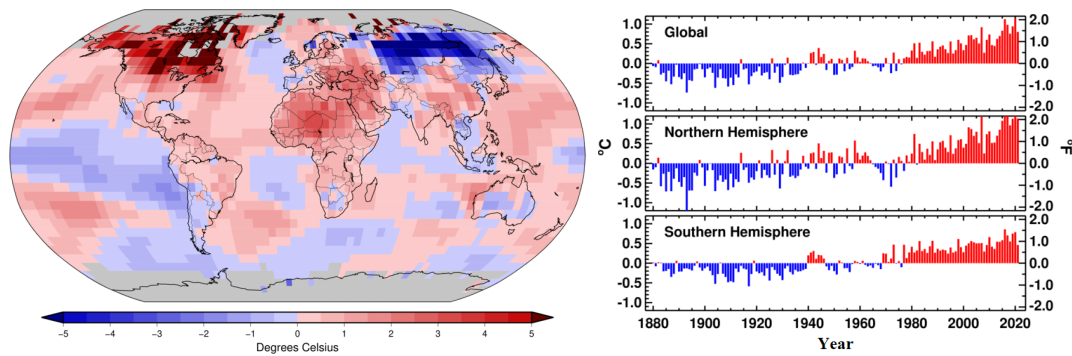


Figure 1.1: Global warming: Land and ocean temperature departure in January 2021 from the average temperature since 1981 up to 2010 worldwide.

(Credit: national centers for environmental information: [1])

to rise, resulting in flooding and erosion of coastal and low-lying areas. This cooling and heating of the weather in different parts of the world have also affected animals' and nature as a whole. To formulate a strategy to address these problems, the Paris agreement requires limiting global warming to well below 2, preferably 1.5 degrees, above pre-industrial levels.

The energy transition period is now underway to fulfill the Paris agreement's goals for access to efficient, resilient, and low-carbon energy services. This transition is a pathway toward transforming the global energy sector from fossil-based to carbon neutrality [2,3]. Renewable energies such as solar, wind, hydroelectric, geothermal, e-fuels, biomass, or nuclear energy and energy efficiency measures can potentially achieve 90% of the required carbon reductions, as shown in figure 1.1. Significant progress and studies have been made for alternatives for cleaner ways of fuelling for the transport sector such as electrified hybrid vehicles, bio-fuels (which are made from corn and sugarcane, such as bio-ethanol) and e-fuels, including hydrogen and ammonia made from renewable energy sources and methanol made from captured  $CO_2$  from power-plant exhausts or even from the atmosphere. In addition, stringent regulations of pollutant emissions now apply to new-generation combustion devices. Therefore, more investigations and efforts are needed to enhance energy efficiency and reduce pollution emissions from future devices using these renewable fuels.

Currently, several legislative strategies have been developed to promote a progressive replacement of fossil fuels by renewable fuels in sectors for which the electrification cannot be envisaged like the aviation and the shipping sectors. However, a real breakthrough in internal combustion engine (ICE) technology is needed to significantly reduce harmful emissions and dependence on fossil fuels by using alternative fuels. For the transportation sector, some promising solutions such as injection at higher pressure and temperature ratios or injection in high-pressure and high-temperature chamber conditions have shown various encouraging indications that should

be targeted to achieve the goals. These high pressures usually result in supercritical injection conditions for which the injection pressure exceeds the critical point of the pure fuel components. The utilization of these supercritical fluids has arisen as a powerful energy-efficient technology addressing climate change needs. Currently, various researches and Ph.D. studies have been done for high pressure combustion [4] and high-pressure injections modeling to better understand the behaviors and the flow regimes at supercritical conditions [5–7].

### 1.1.1 High pressure engines employing renewable fuels as a solution to achieve carbon-neutrality

Modern engines which employ renewable fuels (like  $H_2$ ,  $NH_3$  or methanol for instance) at conditions that exceed the respective fuel thermodynamic critical pressures offer a cheap promising technological approach to achieve carbon-neutrality and near zero-emission goals. Numerous studies on such modern engines demonstrate the increase of the combustion efficiency in gas turbines, diesel engines, and rocket engines [8–10].

One of the most promising internal combustion engines (ICE) is employed hydrogen, due to its carbon-free content and energy efficiency, especially when  $H_2$  is made from renewable sources like solar or wind-turbines. The new studies for these hydrogen engines demonstrate that the efficiency and emission productions of the engines depend on various parameters such as the injector configuration, and the injection pressure. For instance, Takagi et al. [9] have shown that the pressure increase for hydrogen injection positively impacts NOx production. Hence, increased injection and chamber pressure have numerous direct and indirect impacts on the jet characteristics and mixing, the flame structure and unsteadiness, and the pollutant emissions. Another example, as Figure 1.2, shows very recent experiments from [11], demonstrate the effects of varying the ambient pressure on the jet morphology for supercritical n-hexane fuel, ( $T_r = \frac{T_{inj}}{T_c} = 1.09$ , where  $T_{inj} = 554K$  and  $T_c = 507.6K$  is n-hexane critical temperature) at the following conditions: ( $P_{inj} = 200$  bar and  $T_{ch} = 957K$ ). These images particularly highlight the huge change in the jet shape when the expansion ratio  $P_{inj}/P_{ch}$  is increased. The axial location of the Mach disk is also a function of the expansion ratio  $P_{inj}/P_{ch}$  and is independent of fuel types according to [11]. The dome-shaped jet is visible for high expansion ratios to accommodate the larger pressure drop. In addition, the bowl shape of the jet becomes less pronounced when the chamber pressure is increased. They observed that the different disintegration regimes (subcritical or supercritical) depend strongly upon the ambient and injection conditions. Hence, the studying of subcritical and supercritical jets, as an essential parameter affecting the jet topology,

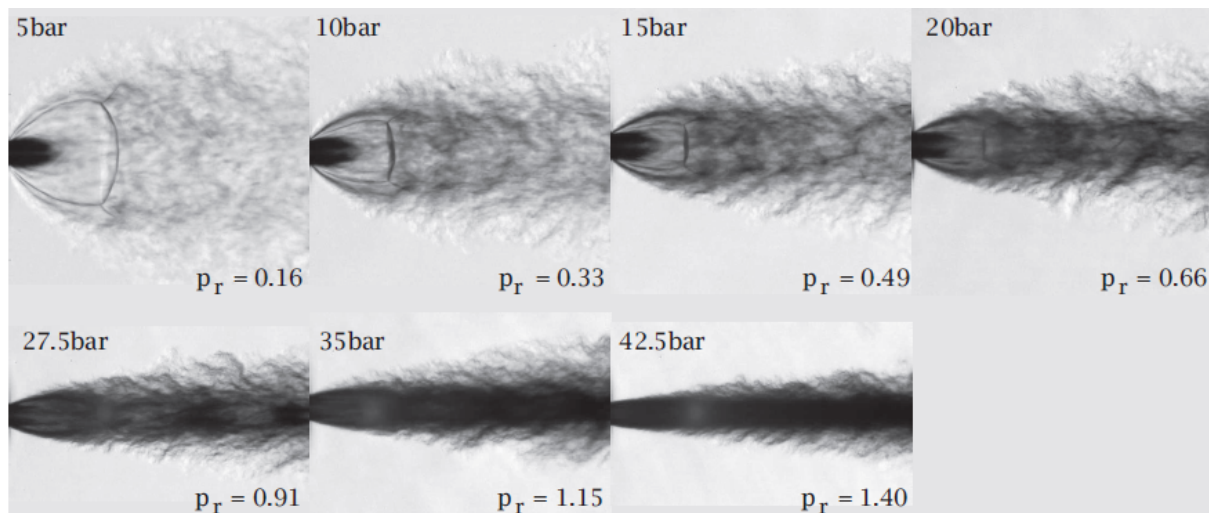


Figure 1.2: Effect of varying the ambient pressure on the injection of a supercritical fuel. ( $p_{inj} = 200 \text{ bar}$ ,  $T_{inj} = 554K$ ,  $T_{ch} = 957K$ ,  $T_r = \frac{T}{T_c} = 1.09$  where  $T_c = 507.6K$  is n-hexane critical temperature.) [11]

should be considered. **It is therefore vital and effective to have a CFD model capable of predicting various real fluid jets mixing at subcritical and supercritical conditions. This is the general objective of this thesis.** Indeed, the availability of such a CFD tool will facilitate the design of modern combustors such as gas turbines, diesel engines and rocket engines to contribute to the desired carbon neutrality.

### 1.1.2 Real fluid jet mixing under subcritical and supercritical conditions

Generally, injector flow dynamics and primary breakup processes (i.e. atomization) are known to be critical in determining engine combustion and emissions. Indeed, fuel injection and primary breakup in engines are typically understood as multiphase phenomena. It is well known that at low (typically subcritical) pressures, the classical atomization exists where a well-defined interface separates the injected liquid from ambient gases. Under these conditions, the surrounding gas inertia (due to injection pressure), the liquid density and viscosity, and mainly the surface tension forces control the primary atomization, and ligaments and droplets formation. However, at high-pressure conditions (typically supercritical relative to the critical pressure of the injected liquid), the situation becomes significantly different, and a distinct gas-liquid interface may formally not exist as only a diffused interface exist between the so-called liquid-like and gas-like. This phase-like are important in the present work and will be defined precisely in Chapter 1. **In summary, the transition between the classical subcritical discontinuous two-phase atomization phenomena which is associated with two-phase interface is relatively well-known processes, however the supercritical continuous gas-like-liquid-like in-**

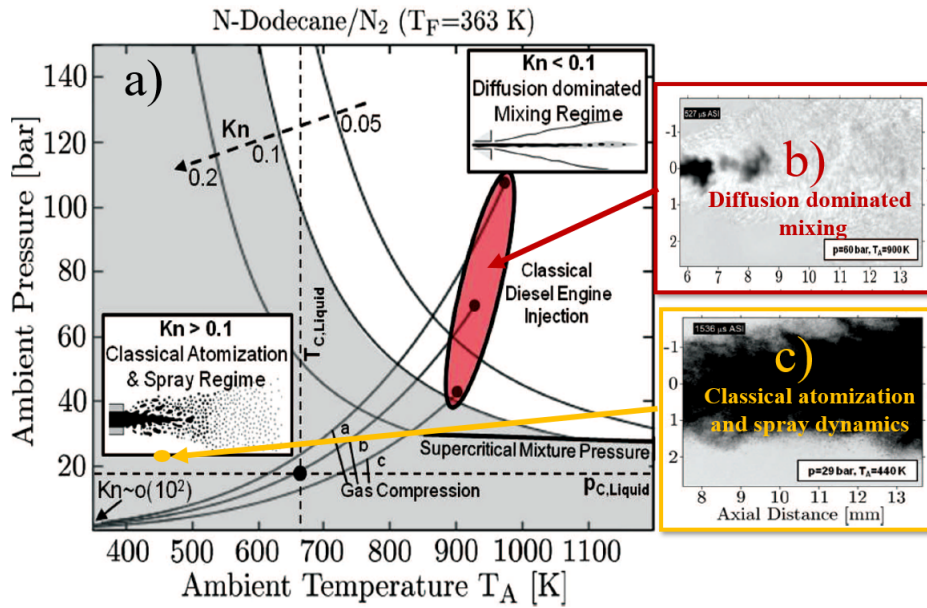


Figure 1.3: Regime diagram for n-dodecane injected at a temperature  $T_F = 363$  K into gaseous nitrogen at varying ambient pressures and temperatures. Regimes of classical sprays and diffusion-dominated mixing are found based on the Knudsen number criterion, studies by [12, 13]. Classical spray phenomena are exhibited at the low-temperature condition (b), while diffusion-dominated mixing dynamics are observed at the high-temperature condition (c).

terfacial diffusion-dominated mixing layers is not well understood, and therefore it will be investigated in this thesis. Some notable and exciting studies about this transition have been done by [12, 13]. Dahms et al. [12] established a theory for this transition by coupling the real-fluid vapor-liquid equilibrium theory (VLE) and Linear Gradient theory (LGT). This coupling reconstructs the molecular vapor-liquid interface structure to quantify the precise state of the interface as a function of specific injection conditions, as shown in Figure 1.3. The keynotes of their conclusions are summarized as follows.

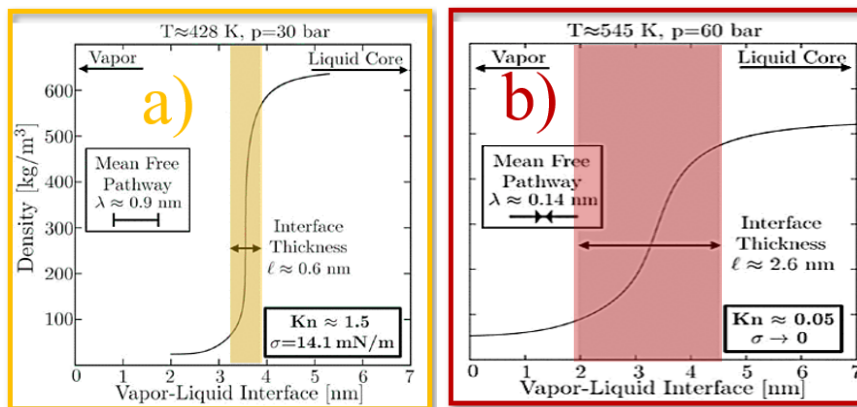


Figure 1.4: Interfacial density profiles and thicknesses for the low-temperature (a) and high-temperature (b) interface states, calculated using Linear Gradient Theory studied by [12]. Regimes of classical sprays and diffusion-dominated mixing are found based on the Knudsen number criterion (1.1-1.2) studies by [12, 13]. Notice that Gradient Theory is entirely valid to calculate the physical mean density profile of molecular vapor-liquid interfaces.

According to Dahms et al. [12], liquid-vapor transition is not necessarily induced by diminished surface tension forces alone but it is also due to the thickening of the interface which starts at high subcritical temperatures coupled with an inherent reduction of the mean free molecular path, as shown in Figure 1.4 (a, b). This occurs through the combination of three phenomenological factors:

- Broadening interface thickness.
- Reduced mean free path.
- A reduction in surface tension.

Figure (1.3, 1.4) have summarized the numerical and experimental studies done by [12, 13]. It shows the regime diagram for n-dodecane injected at a temperature  $T_F = 363$  K into gaseous nitrogen at varying ambient pressures and temperatures. Knudsen-number has been defined by Equations (1.1-1.2) as a criterion to classify the two distinct continuum and non-continuum interfacial regimes, shown in figure 1.3 via red and yellow colors.

$$k_n = \frac{\gamma}{l} \begin{cases} < 0.1 & \text{Continuum regime} \\ > 0.1 & \text{Non-Continuum regime} \end{cases} \quad (1.1)$$

$$\gamma = \frac{k_B T}{\sqrt{2\pi} P \sum_i X_i d_i^2} \quad (1.2)$$

Where  $l$  is the interface thickness and  $\gamma$  the molecular mean free path defined as a function of the  $k_B$ ,  $P$ ,  $X_i$ , and  $d_i$ , the Boltzmann constant, pressure, species mole fractions, and the molecular size of species  $i$ , respectively. As several assumptions have been made to estimate  $k_n$  by Equation 1.2, this criterion is not very accurate. But, it is shown in Figure 1.3 that it can be used to identify the atomization regime. Indeed, the Knudsen-number criterion indicates that the high-temperature interface falls within the fluid mechanic continuum regime ( $\text{Kn} < 0.1$ ), whereas the low-temperature interface exhibits a classical molecular interface. In addition, classical spray phenomena are exhibited at the low-temperature condition as figure 1.3(c), while diffusion-dominated mixing dynamics are observed at the high-temperature condition as shown in figure 1.3(b).

As a result, it can be concluded that the difference in the interfaces thickness in different regimes may be significant as they could influence the two-phase flow numerical results. Hence, this has to be considered for an accurate two-phase subcritical flow modeling. However, since the interface thickness in two phase flows is tiny, around nanometer, a diffuse interface method (DIM) has

been introduced by making the interface numerically thicker [14, 15]. This DIM approach is also very convenient because it is a unique method to simulate simultaneously subcritical and supercritical flows in addition to the transition between them, often encountered in many industrial applications, as it will be shown throughout this manuscript and especially in Chapter 5.

### 1.1.3 Transcritical and supercritical injection regimes

To achieve more efficient and cleaner operations in modern combustion engines, such as cryogenic engines, gas turbines, and high-pressure diesel engines, fuels are injected in the combustion chamber at pressures that exceed the respective fuel thermodynamic critical pressures. In addition, when the fuel is injected at a subcritical temperature, these operation conditions are referred to **transcritical injection regime** in the literature [6, 16–24]. However, the term **supercritical injection regime** is used when the temperature of the injected fuel exceeds its thermodynamic critical temperature. In these two regimes, the fluid properties are known to vary wildly at the phase boundary, especially near the critical point where even with minor variations in temperature or pressure, the jet behaves differently. The studies demonstrated that supercritical fluids are not homogeneous. However, they can be differentiated into two distinct regions with gas-like and liquid-like properties, respectively. These regions are divided by an extension of the coexistence line, commonly called the Widom line or Pseudo boiling line [20]. Figure 1.5 shows an overview of morphology and mixing in the supercritical injection regime, recently studied by Gerber et al. [25]. They experimentally studied and provided an overview on possible phase transition associated with fluid injection in the supercritical injection regime, either crossing the two-phase dome or crossing the Widom-line. Their experiments covered superheated liquid disintegration, pseudo-boiling transition, and single-phase jets under different nozzle/chamber pressure ratios.

Three test fluids, namely n-hexane, n-pentane, and fluoroketone have investigated in [25]. Pseudo-boiling effects emerge when a rapid change in pressure/temperature interact with the non-linear behavior of thermodynamic response functions (such as the density, compressibility or the specific heat capacity) across the Widom line. This situation is encountered when the shock train in moderately under expanded jets interacts with the Widom region, as shown in figure 1.5 with green color. Gerber et al. [25] concluded that the associated density fluctuations cause a significant enhancement in the scattering cross-section and may lead to the inception of thermo-convective instabilities. These findings demonstrate the importance of understanding the interaction and

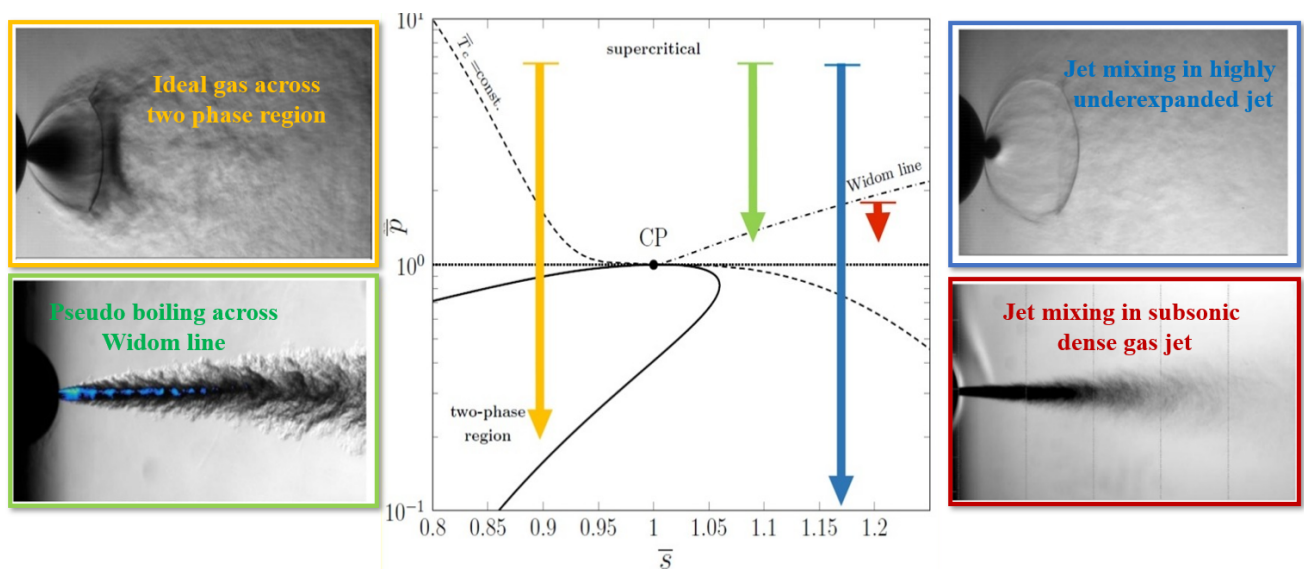


Figure 1.5: Overview of morphology and mixing in supercritical jets [25]. The reservoir conditions are always supercritical, both in pressure and temperature. While the chamber pressure was varied from subcritical to supercritical values.  $\bar{P}$  is the reduced pressure, and  $\bar{s}$  is the reduced entropy. For the sake of simplicity, the paths indicated for the highlighted four jet behaviours in the  $\bar{P} - \bar{s}$  diagram assume isentropic flows.

coupling of compressible real-fluid flows including pseudo-boiling effects. In addition, such studies have demonstrated that simple equations of state (EoS) like the ideal gas, or barotropic EoS, cannot capture the nonlinearities at transcritical regimes [6, 16–24]. **As a result, a real-fluid EoS is mandatory for the CFD simulation of the injection at transcritical and supercritical regimes.**

#### 1.1.4 Effect of nozzle geometry in high pressure injections

Another interesting phenomenon that occurs due to high-pressure injection and the sharpness of the nozzle is cavitation. High-pressure injections will cause very high fuel velocities inside injectors. Due to the injector geometric variations, this high velocity may lead to significant pressure gradients and local depressurization. Hence, cavitation will occur when the static pressure reduces to below the liquid's vapor pressure. Since the cavitation process is the development of vapor bubbles in a flowing liquid, the new studies demonstrate that the initial amount of dissolved ambient gas,  $N_2$ , has a considerable impact on the cavitation intensity by changing the saturation pressure of the liquid fuels, along with other parameters like pressure intensity, geometry sharpness, nozzle material, fuel type, etc. Figure 1.6(right) shows the experimental image of cavitation zone for the n-dodecane- $N_2$  system, studied by [26]. This cavitation in the nozzle will change the flow structure, the atomization topology, and as a result, the combustion characteristics and behaviors of the flow, respectively.

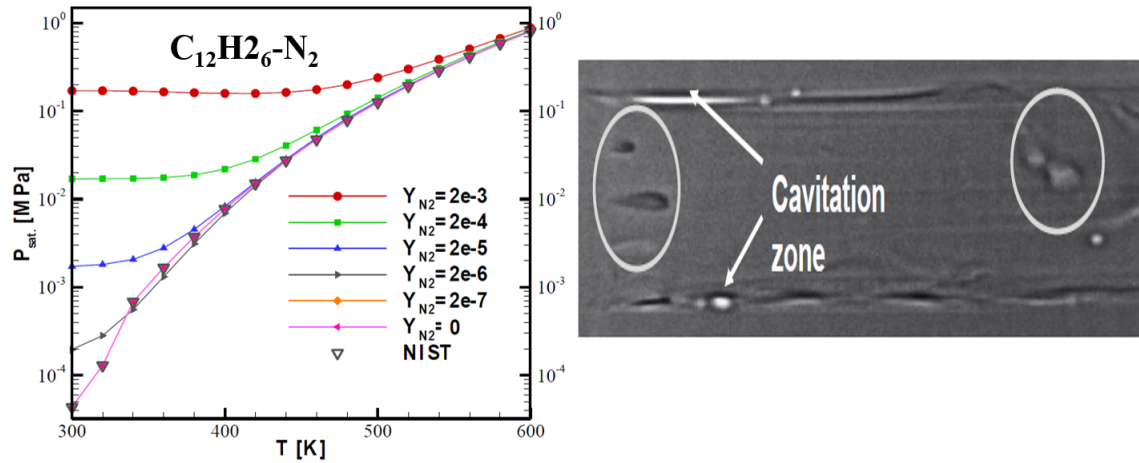


Figure 1.6: The variation of saturation pressure for n-dodecane-N<sub>2</sub> system at a temperature range of 300 K-600 K with different N<sub>2</sub> concentrations [27](left), along with the experimental study of cavitation for n-dodecane-N<sub>2</sub> system inside nozzle (right) [26].

Besides, in the left-hand side of Figure 1.6(right), the recent study of Yang et al. [27], for the same system as [26] demonstrates the variations of saturation pressure for an n-dodecane-N<sub>2</sub> system at a temperature range of 300 K-600 K with different N<sub>2</sub> concentrations. This illustrates that since the higher saturation pressure corresponds to a higher N<sub>2</sub> concentration dissolved gas inside liquid n-dodecane, adding more dissolved gas inside fuel will facilitate the inception of cavitation. This analysis will be very important for the industries that need nozzle cavitation analysis without changing geometry or injection pressure. Hence, having a powerful thermodynamic tool that can consider these tiny details can help better understand the available phenomena on the high-pressure engines, especially for the multi-component systems. As a result, choosing a potential thermodynamic model along with an appropriate CFD two-phase flow solver is mandatory for such high-pressure two-phase flows. These are among the topics researchers have been struggling with for decades, and having an accurate, robust, and efficient simulation of multicomponent jet injection still remains a real challenge [5–7, 17–22, 24].

## 1.2 Objectives of the thesis

As discussed above, this thesis is motivated by an exciting context seeking to contribute to the energy transition to carbon neutrality. For this purpose, a CFD model capable of predicting various real fluid jets mixing under subcritical and supercritical conditions will be developed and validated in this thesis. This model will be based on the Diffuse Interface Modeling (DIM) approach in order to be able to simulate simultaneously subcritical and supercritical flows as well as the transition between the two. Different real fluid EoS will be used and their relevance

to CFD simulation of injection of various mixtures in the transcritical and supercritical regimes will be studied.

### 1.3 Outline of the thesis

This thesis consists of six chapters, including some materials in the appendix.

This begins with **Chapter 2** which will be dedicated to explaining and reviewing the physical concepts and available classical models of single and multi-component two-phase flows under different thermodynamical regimes as subcritical, transcritical, and supercritical regimes. Besides, some vital thermodynamics and mathematical concepts which will be essential and valuable for the following will be reviewed.

Then, the main contributions and discussions to developing a real fluid model for simulating two-phase flows are presented in **Chapter 3** and **Chapter 4**.

**Chapter 3** consists of explaining the numerical and theoretical methods, including the governing equations, thermodynamic tabulation, and look-up methods using uniform tabulation.

In **Chapter 4**, after a short review on the VLE tabulation approach, the difficulties of tabulating properties from the VLE algorithms are explained, and the reasons why grid-table refinement in the vicinity of the phase boundary are discussed. Chapter 4 is dedicated to introducing different approaches for refining the thermodynamic tables, and different types of tabulation, searching, and interpolation approaches will be explained and introduced as possible refinement methods. Finally, the strengths and weaknesses of the proposed methods are summarized.

**Chapter 5** has dedicated to the study of some industrial cases with different applications for better understanding of transcritical injection for single component and multi-component mixtures. This chapter has categorized into two subsections, which has prepared based on the published and under review papers. Hence:

**Sub-chapter 5.1** starts with some 1D and 2D test cases for single component Nitrogen under transcritical and supercritical regimes. Then, the simulation setup for the cryogenic co-injection of liquid nitrogen ( $LN_2$ ) and gaseous hydrogen ( $GH_2$ ) is presented considering two different EoS: PR and SRK. The simulation results are examined and compared with Matheis et al. [28] numerical results and the experimental study of Oschwald et al. [29].

Then, **Sub-chapter 5.2** focuses on the analysis of the coupling between the hydrodynamics and thermodynamics of multi-species(n-hexane-nitrogen) supercritical jets. Generally, various phase transition phenomena, such as droplet nucleation by condensation, which have been shown experimentally to affect the flow significantly and mixing dynamics of the jet, are studied. For this purpose, a tabulated multi-component real fluid model assuming vapor-liquid equilibrium is proposed for the numerical simulation of a supercritical jet of n-hexane injected into supercritical nitrogen. Numerical results are compared with available experimental data and published numerical studies [30,31], showing a good agreement. In addition, comparisons between different turbulence models, including the LES Sigma, Smagorinsky, and RANS  $K - \epsilon$  models, have been performed, showing the relevance of the LES Sigma model for these very complex two-phase flows.

Finally, the conclusions, recommendations and upcoming works are presented in **chapter 6**.

## Chapter 2

# Physical concept and classical models of two phase flows

### Contents

---

<b>2.1</b>	<b>Physical concepts</b>	<b>16</b>
2.1.1	Introduction	16
2.1.2	Review on transcritical and supercritical injection	16
<b>2.2</b>	<b>Classical models of two phase flows</b>	<b>20</b>
2.2.1	Review on numerical and thermodynamic models for two-phase flows	20
2.2.2	DIM for two-phase flow modeling	23
2.2.3	How to select a thermodynamic model	26
2.2.4	Equations of state	27
2.2.5	Vapor Liquid Equilibrium	29
<b>2.3</b>	<b>Conclusion</b>	<b>35</b>

---

This chapter introduces the physical concepts and classical models of single and multi-component two-phase flows under different thermodynamical regimes. Besides, some vital thermodynamics and mathematical concepts which will be essential and valuable for the following will be reviewed. Hence, this begins with some explanations and bibliography study about the transcritical and supercritical injection for single and multi-component two-phase flows. Then, in order to be able to model the specific behaviors at these regimes, the chapter will continue by some bibliography, and comparisons about the available classical models for two phase flow solvers. As a result, the chapter will finish with some fundamental descriptions about the mathematical and thermodynamics aspects of choosing a proper thermodynamic model to close a CFD solver, by briefly

answering the following questions:

1- How to select a thermodynamic model?

2- What is the best Equation of state for a given situation?

3- Are we closer to arriving at a single model for all two-phase regime flows and applications?

Also, since one of the main objectives of this study is to tabulate the thermodynamic properties inside a table, some fundamental concepts about the degree of freedom for single and multi-component two-phase systems have been included.

## 2.1 Physical concepts

### 2.1.1 Introduction

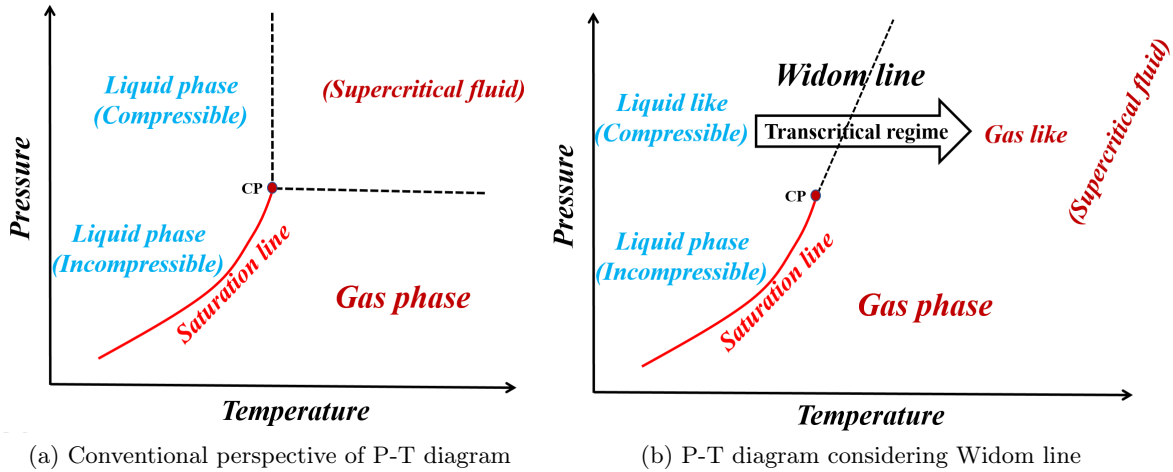
More efficient and cleaner engines is today's one of the highly debated topics in various research laboratories and industries. In modern combustion engines such as cryogenic engines, gas turbines, or high-pressure diesel engines, this target can be met by increasing the operating injection and ambient pressures up to supercritical conditions. Generally, when a fuel at subcritical temperature and supercritical pressure is injected into a high pressure-temperature environment above the fuel's critical point, the fuel jet mixes with the chamber gas pasts its critical temperature. This class of two-phase flows is known as transcritical injection [16–25, 32–35]. Fundamental understanding and simulation of such transcritical flows are among the topics researchers are struggling for decades. One reason for this is the lack of understanding of fuel jet mixing under such transcritical conditions.

### 2.1.2 Review on transcritical and supercritical injection

Interest in the behavior of supercritical fluids is not new, dating back to at least 1869 [33]. Over the past few decades, researchers have conducted several studies to better understand the dynamics of multiphase flows in this regime [17, 20, 22, 24, 32, 34–38].

The traditional perspective about the supercritical fluid behavior was that the distinction between the liquid and gas phases vanishes above the critical point, and a single phase fluid replaces the two-phase system of the subcritical condition. Nevertheless, the supercritical fluid was already known to have properties close to an ideal gas at high temperature ( $T > T_c$ ), and properties close to a liquid at low temperature (see Figure 2.1(a)). Recently, a new map of the (P-T)-diagram has been introduced (see Figure 2.1(b)). The boundary separating liquid-like and gas-like in this figure when the fluid temperature is increased has been the focus of recent investigations (see [5, 20, 24, 34]). Indeed, for a single-component fluid, it is revealed that these two regions could be separated by a virtual line, the so-called Widom line or pseudo-boiling line. As depicted in Figure 2.1(b), this line is the extension of the coexisting line in subcritical conditions, so that the thermodynamic and transport properties around this line are very sensitive to the variation of temperature (T) and pressure (P). Indeed, a slight variation in (T) or (P) leads to a highly non-linear variation in the properties values, especially close to the critical point, as depicted in Figure 2.2(e) for the density and heat capacity of nitrogen as an example.

It is well known that fuels have various special features in the supercritical regime, and great



(a) Conventional perspective of P-T diagram

(b) P-T diagram considering Widom line

Figure 2.1: Fluid state planes at subcritical and supercritical regimes. (a) The traditional perspective about the supercritical fluid behavior was that the distinction between the liquid and gas phases vanishes above the critical point (CP). (b) With the new perspective, the supercritical fluid states are not homogeneously distributed but, it can be differentiated into two distinct regions with gas-like and liquid-like regions. It is revealed that these two regions could be separated by a virtual line, the so-called Widom line or pseudo-boiling line( [20, 24, 34]).

efforts have been made to better understand this regime. Several attempts have been made to find unifying concepts for explaining the behaviour of fuels in different regimes, and transition from one phase to another.

Generally, it has been accepted that the subcritical liquid-to-gas transition is characterized by a structural change from an ordered (liquid) to a disordered (gas) state. In this case, density can be chosen as the appropriate order parameter, which exhibits a sharp discontinuity when phase transition occurs.

However, in the pseudo-boiling transition, no structural change has been observed in macroscopic light scattering experiments [25, 39]. [25] concluded that high-pressure jets have the same scattering footprint and morphological properties as low-pressure jets. However, anomalous (enhanced) scattering is only observed upon multiple crossings of the Widom region, e.g., due to the series of rapid recompressions caused by the shock train. This is caused by the enhancement in compressibility, which induces additional density fluctuations and not by a change in the molecular structure of the fluid. These findings were confirmed at molecular scales by the small-angle X-ray scattering experiments in [40]. The experimental findings of Gerber al. [25] show that density fluctuations, rather than density, are not negligible across the Widom line. They can be detected both at the macroscopic (continuum) and molecular scale. This completely changes the physical meaning of pseudo-boiling/pseudo-condensation transition from the subcritical counterpart.

Across the Widom line, the singularity in response function, as  $(C_p, \beta_T, \alpha_P)$ , isobaric heat capacity  $C_p$ , isothermal compressibility  $\beta_T$ , or thermal expansion coefficient  $\alpha_P$ , leads to an anomalous

fluid behavior as a reaction to a perturbation, associated with fluctuation in pressure and temperature as well. This is not the case for a subcritical transition, where both pressure and temperature remain constant during the entire evaporation/condensation process. In the literature, there are different criteria for distinguishing the liquid-like and gas-like regions based on the isobaric heat capacity, isothermal compressibility, or thermal expansion coefficient [41, 42]. Gallo et al. [41] derived based on experiments and simulations the lines of the maxima of  $C_P$ ,  $\beta_T$ , and  $\alpha_P$  above the critical point of pure water, and they found that the  $C_P$  and  $\alpha_P$  maxima follow a similar path, while the maxima of  $\beta_T$  deviate from that of  $C_P$  and  $\alpha_P$  for high temperatures. Banuti et al. [20] figured out a simple algebraic expression with a good accuracy for the Widom-line in terms of reduced pressure and reduced temperature, which allows for a simple determination of the positions of maxima in thermal expansion and heat capacity. Hence, as a unified parameter for detecting the liquid-like and gas-like from each other, the studies showed that the maximum of heat capacity can be a good candidate to identify the interface between phases [22, 24]. It is interesting to mention that, based on the idea of maximum of heat capacity and the work of Michelsen [43], Yang et al. [17, 22] have proposed a criterion for distinguishing between a liquid-like and gas-like in the supercritical regime so that the fluid has been considered as liquid-like when its compressibility factor is less than  $3.5 \frac{bP}{RT}$ , where  $b$  is the co-volume given in table 1.

Based on the experimental study of Chehroudi et al. [23], Figure 2.2 shows the behavior of the pure nitrogen jet in subcritical (a), transcritical (b), and supercritical (c) conditions ( $P_{c,N_2} = 3.396 \text{ MPa}$ ,  $T_{c,N_2} = 126.2 \text{ K}$ ). The liquid nitrogen jet with different temperatures, varying from 99 K to 110 K, was injected into supercritical gaseous nitrogen with a fixed temperature of 300 K. The chamber pressure for this study varies from subcritical values to supercritical ones, approximately from 3 MPa to 9 MPa. It can be seen that, starting from a subcritical pressure condition, an isobaric path crosses the saturation line (see Figure 2.2(d)). In addition, due to the significant surface tension, the interface between the liquid and the gas plays an important role, and it leads to the appearance of primary and secondary breakup, known as classical atomization (see Figure 2.2(a)). However, as the pressure increases, the magnitude of the surface tension decreases and vanishes at the critical point, which suppresses the formation of ligaments and droplets, as demonstrated in Figure 2.2(b and c). However, liquid-like ligaments (called also finger-like) could be seen in Figure 2.2(b) despite the absence of surface tension. Besides, the nonlinear behavior of different nitrogen properties such as the density and isobaric heat capacity at transcritical regime (at 4 MPa) are plotted in Figure 2.2(e) using the Peng-Robinson equation of state. One

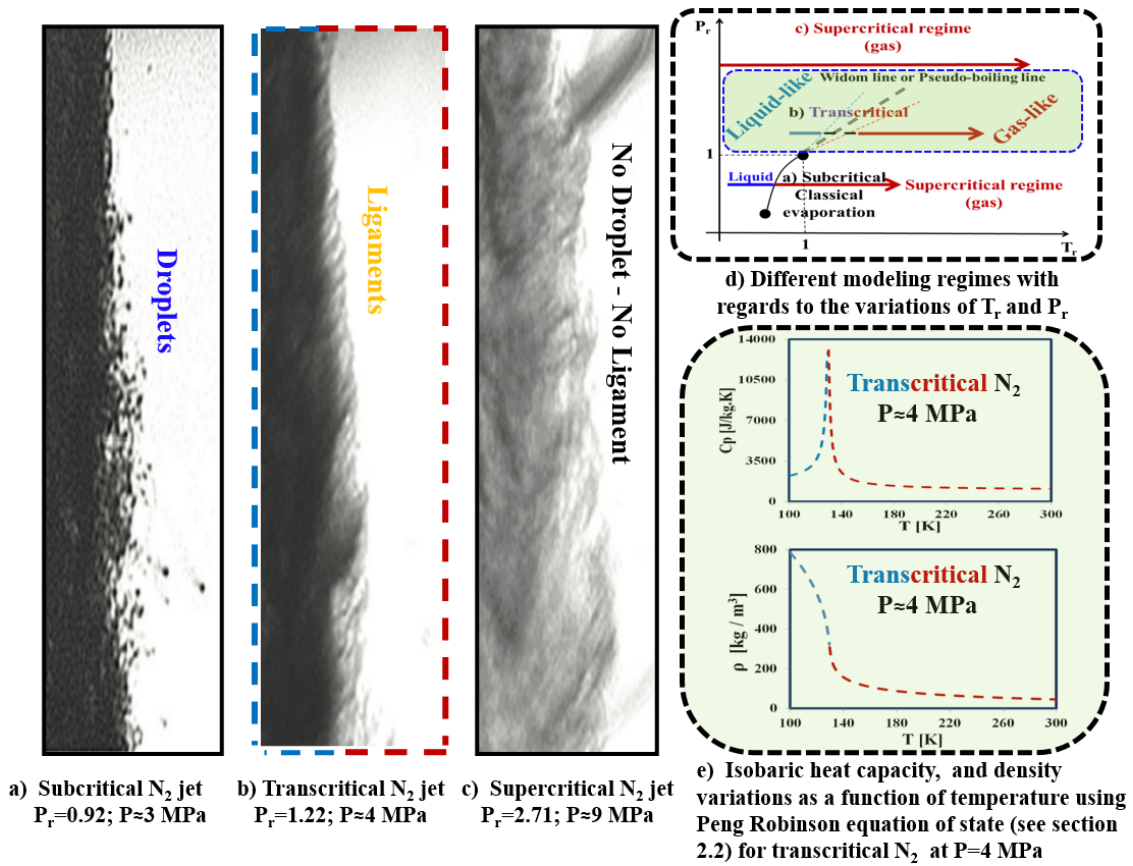


Figure 2.2: Experimental images (adapted from [23]) of pure liquid  $N_2$  injection from subcritical to supercritical pressure conditions (a-c). A schematic showing the three (subcritical (a), transcritical (b), and supercritical (c)) isobaric paths for a single component (a-c). Figure (d) denotes different modelling regimes with regards to the variation of  $T_r$  and  $P_r$ , schematically. The variations of the density, and isobaric heat capacity of pure nitrogen at transcritical condition calculated in this study, using PR EoS, are shown in the Figure (e) where liquid-like properties are colored in blue and gas-like properties are colored in red.

may note that the pseudo-boiling transition region (bounded in Figure 2.2(d) by the dashed lines around the Widom line) becomes larger, as the pressure increases, inducing weaker transcritical non-linearity of the properties. This transcritical behavior has been extensively studied theoretically, experimentally, and numerically by various researchers for single component [21, 23, 34, 38]. In the recent decade, different studies have been done for multi-component fluids transition behavior [17, 18, 22, 32, 34, 35]. However, the transition from subcritical to supercritical regimes is not rigorously following the transition for a single-component fuel, and the interface structure and evolution in transcritical condition is still not well understood. Various experimental and numerical studies such as molecular dynamics simulations as well as CFD simulations have been performed, and they proposed different approaches for introducing a universal criterion for this transition by defining some dimensionless parameters [18, 32, 44].

Crua et al. [18] studied the injection of (n-heptane, n-dodecane, n-hexadecane) into the ambient gaseous nitrogen at different temperatures and pressures. They investigated the transition from

subcritical to diffuse mixing regime as a function of the pure fuels' critical temperature and pressure. However, due to the limited accuracy of the experimental setup, reliable data are still lacking for the validation of numerical models, and there are still multiple doubts and questions about the conditions and mechanisms behind the interface disappearance for multi-component systems.

Yang et al. [17] suggested that the transition from subcritical to the diffusive mixing regime happens at the critical point of the mixture and more specifically at pressures higher than the mixture critical pressure. However, this pressure is not constant and depends on the mixture composition. This important point will be further discussed below in Section 2.2.5.2.

Ayyappan et al. [44] used a high-speed imaging technique to understand the jet behavior of different mixtures of fluoroketone and  $N_2$ . They showed that the composition of fluid in the chamber environment plays a critical role in altering the jet behavior, and that the thermodynamic transition of the liquid jet depends upon the injection Reynolds number and chamber pressure for a single component system. However in a binary system, the transition depends, only and heavily on the partial pressure of the respective components in the chamber environment. When the chamber environment was pure nitrogen in their study, the jet exhibited the Rayleigh mode of instability. As the amount of fluoroketone was increased in the ambient binary environment, the atomization regime shift was observed from the Rayleigh regime to the Taylor regime due to the variations of properties.

## 2.2 Classical models of two phase flows

### 2.2.1 Review on numerical and thermodynamic models for two-phase flows

Various formulations are available in the literature to model two-phase flows. In general, fuel injection modeling can be categorized into Eulerian and Lagrangian approaches. In addition, there are some combined models such as the Eulerian-Lagrangian Spray and Atomization (ELSA) model [45], which proposes an Eulerian approach for the liquid injection combined with a Lagrangian spray modeling approach for the atomized droplets tracking and evaporation. Lots of CFD solvers hire such methods so that the dense zone applies the Eulerian model which switches to the Lagrangian model when a certain criterion is reached, for example based on a critical liquid volume fraction value. Although many different models have been proposed and introduced by various scientists, there are still difficult problems to be solved, such as simulation of transcritical injection, cavitation, atomization and mixing, and many others.

From the numerical perspective, several numerical schemes have been proposed in the literature in the past decades for the numerical simulation of two phase flows in which the interface computation is a key element [15, 17, 22, 46]. Mainly, two types of methodologies have been adopted, namely *interface tracking* and *interface capturing* methods [14, 15, 46–56]. On the one hand, in the *interface tracking* method, the interface is tracked by the motion of particles on the interface, and a special modeling for capturing the interfacial dynamics is required. On the other hand, in the *interface capturing* method, the interface is captured implicitly in each cell of the computational grid with an additional scalar. Hence, in interface-tracking techniques, the interface location is explicitly tracked in a Lagrangian framework, while in interface-capturing methods, the interface is implicitly captured in an Eulerian computational grid. Three main methods have been proposed in this class as

- Volume of Fluid method (VOF), see for instance [49–52]
- Level Set Method (LSM), see for instance [56–59]
- Diffuse Interface Method (DIM), see for instance [14, 15, 47, 55]

Generally, the simulation of single-phase compressible flows is known to be challenging, mainly because of possible appearance of shock waves. However, additional difficulties may appear for two-phase flow solvers due to the abrupt variation of thermodynamic properties across the subcritical interface and also across the Widom line which may be considered as a **transcritical interface**. From a numerical point of view, the non-linearity of the thermodynamic properties (due to evaporation, boiling, flash-boiling in subcritical regime and pseudo-boiling in the transcritical regime) makes the numerical simulation more severe and difficult. In addition to that, spurious pressure oscillations may appear in such multi-phase flow simulations. However, it has been demonstrated by Yi et al. [22] that these spurious oscillations may be tackled when a sufficiently refined grid is employed. Another important issue is related to the fact that the liquid-gas interface disappears during the transition of the fluid to the supercritical state, and vice versa. The interface could also re-appear when a second and different species is injected near a transcritical interface, as discussed in detail in Chapter 5. As a matter of fact, this interface appearance and vanishment phenomena may occur at any location of the liquid bulk surface. This important flow characteristic explains why cryogenic injection simulations require real fluid models, such as the one proposed in this work, and are usually performed using a Diffuse interface method (DIM) because they are difficult to perform using interface capturing with numerical reconstruction methods such as VOF [60] and/or LSM [46]. Indeed, the idea

of adopting the DIM approach seems appropriate for the simulation of the transcritical regime as the liquid-like and the gas-like are separated by a much thicker interface than in sub-critical conditions. Noteworthy, similar approach is also applied for the premixed combustion modeling with a thickened flame model (TFM) [61] designed for increasing the flame thickness in the LES framework.

Another advantage of the DIM method is that explicitly satisfying the interface conditions are not required, and the variation of the interface topology is automatically handled, which is computationally efficient. However, the diffused interface have to be maintained relatively sharp in subcritical conditions and specific sub-grid scale modelling for high frequency interface instability and breakup is required in order to simulate properly the liquid jet primary atomization [62]. In the DIM framework, many two-phase flow models have been developed in the literature with the number of transport equations ranging from three to seven based on the initial equilibrium assumptions, and it has been proved that the robustness of these models is completely coupled with the resolving of large density gradients due to the transition from the liquid to the gas. Among them, the four-equation model, which was used for cavitation and transcritical injection simulations, proved to be very accurate [17, 27]. A comprehensive review of different models for DIM can be found in [15, 22]. In this study, the 4-Equation model of CONVERGE CFD solver is employed [63]. For such a fully compressible solver written under the assumption of thermodynamic equilibrium, the use of an appropriate equation of state will be crucial to be able to handle phase transitions and transcritical flows using the same CFD software. Indeed, as proven by extensive studies, the ideal gas equation of state (EoS) is no longer valid at transcritical conditions. Figure 2.3 presents the density, heat capacity, sound speed, and viscosity profiles for pure nitrogen using different EoS as, ideal gas, PR (Peng Robinson) [64] and SRK (Soave-Redlich-Kwong) [65]. As it can be seen in this figure, compared to the NIST data [66] which is the reference for pure component, ideal gas EoS cannot predict the transcritical behavior of properties, and using more appropriate EoS is mandatory for accurate studies at this regime. Moreover, as its shown in figure 2.3(a), the SRK-EoS can predict the nitrogen density much better than the PR-EoS when compared to the NIST data [66]. These results corroborate many published findings. Indeed, previous researches have carried out various and more comprehensive studies on the accuracy of different EoS, and it has been reported that generally, for cryogenic conditions, the SRK-EoS gives the best prediction of the fluid density [67]. Generally, PR is better for heavy fuels, however SRK is better for light fuels (gases) [35]. Therefore, both SRK and PR will be tested in this work to corroborate previous findings (see below Chapter 4).

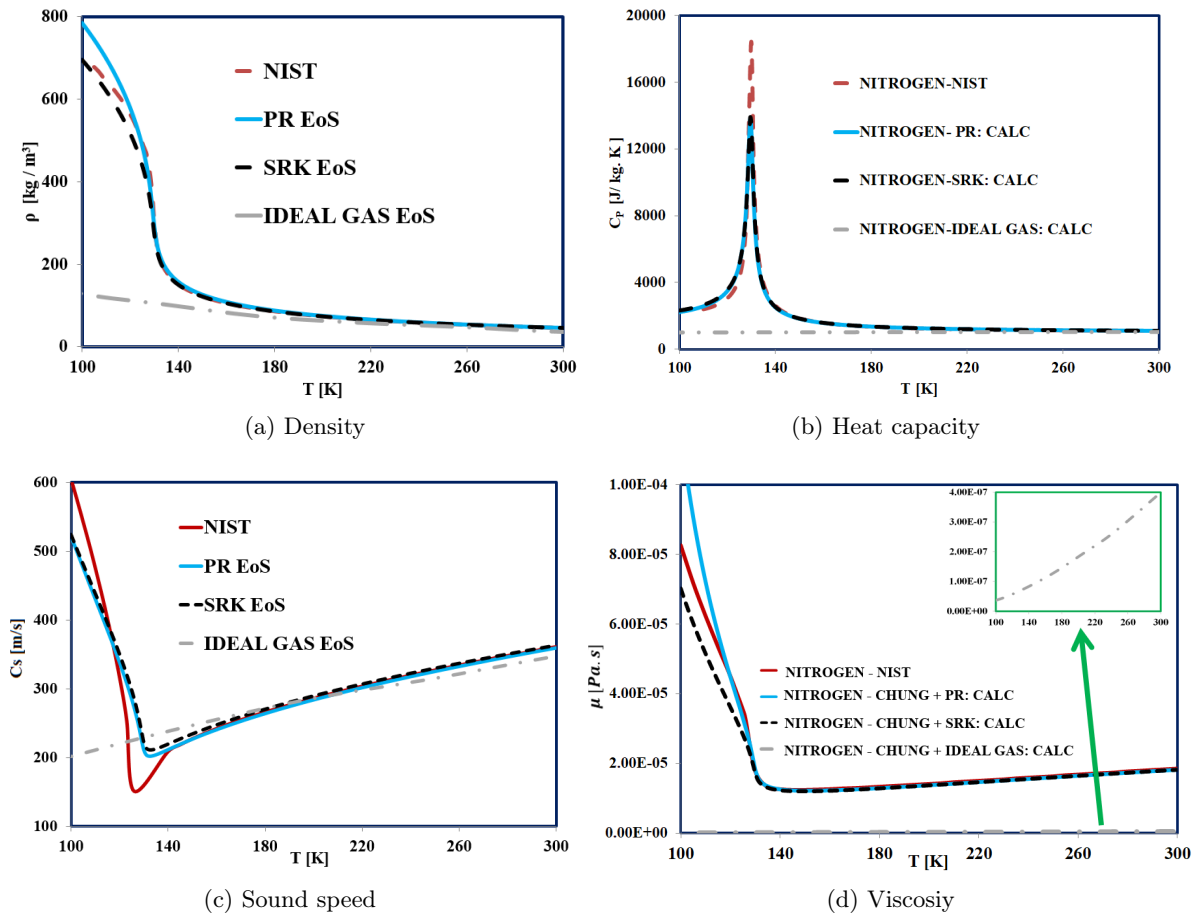


Figure 2.3: Comparison and validation of the thermodynamic model calculated in this study with the data of NIST [66] for different EoS for density, isobaric heat capacity, sound speed, and viscosity, respectively, for pure  $N_2$ . PR, and SRK refer to the Peng Robinson, and Soave-Redlich-Kwong equation of states. The viscosity is calculated by the Chung correlation [68].

## 2.2.2 DIM for two-phase flow modeling

The DIM approach for two-phase flow can be classified into one-fluid and bi-fluid models. One-fluid models are used when mechanical and thermal equilibrium are assumed, such as in the homogeneous equilibrium model (HEM). Otherwise, a non-equilibrium bi-fluid model is required. The most comprehensive model of this type is the well-known 7-Equation model (Baer Nunziato 1986) [47], which allows pressure, temperature, and velocity non-equilibrium between the phases. Besides, the one-fluid model considers that the velocity, pressure, and temperature are the same or homogeneous in each computational cell. Therefore, the entire system of a one-fluid model owns only one continuity, energy, and momentum equation for a single-component fluid. In recent years, lots of researchers have turned to non-equilibrium models. These models are based on multi-parameter approaches that need to specify tentative values before the simulation begins, such as in the delayed equilibrium model (DEM) [69] or the Homogeneous relaxation

model (HRM) [63, 70] summarized in the following Sections. The main challenge in such two phase models is how to calculate the corresponding non-equilibrium contributions at every time step. When a thermodynamic non-equilibrium (metastable state) is considered, the transport equations are solved along with a phase change source term, as in the HRM model, for instance. This source term needs to be modeled for the classical sub-critical phase change as well as the single phase supercritical mixing regime. However, some other models employ a phenomenological concept to capture some relevant physics, such as the HEM, without any tentative values. In the following two subsections, both types of models are analyzed to underline their mathematical significance. Hence, the HEM and the HRM approach as a sample of these two types will be briefly explained. Both are known to be hyperbolic models when appropriate thermodynamic constraints are satisfied.

### 2.2.2.1 Homogeneous Equilibrium Model

One of the most widely used equilibrium models is the Homogeneous Equilibrium Model (HEM). This is due to its simplicity. Indeed, the HEM assumes there exists no difference between the liquid and vapor velocities within a continuum. In addition, the two phases are locally considered to exist at the same temperature and pressure. This model consists of a set of partial differential equations that governs mass, momentum and energy transport of a mixture in full equilibrium. The main drawback of this model is that it cannot reproduce mechanical, thermal or chemical potential non-equilibrium. Another difference between equilibrium and non equilibrium is that equilibrium thermodynamics ignores the time-courses (i.e. relaxation time) of physical processes, and it restricts the processes to the initial and final states of thermodynamic equilibrium. On the other hand, non-equilibrium thermodynamics tries to explain their evolution in time in a continuous and detailed way. Therefore, for non-equilibrium studies, additional modelling equations are needed for an accurate prediction of the physics (see the HRM model below). By ignoring the various diffusion phenomena, the HEM system has formally the structure of the single-phase Euler system. One-dimensional single-component HEM equations can be written as:

$$\left\{ \begin{array}{l} \partial_t \rho + \partial_z(\rho u) = 0 \\ \partial_t(\rho u) + \partial_z(\rho u^2 + p) = 0 \\ \partial_t(\rho E) + \partial_z(\rho E + p)u = 0 \end{array} \right\} \quad (2.1)$$

$(\rho, u, P, E)$  are the mixture's values for density, velocity, pressure, and the specific total energy, respectively.  $E = e + u^2/2$ , where  $e$  is the specific internal energy of the mixture. The

thermodynamic equilibrium assumptions of the HEM are as follows.

$$\left\{ \begin{array}{l} p_l = p_v = p \\ T_l = T_v = T_{sat}(p) \\ g_l = g_v = g \end{array} \right\} \quad (2.2)$$

Where subscripts  $l$  and  $v$  designate the liquid and the vapor phase,  $g$  denotes the Gibbs free energy which is equal to the chemical potential for a single component system and sat used for saturation values. [71].

### 2.2.2.2 Homogeneous Relaxation Model

The Homogeneous Relaxation Model (HRM) employs a non-equilibrium approach for the prediction of mass exchange between the liquid and vapor. It is a well known approach usually used in the literature for predicting cavitation and flash boiling phenomena [72–74]. For that aim, HRM employs a finite relaxation rate to control the phase change process to progressively reach the equilibrium state. The HRM system consists of the mixture Euler equations plus a transport equation for one phase with a relaxation source term for the flow void fraction equation. In most of industrial codes, the void fraction (VOF) equation is be used for the additional equation. One most common and pioneer approach for modeling this mass exchange presented by Bilicki and Kestin (1990) [75]. Bilicki and Kestin [75] proposed a simple linearized form for relaxation source term, shown in the equation 2.3. The mass transfer is modeled by means of a source term,  $\Gamma_{l \rightarrow v}$  which appears on the right hand side in the equation of the mass balance of by 2.3.

$$\Gamma_{l \rightarrow v} = -\rho \frac{\bar{x} - x}{\theta} \quad (2.3)$$

In the above equation,  $x$  is the instantaneous mass fraction,  $\bar{x}$  is the equilibrium mass fraction and  $\theta$  represents the relaxation time scale over which  $x$  relaxes to  $\bar{x}$ . For these kind of closure, the relaxation time scale  $\theta$  can be modeled by the following Eq. 2.15, where  $F$ ,  $\theta_0$  are the time scale factor, and time scale constant, which need to be tuned, with trial and error, for each simulation. In these equations,  $p_{sat}$  is the critical pressure and  $p_c$  is the critical pressure.

$$\begin{aligned} \theta &= F\theta_0\alpha^{-0.54}\phi^{-1.76} \\ \phi &= \frac{p_{sat} - p}{p_c - p_{sat}} \end{aligned} \quad (2.4)$$

Hence, the HEM approach, which employs a phenomenological concept without setting up the tentative values, plus VLE thermodynamic model, will be applied in this study to prevent the need to determine uncertain values of multi-parameter approaches like HRM.

### 2.2.3 How to select a thermodynamic model

Thermodynamic models are different approaches adopted to predict the physical properties of fluids such as density, heat capacities, sound speed, etc. Various mathematical operations are performed on a list of input properties and producing properties. These input properties typically consist of two state variables such as temperature and pressure, in addition to the fluid composition. A thermodynamic property calculation requires the combination of different proper models, good parameters and a stable algorithm. These models include different categories such as equations of state, activity coefficients, empirical models or models specific to a particular system. Depending on the essential knowledge available, these models may be more or less empirical. The models can help to understand a system behavior. However, having a single, simple model that can predict all possible types of fluid behavior is one of the important challenges that researchers are trying to address. Based on previous studies, the current state of knowledge does not allow for such a single, simple approach. Indeed, the task of having a single or even just a set of few models for a wide range of needs is complicated due to the extensive diversity of compounds over broad conditions (temperature, pressure, and concentration) and different types of phase behaviors. In general, there is no silver bullet. For some applications, precise properties may be required. However, for others, only qualitative estimates are sufficient. As a general guideline for engineers, de Hemptinne et al. [71] recommended that any model must be compared with available experimental data. However, a preliminary thermodynamic analysis could help to find the most appropriate approach for different applications by asking the following questions:

- 1- What is the property of interest?
- 2- What are the composition?
- 3- What are the pressure and temperature conditions of the process?

Mainly, there are two types of properties: Single phase properties, and Phase equilibrium properties.

Figure 2.4 shows a proposal for model selection for property calculations done by [71] which shows the importance of equations of state. The black area is two phase domain where vapour-liquid equilibrium is reached. According to the thermodynamic principles, equilibrium is attained on the system at given pressure and temperature when the Gibbs energy is lowest. More detailed

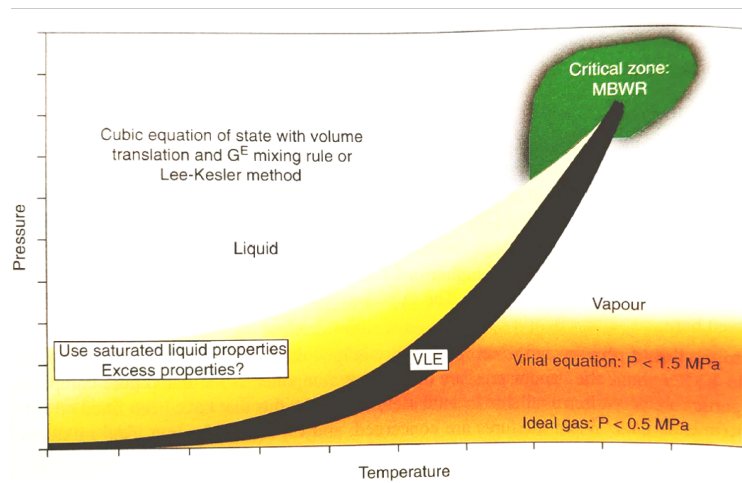


Figure 2.4: A proposal for thermodynamic model selection for property calculations, has been suggested by [71]. The black area is two phase domain, vapour-liquid equilibrium.

information can be found in de Hemptinne et al. [71].

## 2.2.4 Equations of state

As discussed above, each thermodynamic model depends on different items such as equations of state, activity coefficient, empirical, or specific-system models, and one of the important components is the equation of state (EoS). An equation of state is a thermodynamic expression that relates various thermodynamic state variables such as pressure, temperature, volume/density, and composition. In thermodynamic, equations of state are the cornerstone of thermodynamic models. In general, there is no analytic expression and global equation of state that accurately predicts the properties of all substances under all conditions.

Equations of state developed first in the 19th century by van der Waals [76]. It is the first equation of states to consider for the inter-molecular forces for non-ideal gases. The Ideal Gas Law assumes that gases are composed of point masses that experience perfectly elastic collisions. However, real gases deviate from those assumptions at low temperatures or high pressures. At high pressure, the gas particles volume is no longer negligible, and it needs to be taken into account. However at low temperature, due to the lower kinetic energy, the particles do not move fast. Hence, inelastic collisions happen between the particles, and the inter-molecular forces needs to be consider.

Generally, there are different forms for writing the equation of states:

- 1- The caloric equation of state  $e = e(\rho, T, Y)$
- 2- The thermal equation of state  $P = P(\rho, T, Y)$

The caloric equations of state relate the energy  $e$  to the density  $\rho$  and temperature  $T$  for a given species composition  $Y$ . However, the thermal equations of state link the independent variables

Table 2.1: Parameters for cubic equations of state (index c stands for critical value)

EOS	$\delta_1$	$\delta_2$	$(a_c)_i$	$m_i$	$b_i$
<b>PR</b>	$1+\sqrt{2}$	$1-\sqrt{2}$	$0.45727\frac{R^2T_c^2}{P_c}$	$0.37464 + 1.54226\omega - 0.26992\omega^2$	$0.0778\frac{RT_c}{P_c}$
<b>SRK</b>	1	0	$0.42747\frac{R^2T_c^2}{P_c}$	$0.48508 + 1.5517\omega - 0.15613\omega^2$	$0.08664\frac{RT_c}{P_c}$

of  $(P, \rho, T,)$  for a certain composition  $Y$ . It is worth mentioning that using these two types of EOS can be calculated for any arbitrary fluid description, and they will be used as the closure condition for any CFD solvers. Different forms of solvers, such as TPn and UVN [5, 17, 22], have been developed based on these two types of EoSs. In the next chapter, more details will be presented about these two kind of solvers types.

Another important point needs to mention is that the complexity degree enhances with the accuracy of the EOS. In the following, two types of more common real fluid equation of state are presented.

#### 2.2.4.1 Cubic equation of states(semi-empirical equations of state)

The cubic equations of state use the repulsive term proposed by Van der Waals, and they can apply to both gaseous and liquid phases. So far, numerous equations of state are built upon the Van der Waals EoS for real fluids. Soave Redlich Kwang and Peng Robinson are the first significant contributions and the most widely used EoS in CFD solvers due to their simplicity and uncertainty parameters for pure components and mixtures. They were developed to compute the thermodynamic properties for oil and gas industries.

$$P = \frac{RT}{\nu - b} - \frac{a(T)}{(\nu + \delta_1 b)(\nu + \delta_2 b)} \quad (2.5)$$

$$a_i(T) = (a_c)_i [1 + m_i (1 - \sqrt{\frac{T}{T_c}})]^2 \quad (2.6)$$

Figure 2.3 shows the impacts and the accuracy of using different cubic equations of state for different properties.

#### 2.2.4.2 Multi-parameter equations of state

Multi-parameter EOSs are expressed based on the non-dimensional free Helmholtz energy with entropy's and the universal gas constant. Among the multi-parametric models, the Benedict-Webb-Rubin (BWR) equation of state is the most popular form used in various applications.

The general form of BWR are as:

$$P = \rho RT + (B_0 RT - A_0 - C_0/T^2)\rho^2 + (bRT - a)\rho^3 + a\alpha\rho^6 + (c\rho^3/T^2)(1 + \gamma\rho^2)e^{-\gamma\rho^2} \quad (2.7)$$

As equation 2.7 demonstrates, there are some empirical constants as  $A_0$ ;  $B_0$ ;  $C_0$ ;  $a$ ;  $b$ ;  $c$  are determined based on experimental data.

### 2.2.4.3 Real fluid thermodynamic properties

To evaluate some real fluid properties like enthalpy, entropy, and specific heat capacity, at isobaric and isochoric process, departure functions calculations are required. These departure functions, for a given thermodynamic property, are defined as the difference between the value computed for an ideal gas and their real values. The ideal gas part calculated with specific polynomial equation which is only a function of temperature (More details in [5, 77]). The departure terms for internal energy, enthalpy, entropy, and heat capacities are calculated as

$$\begin{aligned} e_d &= \int_{\infty}^{\nu} [T(\frac{\partial P}{\partial T} - P)] d\nu \\ h_d &= \int_0^P [\nu - T(\frac{\partial \nu}{\partial T})] dP \\ s_d &= R \ln(Z) + \int_{\infty}^{\nu} [(\frac{\partial P}{\partial T})_{\nu} - \frac{R}{\nu}] d\nu \end{aligned} \quad (2.8)$$

Beside, the following equations will be used in order to calculate the heat capacities, and sound speed.

$$\begin{aligned} C_p &= C_{\nu} + (\frac{\partial P}{\partial T})_{\rho}^2 (\frac{\partial P}{\partial \rho})_T^{-1} \\ C_s &= \sqrt{(\frac{\partial P}{\partial \rho})_s} = \sqrt{-\nu (\frac{\partial P}{\partial \nu})_s} = \sqrt{-\nu \beta_s} \end{aligned} \quad (2.9)$$

where  $\beta_s$  is the adiabatic compressibility factor demonstrates volume variations as pressure changes at constant entropy. Hence, by use of different equations of state, the real fluid properties calculate.

### 2.2.5 Vapor Liquid Equilibrium

In order to consider phase change, a two phase thermodynamic model is needed for calculating the properties. These thermodynamic models, which are often very complex, can only be used where phenomena are at equilibrium [71]. From the thermodynamic points of view via the second law of thermodynamics, one isolated system owns the maximum entropy at the equilibrium state.

Hence, based on the thermodynamic equations:

$$de = Tds - Pdv + \sum_{k=1} \mu_k dn_k \quad (2.10)$$

$$ds = \sum_j^{N_p} \frac{de_j}{T_j} + \sum_{i \neq j}^{N_p} \frac{P_j}{T_j} d\nu_j - \left( \sum_{i \neq j}^{N_p} \sum_k^{N_c} \frac{\mu_k^j}{T_j} dn_k \right) \quad (2.11)$$

$$ds = \sum_j^{N_p} de_j = 0, \sum_j^{N_p} d\nu_j = 0, \sum_j^{N_p} dn_k^i = 0, k = 1, \dots, N_c \quad (2.12)$$

$$ds = \sum_{i \neq j}^{N_p} \left( \frac{1}{T_i} - \frac{1}{T_j} \right) de_j + \sum_{i \neq j}^{N_p} \left( \frac{P_i}{T_i} - \frac{P_j}{T_j} \right) d\nu_j + \left( \sum_{i \neq j}^{N_p} \sum_k^{N_c} \left( \frac{\mu_k^i}{T_i} - \frac{\mu_k^j}{T_j} \right) dn_k \right) \quad (2.13)$$

At equilibrium state,  $ds=0$  in equation 2.11. Then,  $e_i$ ,  $\nu_i$ , and  $n_i$  are subject to constraints as equation 2.12. As a result, equation 2.12 can be written in the form of equation 2.13. To satisfy the equilibrium constraints, it can be concluded that  $T_i = T_j$ ,  $P_i = P_j$ ,  $\mu_k^i = \mu_k^j$ , which are the thermodynamic equilibrium constraints so that temperature and the pressure as well as the chemical potentials of each component should be the same for each phase of the system (equality of chemical potential of each component + mass balance).

Based on this assumption, various models have developed. The most widely used phase equilibrium model is the vapor-liquid equilibrium (VLE) which is the main concern in current study.

Generally, a full vapor liquid equilibrium calculation includes two parts:

- (1) Stability test
- (2) Isothermal-isobaric flash (TP flash)

which may include a phase split (i.e. phase transition) calculation. The aim of the stability test is to verify the stability of the system. If the result of stability test indicates the system as unstable, it implies an extra phase can be added (or subtracted) in order to stabilize the system. Otherwise, the so-called TP flash computation have to be performed to obtain the final phase composition. More detail can be found in [5, 22]. Figure 2.5 shows the schematic of the thermodynamic solver using VLE approach.

Lots of studies using VLE method demonstrate proper results for spray modeling. However, the main problem of a multicomponent HEM two-phase flow model combined with a Vapor-Liquid-Equilibrium solver (VLE) is its very low efficiency and consequently the high CPU time reported by various researchers. The tabulation approach as one of the possible remedies can overcome most of the above limitations. Indeed, several authors proposed to evaluate the EOS

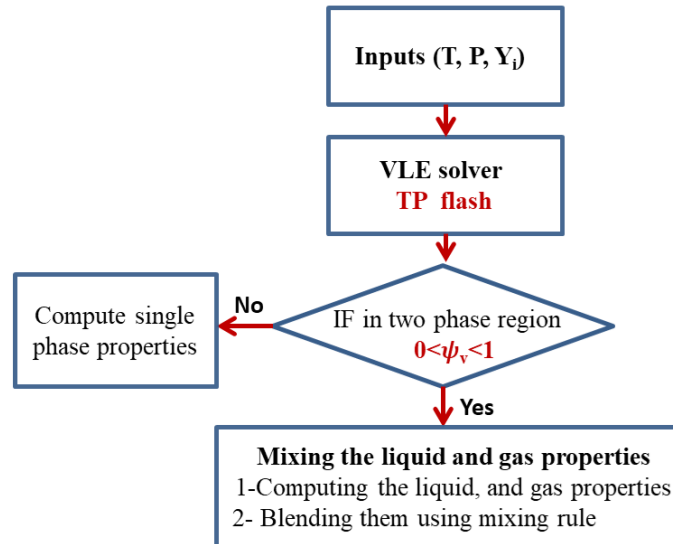


Figure 2.5: Flow chart of the thermodynamic solver for generating the properties table

before the simulation and to store the values in tables. However most of them are for single component system. Generally, the computational expensive Vapor-Liquid equilibrium are computed firstly (and once) and the properties are stored in a table which is used as an input for the two-phase flow model. The simplest two-dimensional (T, P) table can be constructed for a single-component fluid. However, for real-fluids, like diesel or cryogenic, the fuels are multicomponent and the gas phase may contain different species. Hence, understanding the properties physics with different nonlinearity at different regime will be mandatory for tabulation. There are three important aspects of the tabulation approach which is worth mentioning. First, the phase envelope has to be approximated with sufficient accuracy to be able to resolve all the thermodynamic' parameter high gradients near the phase boundaries. Secondly, the storage requirements for the table should be as low as possible to avoid computer memory overflow. Finally, the look-up procedure should be as fast as possible with respect to computation time.

Hence, one of the primary aims of this thesis work is to study various tabulation approaches to use in CONVERGE software for our multicomponent real fluid two-phase flow model to improve the efficiency but also the accuracy of industrial simulations.

### 2.2.5.1 Single component phase diagram and Gibbs's Phase Rule

A phase diagram is a particular type of chart used in thermodynamics to represent the physical state (or phase, such as solid, liquid, vapor phase) of a single-component or multi-component fluids as a function of two or more variable, generally the pressure, the temperature, the volume, the enthalpy, the fraction of a component of the system. The transition between phases is termed

as phase transition or phase change.

The phase transition is defined as “A change in a feature of a physical system that results in a discrete transition of that system to another state which phase transitions often involve the absorption or emission of energy from the system”. Therefore it must be considered for the tabulation. Figure 2.6 represents a Pressure-Temperature diagram which is colored by density value, and calculated by Peng Robinson equation of states, PR EoS. It shows the non linearity near the coexistence line for density property.

Generally, the number of the intensive properties that must be fixed for a system to be entirely determined in a closed system at equilibrium is given by the Gibbs’s Phase Rule :

$$L = N - \phi - R + 2 \quad (2.14)$$

where  $N$  is the number of components,  $\phi$  is the number of phases, and  $R$  is the number of relationships between components (chemical reactions) needed to fully determine the state of the system, i.e. the number of degrees of freedom of the system. Besides, when only a single component single phase is presented, the degrees of freedom are two. It means temperature and pressure can be varied independently for a single component without an additional relationship, the previous equation reduces to.

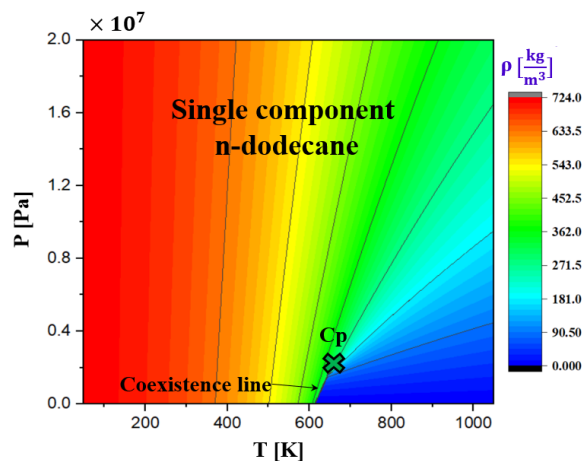


Figure 2.6: Phase diagram for a single component of n-dodecane, plotted in PT diagram colored by density value, and calculated by Peng Robinson equation of states, PR EoS.

$$L = 3 - \phi \quad (2.15)$$

Consequently, when  $\phi$  (single-phase) the system located in a two-dimensional region: the degrees of freedom are two, i.e. the temperature and the pressure can be varied independently. When  $\phi=2$  (two phases) the system located on a lines, that means that only one pressure is possible for each temperature (pressure and temperature are correlated) and finally when  $\phi=3$  (3 phases)

the degrees of freedom are equal to zero and the system is located at its critical point, where the properties of all the phases become the same. Generally, the study of the liquid-vapor mixtures implies a vaporization curve for a single-component system. This curve is going from the triple point to the critical point, as coexistence line, depicted in Figure 2.6. A saturation dome is a graphical representation of the two-phase region where the liquid and vapor co-exist, and which is generally employed to find the specific volume for known pressure and temperature. However, due to the use of VLE approach, there is no dome for single component. Also, mathematically, the critical point can be defined as the location respecting the following expressions.

$$\begin{cases} (\frac{\partial p}{\partial v})_t = 0 & (\frac{\partial t}{\partial s})_p = 0 \\ (\frac{\partial^2 p}{\partial v^2})_t = 0 & (\frac{\partial^2 t}{\partial s^2})_t = 0 \end{cases}$$

The critical point is characterized by highly non-linear behavior of thermodynamic properties. Beyond the critical point, there is transcritical regime as well as supercritical regime so that the gradient of properties will be different from the one in subcritical regimes. Hence, due to different gradients for different properties at different regimes, it must be taken into account when the tabulation process is done.

### 2.2.5.2 Multi components phase diagram

Phase diagrams can also be constructed for a multi-component resulting in a much more complex diagram than a single component one as shown in figure 2.7 .

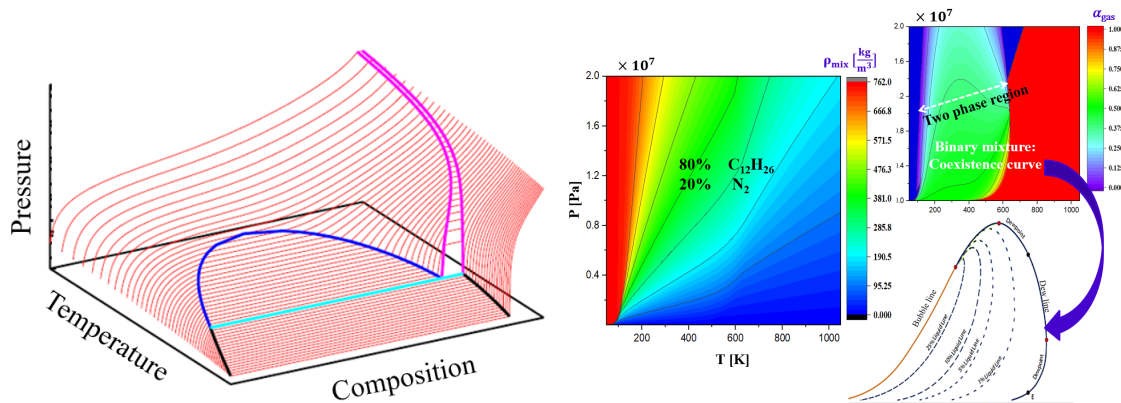


Figure 2.7: Schematic of a phase diagram for a multicomponent system with two components, binary system. The variation of mixture density for a binary system consists of 80% $C_{12}H_{26}$  – 20% $N_2$  at a temperature range of 50 K-1050 K and pressure range up to 20 MPa.

For a binary system (two-component mixture), the number of the intensive properties as equation 2.15 changes to  $L = 4 - \phi$ . Hence, when  $\phi = 1$ , that means that the system has a single phase in a three-dimensional region of the diagram; when  $\phi = 2$ , two phases are present and two degrees of freedom are available describing a two-dimensional area, for  $\phi = 3$ , three phases coexist and the system moves on lines. Figures (2.8) and (2.7(b)) reveal the  $P - T - Y_i$ , pressure-temperature-mass fraction diagram for a binary system consists of 80% $C_{12}H_{26} - 20\%N_2$ , and for a ternary system at a constant pressure and temperature. Based on Gibbs' Phase Rule, the independent intensive variables for a single-phase are usually taken as temperature, pressure, and concentration.

Therefore, the concentration of a component becomes an important variable in multi-component systems which may lead to phase change at constant pressure and temperatures.

Also, it is noteworthy to mention that the studies show that the mixture critical pressure for some composition raises for some multicomponent systems, and a nonlinear relationship exists between the mixture critical point and the critical point of each pure species. On the contrary, the value of the critical temperature of the mixture reduces, as shown in figure 2.9.

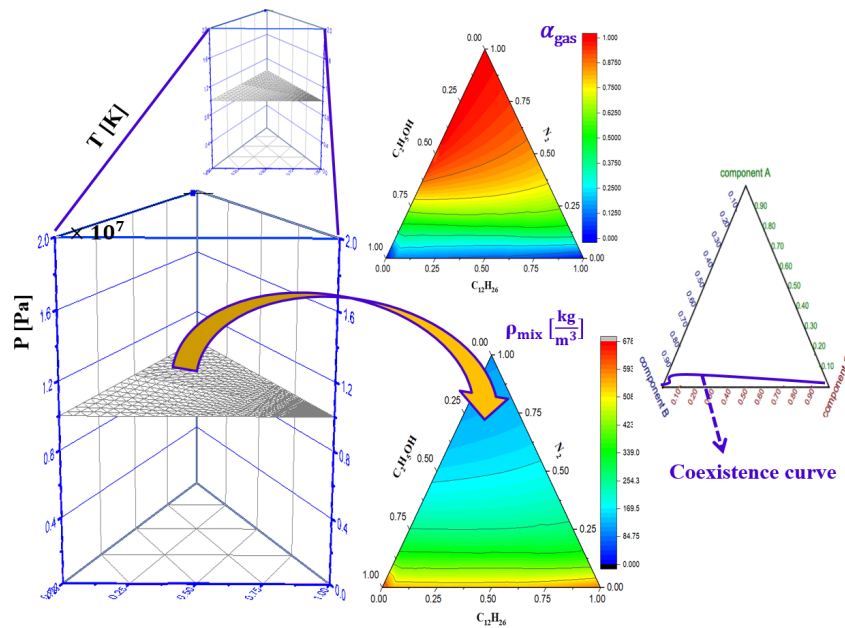


Figure 2.8: Phase diagram for a ternary system consists of n-dodecane-ethanol-nitrogen colored with mixture gas volume fraction and mixture density

However, at a constant pressure like at a chamber, or constant temperature, due to the change of the degree of freedom, the critical point no longer will be as a function of composition for binary mixture. Hence, it has to be taken into account for the tabulation process. This will be studied in chapter 5.

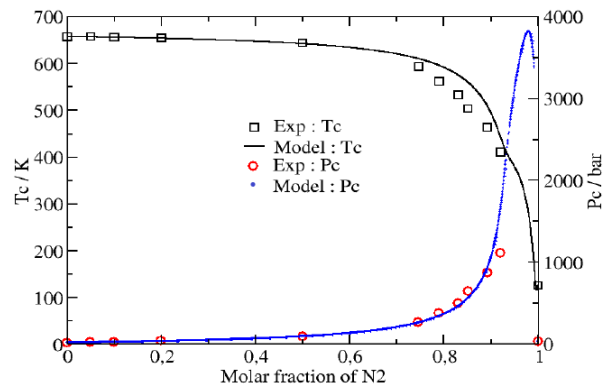


Figure 2.9: Comparison of mixture critical point for  $C_{12}H_{26} - N_2$  system, computed by commercial software Simulis based on Peng-Robinson EoS with experimental data [5]

## 2.3 Conclusion

This chapter has been dedicated to introducing the physical concepts and classical models of single and multi-component two-phase flows under different thermodynamical regimes. Hence, after some explanations and bibliography study about the transcritical and supercritical injection for single and multi-component two-phase flows, some fundamental descriptions about the mathematical and thermodynamics aspects of choosing a proper thermodynamic model under vapor-liquid equilibrium (for a given situation at these regimes) have been presented. As explained, in general, there is no silver bullet for choosing the most accurate equation of state. For some applications, precise properties may be required. However, for others, only qualitative estimates are sufficient. As a general guideline for engineers, it has been recommended that any thermodynamic model must be compared with available experimental data. However, a preliminary thermodynamic analysis could help to find the most appropriate equation of state for different applications by considering the following items as " **the property of interest?** ", " **the composition ?**", and " **the pressure and temperature conditions of the process?**".

## Chapter 3

# High performance simulation using tabulated real fluid EOS considering VLE

### Contents

---

<b>3.1 Real fluid model (RFM)</b> . . . . .	<b>36</b>
3.1.1 Governing equations of the flow solver . . . . .	37
3.1.2 Equilibrium thermodynamic closure of the flow solver, and the tabulation look-up . . . . .	38
3.1.3 Validation of the VLE solver . . . . .	41
3.1.4 Coupling the flow solver with the thermodynamic solver . . . . .	42

---

### 3.1 Real fluid model (RFM)

As discussed in the previous section, many two-phase flow models in the DIM framework have been developed in the literature with the number of transport equations ranging from three to seven based on the initial equilibrium assumptions. In this study, the 4-Equation real fluid (RFM) model developed at IFPEN [17, 22, 78] is employed assuming the flow system to be under the assumptions of thermodynamic equilibrium (i.e. equilibrium of the velocity, pressure, temperature and chemical potential at liquid-vapor interfaces). This two-phase flow model is a fully compressible and homogeneous equilibrium model (HEM) which considers multi-component in both phases.

The set of governing equations as employed in the CONVERGE CFD solver [63] has been used

as a base framework for the development of a modified solver using the tabulated RFM model presented below in this section.

### 3.1.1 Governing equations of the flow solver

The set of governing equations are presented through equations (3.1-3.4) including the density transport equation, species transport equation, mixture momentum equation and mixture specific internal energy equation, respectively.  $(\rho, u_i, P, T, e)$  are the mixture's density, velocity, pressure, temperature, and specific internal energy, respectively.  $(Y_m, h_m)$  are mass fraction and enthalpy of species ( $m$ ) respectively.  $N_s$  is the total number of species.

$$\frac{\partial \rho}{\partial t} + \frac{\partial \rho u_i}{\partial x_i} = 0 \quad (3.1)$$

$$\frac{\partial \rho Y_m}{\partial t} + \frac{\partial \rho Y_m u_j}{\partial x_j} = \frac{\partial}{\partial x_j} (\rho D \frac{\partial Y_m}{\partial x_j}), m = \{1 \dots N_s - 1\} \quad (3.2)$$

$$\frac{\partial \rho u_i}{\partial t} + \frac{\partial \rho u_i u_j}{\partial x_j} = \frac{\partial P}{\partial x_i} + \frac{\partial \tau_{ij}}{\partial x_j} \quad (3.3)$$

$$\frac{\partial \rho e}{\partial t} + \frac{\partial \rho e u_j}{\partial x_j} = -P \frac{\partial u_j}{\partial x_j} + \tau_{ij} \frac{\partial u_i}{\partial x_j} + \frac{\partial}{\partial x_j} (\lambda \frac{\partial T}{\partial x_j}) + \frac{\partial}{\partial x_j} (\rho D \sum_m h_m \frac{\partial Y_m}{\partial x_j}) \quad (3.4)$$

where the viscous stress tensor ( $\tau_{ij}$ ) is given by

$$\tau_{ij} = \mu (\frac{\partial u_i}{\partial x_j} + \frac{\partial u_j}{\partial x_i}) - 2/3 \mu (\frac{\partial u_k}{\partial x_k}) \delta_{ij} \quad (3.5)$$

The thermal conductivity ( $\lambda$ ) and the dynamic viscosity ( $\mu$ ) cover laminar and turbulent contributions. The laminar contribution of  $(\lambda, \mu)$  is computed by Chung et al. [68] correlations. The turbulent conductivity is calculated using a given turbulent Prandtl number as  $(\lambda_t = \frac{C_p \mu_t}{Pr_t})$ , where  $(C_p)$  is the isobaric heat capacity and the turbulent viscosity ( $\mu_t$ ) is computed by the adopted turbulence model. In this work, the standard turbulent subgrid-scale Smagorinsky model is used in the large-eddy simulation (LES) framework [79]. Also, the laminar and turbulent diffusion coefficients are estimated using a given Schmidt number ( $Sc$ ) as  $D = \nu / Sc$ , and  $D_t = \nu_t / Sc_t$ , respectively. It is worth to mention that, for high-speed flows that include discontinuous such as shock-waves, Equation (3.4) can be employed based on a total energy formulation ( $E = e + \frac{u^2_i}{2}$ ) as in Equation (6), to ensure energy conservation.

$$\frac{\partial \rho E}{\partial t} + \frac{\partial}{\partial x_j} (\rho u_j E + u_j P - u_i \tau_{ij} - \lambda \frac{\partial T}{\partial x_j}) = 0 \quad (3.6)$$

### 3.1.2 Equilibrium thermodynamic closure of the flow solver, and the tabulation look-up

The fully compressible multi-component two-phase flow system described above is closed by a real-fluid equation of state (EOS) such as the Peng-Robinson (PR) [64], or Soave-Redlich-Kwong (SRK) [65]. More importantly, a thermodynamic equilibrium hypothesis is also adopted to ensure the hyperbolic mathematical formulation of the RFM model. The current work adopts a tabulation approach where the thermal and transport properties as well as the phase states and compositions are tabulated before the CFD simulation. During the simulation, the various tabulated parameters are robustly interpolated over the entire range of the thermodynamic states based on three inputs for the tables which are the temperature (T), pressure (P) and species mass fraction ( $Y_m$ ,  $m = 1, N_s - 1$ ), where  $N_s$  is the total number of species.

The tabulation is carried out based on the IFPEN-Carnot thermodynamic library which uses a robust isothermal-isobaric (TPn) flash algorithm coupled to various real-fluid equations of state [80]. The mixing rules for the average properties (density, viscosity, speed of sound, etc.) will be presented in the following. This (TPn) flash performs the Vapor-liquid equilibrium (VLE) calculation including the thermal, transport properties and composition in each phase. This tabulation approach offers the advantage of avoiding the direct evaluation of the non-linear cubic EOS along with the VLE calculation during the simulation, which has been proven to be computationally demanding and costly. Moreover, the tabulation approach based on the IFPEN-Carnot thermodynamic library allows to simulate different fuels and surrogates without the need of hard coding a (TPn) flash for each EoS of interest. Besides, when the SRK-EoS or the PR-EoS is used for mixtures, Van-der Waals mixing rules are applied as equation(3.8) for mixtures, where ( $k_{ij}$ ) is the binary interaction parameter (BIP) that can be fitted to experimental data to well represent the phase diagram of a binary system,  $x_i$  is the molar fraction, and  $a_i(T)$  is the parameter calculated using Equation (2.6) for component i.

Besides, the simplistic inverse-distance weighting (IDW) [81] is implemented for the tables interpolation for binary (two-components) mixtures. Hence, the interpolation in the table during the simulation is mainly carried out using two main functions:

1. **A Table look-up function:**

*Compute the thermal, transport properties as well as the phase state using the input parameters (T, P,  $Y_m$ ).*

2. **A Reverse look-up function:**

Compute/Update the temperature using the inputs  $(e, Y_m, P)$ .

A general form of finding an interpolated value of  $u_i$  at a given point  $X$  based on samples  $u_i = u(X_i), i = 1, \dots, N$  using IDW can be expressed as equation (3.7), where  $\omega_i(X) = \frac{1}{d(X, X_i)}$ ,  $X$  denotes an interpolated (arbitrary) point,  $X_i$  is an interpolating (known) point,  $d$  is the given distance from the known point  $X_i$  to the unknown point  $X$ ,  $N$  is the total number of known points used in each local interpolation.

$$u(X) = \begin{cases} \frac{\sum_{i=1}^n \omega_i(X) u_i}{\sum_{i=1}^n \omega_i(X)} & \text{if } d(X, X_i) \neq 0 \text{ for all } i \\ u_i & \text{if } d(X, X_i) = 0 \text{ for some } i \end{cases} \quad (3.7)$$

A general form of a cubic EoS can be written as equation(2.5,2.6) for the SRK and PR EoS, along with the various parameters that are calculated for both equations. The parameters for the two EoS are calculated as listed in Table 1 [64, 65].

$$a(T) = \sum_i \sum_j x_i x_j \sqrt{a_i(T) \cdot a_j(T) (1 - k_{ij})} \quad (3.8)$$

$$b = \sum_i x_i \cdot b_i$$

The procedure of the tabulation using the IFPEN-Carnot thermodynamic library is based on selecting the input parameters  $(T, P, Y_m)$  and the related output properties as  $(\rho, e, C_p, C_v, C_s, \lambda, \mu, \theta, \alpha, \text{PHI})$ . These parameters are stored in the table, as depicted in Figure 3.1. The computation of the output properties is described in the flowchart, as shown in Figure 2.5. Noteworthy, the grid size in each direction  $(T, P, Y_m)$  will be considered uniform, as shown in Figure 3.1. The tabulation procedure is summarized with the following steps.

1. Inputs:  $(T, P, Y_m)$ , where  $(Y_m)$  is the initial (feed) mass fraction of species  $(m)$  and  $(m = 1, N_s - 1)$ , where  $(N_s)$  is the total number of species.
2. Solve VLE problem:  $(\psi_v, x_m, y_m) = \text{VLE}(T, P, z_m)$ , where  $z_m, x_m, y_m$ , are species the initial feed (in mole fraction), species molar fraction in the liquid and gas phase, respectively.  $\psi_v$  is the vapor molar fraction. See [22].
3. If the mixture is in single phase liquid ( $\psi_v = 0$ ) or single phase vapor ( $\psi_v = 1$ ), then the single phase properties are directly computed. In this configuration, if the density is less than  $400 \text{ kg/m}^3$  the phase is assumed to be vapour and if it is greater than  $400 \text{ kg/m}^3$ , it is assumed to be liquid.

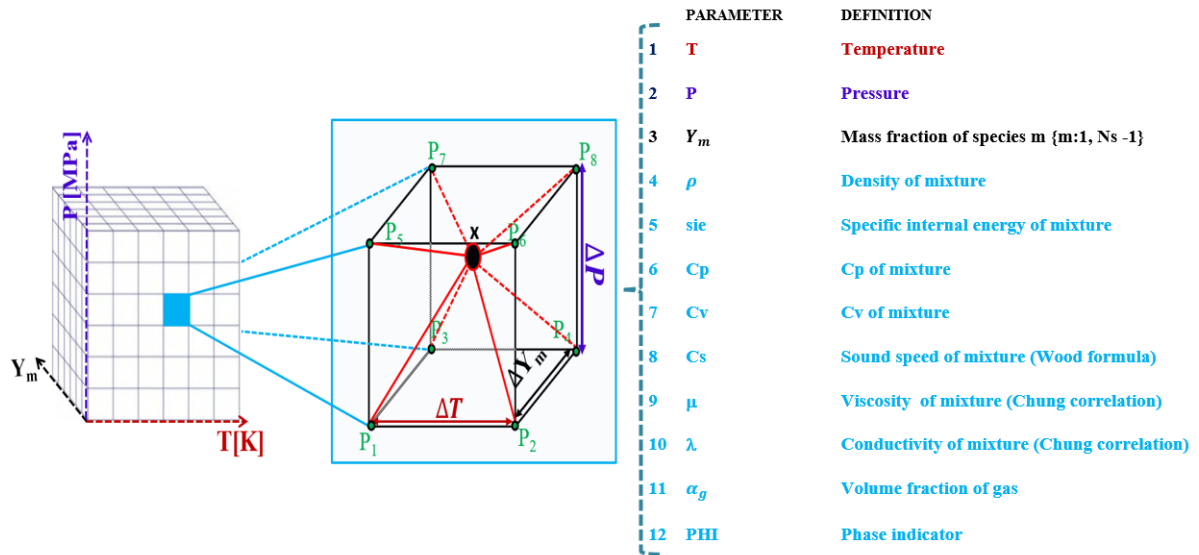


Figure 3.1: Schematic of the thermodynamic table, and the properties calculated, and stored at each cell. P1:P8 are the 8 points of the thermodynamic cell surrounding the unknown point (X). Interpolation approach is based on the inverse distance weighting method.

- If the mixture is in a two phase state ( $0 < \psi_v < 1$ ), compute both the liquid and gas phase properties, then the two-phase mixture properties are evaluated through Equations (3.9-3.15). In (3.9-3.15),  $\alpha_p$  is the phase volume fraction and (p = l; v) stands for liquid and vapor phases, respectively. The vapor volume fraction is computed from the vapor mole fraction ( $\psi_v$ ) as  $\alpha_v = \frac{\psi_v \nu_v}{\psi_v \nu_v + (1 - \psi_v) \nu_l}$ . ( $\rho, e, C_{s,mix;Wood}$ ) are the mixture's density, specific internal energy, and Wood speed of sound.
- Repeat steps (2 and 3) or (2 and 4), until the specified input ranges for ( $T, P, Y_m$ ) are completed for the desired number of points in the table.

$$\rho = \sum_p \alpha_p \rho_p \quad (3.9)$$

$$e = \frac{\sum_p \alpha_p \rho_p e_p}{\rho} \quad (3.10)$$

$$\lambda = \frac{\sum_p \alpha_p \rho_p \lambda_p}{\rho} \quad (3.11)$$

$$C_p = \frac{\sum_p \alpha_p \rho_p C_{p,p}}{\rho} \quad (3.12)$$

$$C_v = \frac{\sum_p \alpha_p \rho_p C_{v,p}}{\rho} \quad (3.13)$$

$$\mu = \sum_p \alpha_p \rho_p \quad (3.14)$$

$$\frac{1}{\rho C_{s,mix,wood}^2} = \sum_p \frac{\alpha_p}{\rho_p C_{s,p}^2} \quad (3.15)$$

### 3.1.3 Validation of the VLE solver

To validate the VLE thermodynamic solver used in the current study, VLE for  $H_2-N_2$  using SRK-EoS has been compared with the available experimental data [82], as shown in Figure 3.2. In this study,  $k_{ij}$  is set to zero. It can be seen that, the calculation results are in a good agreement with the experimental data over the entire range of pressure for the different temperatures. Figure 3.3 shows the variation of different binary mixture properties of  $H_2-N_2$  as a function of temperature and  $H_2$  mass fraction at  $P=4$  MPa, including the mixture density, heat capacity, sound speed, and compressibility factor. These results have been obtained using a uniform table with  $\Delta T = 1K$ ,  $\Delta P = 0.1bar$ ,  $\Delta Y_m = 0.005$  in grid sizes on the three axis. By generating an appropriately refined table, some interesting phenomenon as the heat capacity ( $c_p$ ) peak around the Widom line can be seen in Figure 3.3(b). In this Figure, it is important to note that this ( $c_p$ ) peak exists not only for single component  $N_2$  but also for  $N_2 - H_2$  mixtures, particularly when a small amount of  $H_2$  is mixed with  $N_2$  as long as the mixture remains homogeneous. As soon as the mixture enters the two-phase zone, the heat capacity has no physical meaning any more. The plot shows an average value of  $C_p$  for the saturated liquid and vapour phases, according to equation 3.12. These figures illustrate the strongly non-linear behaviour of these four properties and therefore the importance of using complex EoS for the regions where the compressibility factor value is far from unity, as shown in Figure 3.3(d).

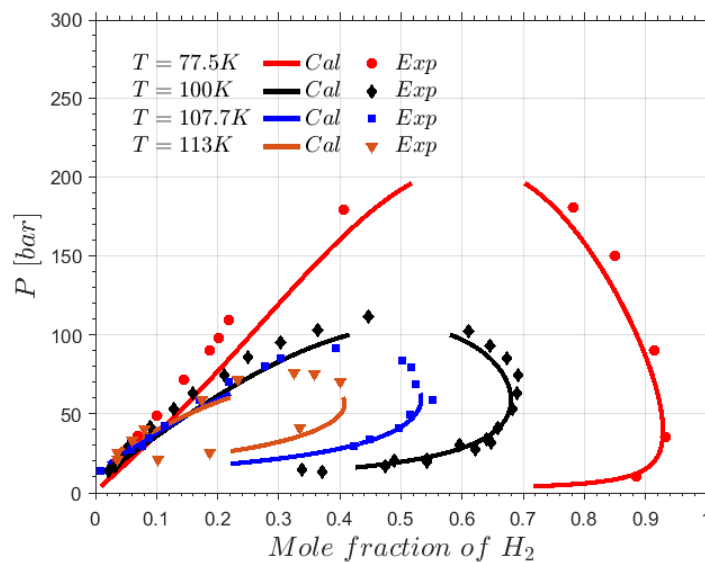


Figure 3.2: Vapor-Liquid equilibrium of  $H_2-N_2$  calculated in this study using SRK-EoS compared to the experimental data [82].

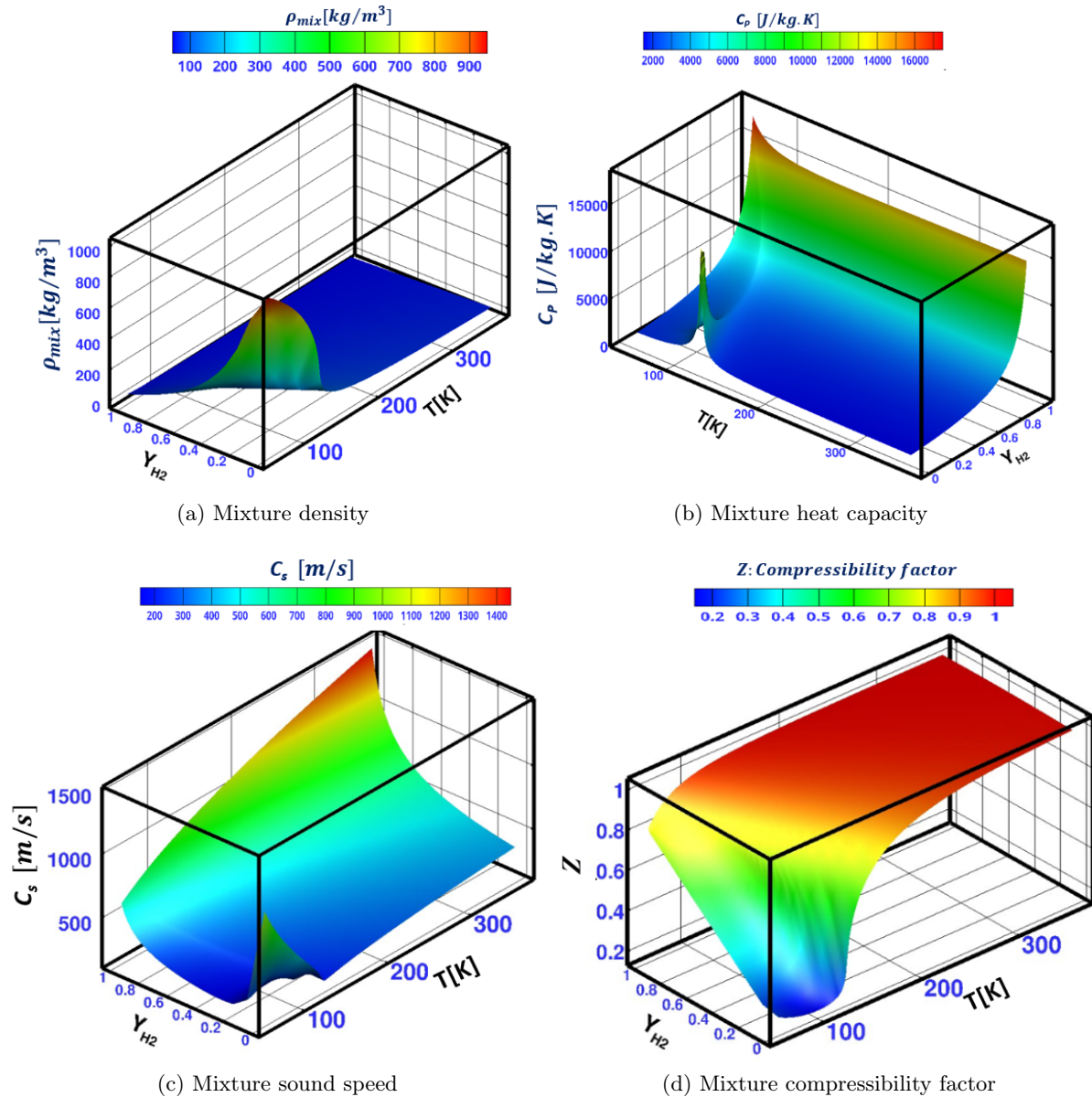


Figure 3.3: Different properties variations as a function of temperature and  $H_2$  mass fraction for binary mixture of  $H_2-N_2$  at  $P=4$  MPa

### 3.1.4 Coupling the flow solver with the thermodynamic solver

The coupling between the flow solver and the thermodynamic solver is one of the critical elements in the RFM model proposed in this article. To our knowledge, most of the available two-phase flow equilibrium solvers in the literature are proposed so that the thermodynamic state in each computational cell will be determined after solving of the mass, momentum, and energy equations [17,22,34,35,53,83]. This means that the flow solver is completely decoupled from the thermodynamic solver, considering the superposition principles. Figure 3.4(a) shows a schematic of this typical and conventional approach [17], where the system molar internal energy ( $U$ ), molar volume ( $V$ ), and molar numbers ( $n$ ) are specified, and all other thermal properties are

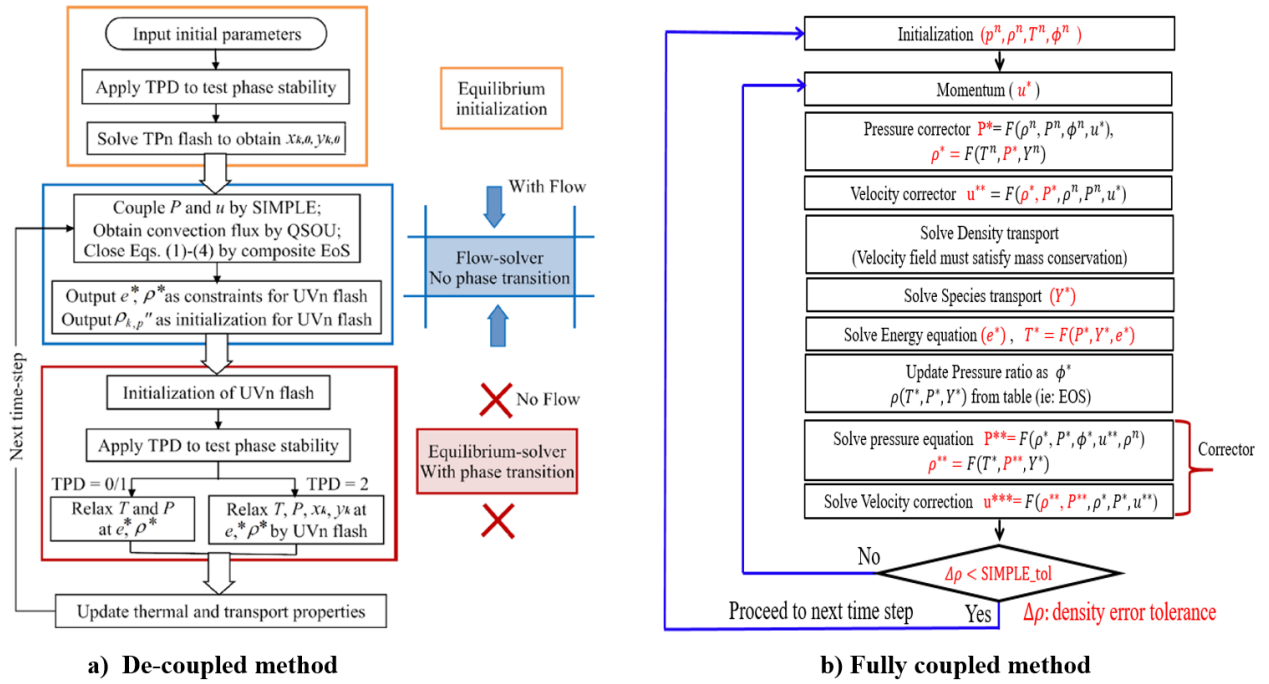


Figure 3.4: (a) Flow chart of the decoupled flow solver and thermodynamic solver used in [17] for the SIMPLE algorithm and (b) the proposed flow chart of the fully coupled flow solver and thermodynamic solver applied in the SIMPLE algorithm.

determined using the so called (UVn) flash. The author's previous studies demonstrate that due to the separation of the flow solver and thermodynamic solver, it may lead to the growth of oscillations on the solution fields which delays the solver's convergence. More information about this conventional decoupled approach can be found in [17,22]. To dampen the difficulties of multi-phase solvers due to the previous decoupled method, a new and novel algorithm is introduced in this study. It is mainly based on the isothermal-isobaric (TPn) flash which is known to be more robust and efficient. As shown in Figure 3.4(b), a strong coupling between the flow solver and the thermodynamic solver is used throughout the different steps of the SIMPLE numerical scheme. In fact, similar strong coupling has been introduced in the PISO numerical scheme, as depicted in Figure 3.5. In the following, these two novel iterative algorithms are discussed in the case of the two-phase RFM model:

1. A modified Pressure Implicit with Splitting of Operator (PISO) method of Issa (1986) [84], see Figure 3.5
2. A modified Semi-Implicit Method for Pressure-Linked Equations (SIMPLE) method of Patankar, 1980, Figure 3.4(b) [85].

The modified SIMPLE algorithm solves the same set of equations as the modified PISO (Equations (3.1-3.4)). However they are solved in SIMPLE so that the momentum equation is solved

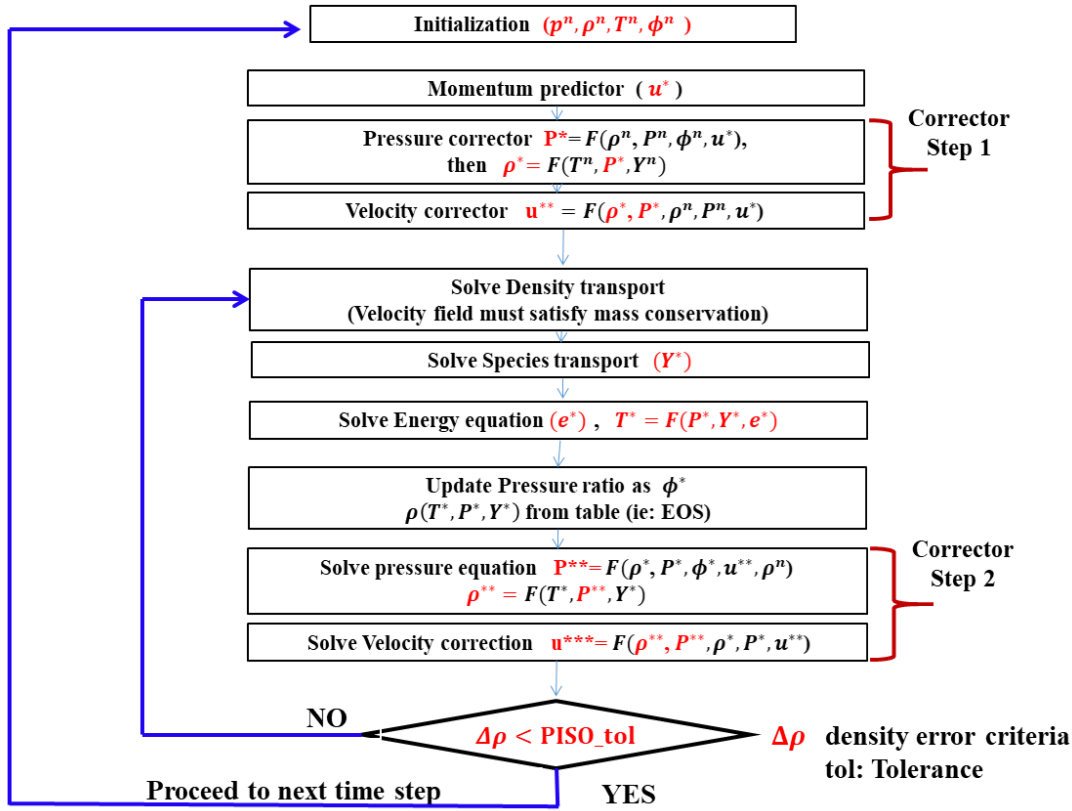


Figure 3.5: Flow chart of the RFM PISO algorithm.

within the iterative algorithm, rather than as a predictor step in PISO. Generally, it has been accepted that SIMPLE has the advantage of respecting the hyperbolic nature of the transport equations, while using the elliptic nature of the pressure equation. The practical difference between SIMPLE and PISO is that SIMPLE more strongly couples the velocity and the pressure while it is numerically more expensive than the PISO approach. Using PISO or SIMPLE should finally be decided depending on the nature of the resolved flow. SIMPLE should be preferred for highly unsteady flows. In order to determine the pressure field, a pressure Poisson equation is derived and solved iteratively using a predictor-corrector PISO or SIMPLE algorithm [63]. Equation (3.16) is a semi-discretized form of this equation where the superscript n represents the previous field values, and (\*) represents the intermediate most up-to-date field values in the iterative algorithm.

$$\frac{\partial \rho}{\partial t} = dt \frac{\partial^2}{\partial x_i \partial x_i} (P^* - P^n) - \left( \frac{\partial \rho_n u_i^*}{\partial x_i} \right) \quad (3.16)$$

Considering that Equation (3.16) is solved in SIMPLE through a double isothermal algorithm as shown in figure 3.4 (b) and assuming low variation of the density with the composition, one can write this equation as equation (3.17).

$$\rho \beta_T \frac{\partial P}{\partial t} = dt \frac{\partial^2}{\partial x_i \partial x_i} (P^* - P^n) - \left( \frac{\partial \rho_n u_i^*}{\partial x_i} \right) \quad (3.17)$$

Where  $\beta_T = \frac{1}{\rho} \left( \frac{\partial \rho}{\partial P} \right)_T$  is the isothermal compressibility factor. Finally, the fully discretized Poisson equation reads,

$$\frac{\partial^2}{\partial x_i \partial x_i} (P^* - P^n) - \frac{(P^* - P^n) \phi^n}{dt^2} = \left( \frac{\partial \rho_n u_i^*}{\partial x_i} \right) * \frac{1}{dt} \quad (3.18)$$

where  $\phi^n = (\rho \beta_T)^n$ , so that

$$\phi = \left( \frac{\partial \rho}{\partial P} \right)_T = \begin{cases} \frac{\rho}{P} & \text{for ideal gas EoS: } P = \rho R T \\ \frac{\rho}{k} & \text{for barotropic EoS: } \rho = \rho_0 e^{(P-P_0)/k} \\ \rho \beta_T = \frac{\gamma}{c^2} & \text{for real-fluid EoS: } \rho = \rho(P, T, Y_m) \end{cases} \quad (3.19)$$

The only unknown of equation (3.18) is now  $P^*$  which can be calculated knowing the first corrector of velocity  $u_i^*$  and the pressure and density values of previous time step,  $n$ . After the momentum predictor and first corrector step have been completed, the other transport equations are solved in series. An important point is the calculation of the temperature after solving the energy equation, as shown in Figure 3.4(b) at each SIMPLE loop. This temperature calculation is carried out using the reverse look-up function  $T^* = F(e^*, P^*, Y_m^*)$ , as explained in Section 2.2. Then, the process of correcting the momentum equation and re-solving is repeated as many times as necessary to achieve the desired accuracy.

To sum up, the implementation of the RFM model can be summarized as follows:

1. Reading the thermodynamic table during the simulation setup and initialize the thermal and transport properties as well as phase state based on the temperature ( $T^n$ ), pressure ( $P^n$ ) and species mass fraction ( $Y_m^n$ ) in the domain, where the exponent (n) denotes the current time step.
2. Solve the momentum predictor, and then the first corrector step.
3. Solve the transport equations in the order shown in the flow chart, as depicted in Figure 3.4(b).
4. At the end of each iteration loop, the convergence is checked based on the density correction error  $\frac{\rho^* - \rho^{n-1}}{\rho^*}$  for density based solver, where  $\rho^*$  : current correction for the density and  $\rho^{n-1}$  is the previous value of the density correction, and  $\frac{P^* - P^{n-1}}{P^*}$  for pressure based solver, where  $P^*$  : current correction for the pressure and  $P^{n-1}$  is the previous value of the pressure correction. If the specified loop tolerance error is reached, the values of the previous time

step are updated before proceeding to the next time step, otherwise a new SIMPLE or PISO loop is performed.

One important subject is related to the density-based solver used in this study to solve the RFM model. Indeed, flow field instabilities may be generated by such solver when the fluid is almost incompressible and the sound speed is high, so that the Mach number tend to zero. In fact, due to the appearance of liquid as incompressible fluid, along side with the gas phase as compressible one, the simulation of such flows may face numerical difficulties due to large gradients of density, speed of sound and time scale. As a result, researchers have categorized the problems into compressible and incompressible one by introducing density-based and pressure-based solvers. On the one hand, the density-based approach was originally designed for high-speed compressible flows so that the continuity equation is used to obtain the density field while the pressure field is determined from the equation of state. The pressure-based solvers, on the other hand, traditionally has been used for incompressible and mildly compressible low mach number flows by manipulating continuity and momentum equations, so that the solution of density transport equation is ignored, and the density field is computed via the equations of state. Preliminary studies of the proposed RFM model solver have shown that the instability and the oscillations of the flow field at low pressure cases could be reduced using a pressure-based solver along with some under-relaxation of the pressure ratio.

## Chapter 4

# Thermodynamic table refinement approaches

### Contents

---

<b>4.1</b>	<b>Review on the VLE Tabulation Approaches</b>	<b>48</b>
<b>4.2</b>	<b>Preliminary Remarks on VLE Tabulation</b>	<b>49</b>
<b>4.3</b>	<b>Introduction to data structuring</b>	<b>54</b>
4.3.1	Uniform Tabulation	54
4.3.2	Non-Uniform Tabulation: Quadtree and Octree	59
4.3.3	IFPEN Shared Memory for refined Uniform Table storage and access	71
<b>4.4</b>	<b>Preliminary highly resolved RFM simulations</b>	<b>72</b>
<b>4.5</b>	<b>Conclusion</b>	<b>78</b>

---

As explained in chapter 2, nonlinear and steep gradients for different properties exist near the phase and phase-like boundaries. It is therefore required to specify a proper table discretization in these regions. After a short review on the VLE tabulation approach, the difficulties of tabulating properties from the VLE algorithms is explained and the reasons why grid-table refinement in the vicinity of the phase boundary are discussed. This chapter is dedicated to introducing different approaches for refining the thermodynamic tables. For this purpose, an introduction about data structuring and how it is usually used to organize the data is discussed. Next, different types of tabulation, searching and interpolation approaches will be explained and introduced as possible refinement methods. Finally, the strengths and weaknesses of the proposed methods are summarized. In addition, some 1D and 2D academic simulations will be presented to better

compare and investigate the full coupling of the thermodynamic and CFD solvers using the presented searching and interpolation approach.

## 4.1 Review on the VLE Tabulation Approaches

As briefly recalled in the previous Chapter, iteratively online solving the Vapor–Liquid–Equilibrium (VLE) using the isoenergetic-isochoric (UV)-flash set of equations are computationally expensive [17, 22, 43, 80, 86]. In addition, the efficiency decreases as the number of species increases for multi-component simulations. Therefore, directly applying VLE is costly for CFD simulations. To reduce the computational effort, different researchers have proposed to calculate the fluid properties before the simulation [78, 87–92]. Then, these properties are stored inside a table, and an interpolation of the updated values is carried out during the simulation. This method has significantly reduced the computational time of the CFD simulations. For instance, Azimian et al. [88] introduced an artificial neural network (ANN) model for generating the water/steam thermodynamic tables to reduce the computational expenses of solving flash calculations. De Föll et al. [91] proposed a tabulation method based on a projection approach for single-component fluids using a quad-tree data structure. Lorenzo et al. [89] suggested a 2D single component look-up table method for water-steam simulation. In their work, bilinear functions were used to regularize the shape of the thermodynamic domain in the energy-volume (UV) space so that an accurate bi-cubic interpolation could be used. Praneeth and Hickey [92] introduced a systematic error quantification and computational cost estimation of EoS for compressible single-component tabulation. They reported that, due to the inherent thermodynamic non-linearity around the pseudo-boiling curve, minor errors in the thermodynamic property estimation could lead to significant variations in the computed pressure and temperature, which directly affects the thermal and transport properties calculations in the flow. Most of the above-mentioned studies have focused on single-component fluids. However, few studies were carried out with multi-component fluid mixture tabulation. One of the notable studies was performed by Brown et al. [87]. They suggested a multi-component two-phase homogeneous equilibrium model (HEM) as a flow solver for binary and quaternary mixtures, allowing a two-dimensional (P, T)-based adaptive inverse interpolation approach. Another notable study was recently conducted by Koukouvinis et al. [86]. In that study, the authors proposed a uniform, tabulated thermodynamic approach based on the NIST-database and VLE using PC-SAFT EoS for the simulation of the ECN spray A injection conditions. They reported that, by using the PC-SAFT EoS and  $\log_{10} P - T$  tabulation approach, the results were independent of table size when bi-linear interpolation was adopted.

Therefore, to summarize, most available studies show that tabulation could be enough accurate and its search algorithm is fast, especially when applied to a mixture with a small number of species, say less than four.

## 4.2 Preliminary Remarks on VLE Tabulation

In this thesis, various studies have been performed for different applications and flow regimes to better understand the tabulation impacts on the CFD simulations. In the following, some explanations about the VLE tabulation difficulties and some issues that can lead to failed simulations will be presented.

Figure 4.1 shows the pressure-temperature diagram for two pure components (n-dodecane and nitrogen), as well as the pressure-composition diagram for the n-dodecane-nitrogen binary mixtures at different temperatures. From the tabulation point of view, there are several details in these diagrams that one should pay attention to. More specifically, Figure 4.1(a) demonstrates the phase boundary variations for pure nitrogen (in black) and pure n-dodecane (in red). This Figure also highlights that the nonlinearity of the phase boundary as functions of pressure and temperature for different pure components is dissimilar. Therefore, to capture the phase boundary during the simulation, as the locus of the properties high gradient, it should be taken into account and identified in the thermodynamic tabulation. Besides, Figure 4.1(b) clearly demonstrates that for binary systems, not only the nonlinearity of phase boundary for different temperatures has increased compared to the pure components, but also, the mixture critical pressure point has increased significantly with decreasing the temperature.

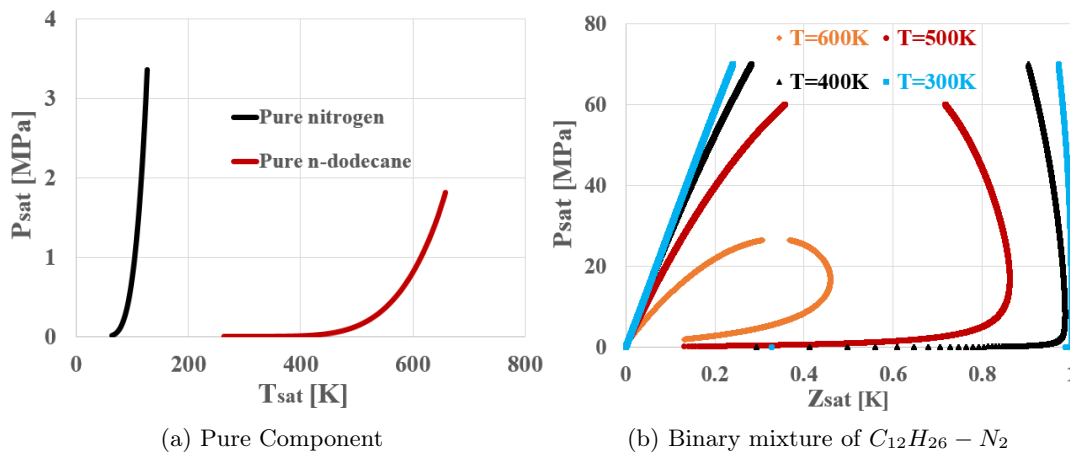


Figure 4.1: (a) Pressure-Temperature diagram for pure n-dodecane, and nitrogen, and (b) Pressure-Molar composition diagram for binary mixture of n-dodecane-nitrogen ( $C_{12}H_{26} - N_2$ ) at different temperatures.

This seems to indicate that different tabulation refinements strategy should be applied for different multi-component mixtures in various flow regimes compared to single-component flows. Another important point that is worth mentioning is the effects of tabulation strategy on the interpolation accuracy of the different properties during the runtime. Indeed, the different non-linearity for the various properties should be taken into account during the table generation step. As examples, the effects of table refinement on the mixture density ( $\rho_{Mix}$ ) and sound speed ( $C_s$ ) non-linearities representation is depicted in the following figure 4.2.

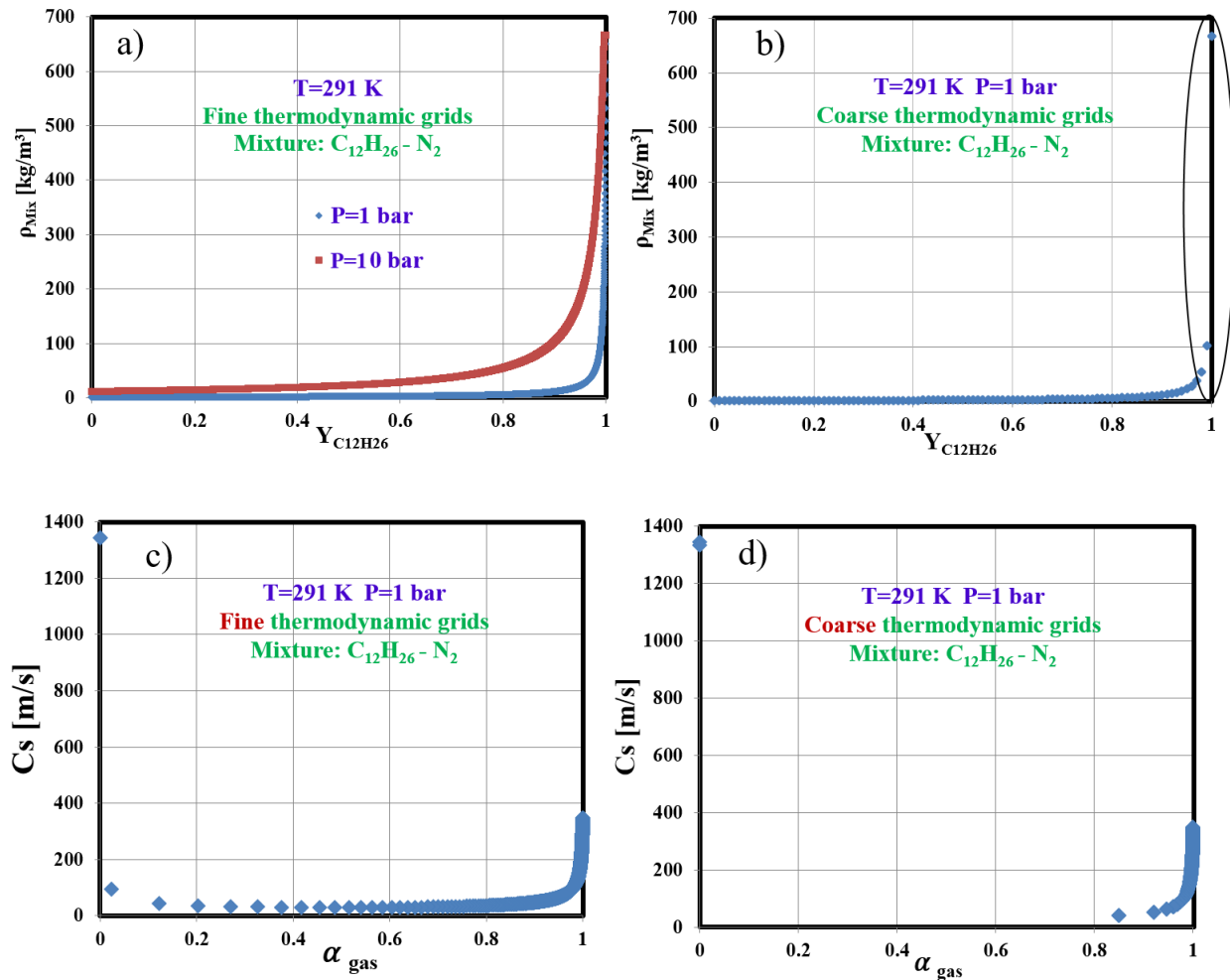


Figure 4.2: Effects of the refinement of the table on the data distributions: (a) The mixture density ( $\rho_{Mix}$ ) variations of n-dodecane-nitrogen ( $C_{12}H_{26} - N_2$ ) as a function of n-dodecane mass fraction at different pressures of  $P = 1$  bar, and  $P = 10$  bar at  $T = 291 K$  for grids refined with 500 points in mass fraction axis. (b) The mixture density variations of n-dodecane-nitrogen ( $C_{12}H_{26} - N_2$ ) as a function of n-dodecane mass fraction at  $P = 1$  bar at  $T = 291 K$  for coarse grids with 100 points in mass fraction axis. (c) The mixture sound speed ( $C_s$ ) variations, using Wood formula [93] for two phase region, of n-dodecane-nitrogen ( $C_{12}H_{26} - N_2$ ) as a function of mixture gas volume fraction at  $P = 1$  bar at  $T = 291 K$  for refined table-grids with 500 points in mass fraction axis. (d) The mixture sound speed variations, using Wood formula [93] for two phase region, of n-dodecane-nitrogen ( $C_{12}H_{26} - N_2$ ) as a function of mixture gas volume fraction at  $P = 1$  bar at  $T = 291 K$  for table-grids refined with 100 points in mass fraction axis

Figure 4.2(a) shows the mixture density variations of n-dodecane-nitrogen ( $C_{12}H_{26} - N_2$ ) as a function of n-dodecane mass fraction at different pressures of  $P = 1$  bar, and  $P = 10$  bar at  $T = 291K$  with a grid table refined with 500 points in mass fraction axis. As shown in this figure, the degree of nonlinearity (i.e the slope of the curve) in the mixture density near the phase boundary location ( $Y_{C_{12}H_{26}} = 1$ ) depends on the pressure, as an independent input of the thermodynamic solver. Hence, a higher number of table grid points in the Y-axis seems to be required for the lower (1 bar) pressure case. Figure 4.2(b) indicates the under-resolved high gradient region for a coarse table with only 100 points in Y-axis. Besides, this coarse grid generation can have some other indirect impacts for capturing the actual two-phase behaviors in the VLE region. For instance, Figure 4.2 demonstrates the mixture sound speed variations, using Wood formula for two-phase region [93] of n-dodecane-nitrogen ( $C_{12}H_{26} - N_2$ ) as a function of mixture gas volume fraction at  $P = 1$  bar at  $T = 291K$  for a grid table refined with 500 points (see Figure 4.2(c)), and a coarse grid table with only 100 points (see Figure 4.2(d)) in the mass fraction axis. As depicted in the latter figure, the coarse grid table poorly capture the behavior and nonlinearity of the two-phase region for the mixture sound speed. Therefore, such coarse table can lead to some nonphysical behavior in the two-phase regions.

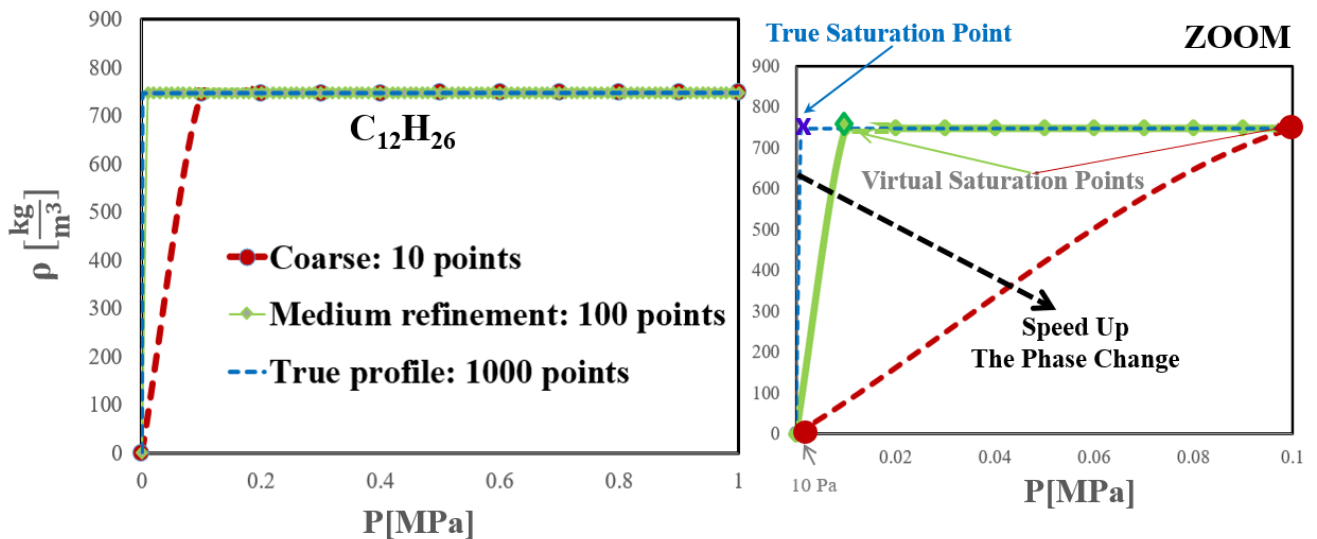


Figure 4.3: Variations of n-dodecane density as a function of pressure at constant temperature

$T=300$  K. Coarse and medium grids generation, the non-refined tables, with red and green colors with different numbers of points on the pressure axis, lead to the appearance of virtual saturation points. The profile with the refined table is shown with blue color as "True profile".

The locus of virtual saturation points have been marked with the red and green color for two different non-refined tables. These nonphysical saturation points lead to movement of the phase transition position, which is a function of the number of grid points, and it commences to various phase change nonlinearities and behaviors for the flow.

Another critical point concerns the capture of saturation points as a cornerstone of the tabulation-based approach, as shown in figure 4.3. This figure shows the n-dodecane density as a function of pressure at constant temperature  $T = 300K$  using increased table refinement (10, 100, 1000) points in the P-axis of the table. The effect of table refinement on the numerical capture of the actual saturation point is highlighted. All tables lead to the appearance of a virtual saturation point that should approach the actual saturation point as the table is refined. The locus of virtual saturation points are marked with different colors in Figure 4.3. These nonphysical saturation points lead to an artificial shift of the phase boundary which affect the phase transition timing and the behaviors of the flow. More importantly, artificially shifting the phase boundary can cause the simulation to fail due to the altered intensity of the phase change. As a matter of fact, the artificially shifting the phase boundary caused by coarse tables is also responsible of the compressibility ( $\frac{dP}{d\rho}$ ) change in the vicinity of the actual saturation point, as depicted in Figure 4.3. This artificial change of ( $\frac{dP}{d\rho}$ ) has an indirect impact on the solver stability due to altered sound speed and compressibility. This compressibility alteration may have a significant effects on the flow especially for nearly incompressible flows for which ( $\frac{dP}{d\rho} \approx 0$ ), as shown in Figure 4.4. This explains why a well-refined table is needed to compute the best approximation of ( $\frac{dP}{d\rho}$ ) at the phase boundary in order to dampen the numerical instabilities of almost incompressible flows, in particular. Figure 4.4 also shows how the density evolves for various degree of compressibility.

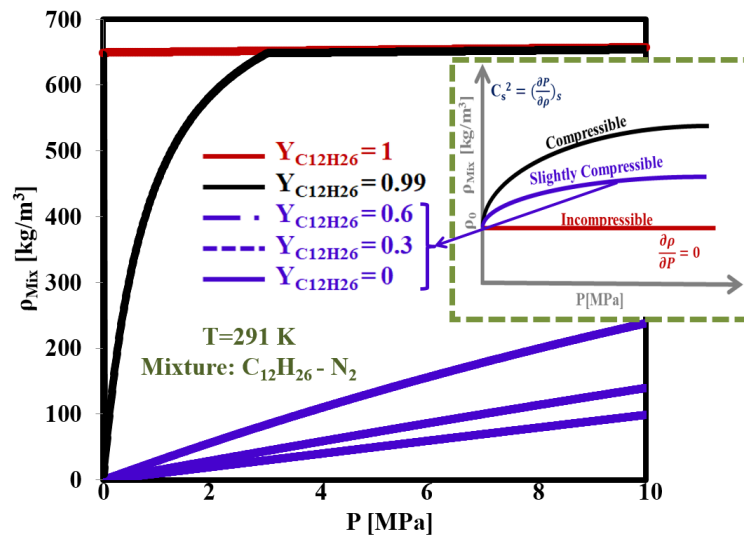


Figure 4.4: Variations of mixture density for the binary mixture of n-dodecane-nitrogen ( $C_{12}H_{26} - N_2$ ) as a function of pressure at different n-dodecane mass fractions at  $T = 291K$ .

Since the variation of density due to pressure changes is negligible for incompressible and is considerable for compressible flow, by changing the saturation points, the compressibility or  $\frac{dP}{d\rho}$  of the flow will be changed.

To summarize, various investigations have been performed above for different flow regimes to better understand the tabulation impacts on CFD simulations. It has been demonstrated that coarse thermodynamic tables and inaccurate interpolation of thermodynamic properties may lead to various inconsistency effects. These issues are summarized as follows:

- Inaccurate saturation points due to coarse tabulation, which are far from the actual saturation points, may cause unrealistic behaviors.
- Coarse thermodynamic grids and inappropriate interpolating of different thermodynamic properties lead to thermodynamic consistency and stability problems during simulations.

Therefore, a proper refinement methodology near the phase and phase-like boundaries needs to be considered, as shown in the P-T diagram of Figure 4.5. The following subsections are dedicated to studying different approaches for structuring the data in order to be able to generate refined table in regions with strong gradients like the vicinity of the phase boundary or the Widom-line.

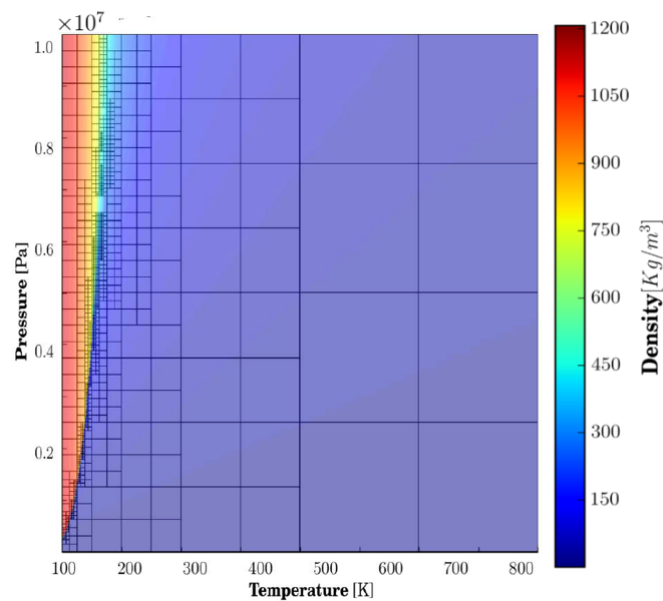


Figure 4.5: 2D refinements near the phase boundary for pure oxygen colorized with density at PT diagram [92]

### 4.3 Introduction to data structuring

In computer science, the organization, processing, retrieving and storing of data in such a way it facilitates efficient access and modification on them are known as data structuring. Various basic and advanced types of data structures are designed to arrange data to satisfy different particular targets [94,95]. In the following, different types of data structuring approaches in the framework of the RFM model will be investigated, and the cons and pros of each approach will be explained. As mentioned section 3, the tabulation approach consists of three steps, as table generation, table lookup, and interpolation. However, using different strategies of data structuring will affect these steps especially in terms of efficiency. Therefore, the desired tabulation method should be accurate, have low-storage requirements, and provide a fast lookup. Generally, in engineering science, the data can be tabulated in different ways based on data structuring. In the following, different types of data structuring and searching will be explained comprehensively.

#### 4.3.1 Uniform Tabulation

A uniform table is a symmetric arrangement of statistical data in rows and columns, known as one of the simplest grid point generation method to distribute the points in a domain. Based on this tabulation approach, all columns of the table share the same scale. Figure (4.6-4.7(a)), respectively displays a uniform grid table for a pure n-dodecane and for a typical n-dodecane-nitrogen mixture (80% of  $C_{12}H_{26}$  and 20% of  $N_2$ ) in a P-T diagram. The table values are stored in each cell-center. This kind of data structuring is known as "node-based" tabulation approach, which depends only on a node at the center of each cell, as already discussed in figure3.1.

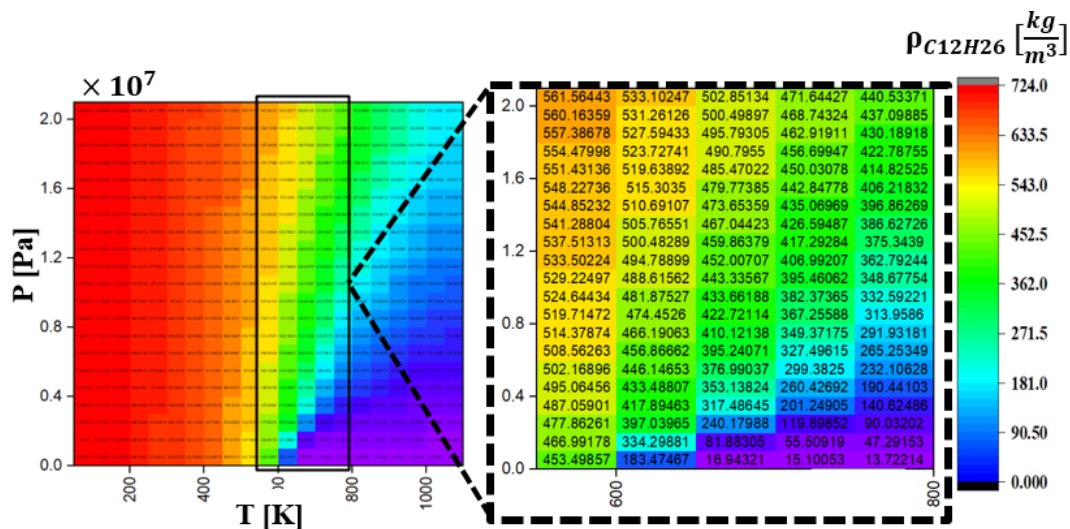


Figure 4.6: P-T diagram for pure n-dodecane colored by density.

Besides, the results also indicate the different nonlinearities at dissimilar conditions for the

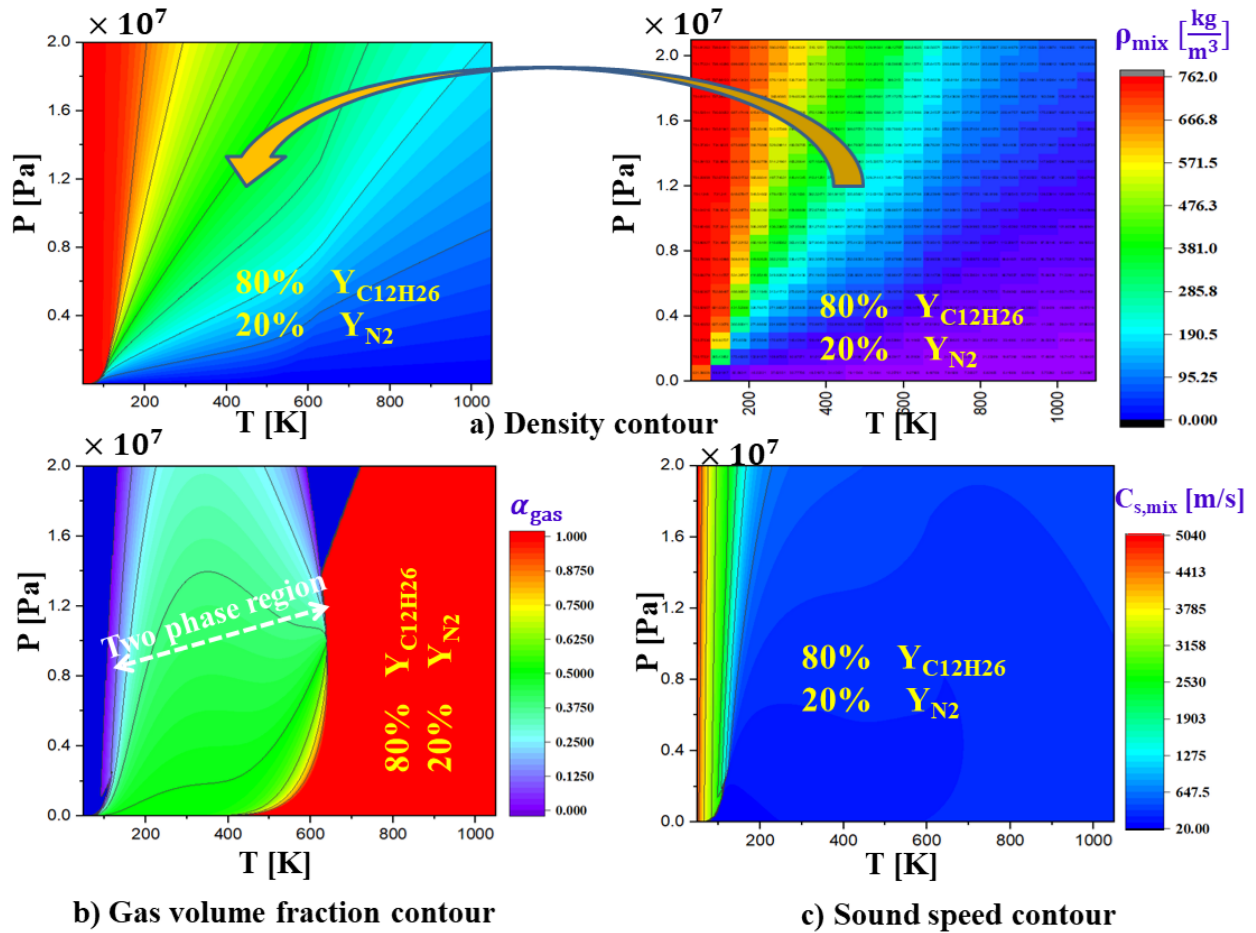


Figure 4.7: (a) Contour plots of mixture density, (b) Mixture gas volume fraction, (c) Mixture sound speed, for a typical n-dodecane-nitrogen mixture (80% of  $C_{12}H_{26}$  and 20% of  $N_2$ ). The results as well indicate different nonlinearities at dissimilar conditions for the properties.

properties, which need to be considered for the tabulation.

#### 4.3.1.1 Generation of a table with uniform distribution

As discussed in the previous chapter, figure 3.1 shows the schematic of the thermodynamic table structure for a uniform table in the case of a binary mixture. P1:P8 are the 8 points of the thermodynamic cell surrounding the unknown point (X). In this configuration, the table cell sizes in pressure ( $\Delta P$ ), temperature ( $\Delta T$ ), and mass fraction ( $\Delta Y$ ) axes can be computed readily by  $\Delta P = \frac{P_{max} - P_{min}}{N_p - 1}$ ,  $\Delta T = \frac{T_{max} - T_{min}}{N_T - 1}$  and  $\Delta Y = \frac{Y_{max} - Y_{min}}{N_Y - 1} = \frac{1 - 0}{N_Y - 1}$ , where *min* and *max* indexes denote the minimum and maximum values prescribed for each axis along with  $N_P$ ,  $N_T$ , and  $N_Y$ , the number of points that will be assigned for the discretization of pressure, temperature, and mass fraction axis, respectively. Besides, it is important to mention the manner of writing the properties in the table. For the current uniform table, the properties will be stored inside the table using a 3D loop as shown in the following C++ commands:

```

for (int k = 1; k < NY+1; k++) {
    for (int j = 1; j < NP+1; j++) {
        for (int i = 1; i < NT+1; i++) {

            T = T_min + delta_T * i;
            P = P_min + delta_P * j;
            Y = Y_min + delta_Y * k;

            Here are calculated the required thermodynamic and transport
            properties assuming VLE and some correlations , as discussed in
            Chapter 3

        }
    }
}

```

Hence, in order to calculate the required properties during the simulation, the following two tasks are carried out:

- **Search task** : It consists in searching the 8 neighbors P1:P8 of the unknown ( $X$ ), as shown in figure 3.1.
- **Interpolation task** : It consists in interpolating the properties values based on the distance weighting approach [81], as discussed in chapter 3, see equation (3.7).

The details of these two tasks are reported in the following section.

#### 4.3.1.2 Searching the 3-D arrays

Since the grid sizes ( $\Delta P$ ,  $\Delta T$ , and  $\Delta Y$ ) are constant and uniform, the searching of the desired cell can be achieved by a local searching in each array, independently of other axes. As a result, the searching duty is to report the indexes of neighbors in each axis. The index of the unknown point in each axis is given by equations 4.1.  $I_{k_{cell,min}}$  is the neighbor index with minimum  $k$  values, in pressure, temperature, or mass fraction arrays, in the proximity of unknown property with the coordination ( $P^*$ ,  $T^*$ ,  $Y^*$ ). Indeed, the neighbors indexes with maximum values can be achieved by  $I_{k_{cell,max}} = I_{k_{cell,min}} + 1$ . The values of  $T_{table,min}$ ,  $P_{table,min}$ ,  $Y_{table,min} = 0$  are the

minimum values that have been assigned for the generation of the thermodynamic table.

$$\begin{cases} I_{P_{cell,min}} = \frac{P^* - P_{table,min}}{\Delta P} + 1 & 1 \leq I_{P_{cell,min}} \leq N_P \\ I_{T_{cell,min}} = \frac{T^* - T_{table,min}}{\Delta T} + 1 & 1 \leq I_{T_{cell,min}} \leq N_T \\ I_{Y_{cell,min}} = \frac{Y^* - Y_{table,min}}{\Delta Y} + 1 & 1 \leq I_{Y_{cell,min}} \leq N_Y \end{cases} \quad (4.1)$$

Finally, the last step is to interpolate between these 8 identified table points to calculate the properties values based on the distance weighting approach [81], as described in chapter 3 by equation (3.7).

#### 4.3.1.3 Logarithmic distribution of table axes

As demonstrated in the previous section, the search task is very efficient using uniform tabulation, as it is performed by jumping to the exact cell being searched using equations 4.1. However, the main problem with the uniform tabulation approach is that for some physical phenomena such as cavitation in high injection pressure nozzles, the pressure range for generating the table is often very wide. Hence, to capture the nucleation and phase boundary evolution in a cavitating flow, the size of the table will be cumbersome using a uniform table. Some researchers proposed the logarithmic distribution approach [86] to discretize the pressure axis. Hence, in order to remain in the uniform structure for searching, and interpolation, the properties are stored inside the table in the logarithmic space with uniform distribution as  $(T, \log_n P, Y)$ , where  $n$  is usually taken equal 10 for a base 10 logarithmic distribution. Therefore, in this case  $\Delta P$  is defined as follows:

$$\Delta P = (\log_{10}(P_{max}) - \log_{10}(P_{min})) / (N_P - 1) \quad (4.2)$$

In this way, the above listed table generation C++ commands are not modified.

Then, after the searching and interpolation steps in the space  $(T, \log_{10} P, Y)$ , one can recover easily to the normal space as  $(T, P, Y)$ . Figure 4.8 exhibits the logarithmic distributions (base 10) of pure n-dodecane density profile as a function of pressure at  $T=293$  K using 1000 points in normal space (a) and logarithmic space (b). As it demonstrates, it designates more points for low pressures and fewer points for high pressures using a logarithmic distribution, with a greater base value than the Neper( $e=2.7182$ ) number. However, to capture the saturation point with a uniform tabulation approach,  $(P_{sat} \approx 140 Pa = \Delta P)$ , at least  $N_p = \frac{1e^6 - 0}{\Delta P} \approx 6800$  points is needed to capture the saturation point. This is so that even with this number of points, any point will not be assigned between the minimum pressure value in the table and the saturation

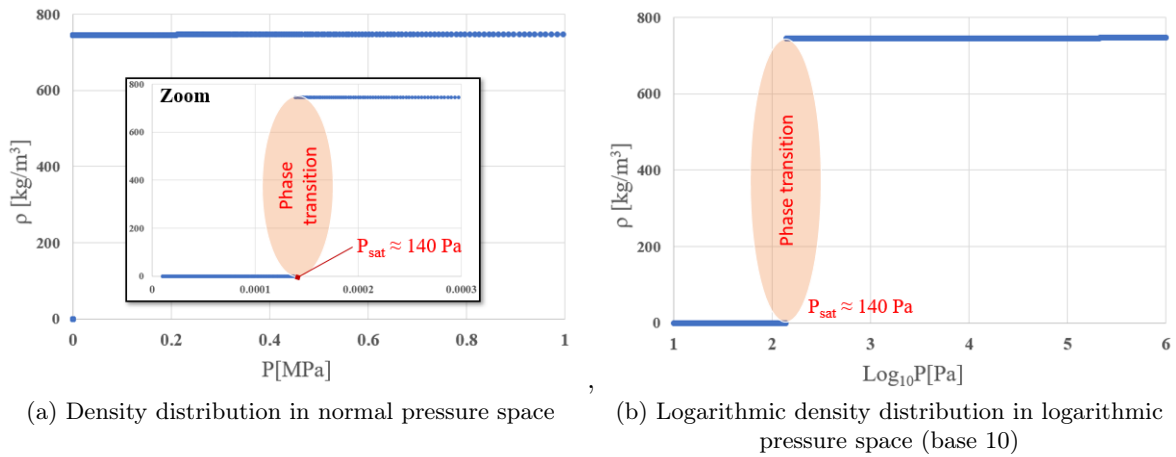


Figure 4.8: Distribution of pure n-dodecane density as a function of pressure at  $T=293$  K using 1000 points the normal space (a), and logarithmic space (b). The pressure axis is in the range  $[0, 1$  MPa] in the normal space which corresponds to the range  $[0, 6]$  in the logarithmic space.

The zoom in (a) shows the phase transition jump of density at the saturation pressure ( $P_{sat} \approx 140 Pa$ ). Note that  $\log_{10}140 \approx 2.2$  in (b). This figure shows that uniform table with a  $\log_{10}P$  axis can be helpful for better discretize the pressure axis. As it demonstrates, there are lots of points before and after the saturation point at  $P_{sat} = 140 Pa$ . Hence, it designates more points for low pressures, and less points for high pressures using logarithmic distribution with the base value more than Neper( $e=2.7182$ ) value.

point. However, logarithmic distribution can completely cover the region before and after the saturation point with much fewer points than the uniform one. Therefore, this difference between the number of points in the logarithmic and uniform distributions will be significant if applied to conditions considering mass fraction and temperature variations.

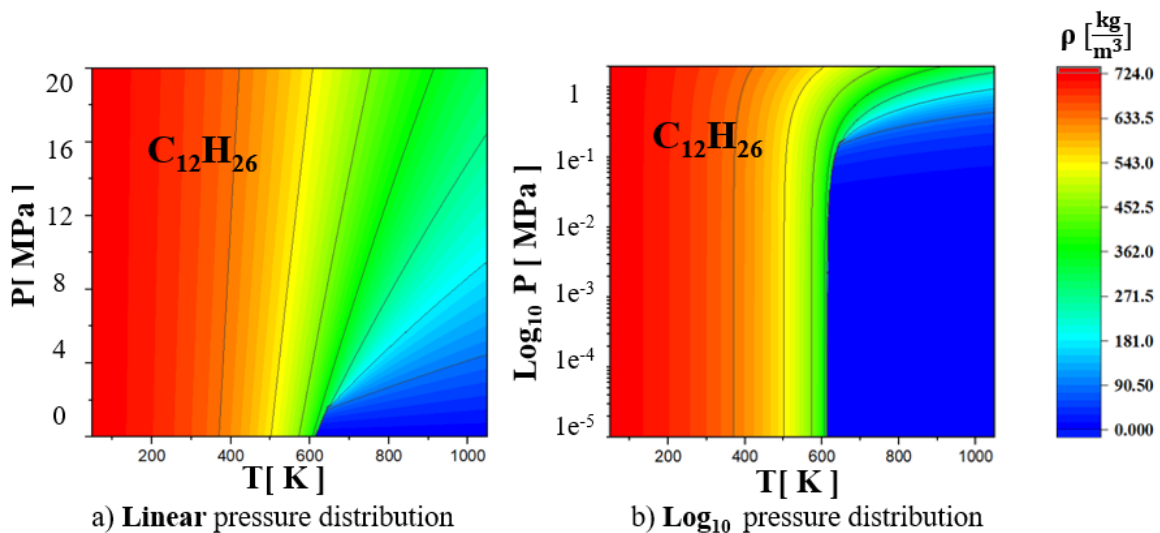


Figure 4.9: Schematic of linear (a) and logarithmic distribution (b) of density contour in pressure axis in  $PT$ , and  $\log_{10}P - T$  spaces

### 4.3.2 Non-Uniform Tabulation: Quadtree and Octree

Another approach that many researchers applied for the tabulation and refinement of data is tabulation with the nonuniform distribution. Generally, a tabulated polynomial data is done using nonuniform structures to have more refinement near desired regions, called Quadtree for two-dimensional (2D) or Octree for three-dimensional (3D) spaces [89–92]. A Quadtree and an Octree are constructed by recursively subdividing the initial base-grid into four and eight cells, respectively until the remaining number of objects in each cell is below a pre-defined threshold or a maximum tree depth is reached. It is worth to note that Quadtree and Octree are also used for automatic mesh refinement (AMR). Figure 4.10 demonstrates typical schematics for the one-dimensional (1D) refinement, the Quadtree 2D refinement (usually used for the tabulation a single component in P-T space), and the Octree 3D refinement (usually used for the tabulation of binary mixtures in P-T-Y space). Hence, each internal node has four children for Quadtree at each refinement level, as shown in 4.10(b), and it has eight children for the Octree case, as shown in 4.10(c). With this algorithm, table refinement is often intended to be applied to nodes near the phase boundary. Hence, it can be a remedy for the problem of memory size due to the uniform tabulation approach.

The main idea of this non-uniform tabulation approach is typically to refine with a portion of 0.5, called refinement ratio ( $h/2$ ) as depicted in 4.10(a), in each level. However, in the presented study, the algorithm has been developed for any arbitrary refinement ratio in k-dimensional (k-d) trees, as reviewed in the following section.

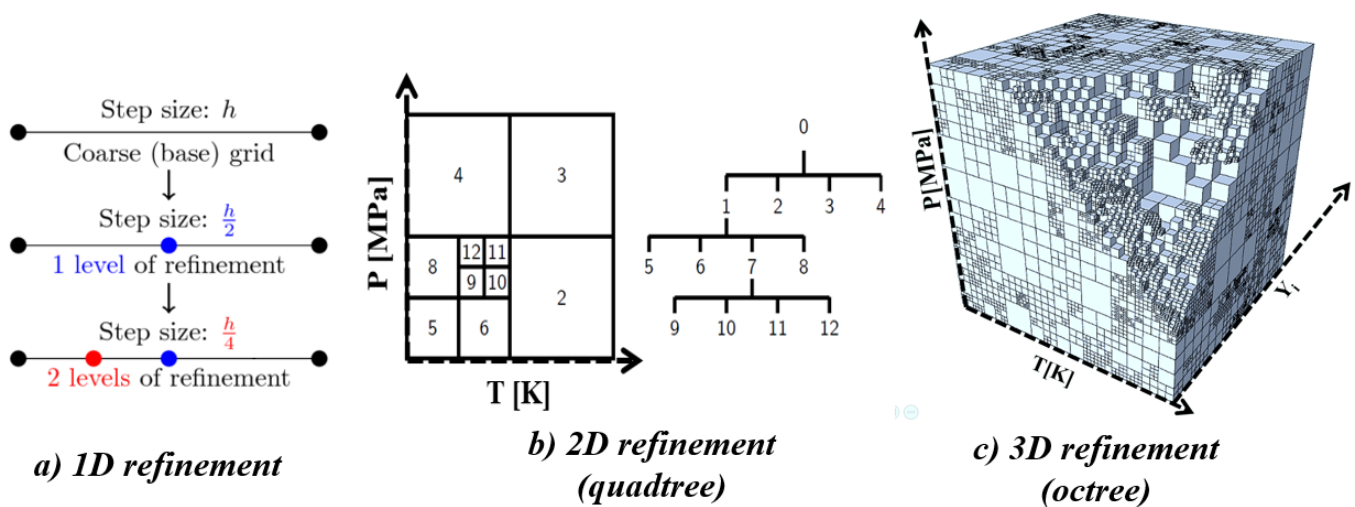


Figure 4.10: Typical schematics for (a) the one-dimensional (1D) refinement, (b) the Quadtree 2D refinement (usually used for the tabulation a single component in P-T space), and (c) the Octree 3D refinement (usually used for the tabulation of binary mixtures in P-T-Y space).

### 4.3.2.1 Introduction to k-dimensional trees

k-dimensional tree (or k-d tree) is a space-partitioning approach for organizing nodes or points in a k-dimensional space (with k, an integer). This approach is used in different sciences such as computer science for image processing, computational sciences for mesh generation, mesh refinement [96–98] and the gaming industry [99]. The k-d tree is a binary tree in which every node is a k-dimensional point. Generally, the generated mesh in terms of the structure can be categorized into organized (or structured) network, like uniform tabulation, and unorganized (or unstructured) networks, like the nonuniform tabulation approach. If all the internal nodes contain exactly four or eight points, the structure is called full Quadtree, or full Octree. The main problem of full Octree-Quadtree is the table size as for uniform tabulation. Hence, it is required applying the refinement to a certain and limited number of cells inside regions of interest, like the phase boundary. However, the generation (known as "Insertion" in data structure science), the searching, and the interpolation steps will be more complex than for uniform tabulation, and some particular approaches are needed to speed up Octree-Quadtree tabulations.

In the following, some basic concepts and terminologies of data structure will be briefly reviewed in order to facilitate the understanding of Octree tables generation algorithms discussed below.

- A tree consists of a set of nodes, and there is exactly one path between any pair of nodes, as shown in figure 4.10(b).
- Point node is used to represent a node in the rooted tree, also called the root point, like point 0 in figure 4.10(b).
- Every node has one parent node. Except, the root has no parent.
- A leaf is a node with no children like the points 2, 3, 4, 5, 8, 9,10,11,12 in figure 4.10(b).
- Siblings are the nodes with the same parent like the points 2, 3, 4 in figure 4.10(b).
- The depth or level of a node is the number of parents that each node has from the root node. For example, nodes 2,3,4 are in level 1, or nodes 9,10,11,12 are in level 3 in figure 4.10(b).

The following main tasks need to be carried out to generate a table using the Octree refinement algorithm for binary mixtures.

#### 1. Initialization phase:

- 1.1- Define the range of (T, P , Y)

1.2- Generation of root nodes in level zero using uniform refinement in the desired range of temperatures, pressures, and mass fractions.

**2. Determine the appropriate child node to store the point, start with root node as the first iteration for current node**

Insertion step: If the given node has not satisfied the criterion, insert and write the node with the desire properties inside table.

Insertion criterion: In this study, different criteria have been tested so that one of the proper criteria for detecting the phase boundary, as a region that needs more refinement, can be  $1e^{-7} < \theta < 0.1$  and  $0.9 < \theta < 1 - 1e^{-7}$ , where  $\theta$  is the vapor fraction.

**3. If the given node has satisfy the criterion, replace it with a region node, as,**

3.1- Form a cube, and dedicate a center and boundaries for this node. The following C++ code define an object oriented class for the inserted cube)

```
Cube::Cube(double z_min, double z_max, double y_min, double y_max
, double x_min, double x_max)
{
    this->x_low = x_min;
    this->x_high = x_max;
    this->y_low = y_min;
    this->y_high = y_max;
    this->z_low = z_min;
    this->z_high = z_max;
    delta_x = abs(x_high - x_low);
    delta_y = abs(y_high - y_low);
    delta_z = abs(z_high - z_low);
    x = x_low + delta_x / 2;
    y = y_low + delta_y / 2;
    z = z_low + delta_z / 2;
}
```

3.2- Divide the current 3D volume into eight boxes, children, and return children's information, like coordination, level, indexed, etc. It is worth mentioning that the refinement ratio value is 50 % for each axis in this study. However, it can be applied to any refinement ratio.

```

double delta_x = abs(x_high - x_low) / level_one_partitions_x;
double delta_y = abs(y_high - y_low) / level_one_partitions_y;
double delta_z = abs(z_high - z_low) / level_one_partitions_z;

unsigned int x_offset, y_offset, z_offset;
for (z_offset = 0; z_offset < level_one_partitions_z; ++z_offset)
{
    for (y_offset = 0; y_offset < level_one_partitions_y; ++y_offset)
    {
        for (x_offset = 0; x_offset < level_one_partitions_x; ++x_offset)
        {
            double x_min = this->x_low + (x_offset * delta_x);
            double x_max = x_min + delta_x;

            double y_min = this->y_low + (y_offset * delta_y);
            double y_max = y_min + delta_y;

            double z_min = this->z_low + (z_offset * delta_z);
            double z_max = z_min + delta_z;

            Node* new_child = create_node(1, z_min, z_max, y_min, y_max, x_min, x_max);

            root->add_child(new_child);
        }
    }
}

```

Figure 4.11: Snapshot of the implemented Octree code

#### 4. Go back to step 2.

Repeat this process until all the nodes do not satisfy the criterion or arrive at the desired maximum level.

To do this, "Recursive function," which references itself, has been used in object-oriented architecture with defining different classes and objects, as shown in Figure 4.11.

**4.3.2.1.1 Space-filling curve (graph traversal algorithms)** Since properties must be searched and interpolated during the CFD simulation, the order of writing data to the table will be important and will influence the CPU time consumed by these tasks. In mathematics and computer science, a space-filling curve is an approach that enables to fill a multi-dimensional space with a continuous curve. Hence, the thermodynamic domain becomes recursively divided by a tree, and the leaves are connected using a space-filling curve. Figure 4.12 demonstrates two different algorithms for space-filling curves as BFS, which stands for Breadth-First Search (a), and DFS, which stands for Deep First Search (b). BFS and DFS are the traversing approaches adopted to searching a graph to visit all the graph's nodes. The difference between BFS and DFS is that BFS proceeds level by level while DFS follows a path from the starting node to the ending node in the last level and then another route from the start to the end. This process will be repeated until all nodes are visited.

As shown in figure 4.12(a), in the BFS approach, all the nodes will be touched level by level. If the nodes are diagnosed as leaves nodes in the same level, the blue cells do not have any children; they will be stored sequentially inside the table, nodes 1-7 in level 1. However, if the nodes are diagnosed as parents nodes, the orange cells in the same level, the nodes with children, will be ignored to store inside the table, and they will be saved in another array for more investigation

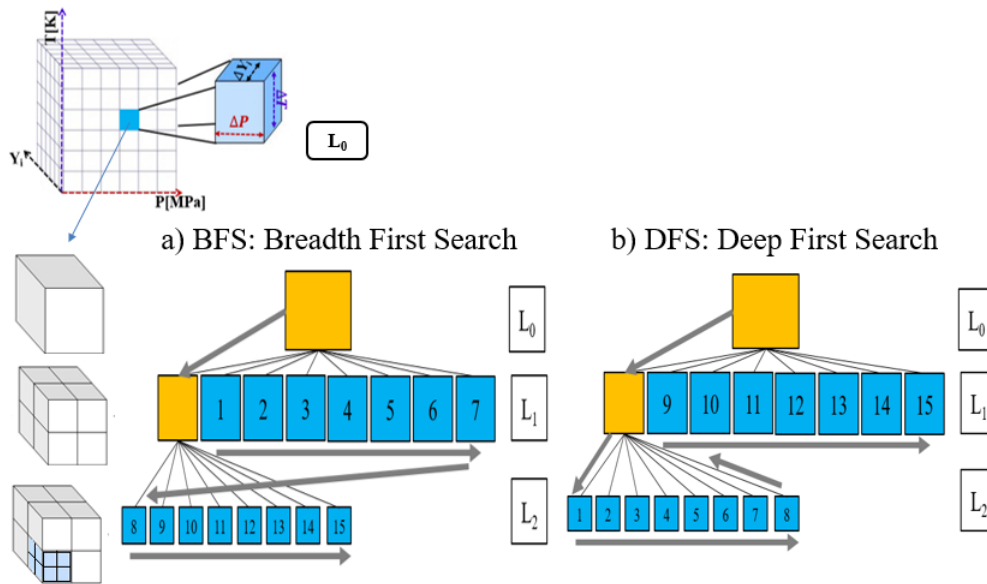


Figure 4.12: Two different algorithms for space-filling curve as BFS, which stands for Breadth-First Search (a), and DFS stands for Deep First Search (b). As shown, BFS and DFS generate different neighbors, affecting the searching algorithm mechanism and interpolation approach.

in the next level, node 8-15 in level 2.

However, as shown in figure 4.12 (b), in the DFS approach, all the leaves nodes, blue cells will be touched and saved inside the table, regardless of their levels. The algorithm starts at the root node, the leaf nodes of each parent save sequentially, nodes 1-8 in level 2, and then nodes 9-15 in level 1. Hence, as figure 4.12 (a-b) demonstrates, BFS and DFS generate different neighbors, affecting the searching algorithm details and efficiency. It is worth mentioning that the studies in this thesis has demonstrated that for a big table size, the BFS approach has more expensive searching CPU time rather than the DFS approach.

#### 4.3.2.2 Searching in nonuniform tables

Searching in the data structure can be done by implementing searching algorithms. As mentioned before, searching algorithms are created and designed to retrieve any element from any data structure formats. The complexity and the performance of different searching algorithms entirely depend on the **array size** and the **array data distribution type** as uniform, exponential, or normal distributions [100]. These algorithms are examined using the time taken to search and find a particular data member by comparing their complexity based on:

- The best possible time
- The average time

- The worst-case time

Based on the type of searching method, the searching algorithms are classified into two categories as:

- **Sequential Search**, like linear search, as shown in figure 4.13(a): This is traversed sequentially, and every element is checked in this algorithm approach.
- **Interval Search**, as shown in figure 4.13(b,c): These searching algorithms are designed for sorted data structures, like binary search, interpolation search, etc.

**4.3.2.2.1 Linear Search :  $o(1) < < o(n)$**  The linear search is the most straightforward algorithm that employs a loop to sequentially step through an array, starting with the first element. The mechanism of this algorithm is based on the comparison of each element with the value being searched until the value is found or it reaches the array end, as shown in figure 4.13(a). The space complexity for this searching algorithm is  $O(n)$ , which means with the complexity of  $n$  for  $n$  component. For this algorithm, the best case time complexity occurs as  $O(1)$  when the search element is present at the first element; the worst complexity of  $O(n)$  occurs for the last search element in the array. Hence, it could be concluded that the average complexity for this searching algorithm is  $O(n)$  for component  $n$  in the array.

**4.3.2.2.2 Binary Search  $o(1) < < o(\log(n))$**  In this algorithm, the mechanism is so that the value of the desired element compares with the present element at the center of the array. If it matches, then the search is successful; otherwise, the list is divided into two parts: one from the 0th element to the central element, which is the center element (first half), and another from the center element to the last element (which is the second half) where all values are more significant than the center element. Figure 4.13(b) exhibits the schematic of searching using the so-called binary algorithm. The main feature of this binary search is to search through large sorted arrays with the run time complexity of  $o(\log n)$ , which is faster than a linear search algorithm. For this algorithm, the best case time complexity occurs as  $o(1)$  when the search element is present at the array's center; the worst complexity occurs at  $o(n \log n)$ .

**4.3.2.2.3 Interpolation Search:  $o(n) < < o(\log \log n)$**  An Interpolation Search is an improvement over binary Search for scenarios where the values in a sorted array are uniformly distributed. The binary search goes to the middle element to check. On the other hand, interpolation search may go to different locations according to the value of the key being searched,

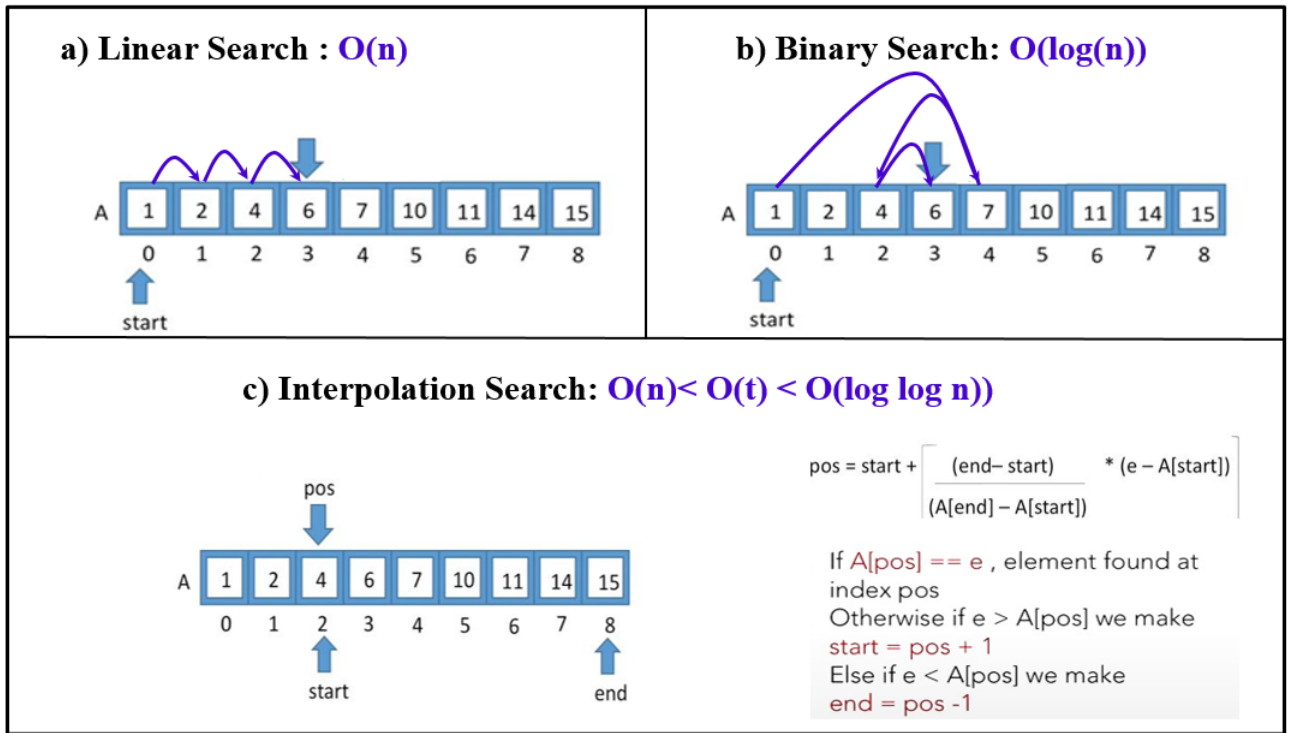


Figure 4.13: Different types of searching algorithms, and CPU time complexity

as explained in figure 4.13(c). The worst complexity for this algorithm occurs at  $o(n)$ , and the average run time is  $o(\log \log n)$ . In many applications, binary and interpolation algorithms are commonly used to search ordered datasets and these two algorithms have been used in the current thesis for the RFM model using octree tables. However, due to the exponential increase in the rate of data size in industries, researchers developed many searching algorithms such as jump search, exponential search, Fibonacci search, etc... to reduce the complexity of the searching algorithm for different distributions and table sizes. Besides, different researchers developed various models like the hybrid approaches, which combine the approaches as mentioned earlier. [100] recently proposed a hybrid algorithm based on the idea of the interpolation and binary search algorithms for searching ordered datasets with unknown distributions in which the datasets change dynamically. They concluded that the performance of hybrid, binary, and interpolation searches depends specifically on data distributions, the data size, and the data performance, which will affect the searching complexities as shown in figure 4.14(a-c). Figure 4.14 exhibits Binary, Interpolation, and two other hybrid searches models run time variations for different array sizes as uniform distribution (a), normal distribution (b), exponential distribution (c) studied by [100]. Adaptive search and IBS are the approaches (interpolated binary searches; hybrid model) that have been developed by [100]. As the figures demonstrate, the time costs will differ for various distributions using different algorithms, and there is no optimum algorithm for searching with

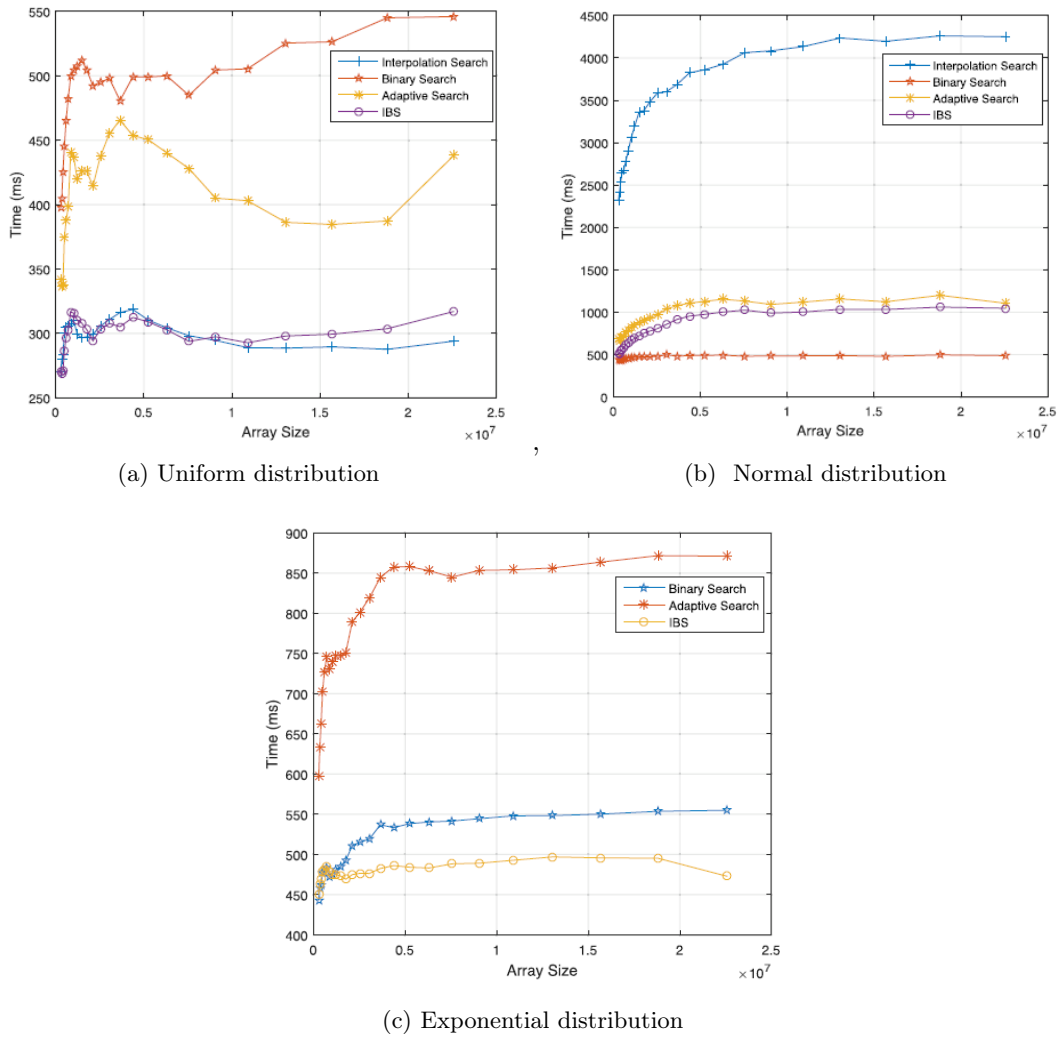


Figure 4.14: Binary, Interpolation, and two other hybrid searches models run time variations for different array sizes for an indeterminate uniform data distribution (a), a normal data distribution (b), an exponential data distribution (c) studied by [100]. Adaptive search and IBS approaches (interpolated binary searches; hybrid model) have been developed by [100]. As the figures demonstrate, the costs will differ for various distributions for different algorithms, and there is no best approach for unknown distributions.

unknown distributions.

A point worth mentioning is that the study of the RFM model demonstrates that the CPU time of searching for binary mixtures in 3D arrays of (T, P, Y) will be exponentially increased compared to the 1D arrays searching, as studied by [100], which needs to be taken into account. Hence, increasing the sizes of arrays in any temperature, pressure, or mass fraction arrays will significantly affect the CPU time of searching and simulations, which needs to be considered.

**4.3.2.3 Neighbors in BFS and DFS frameworks**

The last step before interpolation is dedicated to finding neighbors using different approaches, as the closest points for approximating the value of a given property at a given set of discrete neighbor points. As described in the graph traversal algorithms section, different methods can be performed for traversing and writing the data inside the table, as shown in figure 4.12. Figure 4.15(a-c) demonstrates the schematics of BFS or level by level (a), DFS, or sorted (b) arrays, in addition with the schematic of T-Y diagram for unstructured framework (c). As mentioned before, BFS and DFS, as different algorithms for graph traversal, generate different neighbors in their arrays, figure 4.15(a-b). Generally, the data in BFS are primarily sorted based on their levels and then sorted from the minimum to maximum at each level for each array. Hence, for binary mixture, the searching will be done primarily based on mass-fraction (Y), then the pressure (P), and finally temperature (T), as explained at the end of section 3.1.1 for the RFM model. However, for the DFS approach, since the arrays are sorted from the minimum to the maximum values of each axis, the arrays searching are independent of their levels. Hence, three additional steps are required for finding the closest neighbors for the BFS approach compared to the DFS.

- Adding new array as level array in the table for each point
- Calculating the eight closest neighbors of an unknown point in all the levels for each array (T, P, Y), as shown in the C++ code, equations 4.3. It is worth mentioning that the eights

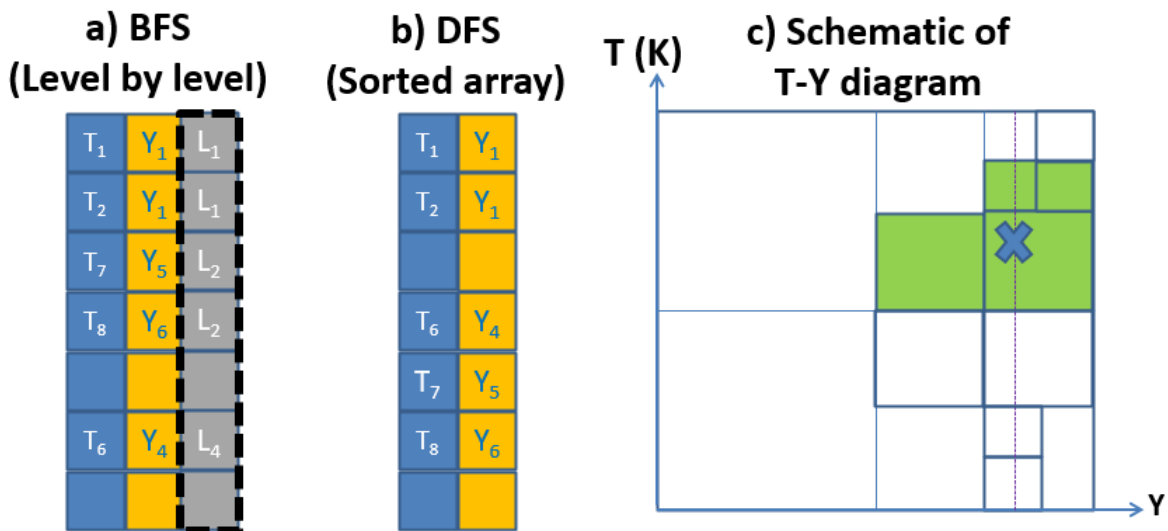


Figure 4.15: Schematics of BFS or level by level (a) and DFS, or sorted (b) arrays in addition with the schematic of P-Y diagram for unstructured framework(c).

neighbor points can be in different levels. Hence, the  $\Delta T$ ,  $\Delta P$ , and  $\Delta Y$  which are the cell size in each level need to be calculated for every eight neighbors based on the difference with the unknown point.

- The minimum  $Distance(point)(level)$  in all levels for each 8 points will be selected as the criterion for finding the closest neighbors, based on the algorithm in equation 4.3.

$$\left\{ \begin{array}{l}
 \text{for level} = 1: \text{ maximum level: level}++ \\
 \text{for point} = 1: 8: \text{ point}++ \\
 \Delta T[level] = \Delta T[level = 0, uniform]/2^{(level)} \\
 \Delta P[level] = \Delta P[level = 0, uniform]/2^{(level)} \\
 \Delta Y[level] = \Delta Y[level = 0, uniform]/2^{(level)} \\
 \text{Distance [point][level]} = \sqrt{\frac{(T^* - T[point][level])^2}{\Delta T^2[level]} + \frac{(P^* - P[point][level])^2}{\Delta P^2[level]} + \frac{(Y^* - Y[point][level])^2}{\Delta Y^2[level]}} \\
 \text{end} \\
 \text{end}
 \end{array} \right. \quad (4.3)$$

#### 4.3.2.4 1D test cases for tabulation

Before the comprehensive investigation that will be carried out in the next chapter to validate the proposed RFM model in different thermodynamic flow regimes with various physics and conditions, some academic test cases such as the double expansion and the shock tube test cases are studied in this section to examine the presented tabulation methods discussed previously. Primarily, the results have demonstrated a good agreement with the available data presented in the literature [5, 17, 22, 27] using different solvers and thermodynamic approaches. The principal and notable difference between the tabulation methods studied are the tables size and the computational costs (i.e. CPU time). It has been demonstrated that a nonuniform table's approach, even with low-level refinement, are very time-consuming compared to the uniform tabulation approach. More analysis details can be found in the following sections.

**4.3.2.4.1 Double expansion test case** The two-phase expansion tube, or double-expansion tube is a two-phase test case also known as the cavitation test [48, 54]. This test is performed in a 1m long tube filled with n-dodecane combined with some volume fraction of gaseous nitrogen at atmospheric pressure. The initial discontinuity is set at 0.5 m so that the left and right-hand side velocities are selected as -1.0 m/s and 1.0 m/s, respectively. The computational mesh counts

1000 cells uniformly running over the 1m long tube. In such a situation, some variables such as pressure, temperature, and sound speed, decrease across the rarefaction waves so that the velocities reach zero at the center of the domain. As it shows, by increasing the amount of nitrogen dissolved gas inside the fuel, the fluid behavior, such as a drop in sound speed value, changes from liquid to gas. This phenomenon is well predicted by the different models, which is shown in Figure 4.16. It is worth to recall that the IFP-C3D solver [5, 17, 22, 27] is not using a tabulation method but directly solves a thermodynamic (UV)-flash for the calculation of the different physical properties for the required  $C_{12}H_{26} - N_2$  mixture. Hence, this study illustrates that the RFM model can probably solve pressure rarefaction inside a typical Diesel injector. Besides, different tabulation approaches have been tested. First of all, it would be interesting to mention that the CPU time for studying a 1ms double expansion test case is around 3-7 minutes using uniform tabulation for the different conditions.

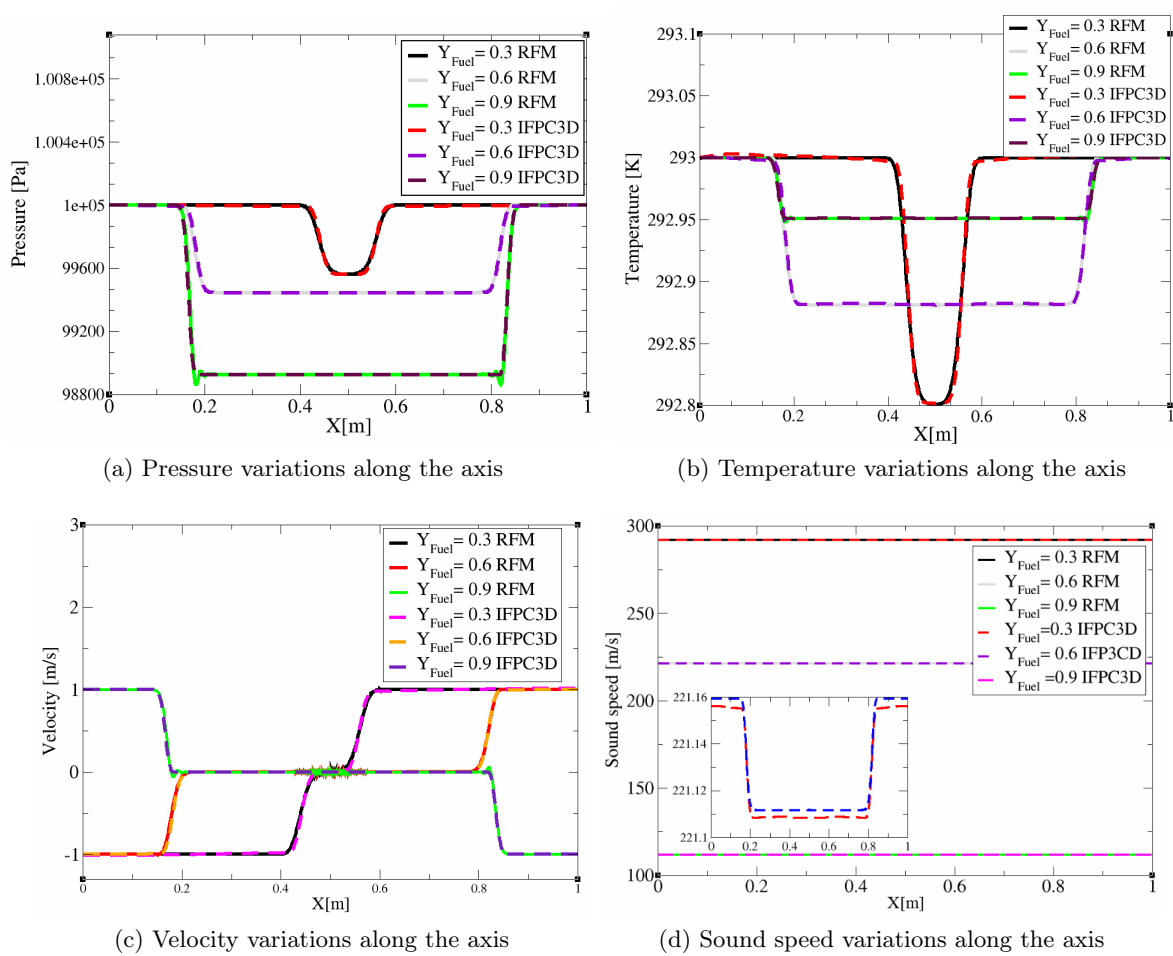


Figure 4.16: Double expansion test case results at  $t = 3.5ms$ . Numerical comparisons between the RFM model using a uniform tabulation method, and the results of the IFP-C3D solver [5, 17, 22, 27], which employs an online (UV)-flash calculations for the physical properties of  $C_{12}H_{26} - N_2$  mixture for various specified initial mass fractions.

However, for simulating the same test cases with identical setups, using non-uniform algorithms, the order of searching CPU time has been found varying from 1 hour to 10 hours, depending on the maximum level of refinement and the size of tables. It is worth to note that such long simulations are similar to one consumed by the IFP-C3D solver while using the online (UV)-flash calculations [5, 17, 22, 27]. Hence, the studies prove the computational efficiency of uniform tabulation, even with high number of points, compared to the nonuniform tabulation approaches.

**4.3.2.4.2 Shock tube test case** Here different shock tube test cases have been analyzed to confirm the conclusions of the previous test case. This is a well-known test case for which the tube is initially filled with homogeneous mixtures of n-dodecane–nitrogen with different mass fractions. The initial discontinuity is located at 0.5 m. The left side with 0.2 MPa is at a higher pressure than the right side which is at 0.1 MPa. The temperatures on the left and right-hand sides are set as 354K and 337K, respectively, the same as those in [5, 17, 53]. The computational mesh consists of 1000 cells uniformly running over a 1m long tube.

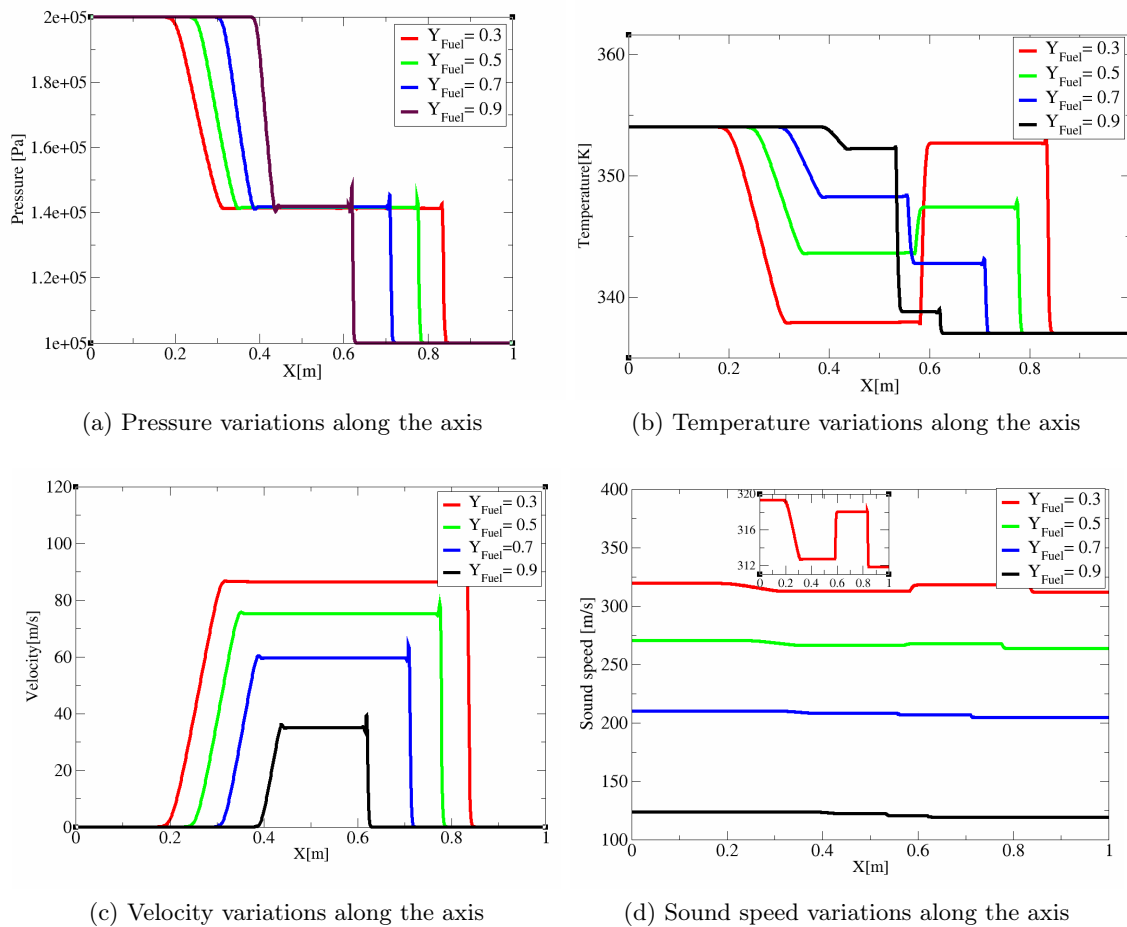


Figure 4.17: Different physical properties of  $C_{12}H_{26} - N_2$  mixture in shock tube test case for various mass fraction along 1m long tube

Figure 4.17 (a-d) shows the variations of pressure (a), temperature (b), velocity (c), and sound speed (d) in different mass fractions at 1ms of computation for n-dodecane–nitrogen, respectively. Just after the diaphragm is removed, a compression shock runs into the low-pressure region, while a rarefaction (expansion) wave moves back into the high-pressure part of the tube. The CPU time for simulating 1 ms in this shock tube test case is comparable between the tabulation methods. Using uniform tabulation is around 5-10 minutes depending on the initial mass fraction condition. However, for simulating the same test cases with identical setups, the order of nonuniform refinements approach CPU time are varied from 1 hour to 10 hours, which are directly affected by the size of data, the level of refinements. Hence, this test case confirms the computational efficiency of uniform tabulation compared to the nonuniform tabulation approaches. More simulations and validations can be found in the next sections, and Appendix A-b.

### 4.3.3 IFPEN Shared Memory for refined Uniform Table storage and access

The main objective of this study is to investigate, recommend, and develop a model to reduce the CPU time and memory storage requirement for multicomponent real fluid simulation in industrial applications. One solution to reduce the memory issue is to apply the shared memory technique patented by IFPEN [101]. Shared memory is about having a piece of memory that numerous cores (or processors) can access in reading, writing, or both. Hence, using this approach, the thermodynamic table is not stored on each processor and its size can be therefore extended to almost the size of one node of the supercomputer, which is currently about 100 Gb for the ENER440 supercomputer of IFPEN.

## 4.4 Preliminary highly resolved RFM simulations

To check the tabulated RFM model applied for a uniform big size table using the IFPEN shared memory technique, preliminary highly resolved 2D simulations of pure n-dodecane injection into hot nitrogen environment are carried out using a high mesh resolution. A typical Diesel fuel injector with a nozzle diameter of  $90\mu m$ , with different injection temperatures ( $T_{inj} = 600K, 658K$ ) and chamber pressures ( $P_{ch} = 6MPa, 11MPa$ ), similar to the ECN spray-A conditions, is considered [17, 86, 102]. These 2D simulations cases, as shown in table 4.1, are similar to the one already performed by the Prof. Battistoni group [38, 103] and Prof. Gavaises group [104]. Figure 4.18 presents the 2D computational domain as well as the boundary conditions used in this study. At the jet inlet, liquid n-dodecane is injected with a uniform velocity profile with a constant temperature. A pressure outflow boundary condition was used for the right, top, and bottom side boundaries. No-slip and isothermal conditions were specified for the left side wall boundary at  $T = 972K$ , including the injector wall. The mesh generated for this simulation has a total cell count about 11 million cells, with  $\Delta x = \Delta y = 1.25\mu m$ . Also, the RFM model thermodynamic closure for the (n-dodecane/ nitrogen) binary mixture is based on the PR-EoS, with thermodynamic table refinement in  $[T, P, Y_{C_{12}H_{26}}]$  axes of (101, 601, 401) points, respectively. In this case, the total size of the table is around 1.6 GB, which can be stored on only one node of the IFPEN ENER440 supercomputer using Intel Skylake G-6140 processors (CPU) with a total memory of 1.9 GB. In this case, we need therefore to use the shared memory feature because the CFD CONVERGE solver requires more than one GB for the current refined mesh. A density-based solver, where the pressure-velocity coupling is achieved using a modified PISO method, explained in chapter 3, was used for this simulation. The time step is automatically controlled based on a maximum CFL number of 0.8, reaching a value in the range ( $1ns - 3ns$ ). The computational cost of this simulation is around 48 hours for a simulation time  $60\mu s$  using 360 CPU.

Table 4.1: Operating conditions for the transcritical n-dodecane-  $N_2$  injection similar to the the study performed by Prof. Battistoni group [38] and Prof. Gavaises group [104].

	$T_{inj}(K)$	$T_{ch}(K)$	$P_{ch}(MPa)$	$U_{inj}(m/s)$
<b>Case 1</b>	600	972	6	200
<b>Case 2</b>	600	972	11	200
<b>Case 3</b>	658	972	6	200
<b>Case 4</b>	658	972	11	200

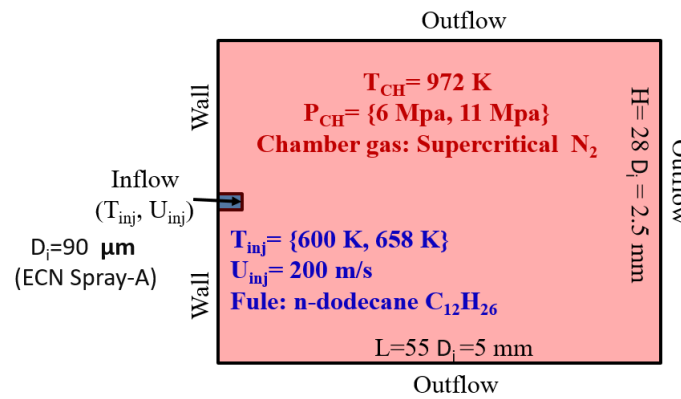


Figure 4.18: Geometry setup, boundary conditions and working parameters used in the case of n-dodecane liquid injection into supercritical nitrogen.

### Ambient chamber pressure effects

Figure 4.19(a-h) demonstrates the instantaneous contour plots at  $t = 60\mu s$  for temperature, n-dodecane mass fraction, density, and phase indicator contours for two different chamber pressures ( $P_{ch} = 6MPa, 11MPa$ ), respectively. As shown in these figures, these results have been obtained from simulations of n-dodecane injected at  $T_{inj} = 600K$  and inflow velocity of 200 m/s into nitrogen at  $T_{ch} = 972K$ , cases 1-2 in table 4.1, for two different chamber pressures: first column  $P_{ch} = 6MPa$ , and left column  $P_{ch} = 11MPa$ . Phase indicator PHI = 0 designates a liquid state with blue color, PHI = 1 designates a gas state with red color, and PHI = 2 refers to a two-phase state with black color. As density contours demonstrate, in figure 4.19(e, f), the effect of increasing chamber pressures from 6MPa to 11MPa can be seen in the chamber gas density, which has filled with supercritical nitrogen at  $T_{ch} = 972K$ . Also, due to the change of pressure at the chamber, the change of liquid n-dodecane density is explored in the results. The density ratios between the liquid and gas,  $\rho_L/\rho_g$ , at these different pressures, lead to the change of jet cone angle and atomization. Besides, figure 4.19(g, h) exhibits different phase states behavior for the jet, especially for two-phase states. Results show that the formation of liquid-like jet structures (ligaments),  $P > P_{cr,C12H26} = 1.8MPa$ , are varying for different pressures. At low chamber pressure (6MPa), small scales are visible as in a pure atomization regime. However, it cannot be seen at high pressure (11MPa).

### Injection temperature effects

To investigate the effects of changing the liquid inlet temperature, different injection simulations have been performed, as previously for both chamber pressures (6MPa and 11MPa), in the chamber filled with supercritical nitrogen at temperature ( $T_{ch} = 972K$ ). Compared to the previous simulation the inlet n-dodecane temperature is increased to  $T_{inj} = 658K$ . Figure 4.20(a-h)

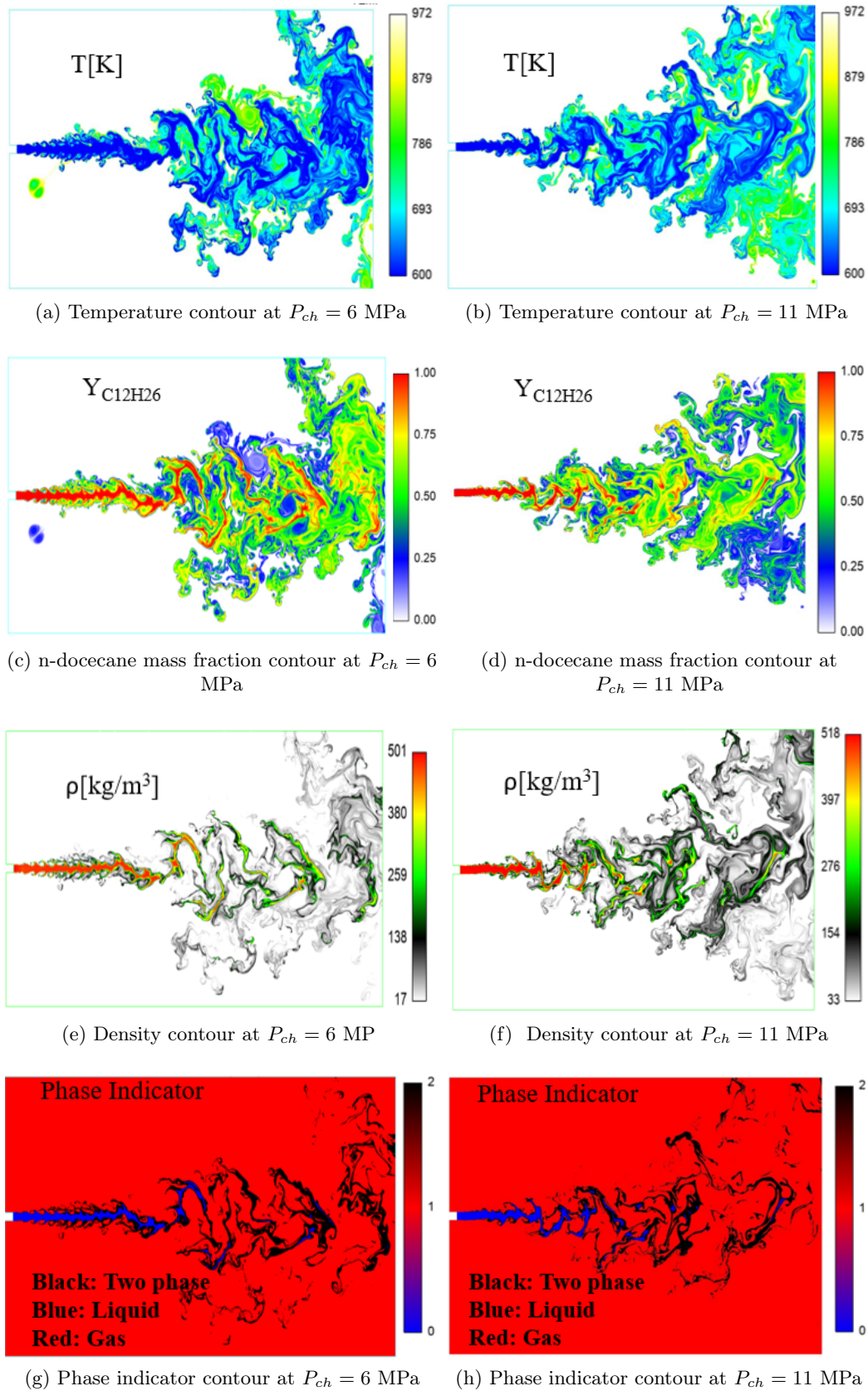


Figure 4.19: Instantaneous contour plots at  $t = 60\mu s$  obtained from simulations of n-dodecane injected at  $T_{inj} = 600K$  and inflow velocity of 200 m/s into nitrogen at  $T_{ch} = 972K$ , for two different chamber pressures: first column  $P_{ch} = 6MPa$ , and left column  $P_{ch} = 11MPa$ . Phase indicator, PHI = 0 designates a liquid state with blue color, PHI = 1 designates a gas state with red color, and PHI = 2 refers to two phase state with black color.

shows the instantaneous contour plots at  $t = 60\mu s$ , for the same parameters as previously (i.e. temperature, n-dodecane mass fraction, density, and phase indicator) for the two chamber pressures. As shown in Figure 4.20(e-f), the density values differences can be seen for injected fluid n-dodecane, compared to  $T_{inj} = 600K$  case, shown in figure 4.19(e-f). This leads to the change of the mixing processes inside the chamber. Figure 4.19(g, h) exhibits different phase states behaviors for the jet structure, compared to  $T_{inj} = 600K$  case, shown in figure 4.19(e-f). As it demonstrates, the two-phase states is not observed. Indeed, at this higher injection temperature than the mixture critical temperature which is lower than the critical temperature of pure n-dodecane,  $T_c \approx 658K$ , n-dodecane is injected in the liquid-like state.

To have a better insight, Figures 4.21 and 4.22 exhibit, the temperature-nitrogen mole fraction diagrams colored with mixture density, and the phase indicator, respectively, for  $P_{ch} = 6 MPa$  (left) and  $P_{ch} = 11 MPa$  (right). As the density contours show in Figure 4.21, not only the density magnitude has increased at higher pressure (see the values for pure n-dodecane (at  $X_{N_2} = 0$ ), for instance, but also the density distribution at different compositions and temperatures has also varied significantly. Besides, Figure 4.22 indicates the effect of the pressure on the distribution of the phases (liquid, gas and two-phase) in the temperature-compositions diagram. The yellow cross shows the locus of mixture critical points at the two different pressures. Also, AMT, which denotes adiabatic mixing temperature, demonstrates the locus of mixture temperature at adiabatic conditions for two different conditions with inflow temperatures of  $T_{inj} = 600K$  colored with gray, and  $T_{inj} = 658K$  colored with orange in Temperature-nitrogen mole fraction diagram. The first pressure effect can be observed in the liquid region in which n-dodecane has remained in the liquid states for higher temperatures for  $P_{ch} = 11 MPa$ , compared to  $P_{ch} = 6 MPa$ . The second effect is about the shift of phase boundary and mixture critical point to higher  $X_{N_2}$  when the pressure is increased. This leads to an enhanced mixing at high pressure, as shown in Figure 4.19(g,h) with shorter liquid core at 11 MPa.

Finally, it is worth mentioning that the presented results are in good agreement with the numerical studies of [38] using also PR EoS, and [104] using PC-SAFT EoS. Figure 4.23 demonstrates the instantaneous contour plots at  $t = 60\mu s$  obtained from the present tabulated simulation (a) of n-dodecane injected at  $T_{inj} = 658K$  and inflow velocity of 200 m/s into nitrogen at  $T_{ch} = 972K$ ,  $P_{ch} = 6 MPa$ , compared to the study of [38] using direct evaluation of real fluid equations of state (b), for different properties, as mixture isobaric heat capacity, mixture viscosity using Chung correlation in both studies [68], and pressure, from top to down, respectively. Globally, it shows the agreement between these two studies. Also, by comparing the mixture isobaric heat

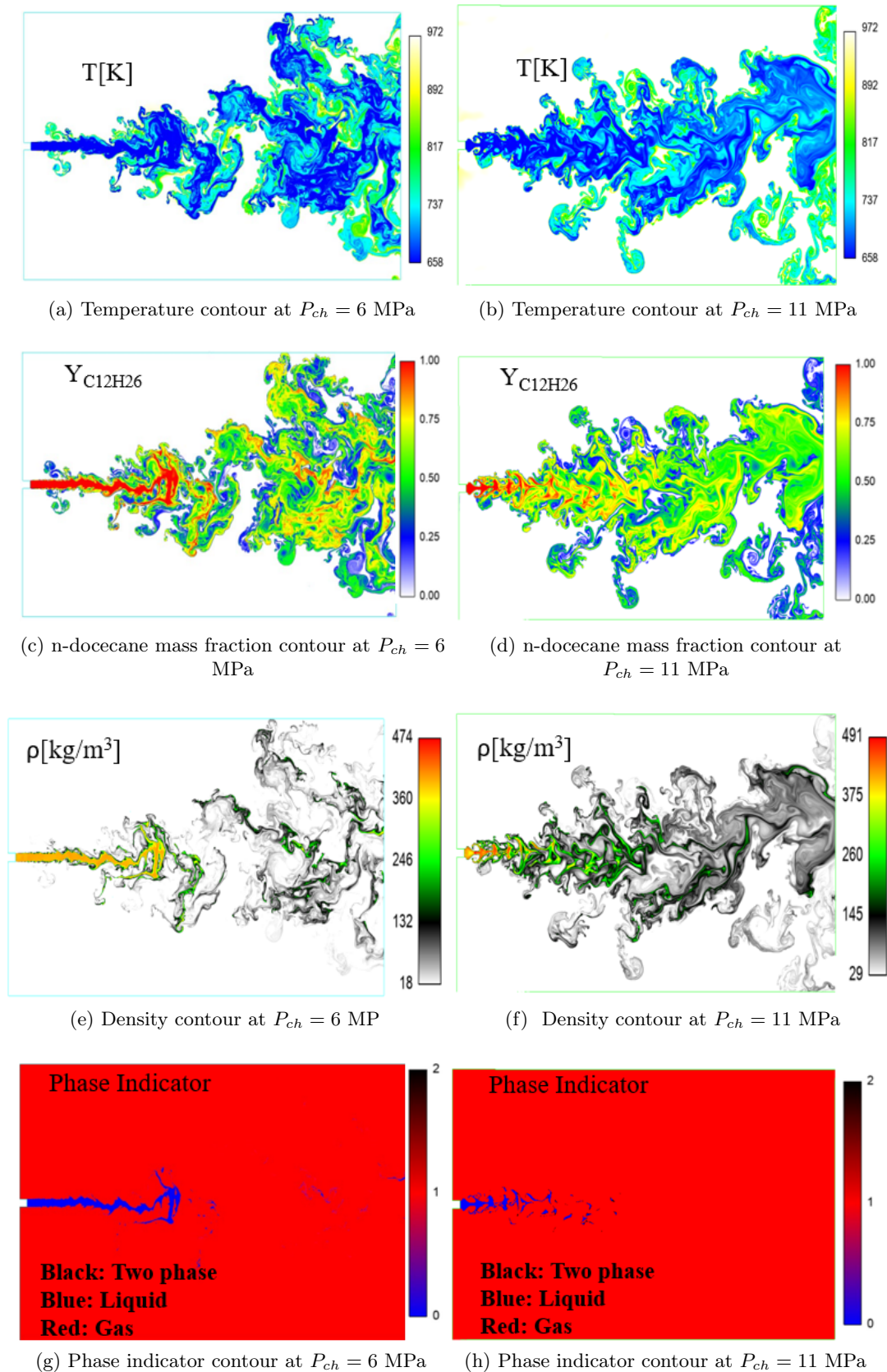


Figure 4.20: Instantaneous contour plots at  $t = 60\mu s$  obtained from simulations of n-dodecane injected at  $T_{inj} = 658K$  and inflow velocity of 200 m/s into nitrogen at  $T_{ch} = 972K$ , for two different chamber pressures: first column  $P_{ch} = 6MPa$ , and left column  $P_{ch} = 11MPa$ . Phase indicator, PHI = 0 designates a liquid state with blue color, PHI = 1 designates a gas state with red color, and PHI = 2 refers to two phase state with black color.

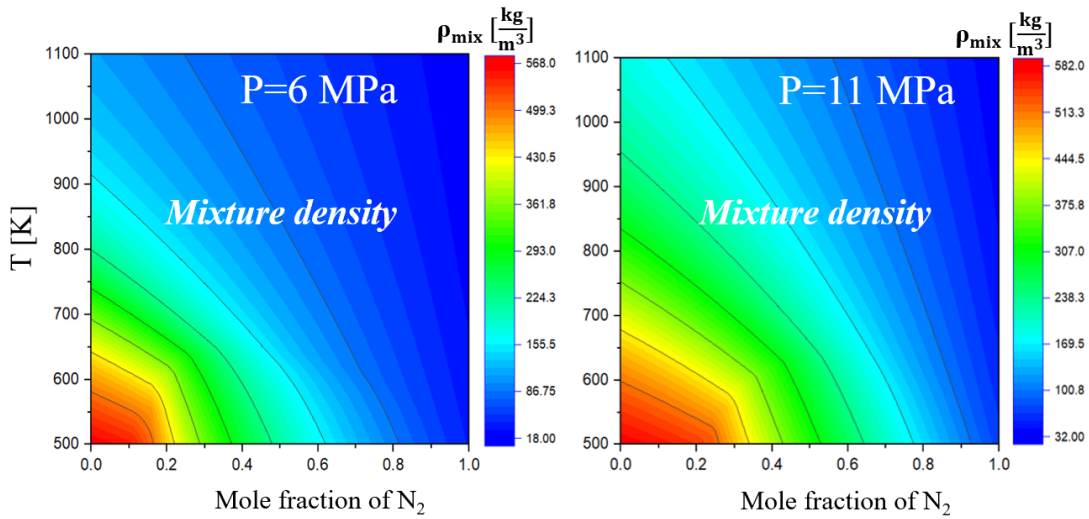


Figure 4.21: Temperature-nitrogen mole fraction diagram colorized with mixture density at two different pressures  $P_{ch} = 6$  MPa, and  $P_{ch} = 11$  MPa

capacity as well as viscosity values between the two models, it proves the accuracy of searching and interpolation in this study, compared to the study of [38] which hires the direct evaluation of real fluid equations of state. Moreover, the comparison of the pressure results between these two models demonstrate less pressure oscillations (minimum pressure in this study is around  $4.4MPa$ , light blue) in this study. As a result, the preliminary study has demonstrated a good agreement and prediction of the tabulated RFM model with the available studies in the literature [5, 22, 38, 103, 104]. In the next chapter, more qualitative and quantitative investigations will be carried out for different applications with various physics using this tabulated RFM model.

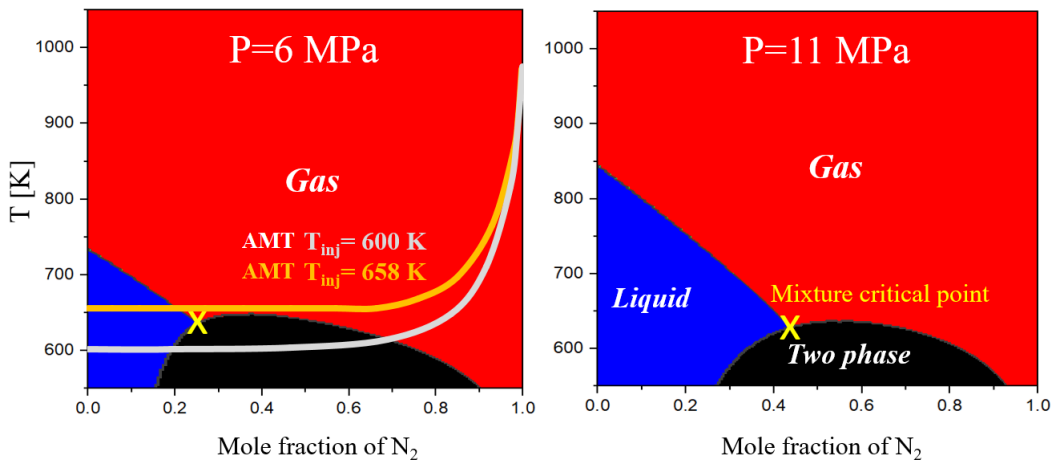


Figure 4.22: Temperature-nitrogen mole fraction diagram colorized with phase indicator, phase state contour, at two different pressure  $P_{ch} = 6$  MPa, and  $P_{ch} = 11$  MPa. The yellow cross shows the locus of mixture critical points at the two different pressures. Also, AMT, which denotes adiabatic mixing temperature, demonstrates the locus of mixture temperature at adiabatic conditions for two different conditions with inflow temperatures of  $T_{inj} = 600K$  colored with gray, and  $T_{inj} = 658K$  colored with orange in Temperature-nitrogen mole fraction diagram at  $P_{ch} = 6$  MPa.

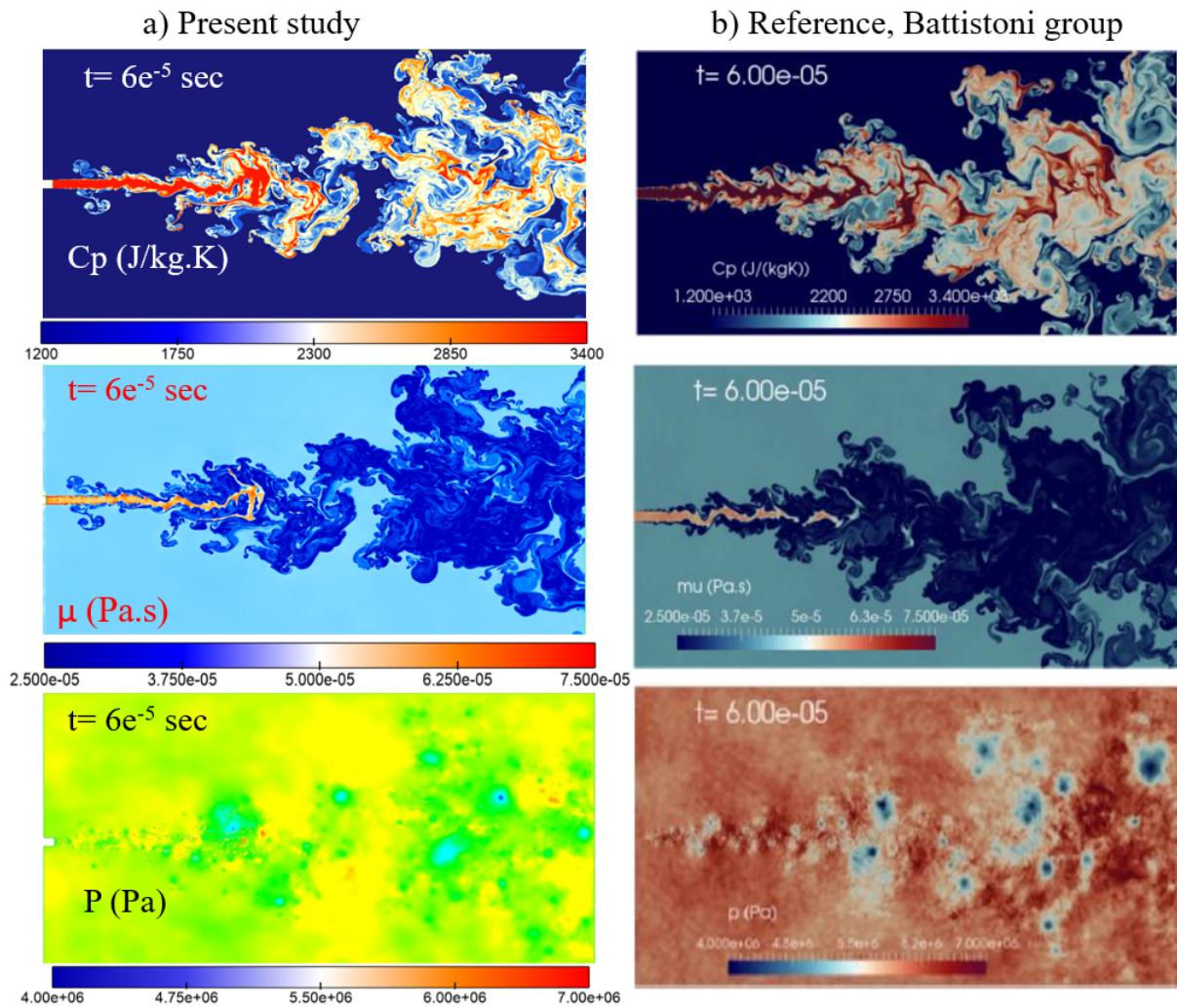


Figure 4.23: Instantaneous contour plots at  $t = 60\mu s$  obtained from the present tabulated simulation (a) of n-dodecane injected at  $T_{inj} = 658K$  and inflow velocity of 200 m/s into nitrogen at  $T_{ch} = 972K$ ,  $P_{ch} = 6$ , compared to the study of [38] using direct evaluation of real fluid equations of state (b), for different properties, as mixture isobaric heat capacity, mixture viscosity using Chung correlation in both studies [68], and pressure, from top to down, respectively.

## 4.5 Conclusion

This chapter has been dedicated to the explanations of the VLE tabulation characteristics and issues. By introducing the different tabulation approaches for better refinements in uniform and nonuniform frameworks, they have been analyzed for VLE of single and multicomponent systems. These tabulation approaches have different table generation, searching, and interpolation steps. The strengths and weaknesses of these different steps have been analyzed and identified. Some 1D, 2D academic simulations have been presented in order to select the best tabulation method with low cost and memory requirements. The numerical results have shown the full coupling of the thermodynamic and CFD solvers using the presented searching and interpolation approaches. It has been demonstrated that the CPU time of real fluid tabulation approaches with nonuniform

approaches, like octree and quadtree, is very expensive compared to the uniform approach, especially for conditions requiring an extensive range of the table. It has also been seen that this high CPU time for the nonuniform tabulation approach may exceed the CPU time of direct evaluation of VLE real fluid in CFD code, without tabulation, for some conditions. Hence, although some researchers [88–92] have proposed nonuniform tabulation approaches for more refinements, it will not be recommended for industrial applications due to the high searching CPU time of these approaches. This increase in CPU search-time becomes more critical when the number of species is added, as can be seen and be compared in figures 2.8 and 2.7, due to the structure of mixtures in the thermodynamic spaces. Besides, a highly refined uniform table using Shared Memory has been proposed for industrial applications (without combustion), which require only a few species, typically no more than three. Indeed, using the RFM modeling approach for combustion, for example, is still among the future challenges.

## Chapter 5

# Application to “ High-pressure modeling of multi-component two phase flow with phase change”

### Contents

---

<b>5.1</b>	<b>Towards understanding the structure of subcritical and transcritical multi-species liquid-gas interfaces</b>	<b>82</b>
5.1.1	Transcritical mixing and evaporation study	85
5.1.2	Transcritical single-component Cryogenic injection	89
5.1.3	Binary coaxial injection of $LN_2$ with hot $GH_2$	93
5.1.4	Conclusion	104
<b>5.2</b>	<b>Exploring the interaction between phase separation and turbulent fluid dynamics in multi-species supercritical flow jets</b>	<b>106</b>
5.2.1	Introduction	106
5.2.2	Equilibrium thermodynamic closure of the flow solver, and the tabulation look-up	109
5.2.3	Analytical study of condensing supercritical jet	111
5.2.4	Results and discussion	113
5.2.5	Quantitative validation	126
5.2.6	Conclusion	130

---

This section examines the presented tabulation approach of real fluid thermodynamics as a closure to the fully compressible multi-component two-phase flow, based on the homogeneous equilibrium method and a diffuse-interface approach. Hence, two prominent industrial test cases with different thermo-hydro-mechanical behaviours have been selected, studied, and validated with the available experimental data. As a result, the upcoming studies are structured in two different parts, which build upon this section.

In **section 5.1**, the main objective is to understand the subcritical and transcritical multi-species liquid-gas interface structure. This will be done by simulation of a classical cryogenic injection of liquid nitrogen coaxially with a hot hydrogen jet, using thermodynamic tables generated by two different equations of state: Peng–Robinson (PR) and Soave–Redlich–Kwong (SRK). The numerical results are finally compared with available experimental data and published numerical studies with satisfactory agreement.

Then, **section 5.2** focuses on analyzing the coupling between the hydrodynamics and thermodynamics of multi-species supercritical jets. This has been done by studying various phase transition phenomena, such as droplet nucleation by condensation, which have been shown experimentally to affect the flow and mixing dynamics of the jet significantly. The predicted results with this tabulation approach are in good agreement with experiments.

## 5.1 Towards understanding the structure of subcritical and transcritical multi-species liquid-gas interfaces

In recent years, researchers have performed different studies for multi-component systems to have a clearer picture of the mixing jet behavior for multi-component systems, without considering the complexities of combustion, known as cold flow studies [17,28,34,53,102,106]. In this section, different studies will be carried out for pure single-component as well as for binary mixtures to better understand and highlight the main difference between them, and to investigate the phase transition and mixing processes in subcritical, transcritical and supercritical regimes. Among them, one of the fundamental studies could be the study of cryogenic nitrogen ( $N_2$ ) injected co-axially with warm hydrogen ( $H_2$ ) into supercritical nitrogen ambient [29,102]. Figure 5.1(a) represents a schematic of such a cryogenic injection flow close to the mixing injector orifice. As can be seen, there are two different propellant streams ( $N_2$  and  $H_2$ ), called main stream and secondary stream, respectively. The mainstream cryogenic liquid  $LN_2$  with the temperature of 118 K at subcritical temperature regime (as  $T_c=126.2$  K, and  $P_c=3.396$  MPa of  $N_2$ ), is injected co-axially with a warm secondary stream of gaseous  $GH_2$  with the temperature of 270 K, ( $U_{N_2}^{inj} = 5m/s$ ) < ( $U_{H_2}^{inj} = 120m/s$ ). These streams are injected into a chamber filled with gaseous  $GN_2$  at  $T_{Ch}=300$  K, and  $P_{Ch}=4$  MPa, and hence at supercritical condition. The configuration sketched in Figure 5.1(a) is intended to summarize the discussion throughout this section by showing the main characteristics of the flow field with a transcritical and subcritical interface simultaneously. Since a large number of thermodynamic and physical parameters are involved in this problem, it cannot be treated in a single study.

The current work focuses on studying the phase transition characteristics in order to reveal the parameters with the dominant roles. As shown in Figure 5.1(a), the main  $LN_2$  flow field immediately downstream of the injector orifice is heated and forms a thermal mixing layer between the propellant jets and chamber gas, here between the liquid-like nitrogen and supercritical fluids. From a thermodynamic viewpoint, as previously discussed, one of the main characteristics for transcritical interface is the appearance of extrema for heat capacity at the Widom line, as shown in Figures 2.3b and 5.1c. However, due to the different velocities of the propellant between the main flow  $LN_2$  and the secondary flow  $GH_2$ , the composition may vary significantly depending on the position, and as a consequence the fluid properties vary accordingly. Indeed, the  $GH_2$  jet can cover entirely or not the  $LN_2$  jet liquid core. It is noteworthy to mention that the mixture critical point will change as soon as the composition changes in the multicomponent mixtures,

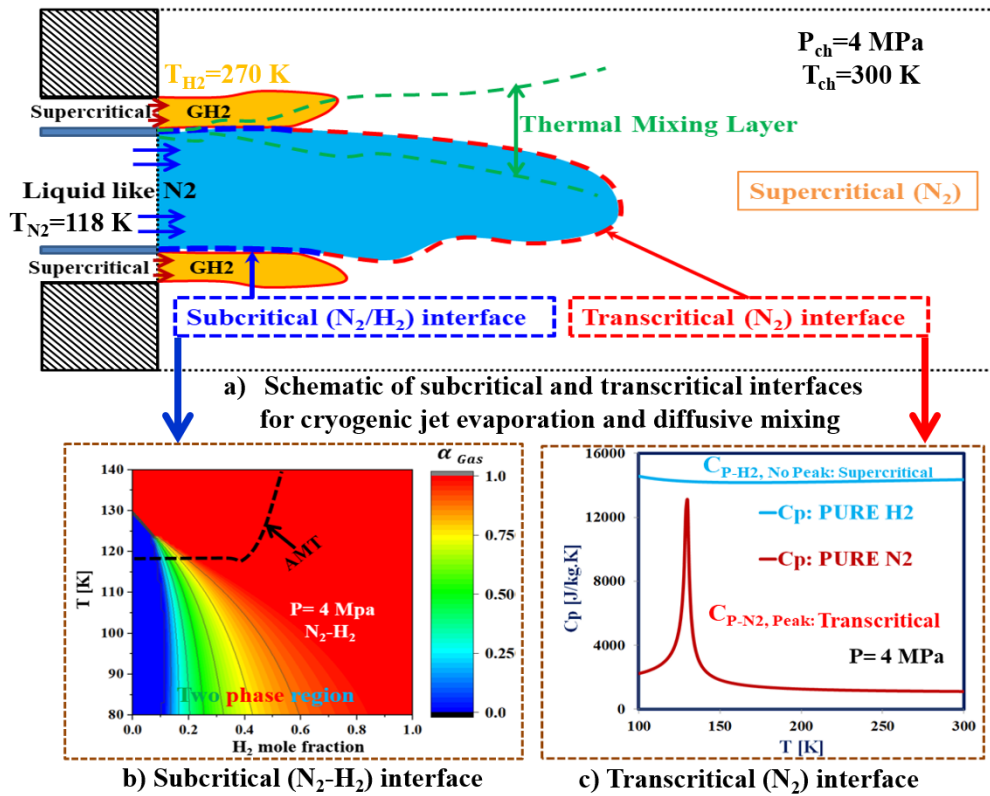


Figure 5.1: (a) Schematic for a liquid-like  $LN_2$  main stream injected in the center, and a secondary hot supercritical gaseous  $H_2$  injected co-axially into a combustor at a pressure higher than the critical pressures of the two non premixed components. This figure sketches the case in which the liquid core is partially covered by  $GH_2$  jet. The liquid core interface is divided into two parts. The leading interface part 1 is a transcritical interface (see the dashed line colored in red). A subcritical interface is formed upstream between the main  $LN_2$  flow and the secondary  $GH_2$  flow (see the dashed line colored in blue). (b) The gas volume fraction contour plot in a temperature and  $H_2$  composition diagram shows the locus and the thermodynamic states for subcritical ( $N_2 - H_2$ ) interface. (c) The isobaric heat capacity of  $N_2$ , has a peak value, on the widom line, at the transcritical interface between  $LN_2$  and  $GN_2$ .

and a linear relation between the critical point of a mixture and that of each pure species does not exist. Hence, the bubble line and dew line locus will be shifted in proportion to the composition value. Figure 5.2 as well shows the phase boundary movements as well as critical point variations for different compositions for the binary mixture of  $N_2 - H_2$ , and it demonstrates that by mixing of two supercritical components, it may actually find a subcritical behaviour for the mixture. However, due to this fact that the pressure in the chamber approximately remains constant, the critical point as well as the bubble line and dew line locus no longer will depend on the mixture composition, as shown in Figure 5.1(b). Figure 5.1(a) sketches the case in which the liquid core is partially covered by  $GH_2$  jet. In this case, the liquid core interface is divided into two parts. On the one hand, the leading interface part is a transcritical interface where the surface tension is null and only diffusive mixing can take place. Figure 5.1(c) shows the specific heat capacity non-linearity taking place at such transcritical interface. On the other hand, a

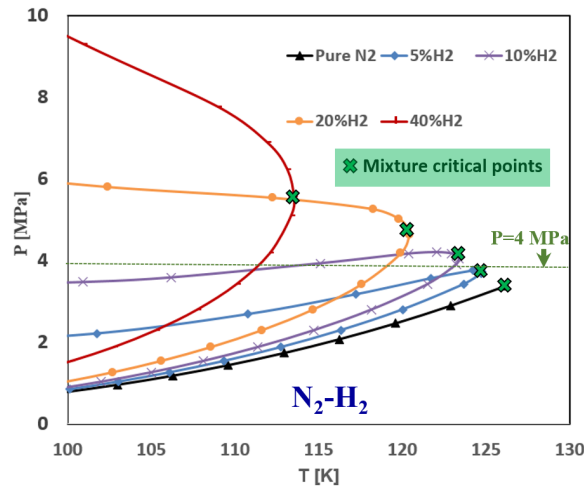


Figure 5.2: Phase envelope movements and critical point variations for different compositions for  $N_2 - H_2$  mixture.

subcritical interface is formed upstream between the main  $LN_2$  flow and the secondary  $GH_2$  flow (see Figure 5.1(a)). For such subcritical interface, primary atomization may occur depending on the magnitude of the surface tension. The path followed by the fluid close to the interface can be sketched by the dotted line in figure 5.1(b). This figure shows the phase diagram of the  $H_2 - N_2$  mixture at the system pressure of 4 MPa. At the left of the figure, the injected liquid-like  $N_2$  has a temperature of 118 K. When the fluid moves to the right, it is progressively mixed with  $H_2$  at 270K. The temperature of the jet could be increased in an adiabatic manner by neglecting the heat exchange. This means that it has the temperature that is such that the enthalpy of the mixture is equal to the weighted average of the enthalpies of the pure jets. In other words  $(H_{Mix}(AMT, P_{ch}, z_{H_2}) = z_{H_2}H_{H_2}(T_{H_2}^{inj}, P_{ch}) + (1 - z_{H_2})H_{N_2}(T_{N_2}^{inj}, P_{ch}))$ . The resulting temperature as a function of the fluid composition is shown in figure 5.1(b). It is called the Adiabatic Mixing Temperature (AMT). The same figure also shows the phase diagram of the mixture: when  $\alpha_{gas} = 1$ , the fluid behaves as a gas (in the right part, rich in hydrogen). When  $\alpha_{gas} = 0$ , the fluid behaves as a liquid (on the left part of the diagram. Approximately, between the compositions of 10 to 65%  $H_2$ , the fluid is in two-phase condition, and this is despite the fact that both of the pure components are supercritical. In addition, it is also the location of phase change (evaporation or condensation) as the adiabatic mixing temperature (AMT) is crossing the two-phase dome, as depicted in Figure 5.1(b). In fact, this subcritical interface is due to the movement of the mixing critical point of the binary ( $N_2, H_2$ ). The gas volume fraction contour plot, in a temperature and  $H_2$  composition diagram is plotted at  $P=4$  MPa in Figure 5.1(b) in order to show the locus and the thermodynamic states for subcritical ( $N_2 - H_2$ ) interface. By changing the flow rate of the propellants, the position of the transition between the subcritical

and the transcritical interfaces is going to change. Consequently, this may induce changes in the jet shape, structure and liquid length, and as a result the mixing process. Also, it should affect the interface modeling as discussed above. Besides, the transition from subcritical multi-component interface to transcritical interface will be affected also various other parameters, such as turbulence, thermal mixing layer, and the hydrodynamic instabilities, like Kelvin Helmholtz, by making delay or fasting it, which needs to be further addressed.

### 5.1.1 Transcritical mixing and evaporation study

The study of transcritical mixing and evaporation is the main objective of this part, as discussed before in Figure 5.1. Hence, a series of different 1-D, 2-D, and 3-D test cases for single component and binary mixture are computed, and will be analyzed for better understanding the mixing of jets involving subcritical and transcritical interfaces.

In order to validate the RFM model along with the density-based approach proposed above, numerical simulations for different shock tube test cases are carried out as summarized in Table 5.1. The tube is 1 m long with initial discontinuity at 0.5m, where the left and right hand side of the tube are initiated as listed in Table 5.1. The notation L and R in Table 5.1 stands for the left and right sides of the tube, respectively.

Case 1, represents the simulation of a shock tube for cryogenic  $N_2$ , at supercritical conditions. For these simulations, a first order time accuracy and a second order spatial accuracy are used. Also, for the sake of stability and accuracy, the CFL number is set to 0.1. The results in this study are compared with the study of Ma et al. [34]. These authors have developed a fully conservative solver using the PR-EoS without phase change. Since the pressures and temperatures in both side of shock are above the critical point of nitrogen ( $T_{cN_2} = 126.2K, P_{cN_2} = 3.4MPa$ ), then, the fluid is in a supercritical state. The results of case 1 depicted in Figure 5.3, shows that compared to Ma et al. [34] numerical results, the RFM-SIMPLE has a good agreement. However, small differences can be seen in Figure 5.3 due to the use of the entropy-stable model for damping the spurious oscillations, as discussed in their part.

Table 5.1: Initial conditions for pure  $N_2$  transcritical shock tube test cases for different pressures

	$P_L(MPa)$	$P_R(MPa)$	$T_L(K)$	$T_R(K)$	$U_L = U_R(m/s)$	Numerical scheme
<b>Case 1</b>	60	6	158	224	0	<i>SIMPLE</i>
<b>Case 2</b>	40	6	158	224	0	<i>SIMPLE</i>
<b>Case 3</b>	20	6	158	224	0	<i>SIMPLE</i>
<b>Case 4</b>	20	6	158	224	0	<i>PISO</i>

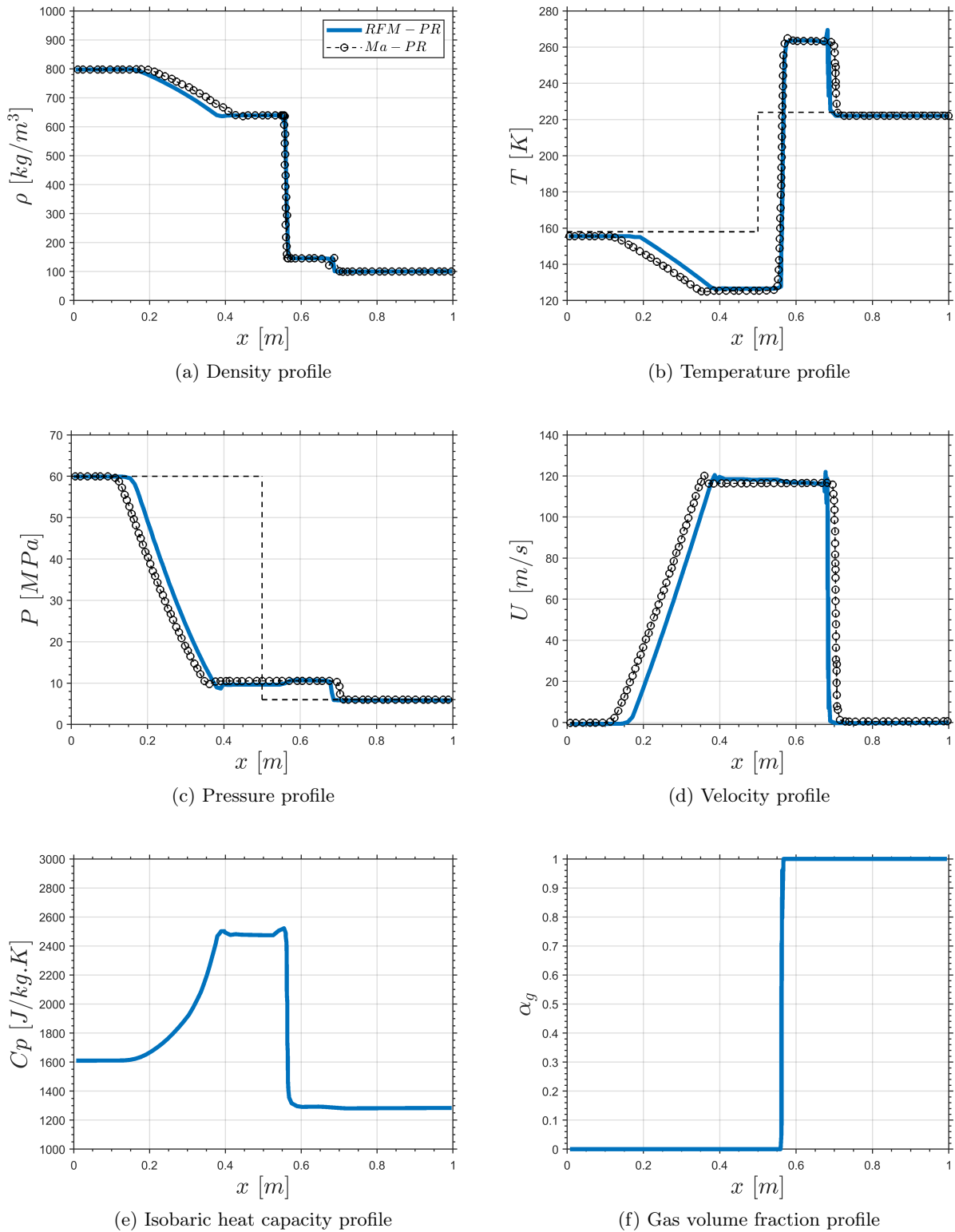


Figure 5.3: Case 1, comparison of different results for the density, temperature, pressure, velocity, heat capacity, and gas volume fraction, respectively, using PR-EoS, for the transcritical shock tube between the presented model in this study named the RFM and Ma et al. [34] at  $500\mu s$ . CFL = 0.1 for the RFM model and CFL=0.8 for the Ma model. The thin dashed lines are the initial conditions.

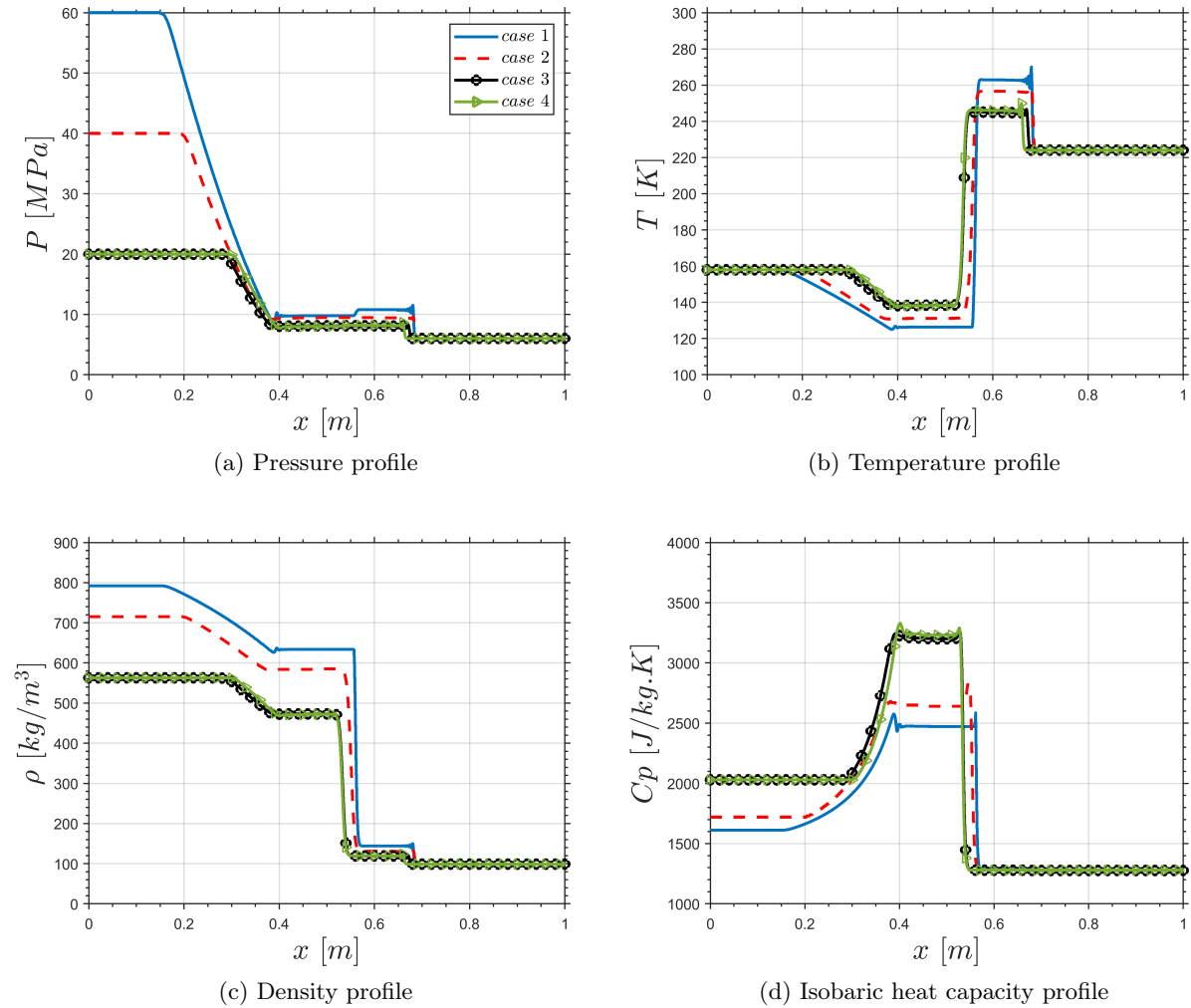


Figure 5.4: The impacts of pressure variations on the properties evolution for the transcritical shock tube test case, defined as case 1:3 in table 5.1, using PR-EoS, on (a) Pressure profile, (b) Temperature profile, (c) density profile, (d) Isobaric heat capacity, using SIMPLE numerical scheme, at  $t=500\mu s$ . Also, a comparison between SIMPLE and PISO schemes for cases (3-4) shows a good agreement between them at this condition.

Noteworthy that such entropy-stable model have not been considered in the RFM model. The conformity of the results using different mesh sizes proves the non-grid dependence of the RFM results. Also, as demonstrated in the Figure 5.3 (e,f) showing isobaric heat capacity and the gas volume fraction profiles, respectively, the isobaric heat capacity has its maximum values in the liquid-like region between  $x=0.35$  m and  $x=0.55$  m where  $T$  is around 127 K (Figure 5.3(b)) and  $P$  is around 10 MPa (Figure 5.3(c)). These thermodynamic conditions are close to the transcritical interface separating the liquid-like and the gas-like sides. These results shows the ability of the RFM model to deal with the properties non-linearity near the Widom line and close to the critical point.

Furthermore, in order to examine the behaviors of pressure variations on the transcritical flows, a pressure sensitivity study, as mentioned in table 5.1 for cases (1-3), is performed. Figure 5.4(a-d)

show the evolution of pressure, temperature, density, and isobaric heat capacity respectively, for the different cases. The numerical results show that the impact of enhancing pressure on the compression shock as well as rarefaction wave are distinguishable. One interesting point is about the variation of the isobaric heat capacity at the interface between the low and high pressure regions on the flow. Not only the initial value of isobaric heat capacity reduces by increasing the pressure, but also the variation of isobaric heat capacity,  $C_{pmax}$  at the interface increases due to the proximity of the transcritical regimes. This increase of isobaric heat capacity at the jet interface can act like a stronger thermal shield between the liquid-like core and the ambient. Finally, a comparison between SIMPLE and PISO schemes for test cases (3-4), in the same condition, shows a good agreement between the numerical schemes when the RFM model is applied at such transcritical conditions.

### 5.1.2 Transcritical single-component Cryogenic injection

This section is dedicated to the study of turbulent jet mixing process of cryogenic nitrogen ( $LN_2$ ) injected into a quiescent nitrogen ( $GN_2$ ) under transcritical and supercritical regimes. In this study, the simulation characteristics are same as Mayer's experimental study, near critical and supercritical conditions [21]. The critical point for pure  $N_2$  are ( $T_{cN_2} = 126.2K, P_{cN_2} = 3.396MPa$ ). A cryogenic  $LN_2$  is injected from the nozzle with the diameter of 2.2 mm with a uniform velocity of 4.9 m/s for three different test cases with different temperature and pressures as listed in Table 5.2. PR-EoS is used for generating the thermodynamic table used for solving the RFM model using PISO as CFD solver. A 2-D rectangular computation domain is employed

Table 5.2: Operating conditions for the transcritical cryogenic  $N_2$  injection similar to the Mayer's experimental study [21].

	$T_{inj}(K)$	$T_{ch}(K)$	$P_{ch}(MPa)$
<b>Case 5</b>	126.9	298	6
<b>Case 6</b>	150	298	6
<b>Case 7</b>	135	298	4

following similar studies in the literature [17, 38, 107]. Figure 5.5 presents the computational domain as well as the boundary conditions used in this study. At the jet inlet, a uniform velocity with a constant temperature are used. A pressure outflow boundary condition is used for the right, top, and bottom side boundaries. No-slip and isothermal condition are specified for the left side boundary including the injector wall. The total cell count of 1 million cell is generated for this simulation so that the nozzle inlet is discretized by around 100 computational cells. Figure 5.6 demonstrates instantaneous numerical results at  $t=2, 4,$  and  $5$  ms, for Case 5. It shows different contour plots of the density, isobaric heat capacity, and phase indicator (denoted PHI). PHI=0 designates a liquid state and PHI=1 designates a gas state.

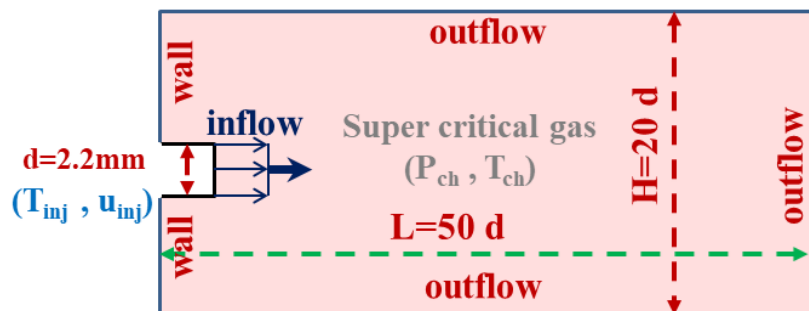


Figure 5.5: Setup of transcritical jet simulation

Figure 5.6(a) shows the liquid-like flow of nitrogen with a density of  $585 \text{ kg/m}^3$  penetrating into the supercritical nitrogen with a density of around  $66 \text{ kg/m}^3$ . The phase indicator parameter (PHI) (see Figure 5.6(c)) shows that, according to the transcritical thermodynamic theory, the  $LN_2$  liquid-like is diffusing and mixing with the  $GN_2$  gas-like ambient through a transcritical interface. Figure 5.6(b) shows another important phenomenon regarding the so-called finger-like or ligaments appearance in the transcritical regime. Despite the absence of surface tension at the transcritical interfaces, interface instabilities and ligaments have been observed experimentally as in Figure 2.2(b). It is also important to observe in Figure 5.6(b) that the peak  $C_{p,max}$  is also present on the periphery of the ligaments in addition to around the liquid-like core.

Besides, Figure 5.7 shows the contour plots of temperature and vorticity, which demonstrates the full coupling between the flow solver and thermodynamic non-linearities. The position of the transcritical interface between the liquid-like and gas-like corresponds to the Widom (pseudo-boiling) line, as shown in Figure 5.7(a) by a  $C_{p,max}$  white iso-line. It can also be observed that the flow vorticity reaches a maximum value at the interface. In addition, the formation of a high specific heat layer ( $C_p$ ) at the interface leads to a non-uniform heat distribution that can result in thermal breakup of the transcritical jet. Besides, due to the hypersensitivity of the thermodynamic properties in the transcritical region, local turbulent fluctuations can bring radical changes to the jet structure. This phenomenon is referred to as the Turbulence-Thermodynamic Integration in [107]. It is also well known that the shear layer is the location where the Kelvin-Helmholtz (K-H) instability develops, which has an important role on the jet breakup mechanism. This study reveals that K-H instability also has a crucial role at the transcritical regime. However, due to the absence of surface tension and a relatively smaller density gradient at the wider transcritical interfaces, the K-H instability develops more slowly than under subcritical conditions and its effect is limited to promoting the transition to the fully turbulent regime by large-scale entrainment, as shown in Figure 5.7(b).

Figure 5.8 presents the numerical results of Case 6 in terms of temperature, and isobaric heat capacity profiles at  $t=5 \text{ ms}$ . It can be seen that moving to the supercritical regime (by increasing  $T_{inj}$  to  $150 \text{ K}$ ) makes no maximum  $C_p$  appearing at the interface, as depicted in the zoom in Figure 5.8. In these purely supercritical conditions, the  $C_p$  values have a linear evolution between that of the gaseous jet core and the ambient gas.

The numerical results of Case 7 where the jet core is at  $T_{inj}=135\text{K}$  and the ambient pressure is at  $P_{ch}=4 \text{ MPa}$ , are presented in Figure 5.9.

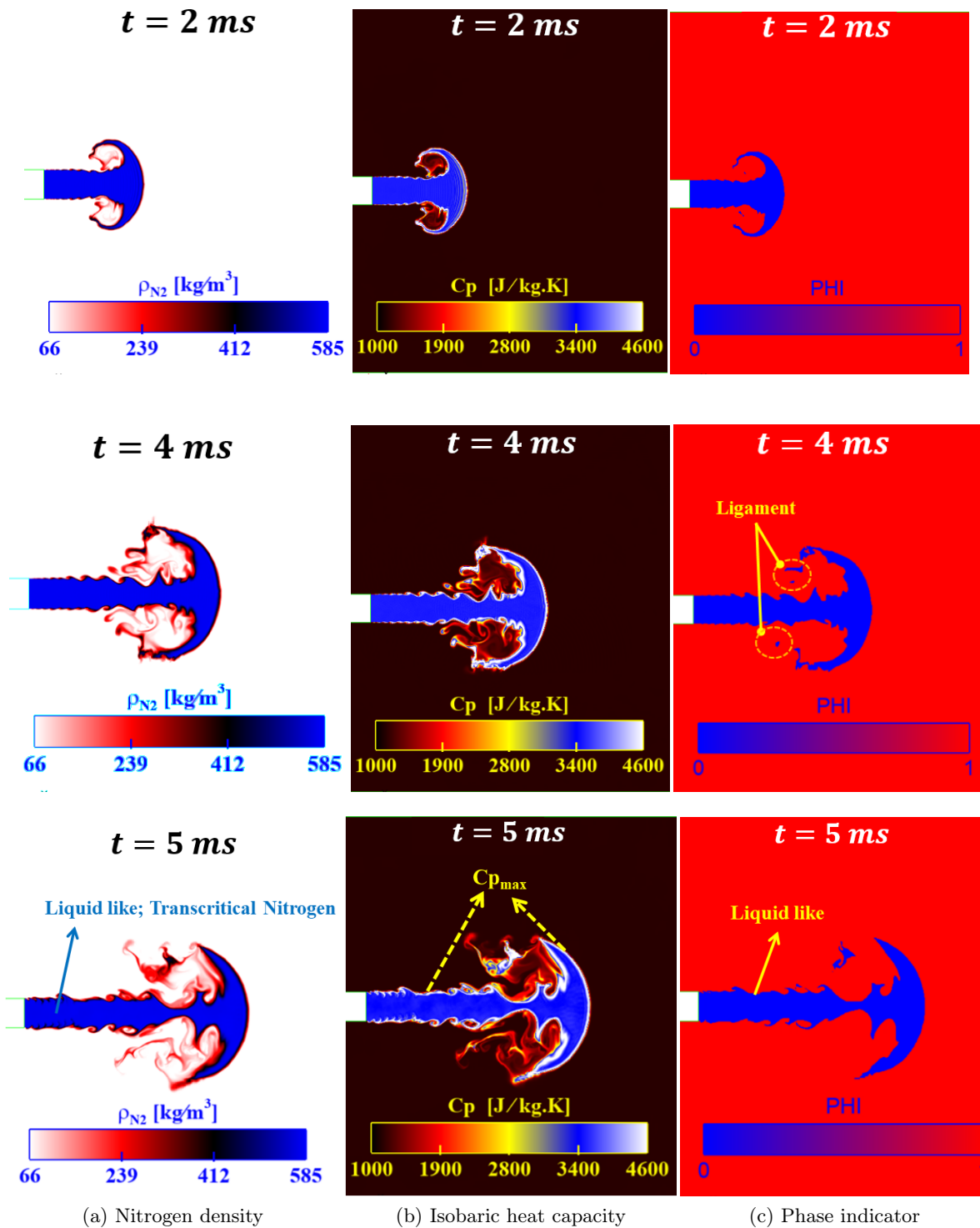


Figure 5.6: Case 5 instantaneous contour plots of density, heat capacity, and phase indicator (PHI); PHI=0 designates a liquid state and PHI=1 designates a gas state.

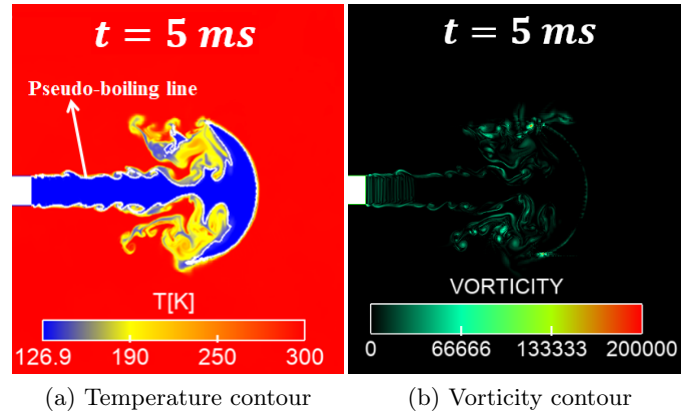


Figure 5.7: Case 5 instantaneous contour plots of temperature and vorticity fields at transcritical condition at  $t=5$  ms. The position of interface between the liquid like and gas like at Pseudo boiling line, at temperature contour, is determined by  $C_{p,max}$  iso-line, colored by white. The  $C_{p,max}$  at the interface acts like a thermal shield for the jet.

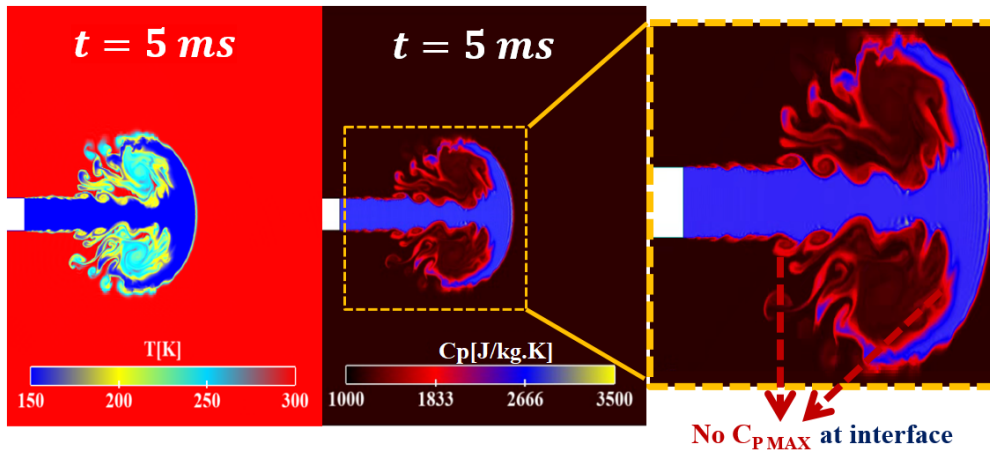


Figure 5.8: Case 6, instantaneous contour plots of temperature and isobaric heat for supercritical nitrogen injection at  $T=150$ K and  $P= 6$  MPa after  $t=5$  ms.

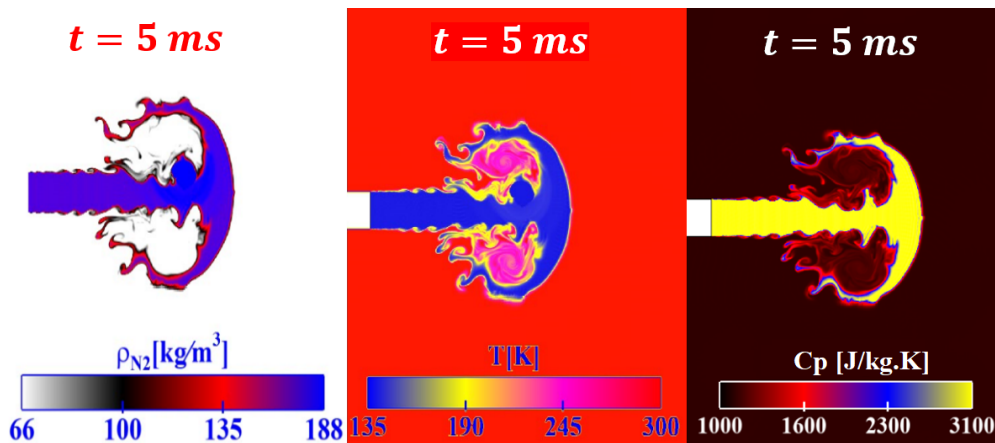


Figure 5.9: Case 7, instantaneous contour plots of density, temperature, and isobaric heat capacity for supercritical nitrogen injection at  $T=135$ K and  $P= 4$  MPa after  $t=5$  ms. Isobaric heat capacity ( $C_p$ ) reduces continuously from liquid jet to the chamber, and there is no peak at  $C_p$ , no thermal shield at the interface, no thermal shield, and it has a symmetrical distribution. Hence, there is no crossing of Widom line, which proves that the jet is in supercritical regime.

It can be seen that for these (T, P) conditions closer to the  $N_2$  critical point ( $T_c=126.2$  K,  $P_c=3.396$  MPa), the fluid has proved to be in gas-like state due to the absence of  $Cp_{max}$  at the interface, not touching the Widom line. It is well known that in this supercritical regime, the fluid acts like a weakly compressible single fluid in the chamber as well as in the jet core. As a result the interface has disappeared completely. However, two important phenomena can be observed in the supercritical regime simulations compared to the transcritical one. Firstly, the jet has more symmetrical shape in the supercritical regime, as it may be seen by comparing Figure 5.6, and Figures 5.8-5.9. Secondly, the jet mixing, especially at the jet tip, is comparable in both regimes.

### 5.1.3 Binary coaxial injection of $LN_2$ with hot $GH_2$

This section is devoted to the study of turbulent jet mixing process of binary mixture similar to the one sketched in Figure 5.1. In modern Liquid Rocket Engines, the chamber operating pressure lies above the critical pressure of the propellants. In these conditions, known as transcritical conditions, the fluid properties significantly differ from an ideal gas and the jet behavior differs significantly from injection at low pressures. In the recent decades, several researchers have investigated the cryogenic rocket engine processes [28, 29, 34, 67]. However, the structure of the liquid-gas interface for binary systems has not been clearly described. In this section, we will study a selected operating point from a series of experiments from [29] for which quantitative density measurements were obtained for a classical cryogenic injection of liquid nitrogen ( $LN_2$ ) co-axially injected with hot hydrogen ( $H_2$ ) jet into supercritical nitrogen at 4 MPa, when compared to the pure  $N_2$  and pure  $H_2$  critical pressures ( $P_c=3.35$ MPa for  $N_2$  and  $P_c=1.296$  MPa for  $H_2$ ).

#### Configuration description and numerical methods (Case 8)

Figure 5.10 shows a schematic of the experimental setup that has been investigated [29], along with a computational grid cross section showing the cylindrical chamber ( $D = 10$  cm) initially filled with  $GN_2$  at  $P_{ch} = 4$  MPa and 298.15 K. The inner  $LN_2$  injector diameter is  $D_i = 1.9$  mm. The inner and outer diameters of the  $GH_2$  rings are  $D_{H_2,i} = 2.4$  mm and  $D_{H_2,o} = 3.4$  mm, respectively. The inlet velocity of  $LN_2$  and  $GH_2$  are 5 m/s and 120 m/s, respectively. A 3D simulation setup was employed for which the computational grid has been generated in a rectangular domain with the dimensions  $L_x = 100$  mm in the stream-wise and  $L_y = L_z = 40$  mm in the lateral directions, similar to [28].

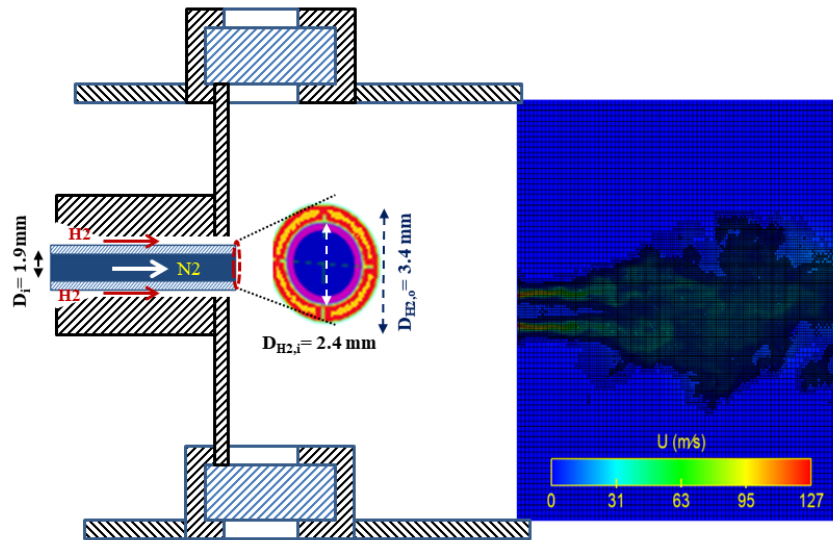


Figure 5.10: Case 8: (Left) Schematic of the injector experimental configuration: blue and red color indicate  $LN_2$  and  $GH_2$  canals, respectively. (Right) Computational domain in the central cut-section of the simulated 3D geometry. AMR is used based on the criterion of the minimum velocity of 0.1 m/s.

The base mesh cell size is set to 0.5 mm and refined to 0.1 mm in the flow field using AMR, Figure 5.10(right). The sub-grid criterion for adaptive mesh refinement has been chosen for the cells based on a minimum velocity of 0.1 m/s. The study employs the sub-grid scale Smagorinsky turbulence model in the LES framework. The thermodynamic models are based on two different EoS, PR and SRK, in order to compare their performance and to observe and measure the magnitude of changes due to the choice of EoS. To assess the VLE calculation based on the EoS, the VLE of a binary mixture of  $N_2$ - $H_2$  has been computed, and will be validated with the Experimental data from [28] in the next section. The time step is automatically adjusted based on a maximum CFL number of 50 reaching a value in the range of  $10^{-8}s - 10^{-9}s$ . The typical CPU time for the simulation discussed below is 40 hours for a simulation time of 1 ms using 360 cores (i.e., 20 Intel Skylake G-6140 processors with 18 cores running at 2.3 GHz), which is much more efficient than our previous simulations [17, 22] using VLE thermodynamic flashes called during the simulations.

## Results and discussion

### Flow mixing hydro-thermodynamics and interface features

Figure 5.11 displays the temporal evolution (at 0.25, 3, and 5 ms) of mixture density, and  $H_2$  mass fraction in the central cut section of the geometry using PR EoS. As shown, the liquid nitrogen core with the density of around  $610 \text{ kg/m}^3$  is injected into the chamber filled completely with  $GN_2$ , with the density of around  $50 \text{ kg/m}^3$ .

Besides, in the outer-loop, the warm hydrogen with the density of around  $3.5 \text{ kg/m}^3$ , is coaxially injected and mixed with the  $LN_2$  jet core, inside the  $GN_2$  chamber.

Figure 5.12 depicts an instantaneous snapshot of the  $H_2$  density, temperature, and phase indicator distribution (PHI=0, 1, 2 denotes liquid, gas, and two-phase state, respectively) using PR, and SRK EoS, respectively. In this Figure, the cryogenic  $LN_2$  at  $T_{N_2}^{inj}=118\text{K}$  may be identified as the dark core in the temperature contour, Figure 5.12(a, d), which is surrounded by a co-flow warmer  $GH_2$  injected at  $T_{H_2}^{inj}=270\text{K}$  into the  $GN_2$  at  $T_{ch}=298.15\text{K}$  and  $P_{ch}=4 \text{ MPa}$ . Because the chamber pressure is higher than the critical pressure of both propellants, ( $P_c=3.35 \text{ MPa}$  for  $N_2$  and  $P_c=1.296 \text{ MPa}$  for  $H_2$ ) and the cryogenic  $LN_2$  is injected at  $118\text{K}$ , a temperature much smaller than its critical temperature ( $T_c = 126.2 \text{ K}$  for  $N_2$ ), the jet flow belongs to the transcritical flow regime. It is worth mentioning that the critical pressure path of  $H_2$ - $N_2$  mixture reaches higher pressures than  $4 \text{ MPa}$ . In this regime, Crua et al. [18] experiments varying the ambient pressure above pure fuels critical pressure have revealed the existence of a subcritical relatively sharp liquid-gas interface that is progressively thickened [32] and replaced by a diffusion-dominated mixing regime at a sufficiently high ambient pressure. These experiments have been corroborated recently by Yang et al. [17] LES simulations of the Spray-A injector in the transcritical regime. However, when and how this transition to a diffusion-dominated mixing regime occurs is not well understood. According to Yang et al. [5], this transition should take place when the ambient pressure exceeds the mixture critical pressure. Nevertheless, it is worth recalling that the latter is a local variable that depends on the local composition. Similar to Diesel injection [17], a two-phase region around the liquid core is identified by the phase indicator (PHI=2, yellow color in Figure 5.12(c, f)). It is interesting to see also in Figure 5.12 (b, e) that the temperature within the mixing layer in the two-phase region drops below its inflow value of  $118 \text{ K}$  to approximately  $114 \text{ K}$  due to the evaporation latent heat, which is revealed to be significant in the current transcritical condition. Another remarkable effect also discussed by Matheis et al. [28], can be observed for the  $H_2$  partial density in Figure 5.12 (a, d) for both EoS. Indeed,  $H_2$  is injected with a density of  $3.56 \text{ kg/m}^3$  and reaches a much higher partial density of almost  $4.7 \text{ kg/m}^3$  within the two-phase region due to its condensation.

As an important milestone for this study, the binary phase diagram for  $N_2$ - $H_2$  has been compared with the study of Matheis et al. [28], and very similar numerical results are obtained, as shown in the  $T - z_{H_2}$  diagram plotted in Figure 5.13. Pure  $LN_2$  ( $z_{H_2} = 0$ ) at  $118 \text{ K}$  as injection temperature, and  $GN_2$  at  $298 \text{ K}$  as chamber temperature as well as  $z_{H_2} = 1$  for pure  $H_2$  at  $270 \text{ K}$ , on the right-hand side, can be identified in Figure 5.13. In between, the LES numerical results

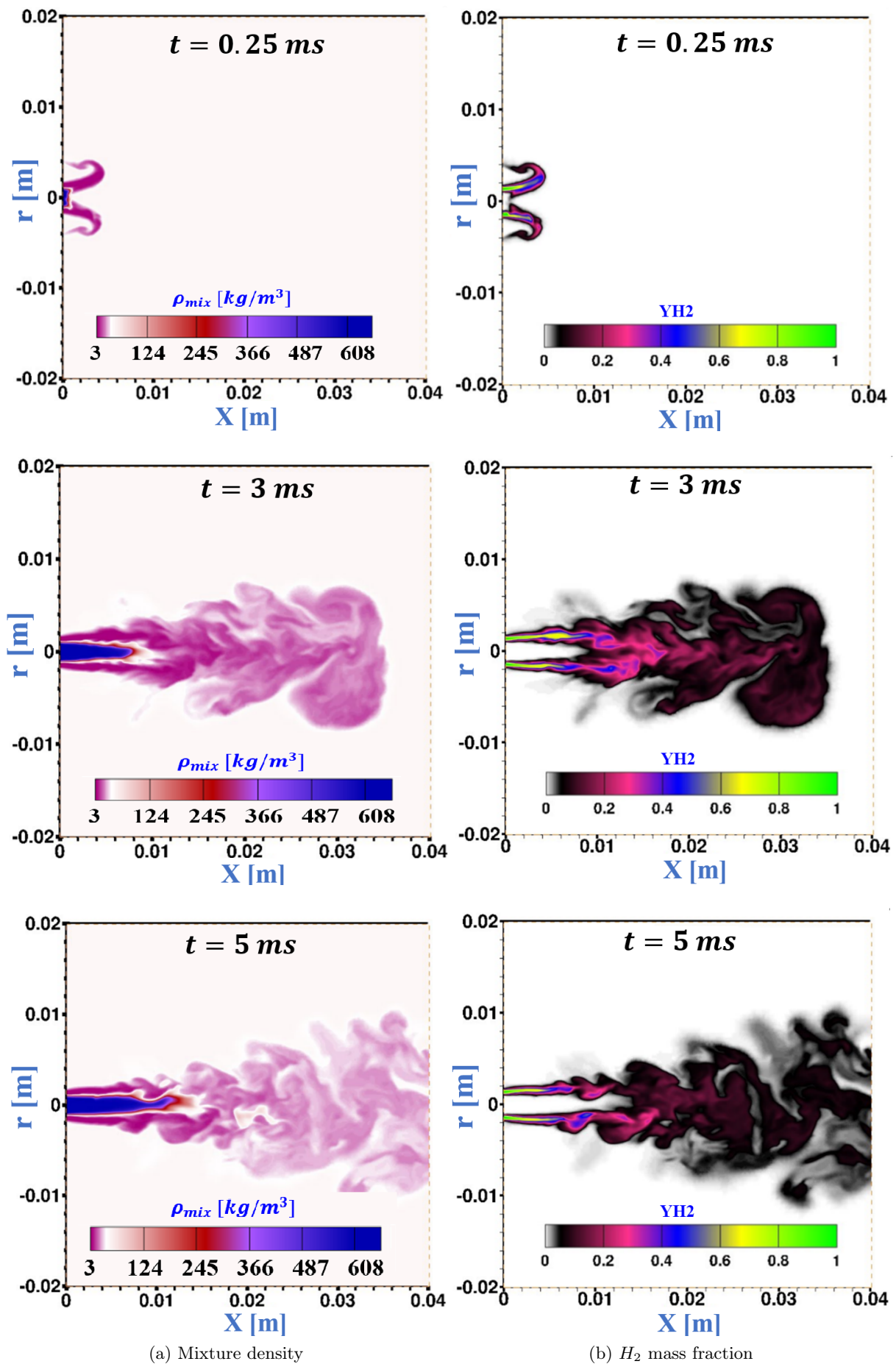


Figure 5.11: Distribution of mixture density (Left), and  $H_2$  mass fraction (Right)

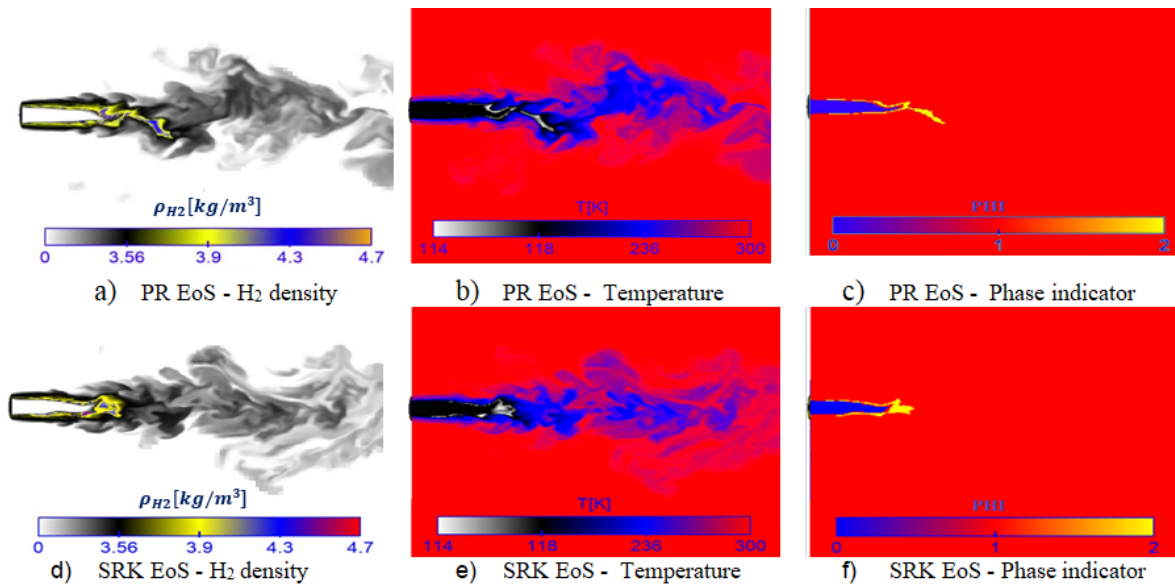


Figure 5.12: Distribution of  $H_2$  density, temperature, and phase indicator (in the central cut-section) using the two different EoS at  $t = 4.5$  ms. PHI=0, 1, 2 denotes liquid, gas, and two-phase states.

show that either the injected cryogenic  $LN_2$  or the hot  $GN_2$  in the chamber are mixed with the injected warm  $GH_2$ , as shown by the blue circles in Figure 5.13. Adiabatic mixing temperature (AMT) is also plotted in Figure 5.13. The LES results are more scattered, compared to AMT results, due to the turbulent mixing which is obviously not adiabatic. More precisely, it can be seen in Figure 5.13 that the mixing process does not follow the adiabatic mixing lines. On one hand, a relatively small deviation of the LES scatter plots can be observed inside the two-phase dome in the zoom provided in Figure 5.13.

On the second hand, the highest deviation of the LES scatter plots is obtained in the fully turbulent mixing region between the injected  $GH_2$  layer and ambient  $GN_2$ , as shown around the black AMT line in the upper part of Figure 5.13. Figure 5.14 depicts the temporal variation of the mixture isobaric heat capacity as well as the reduced mixture temperature of the flow field defined using the mixture critical temperature ( $T_{c,mix} \approx 125K$ ) at the chamber pressure, as depicted in the zoom of Figure 5.13. As it can be seen in the isobaric heat capacity distribution in Figure 5.14(a), the injected pure  $GH_2$  owns the highest value of heat capacity, around  $14000J/kg.K$  (in yellow). The  $GH_2$  jet mixes quickly at its inner side with the  $LN_2$  having a heat capacity value of about  $4500J/kg.K$ , and at its outer side with the ambient  $GN_2$  of the chamber having a heat capacity value of about  $2000J/kg.K$ . Because of the higher velocity of the  $GH_2$  jet compared to the cryogenic  $LN_2$  one, the transcritical interface (as sketched in Figure 5.1(a)) has disappeared and replaced by a multi-component subcritical interface and a two-phase region all around the liquid core, as shown in Figure 5.12(c, f). Figure 5.14(b) shows the reduced

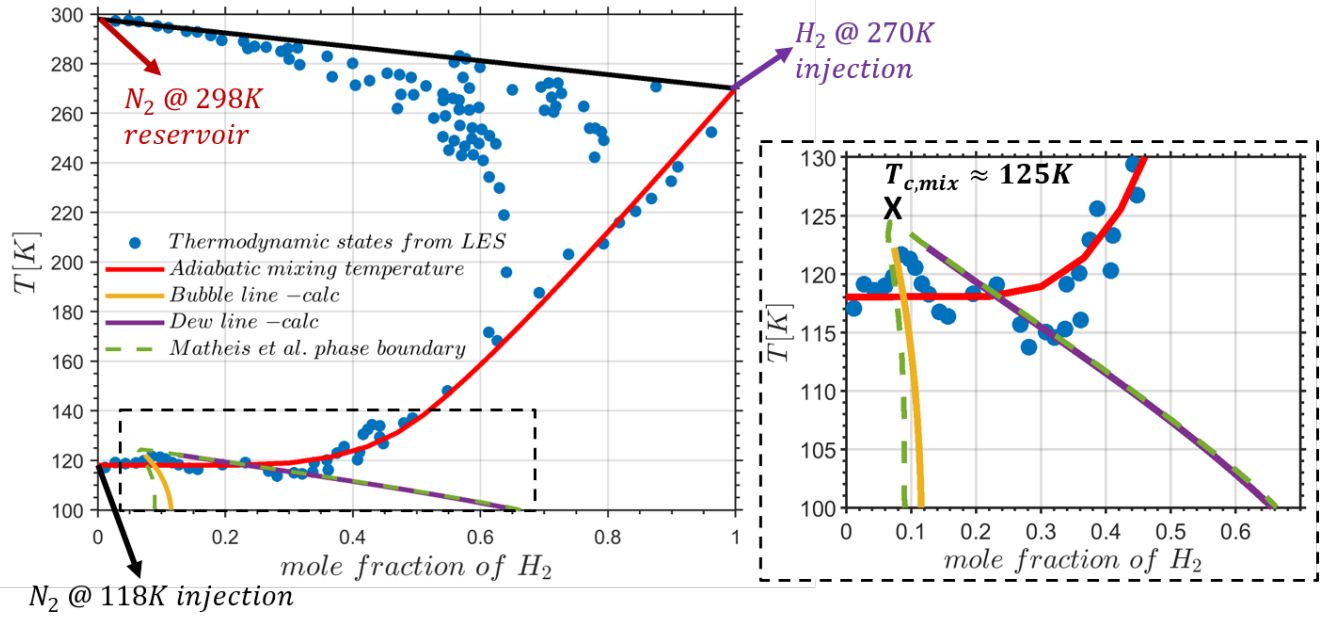


Figure 5.13: Temperature  $H_2$ -composition phase diagram for binary mixture of  $N_2$ - $H_2$  at  $P=4$  MPa, calculated by PR-EoS, compared with [28], used PR-EoS, along with the adiabatic mixing temperature (AMT)

temperature distribution defined as  $T_r = T/T_{c,mix}$ . It confirms the subcritical nature of the  $LN_2$  core as  $T_r < 1$  is depicted in white color in this region.

Also, the two-phase narrow layer (depicted in grey color in Figure 5.15) is revealed to be in subcritical state with  $T_r < 1$ , as shown by the  $T_r$  profile where the vapor volume fraction  $\alpha_g$  is between zero and one. It is also worth mentioning that in Figure 5.14 the mixture isobaric heat capacity at the periphery of the circular jet is not symmetric due to multiple reasons such as phase change and turbulence interactions, thermal layer development, and the Kelvin-Helmholtz instability. These complex phenomena contribute to the break up and mixing processes of the jet, similarly to the single-component transcritical case discussed above in Section 3.2. Figure 5.16(a) shows gas volume fraction contour in which the gas region (in red), the liquid region (in blue), and the two phase layer in between demonstrate again the locus of the subcritical interface for the multi-component system of  $H_2$ - $N_2$  at 4 ms. These results corroborates the latest experimental findings from Crua et al. [18], who have proved that there exists phase transition even when the operating conditions are at supercritical condition with regards to the pure fuel critical point. Besides, Figure 5.16(b) demonstrates the compressibility factor distribution at 4 ms which confirms the importance of using complex EoS for this study. Indeed, it can be seen in this figure that the compressibility factor varies from 0.184, inside the liquid core, up to around 1 in the supercritical gas region. For the most part of flow field involved in the injection and the mixing, the compressibility factor is far from unity which demonstrates the real fluid behavior.

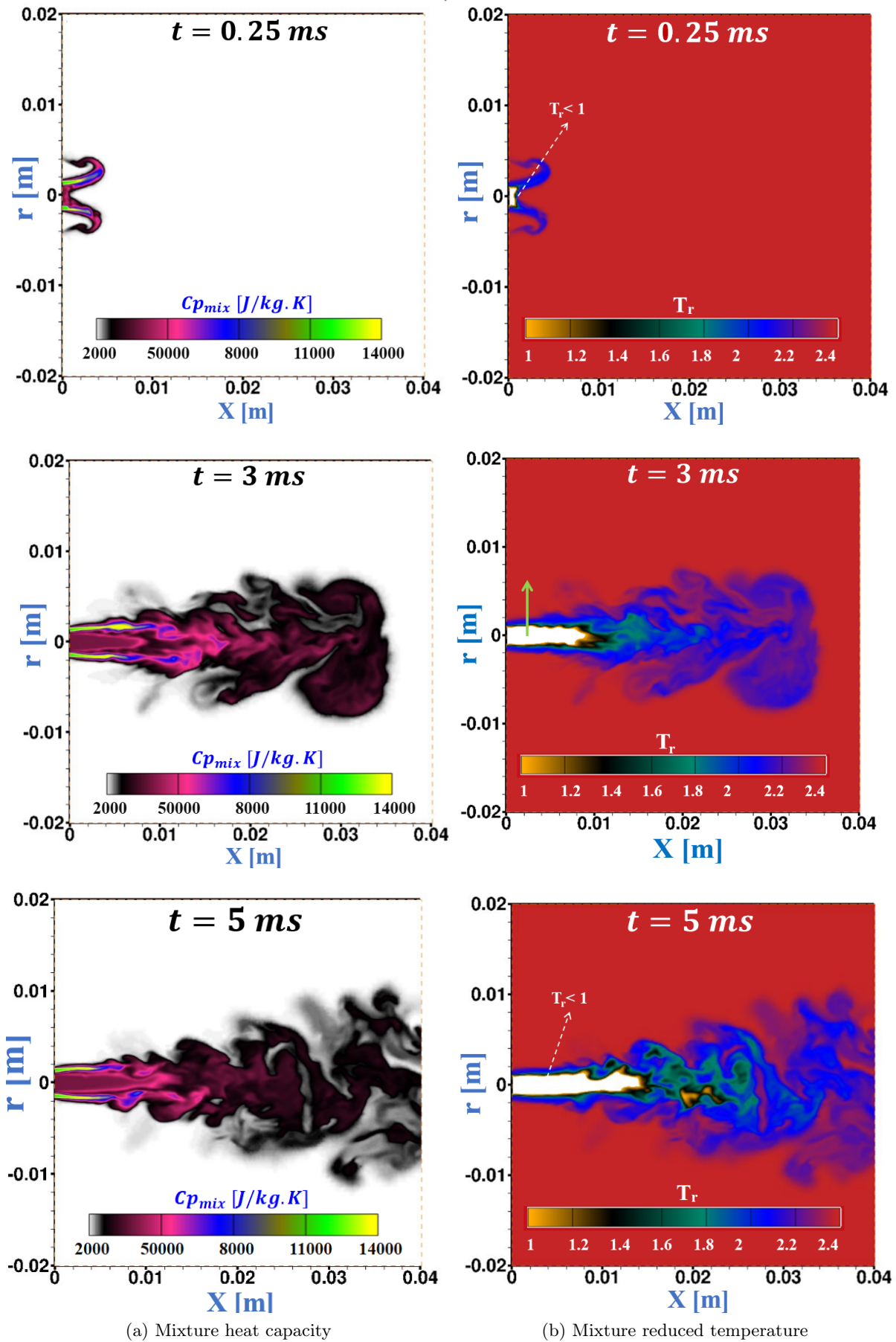


Figure 5.14: Distribution of mixture heat capacity (Left), and reduced temperature.  $T_r = T/T_{c,mix}$  (Right) where  $T_{c,mix}$  is the mixture critical temperature. The subcritical region for the mixture where  $T_r < 1$  is colored by white colour.

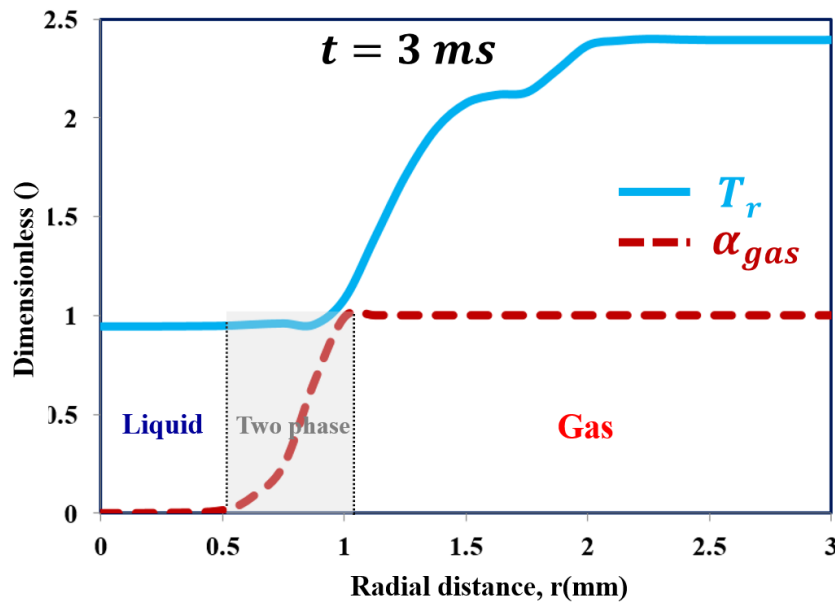


Figure 5.15: Radial reduced temperature and gas volume fraction profiles at  $X=3$  mm after  $t=3$  ms. The radial axis is displayed in Figure 5.14(b).

Moreover, Figure 5.16(c-left) shows the sound speed distribution.

A well-known decrease of the mixture sound speed in the two-phase layer (in blue) is predicted by the current numerical results. As a matter of fact, the Wood formula is used in the two-phase region as a mixture rule. The behavior of the Wood sound speed is therefore depicted in Figures 5.16(c-right). One may also note that for supercritical temperatures ( $T=270\text{K}-290\text{K}$ ), the mixture sound speed variations as a function of  $H_2$  composition are monotone, compare to the non-monotone variations of subcritical temperatures ( $T=118\text{K}-126\text{K}$ ).

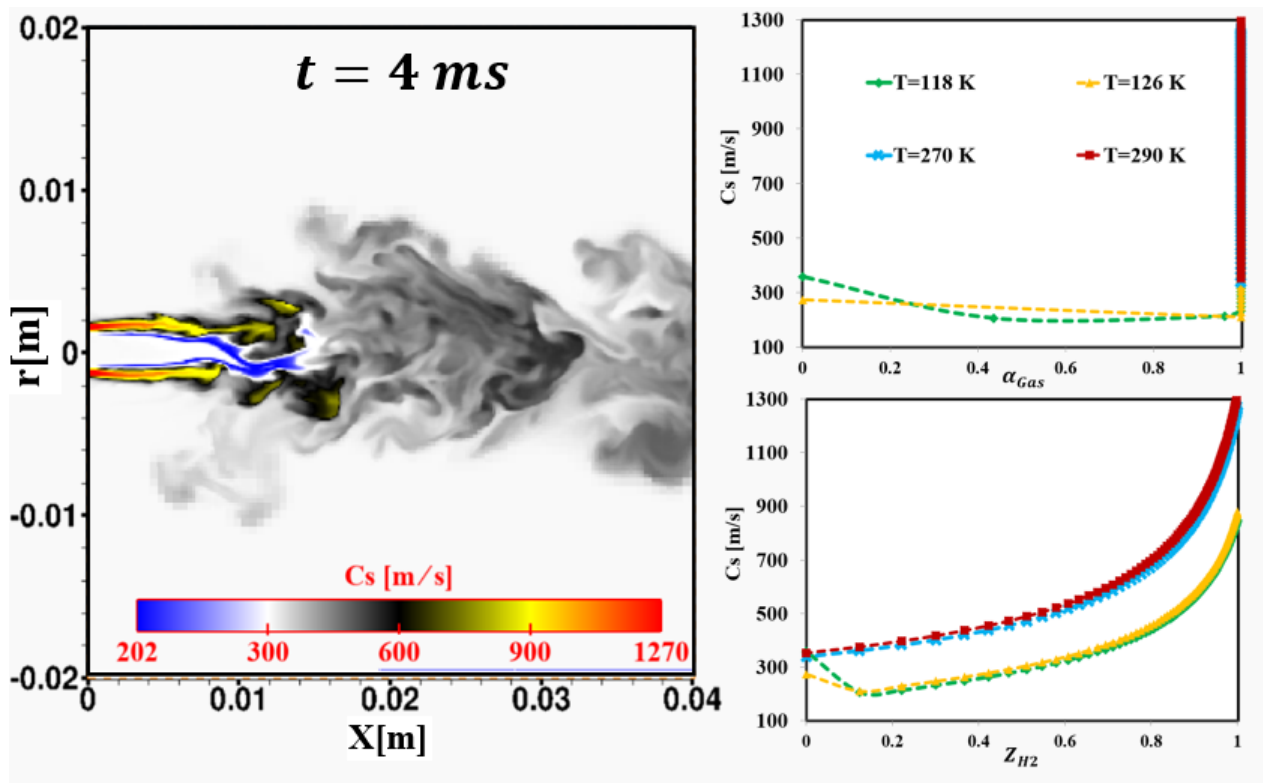
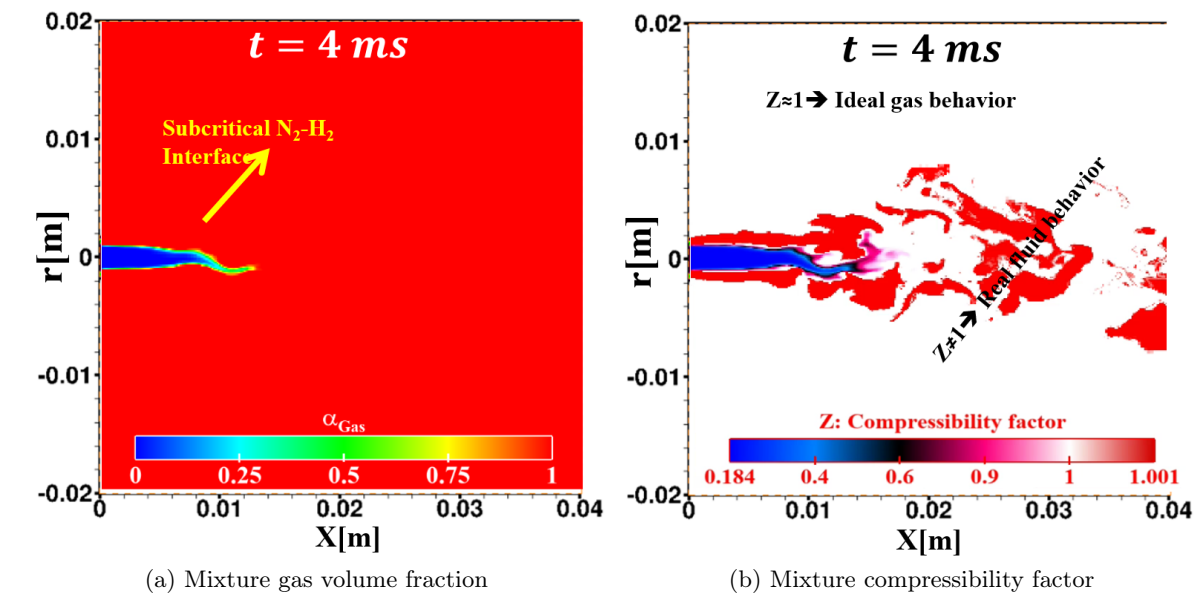


Figure 5.16: Different properties contours plotted at  $t=4$  ms as (a) Mixture gas volume fraction, (b) Mixture compressibility factor, and (c) Mixture sound speed.

### Experimental validation

To validate the LES simulations, a comparison between the experimental data [29] and the numerical study of Matheis et al. [28] as well as the current study is shown in Figure 5.17. The  $N_2$  radial and axial partial density profiles extracted at 4 mm from the nozzle exit and the center line, respectively are depicted in Figures 5.17(a, b), using PR and SRK EoS. With PR-EoS, very similar radial profiles are obtained when compared to Matheis et al. [28]. Both studies have overestimated the maximum  $LN_2$  density value of around 608 kg/m<sup>3</sup>, compared to the experimental value of 390 kg/m<sup>3</sup> [29]. However, the current results using SRK-EoS show a smaller deviation from the experiments with a maximum of  $LN_2$  density value around 530 kg/m<sup>3</sup>. This better prediction of SRK compared to the PR for cryogenic fuels has also been reported by other researchers in recent years [34, 67]. Figure 5.17(c, d) also compare the radial and axial partial density profile of  $H_2$  with the experiments. Figure 5.17(c) displays the maximal values of the radial  $H_2$  density distribution.

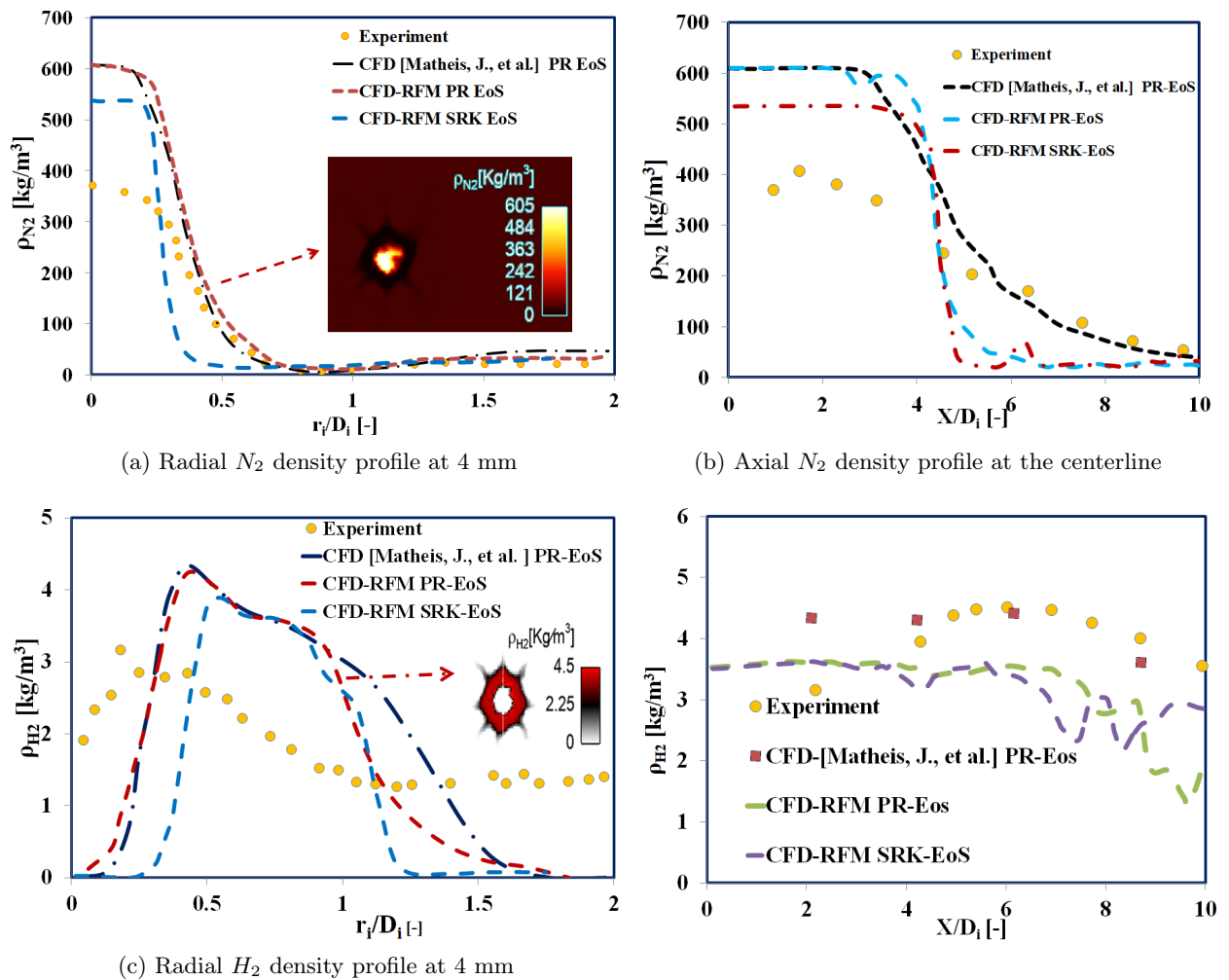


Figure 5.17: Axial and radial density profiles compared to the experimental [29] and the LES study Matheis et al. [28].  $D_i = 1.9mm$

This Figure shows similar profiles as in [28] and the same trends as experiments [29]. Also, Figure 5.17(d) shows a qualitatively good agreement between the two different EoS and the experimental results. Matheis et al. [28] explained that due to the conformity of EoS with the NIST [66], as shown in Figure 2.3, the deviation with the experiments cannot be attributed only to the inaccuracy of the EoS, and it may be the result of uncertainties in the experimental measurements. Indeed, due to the  $H_2$  partial density high value ( 2-4 kg/m<sup>3</sup>) close to the injector in Figure 5.17(d), the injection conditions seem to be at the origin of these large deviations with the experiments.

The last point but not the least is related to the pressure oscillations in the flow field, employing the presented RFM model. As demonstrated in the Figure 5.18, low oscillations in the pressure field is obtained due to the strong coupling between the flow solver and the thermodynamic closure in the modified PISO or SIMPLE algorithm proposed in this article. In addition, a time step about ( $10^{-8}s$ ) corresponding to a maximum CFL number of 50 have been used in these simulations. As a result, the presented studies in this section can confirm the computational efficiency, robustness, and accuracy of this tabulated real fluid modelling approach.

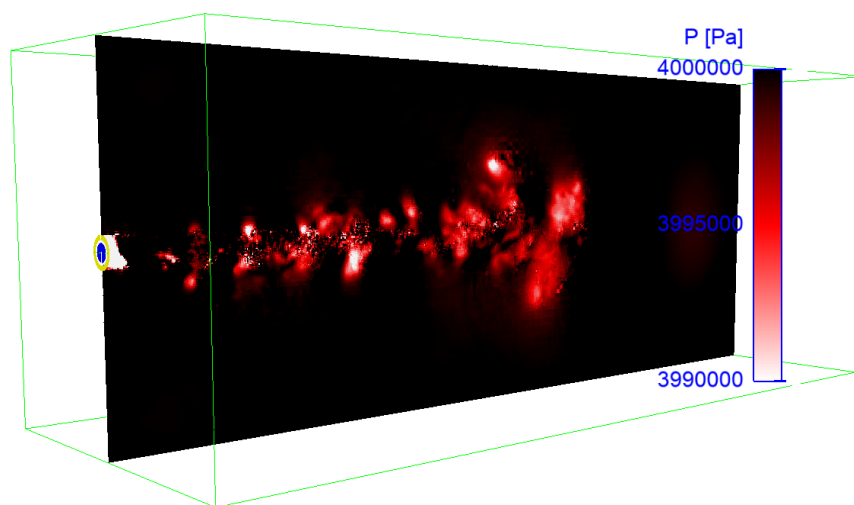


Figure 5.18: Pressure oscillations of the flow field in the chamber at the central cut section. The initial ambient pressure in the chamber is  $P=4$  MPa.

### 5.1.4 Conclusion

In this section, the presented modeling approach has been applied to the simulation of a series of academic tests as 1-D, 2-D, and 3-D test cases, using different equation of states, namely PR and SRK, to primarily demonstrate the computational efficiency, accuracy, and robustness of the proposed RFM model. Then, it has been applied to better understand the structure of subcritical and transcritical liquid-gas interfaces and related hydro-thermodynamic features of a cryogenic transcritical single-component jet as well as a binary mixing jet. The main objective was to better understanding the structure of subcritical and transcritical liquid-gas interfaces in order to quantify the effects of real fluid thermodynamics on liquid fuels injection process for multi-component systems. Several conclusions are drawn from these studies:

1. The 1-D studies, cases (1-4), for transcritical shock tube test cases confirm that the modified SIMPLE and PISO algorithms for RFM model are in a good agreement compared to the available data in the literature.
2. The LES studies of cryogenic single-component case, cases (5-7), (liquid-like nitrogen injected into gas nitrogen) has demonstrated its transcritical interface feature by exhibiting the well known thermal shield, as a layer of large isobaric heat capacity separating the liquid-like and the gas-like regions..
3. The LES study of classical cryogenic injection of liquid nitrogen injected coaxially with warm hydrogen jet, case 8, shows some interesting thermodynamic phenomena such as the condensation of  $H_2$  as well as cooling effects in the two-phase layer around the liquid core, which demonstrate the subcritical nature of the interface.
4. Another interesting observed phenomenon for case 8 is related to the mixing of  $N_2$  and  $H_2$  which leads to locally increased mixture critical points. Therefore, due to the mixing process around the liquid core interface, some flow zones may move from supercritical mixing regime to the subcritical phase change regime inducing condensation and evaporation.
5. The numerical results have been finally compared with available experimental data [29] and published numerical studies [28], with satisfactory agreement. Moreover, it has confirmed the importance of using a powerful real fluid EoS. The current investigations have illustrated that the SRK EoS has a better prediction of the fluid density compared to the PR EoS, corroborating the results reported by [28].

6. Finally, compared to our previous studies [17, 22, 27], the computational efficiency, accuracy, and robustness of this proposed tabulated RFM model as a remedy to the direct evaluation of costly phase equilibrium solver have been confirmed.

## 5.2 Exploring the interaction between phase separation and turbulent fluid dynamics in multi-species supercritical flow jets

This study focuses on the analysis of the coupling between the hydrodynamics and thermodynamics of multi-species supercritical jets. Various phase transition phenomena, such as droplet formation process by condensation, which have been shown experimentally to significantly affect the flow and mixing dynamics of the jet, are studied. For this purpose, a tabulated multi-component real fluid model is proposed for the numerical simulation of a supercritical jet of n-hexane injected into nitrogen gas. Numerical results are compared with available experimental data but also with published numerical studies, showing a good agreement. In addition, comparisons between different turbulence models, including the LES Sigma, Smagorinsky and RANS  $K - \epsilon$  models have been performed, showing the relevance of the LES Sigma model for these very complex two-phase flows.

### 5.2.1 Introduction

As explained, two-phase flows covering LL and GL conditions are known in the literature as the transcritical regime [18, 20, 24, 25, 35, 36, 108, 109]. At subcritical conditions, the phase transition phenomena are either classified as evaporation or condensation. Generally, it has been accepted that the subcritical liquid-to-gas transition is characterized by a structural change from an ordered (liquid) to a disordered (gas) state. In this case, density can be chosen as the appropriate order parameter, which exhibits a sharp discontinuity when phase transition occurs [111–113]. Besides, pseudo phase transition (i.e. pseudo-boiling or pseudo-condensation) may occur in the supercritical state at the crossover between LL and GL fluids, where the density changes sharply but continuously. The locus where this sharp transition from LL and GL fluids is currently not well understood. The Widom line [20, 108, 111, 112], defined as the heat capacity maximum, is usually used to separate the LL and GL supercritical fluids. However, the Widom line cannot be clearly defined at high pressure and high temperature (see Figure 5.19(b)), where the minima of the thermal diffusivity coefficients are found to be more appropriate by Gorelli et al. [113] for tracking the transition between the supercritical LL and GL fluids. In the pseudo-boiling transition, no structural change has been observed in macroscopic light scattering experiments [25, 39]. As such, these phenomena share a nonlinear behavior similar to that of the subcritical condition when the coexistence line is crossed, as illustrated in Figure 5.19.

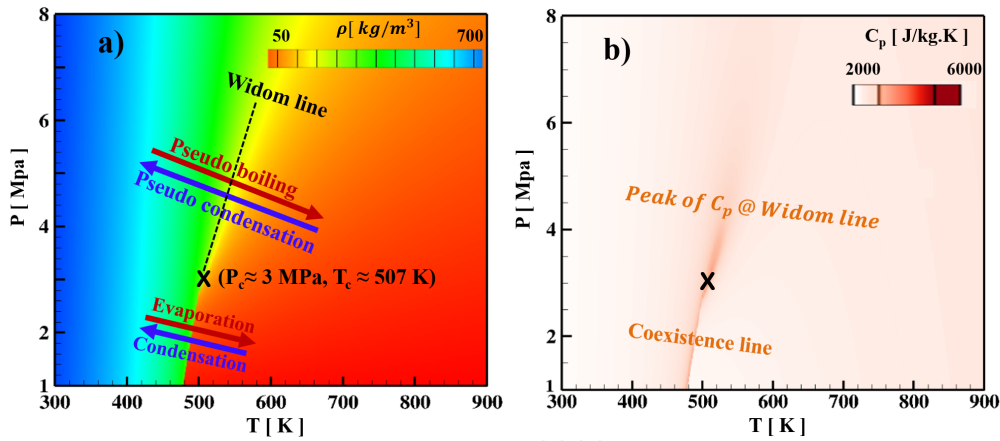


Figure 5.19: Illustration of the phase transition in subcritical states (i.e., evaporation and condensation processes) when the coexistence line is crossed, and gradual phase change processes in the transcritical regime (i.e., pseudo-boiling and pseudo-condensation) when crossing the Widom line. Pressure-Temperature diagram: (a) Density contour mapped by coexistence and Widom lines, and (b) Heat capacity contour for  $C_6H_{14}$ . Nonlinear behavior is present along the Widom line but also along the liquid-vapor coexistence line.

For pure n-Hexane ( $C_6H_{14}$ ), this figure shows the phase transition in subcritical states (i.e., evaporation and condensation processes) when the coexistence line is crossed. Also, the gradual phase-change processes in the transcritical regime (i.e., pseudo-boiling and pseudo-condensation) as soon as it meets the Widom line. This illustrates that phase transition, including bubble or droplet formation process, evaporation, and condensation, are mainly driven by changes in pressure or temperature for a single-component fluid. As a matter of fact, researcher's interest in the behavior of supercritical fluids dates back to at least 1869 [33]. However, despite recent theoretical, experimental, and computational efforts, these phenomena are still not fully understood especially for multicomponent systems. In the past decades, extensive studies have been performed for understanding the behavior of a single-component phase transition [16, 19, 20, 22, 23, 35, 108, 113, 114]. One of the pioneering and remarkable studies was conducted by Chehroudi et al. [23]. They experimentally studied the jet behavior of pure liquid nitrogen injected into gaseous nitrogen at subcritical and supercritical pressures. They observed that in subcritical pressures, due to the significant surface tension, the interface between the liquid and the gas plays an important role, and it leads to the appearance of the primary and secondary breakup, known as classical atomization. However, as the pressure increases, the magnitude of the surface tension decreases and vanishes at the critical point, which suppresses the formation of ligaments and droplets for supercritical pressures. However, liquid-like ligaments (also called finger-like) could be seen in their shadowgraphy experimental results despite the absence of surface tension, especially for the transcritical injection regime. Therefore, injection above the critical pressure of a single-component propellant can be considered as a diffuse inter-

face mixing process rather than a classical atomization of the interface. However, the same is not valid for multicomponent systems for which the local critical pressure of the mixture could dramatically exceed the value of the pure components. Indeed, various studies have been carried out for multicomponent systems, and their interfacial phase transition has been revealed to be more complex than for a single-component system, mainly due to the variation of the mixture critical point with the local composition of the fluid [21, 22, 30, 102, 108, 115–117]. Furthermore, this difference in phase transition mechanisms between single and multicomponent systems leads to various interface structures that influence the jet behavior [18, 30, 108, 116]. Crua et al. [18] studied the injection of liquid (n-heptane, n-dodecane, n-hexadecane) into supercritical nitrogen at different temperatures and pressures. They investigated the transition from a two-phase to a single-phase mixing regime and established a criterion for switching between the two regimes as a function of the critical temperature and pressure of the pure fuels. However, due to the limited accuracy of the experimental setup, reliable data are still lacking for the precise identification of the transition between the two-phase and single-phase mixing regime that could be used for validating numerical models. In addition, there are still multiple doubts and questions about the conditions and mechanisms behind the interface disappearance for multicomponent systems.

Other interesting experimental studies have recently done by Gerber et al. [25, 39]. These studies focused in particular, on under-relaxed jets for which a shock waves train was observed in the near nozzle region. They concluded that high-pressure jets have the same scattering footprint and morphological properties as low-pressure jets. However, enhanced scattering is only observed upon multiple crossings of the Widom region, e.g., due to the series of rapid recompressions caused by the shock train. This enhanced scattering is caused by the enhancement in compressibility and density fluctuation when the fluid switches between LL and GL. Therefore, the experimental findings of Gerber et al. [25, 39] show that density fluctuations are not negligible across the Widom line. They can be detected both at the macroscopic (continuum) and molecular scale. Indeed, these findings were confirmed at molecular scales by the small-angle X-ray scattering experiments in [40]. This completely changes the physical meaning of pseudo-boiling/pseudo-condensation transition from the subcritical counterpart (evaporation/condensation).

Another interesting study was recently carried out by Traxinger et al. [30]. They experimentally and numerically studied a multicomponent system consisting of a high-pressure n-hexane jet at three different temperatures (480K, 560K, 600K), injected into a chamber filled with supercritical nitrogen at ( $P = 5MPa$  and  $T = 293K$ ). Specifically, the focus was on the phase separation of an initially supercritical fluid due to the interaction with its surrounding. Simultaneous shad-

ography and elastic light scattering (ELS) experiments were conducted by Traxinger et al [30] to capture both the flow structure as well as the phase separation. Remarkable results have been shown experimentally for the case of supercritical n-hexane with  $T=560$  K, exceeding its critical temperature and pressure, injected into supercritical nitrogen at  $T = 293K$  and  $P = 5MPa$ . Indeed, the condensation of n-hexane has been observed in these conditions, as expected from their priory thermodynamic study. The phase transition is initiated in the mixing layer some distance downstream of the nozzle and eventually mixes with the jet core at large distances. In addition, at a higher injection temperature of n-hexane ( $T = 600K$ ), this phenomenon of phase transition does not occur, and the gaseous fuel injected into the chamber gradually mixes with the ambient gas. Finally, a classical subcritical atomizing n-hexane jet was imaged at the lowest n-hexane injection temperature ( $T = 480K$ ). The various experimental and numerical results of Traxinger et al. [30] will be used in the present work to validate our Computational Fluid Dynamics (CFD) tabulated Real-Fluid Model (RFM).

This section is organized as follows. Section 5.2.2 is dedicated to the validation of properties and VLE solver. Section 5.2.3 is devoted to understanding the condensation phenomenon during the supercritical injection of hexane into nitrogen using a real fluid modeling approach. In addition, comparisons between various turbulence models, including large-eddy simulations (LES Sigma [118] and Smagorinsky [119]) models as well as a Reynolds Averaged Navier-Stokes (RANS  $K-\epsilon$ ) [120] model have been carried out for such two-phase flows. Then, numerical results are compared to available experimental data but also published numerical studies in subsection 5.2.4, and 5.2.5. Finally, the conclusions are presented in section 5.2.6.

### 5.2.2 Equilibrium thermodynamic closure of the flow solver, and the tabulation look-up

For the supercritical jet with  $(C_6H_{14}, N_2)$  binary mixture, the real-fluid Peng-Robinson (PR) [64] equation of state (EOS) has been selected for the thermodynamic closure of the RFM model transport equations (3.1 - 3.4). Also, in this study,  $k_{ij}$  is set to zero, see equation 3.8. ( $k_{ij}$ ) is the binary interaction parameter (BIP) that can be fitted to experimental data to well represent the phase diagram of a binary system.

Figure 5.20 shows the comparison and an excellent agreement of the thermodynamic properties calculated in this study using the PR EoS [64], with the reference data taken from NIST [66], for pure n-hexane at  $P = 5MPa$  for the density and specific heat capacity.

As explained in the introduction, the state properties significantly deviate from those of the

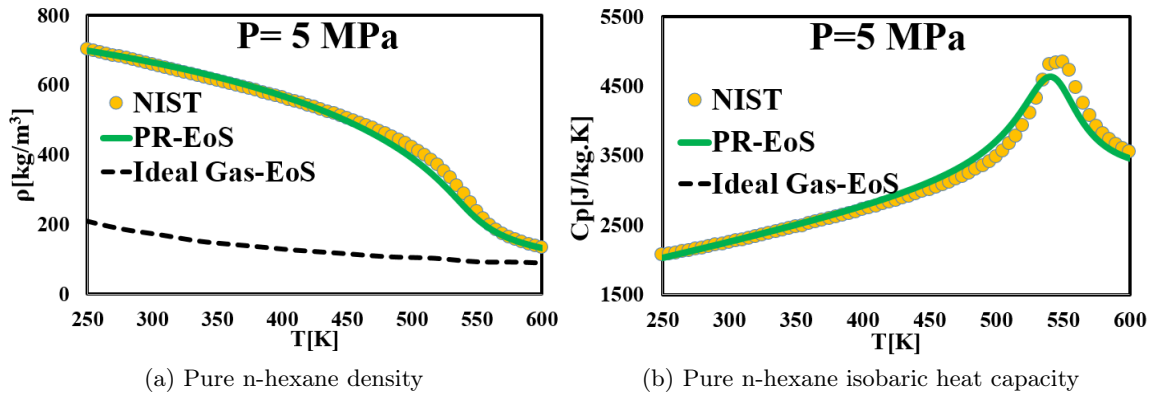


Figure 5.20: Comparison of PR-EoS and ideal gas EoS with reference data obtained from NIST [66] for n-hexane at  $P = 5 \text{ MPa}$  showing a) Density, and b) Isobaric heat capacity profiles. The results, using PR-EoS, Peng Robinson equation of state, are in a good agreement with NIST data [66], however the fluid properties specially for isobaric heat capacity (outside the range) significantly differ from an ideal gas at this high pressure  $P = 5 \text{ MPa}$ .

ideal gas as they introduce some thermodynamics' non-idealities and transports anomalies at supercritical pressures due to intermolecular forces, as shown in Figure 5.20. Indeed, as it can be seen in Figure 5.20, compared to the density and isobaric heat capacity from NIST [66] for n-hexane at  $P = 5 \text{ MPa}$ , ideal gas EoS cannot predict the transcritical behavior of such properties. However, more accurate and complex EoS, as PR EoS, can predict the transcritical behavior with a good agreement, especially for the isobaric heat capacity. Generally, it is well known that cubic EoSs with van der Waals (vdW) mixing rule are not really well suited for computing densities [22, 108]. However, our achievement in this study demonstrate that the PR EoS [64] can acceptably predict the density and specific heat capacity for n-hexane (a relatively light component) at  $P = 5 \text{ MPa}$ , which are in an excellent agreement with the reference data taken from NIST [66], as shown in Figure 5.20. To validate the VLE thermodynamic solver, the

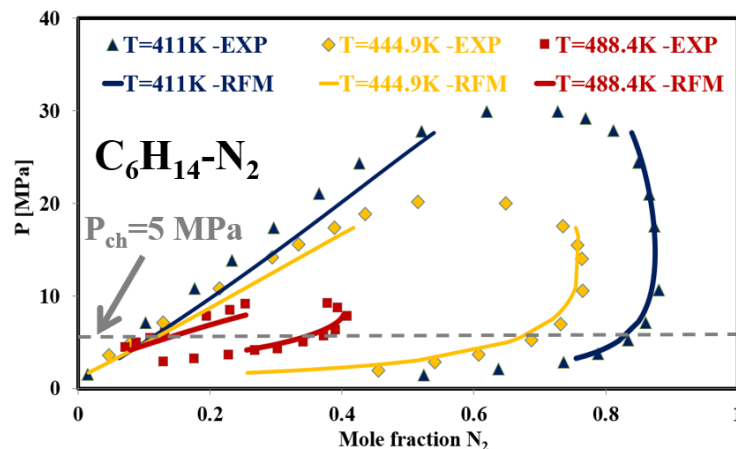


Figure 5.21: Vapor-Liquid equilibrium of  $\text{C}_6\text{H}_{14} - \text{N}_2$  calculated in this study using PR-EoS compared to the experimental data [110]

VLE for a binary mixture of  $C_6H_{14} - N_2$  using PR-EoS has been compared with the available experimental data [110], as shown in Figure 5.21. It can be seen that the calculation results of the VLE solver are in good agreement with the experimental data over the entire ranges of pressure for the different temperatures. Furthermore, Figure 5.22(a,b) shows the variation of the mixture density and heat capacity, respectively, for a binary mixture of  $C_6H_{14} - N_2$  as a function of temperature and  $N_2$  mole fraction at  $P=5$  MPa. These results have been obtained using a uniform table with  $\Delta T = 1K$ ,  $\Delta Y_{N_2} = 0.005$  in grid sizes on the axis. Due to the different nonlinearity of the properties shown in Figure 5.22(a,b), a grid independence for the thermodynamic table is mandatory, which should correctly capture various interesting phenomena such as the heat capacity peak ( $C_{p,mix}$ ) around the Widom line for certain compositions of this multi-species system, see Figure 5.22(b).

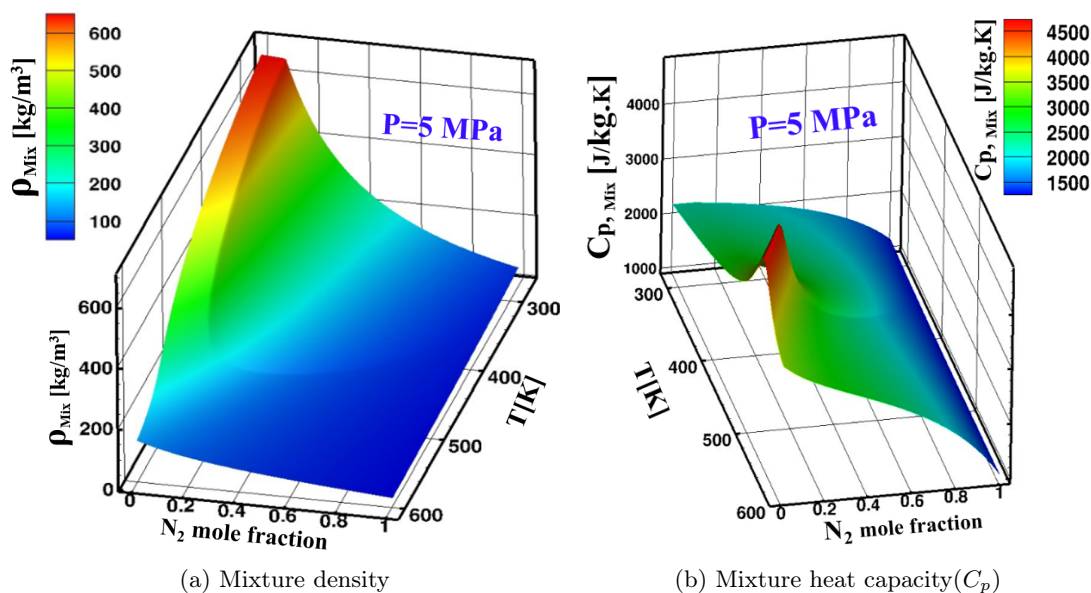


Figure 5.22: Contour plots of mixture density(a), and mixture heat capacity(b) for  $C_6H_{14} - N_2$  at  $P_{ch} = 5MPa$ . As the plots show, due to the different non-linearity for various properties, the grid independency for having a refined thermodynamic table is mandatory.

### 5.2.3 Analytical study of condensing supercritical jet

As reported in the Introduction, condensation of the n-hexane has been recently shown experimentally by Traxinger et al. [30] when it is injected in supercritical state at  $560K$  into a cold gaseous nitrogen at  $T = 293K$  and  $P = 5MPa$ . They observed that condensation is initiated in the mixing layer and eventually mixes in the core of the jet forming a spray of droplets at great distance from the nozzle. In such conditions, the mixture temperature distribution in the chamber is usually varying in the range between  $T_{inj} = 560K$  and  $T_{ch} = 293K$ .

Indeed, assuming an adiabatic process neglecting heat exchange, the enthalpy of the mixture at equilibrium  $H_{mix}$  is equal to the weighted molar average of the enthalpy of the pure components,  $H_{N_2}$  and  $H_{C_6H_{14}}$  :

$$H_{mix}(T_{AM}, P_{ch}, z_{N_2}) = z_{N_2}H_{N_2}(T_{ch}, P_{ch}) + z_{C_6H_{14}}H_{C_6H_{14}}(T_{inj}, P_{ch}).$$

The adiabatic mixture temperature, denoted ( $T_{AM}$ ) is the solution of this equation, as the enthalpy values are calculated using PR-EoS using our in-house thermodynamic library.  $z_{N_2}$  is the mole fraction of  $N_2$  (with  $z_{N_2} + z_{C_6H_{14}} = 1$ ).  $T_{inj}$ ,  $T_{ch}$ ,  $P_{ch}$  denote the temperature of the injected n-hexane at the exit of nozzle, the initial temperature of  $N_2$  in the chamber, and the initial chamber pressure (here constant and equal to  $5MPa$ ), respectively. More details on AMT can be found in [121]. Figure 5.23(a,b) displays the AMT temperatures (dashed lines) for two different chamber pressures at  $P = 1MPa$  and  $P = 5MPa$  in a  $T-x_{N_2}$  phase diagram (triangle) obtained using PR-EoS. As shown in Figure 5.23(a), the AMT, dash lines, are plotted with the same inflow temperature,  $T_{inj} = 554.8K$  and chamber temperature,  $T_{ch} = 293K$ . For the low pressure case,  $P = 1MPa$ , the AMT does not cross the corresponding two-phase boundary, and hence the jet is supposed to stay in the single-phase mixing regime. However, for the higher pressure case,  $P = 5MPa$ , the AMT crosses the corresponding two-phase boundary very close to the  $N_2$  mole fraction of one and it is therefore expected that the jet enters the two-phase region near the periphery of the jet as shown experimentally in Traxinger et al. [30].

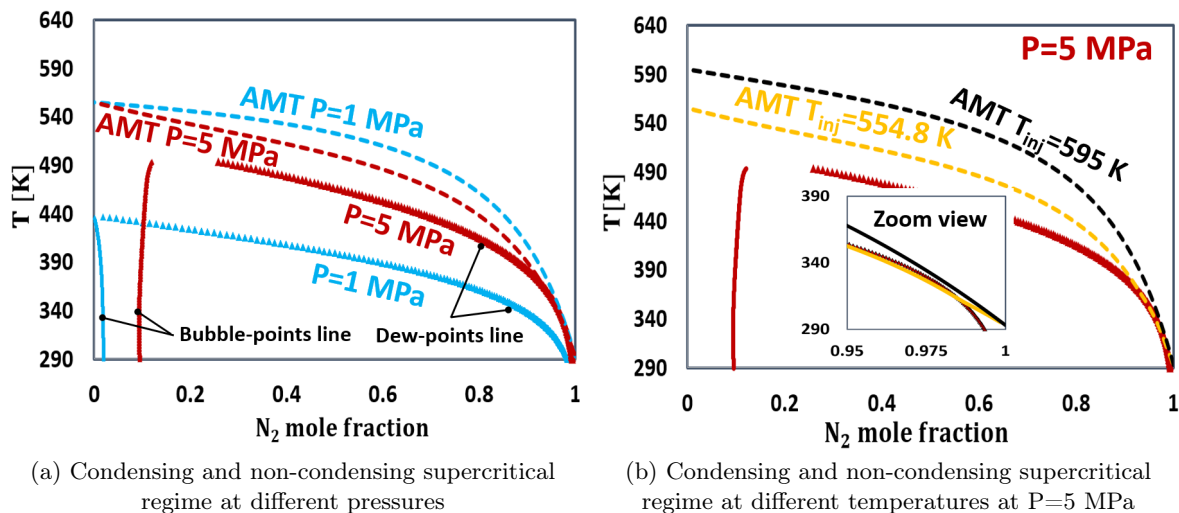


Figure 5.23: Condensing and non-condensing supercritical regime (a) at different pressures, (b) at different temperatures. AMT denotes adiabatic mixing temperature, plotted by dash lines, and by crossing the phase boundary(dew points line), the droplet nucleation, and the condensation begins and develops at the periphery of the jet. If the AMT doesn't cross the two-phase dome, it will remain at supercritical regime without any nucleation process, non-condensing supercritical regime (pure supercritical regime).

In addition, it can be seen in Figure 5.23(a) that the slope ( $dT/dx$ ) of the phase diagram (near  $x_{N_2} = 1$ ) can control the phase separation process (condensation) and the formation process of spray droplets for certain temperature and pressure ranges of the supercritical injection regime. Besides, Figure 5.23(b) shows and confirms the same behavior for a constant pressure,  $P = 5MPa$  but at two different n-hexane inflow temperatures,  $T_{inj} = 554.8K$ , and  $T_{inj} = 595K$ . Indeed, this figure shows that by increasing the inflow temperature to  $595K$ , the AMT no longer crosses the phase boundary. Therefore, this theoretical analysis has demonstrated that due to the slope ( $dT/dx$ ) near  $x_{N_2} = 1$  in the phase diagram, the periphery of a supercritical jet may or may not nucleate and condense. This proves that jet structure in a multicomponent system does not follow the same behavior as in a single-component jet. In summary, for supercritical jet of  $C_6H_{14}$  injected into  $N_2$  colder ambient, droplet formation process by condensation are expected to be triggered at the jet's periphery when the AMT crosses the two-phase region. Otherwise, the periphery of the supercritical jet is going to mix with the ambient gas remaining in the supercritical regime without any droplet formation process. This supercritical droplet formation process/condensation phenomenon, which has been the subject of some recent studies [30, 116], will be investigated in more detail in the next section based on the tabulated RFM model applied in the LES numerical framework.

## 5.2.4 Results and discussion

### 5.2.4.1 Test cases definition

This section is devoted to the numerical study of the turbulent jet mixing process of n-hexane ( $C_6H_{14}$ ) injected into supercritical nitrogen ( $N_2$ ). More precisely, following the investigations of Traxinger et al. [30], n-hexane is injected at three temperatures ( $480K$ ,  $560K$ ,  $600K$ ) into a chamber initially filled with  $GN_2$  at an ambient pressure of  $P_{ch} = 5MPa$ . The critical pressure and temperature of pure  $C_6H_{14}$  and  $N_2$  are ( $P_c \approx 3MPa$ ,  $T_c \approx 507K$ ) and ( $P_c \approx 3.4MPa$ ,  $T_c \approx 126.2K$ ), respectively. Hence, the ambient pressure,  $5MPa$  correspond to a reduced pressure  $P_{r,C_6H_{14}} \approx 1.67$  for pure n-hexane, and  $P_{r,N_2} \approx 1.47$  for pure  $N_2$ . However, due to the mixing of two components, the mixture critical point will vary locally as function of the mixture composition. Therefore, with respect to the mixture critical temperature of  $C_6H_{14} - N_2$  at  $P_{ch} = 5MPa$ , n-hexane is injected in subcritical state when it is at  $480K$  and it is injected in a supercritical state when it is heated to  $560K$  or  $600K$ . The three simulation cases are summarized in Table 5.3, where  $T_{t,C_6H_{14}}$  is the temperature in the injector reservoir.

Table 5.3: Operating conditions used for the current numerical study similar to the experimental study of [30].

<i>Case</i>	$P_{ch}$ [MPa]	$T_{ch}$ [K]	$T_{t,C_6H_{14}}$ [K]	$T_{C_6H_{14}}$ [K]	$u_{C_6H_{14}}$ [m/s]	Injection state
T480	5	293	480	479.3	51	subcritical
T560	5	293	560	554.8	72.1	supercritical (condensing)
T600	5	293	600	595	90.3	supercritical

The temperature  $T_{C_6H_{14}}$  as well as the mean velocity at the nozzle exit  $u_{C_6H_{14}}$  were calculated based on the assumption of an isentropic nozzle flow as explained by Traxinger et al. [30].

### 5.2.4.2 Configuration setup

Figure 5.24(a,b) present the boundary conditions, the computational domain, as well as the mesh structure, respectively, employed in this study. The nozzle orifice diameter ( $D_i$ ) is  $236\mu m$ , as can be seen in this figure on the left side of the hexahedral computational domain. The length and width of the grid are  $90D_i$  and  $40D_i$ , respectively. These dimensions proved to be large enough to avoid edge effects on the numerical results. The base grid size was set to  $30\mu m$ . Besides, fixed embedding has been used to refine the grid at specific locations especially near the nozzle exit, where the grid size was specified to be  $7.5\mu m$ . This minimum value is the same refined value used in [30]. At the jet inlet, uniform velocity and temperature profiles for  $u_{C_6H_{14}}$  and  $T_{C_6H_{14}}$  are used, as defined in Table 5.3. In addition, no-turbulent fluctuations are specified at the inlet injection boundary. A pressure outflow boundary condition is used for the outlet boundary. The chamber pressure for all the cases were set to  $P_{ch} = 5MPa$ . No-slip and adiabatic conditions are specified for the walls indicated in Figure 5.24(a).

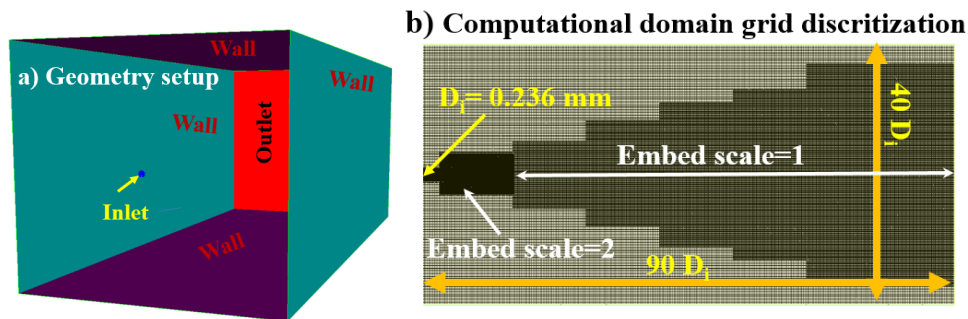


Figure 5.24: Schematic of the injector setup as (a) Geometry setup, and (b) Computational domain grid discretization. Fixed embedding has been used to refine the grid at specific locations in the domain. (Local grid size = (Base grid size) /  $2^{embed_{scale}}$ ). The base grid size was set to  $30\mu m$  so that the minimum grid size near the nozzle exit has been specified to be  $7.5\mu m$  using an  $embed_{scale} = 2$ .

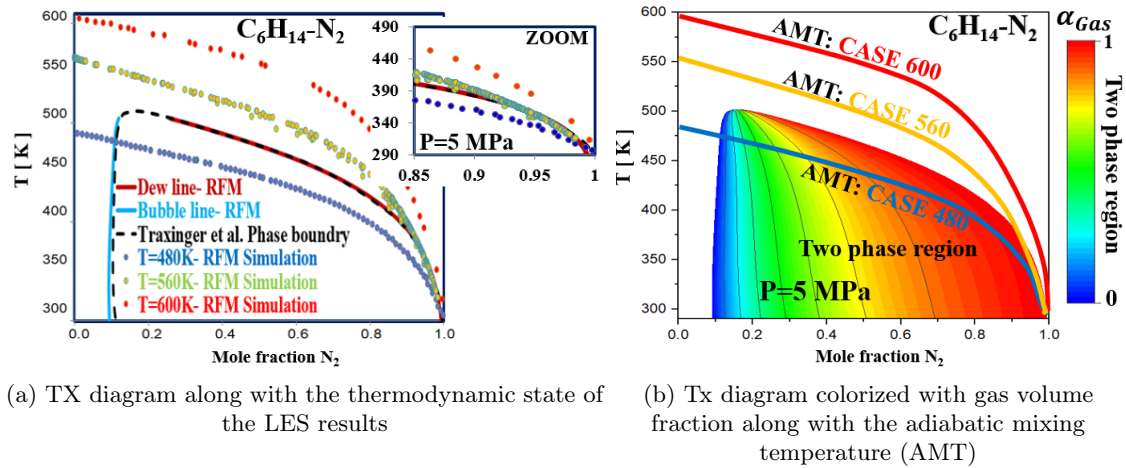
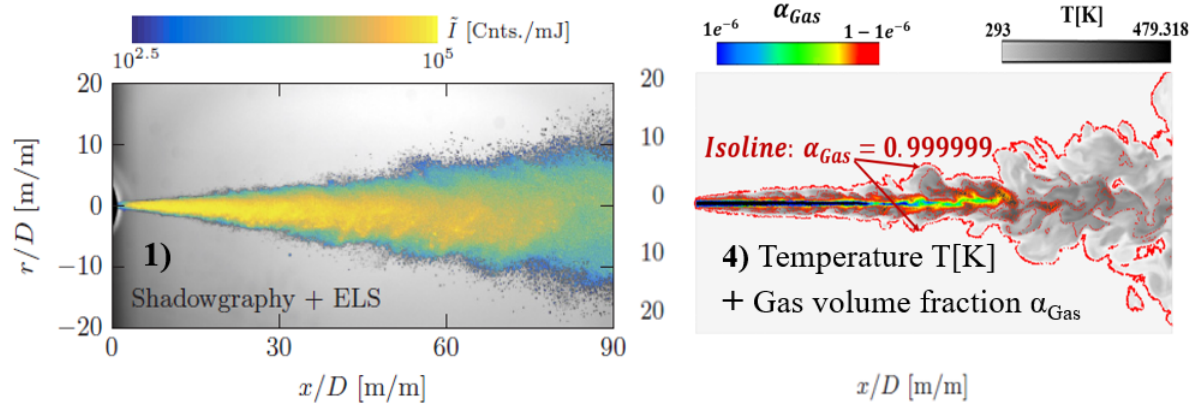


Figure 5.25: Temperature  $N_2$ -composition phase diagram for binary mixture of  $C_6H_{14} - N_2$  at  $P = 5$  MPa, calculated by PR-EoS along with the adiabatic mixing temperature (AMT). (a) includes the comparison with [30] along with the three scatter plots of the numerical LES mixing temperature results. The low scattering of the LES mixing temperatures indicate almost adiabatic injection flows. The graphical insert shows that the LES mixing temperature scatterplots for the T560 case do intersect the dew line and enter the two-phase region. (b) includes the theoretical AMT for the three cases and show the same behavior as the RFM model for case T560. The two-phase region background is colored by the gas volume fraction values.

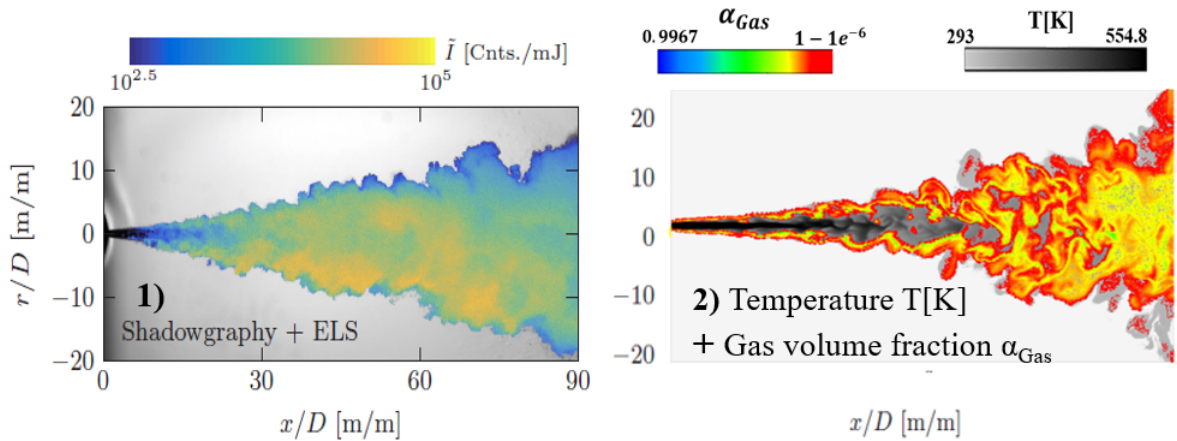
The time step is automatically adjusted in the solver based on a maximum Courant-Friedrichs-Lewy (CFL) number of 50 reaching a value in the range of  $[10^{-8} - 10^{-9}]$  seconds.

### 5.2.4.3 RFM model results

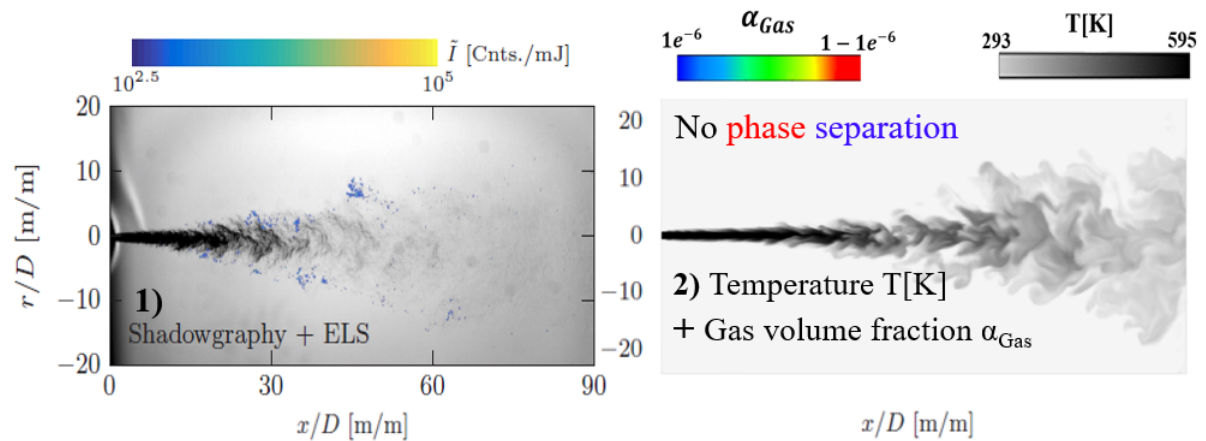
Figure 5.25(a,b), respectively, shows the numerical results of the RFM model, obtained when the LES-Sigma turbulence model [118] is employed, in terms of mixing temperatures versus AMT for the three different test cases (T480, T560, and T600) defined in Table 5.3. Specifically, Figure 5.25(a) demonstrates a good agreement between the predicted phase boundary calculated in this study compared with [30]. The low scattering of the LES mixing temperatures in Figure 5.25(a) indicates almost adiabatic mixing injection (between n-hexane and  $N_2$ ). The graphical insert shows that the LES mixing temperature scatter plots for the T560 case do intersect the dew line, enter the two-phase region and may induce condensation. Figure 5.25(b) includes the theoretical AMT (defined in Section 3.5) for the three cases and show the same behavior as the RFM model for case T560. In Figure 5.26(a-c), the experimental single-shot images of [30] (left frame 1) are qualitatively compared with instantaneous numerical snapshots (right frame 2) for the three cases (T480, T560, and T600) obtained using the RFM model, when the LES-Sigma turbulence model [118] is employed.



(a) Case T480



(b) Case T560



(c) Case T600

Figure 5.26: Comparison of experimental (left(1)) and numerical snapshots (right(2)) for the three test cases (T480, T560, and T600). The ELS image superimposed onto the corresponding shadowgraph are used to visualize both the flow structure as well as the thermodynamic state (adapted from [30]) in quasi-steady state condition.  $\alpha_{Gas}$  is the gas volume fraction

For the experiments, the elastic light scattering (ELS) images superimposed onto shadowgraph images, to visualize both the flow structure and the thermodynamic state. Similarly for the numerical side, the gas volume fraction  $\alpha_{Gas}$  distribution is superimposed onto the temperature contours in a plane passing through the axis of the nozzle to indicate regions of two-phase flow and especially the lowest values of  $\alpha_{Gas}$  near the periphery of the jet. These numerical results were taken at a point in time so that the jet could be considered as quasi-steady.

In doing so, a direct comparison of the two-phase droplet regions in the experiment and LES is rendered in Figure 5.26(a-b). More precisely, in the subcritical Case T480, n-hexane is injected in a liquid state as depicted in blue color in Figure 5.25(b) indicating tiny  $\alpha_{Gas}$  in the liquid core. In this case, a classical atomizing jet is shown experimentally in Figure 5.26(a). A spray can be seen clearly in this (shadowgraph + ELS) experimental image with distinct droplets at the periphery of the jet (especially for  $X/D > 50$ ). Also, the ELS experiments have revealed a strong phase separation within the jet by showing high scattering intensity, (see I the palettes shown in Figure 5.26). Turbulent diffusion of  $N_2$  into the injected n-hexane liquid core causes this mixture to enter the two-phase dome at a mole fraction of  $N_2$  of about 0.1, as shown in Figure 5.25. This strong phase change can be seen in the numerical result shown in Figure 5.26(a) where the liquid core is represented (in blue) as the low gas fraction region.

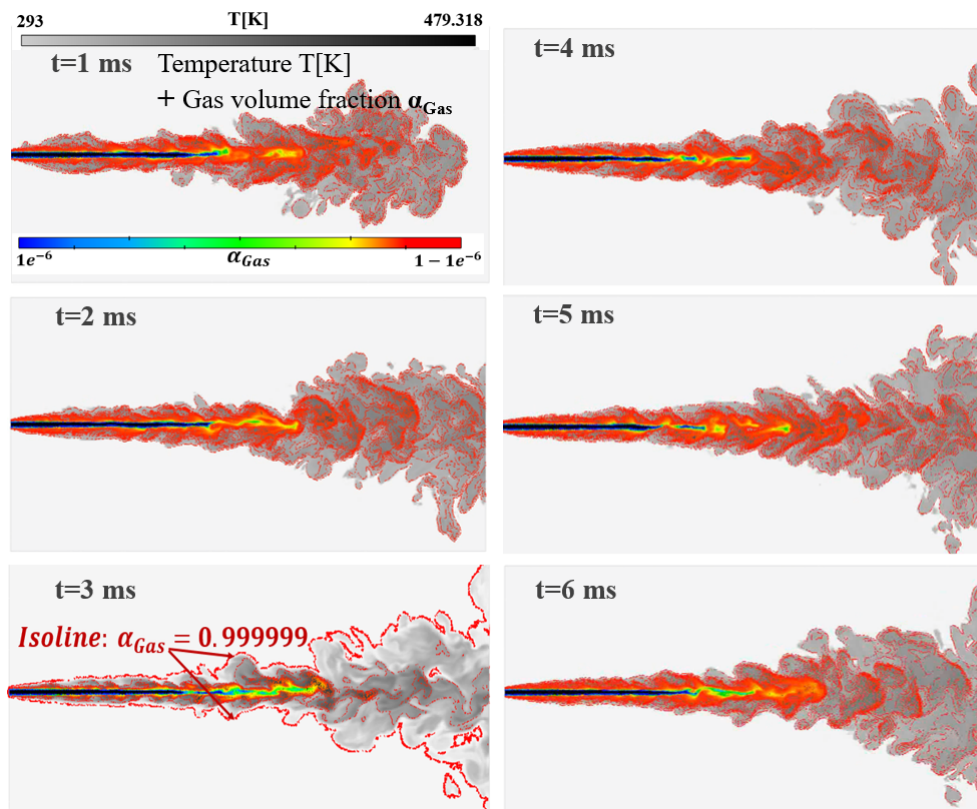


Figure 5.27: Temporal evolution of (temperature + gas volume fraction( $\alpha_{Gas}$ )) contours using Sigma turbulence model for case T=480.

The rest of jet is in two-phase state representing the droplets spray and highlighting the flow structure at its periphery. This flow structures can be also seen in Figure 5.27 which demonstrates the temporal evolution of superposed temperature and gas volume fraction ( $\alpha_{Gas}$ ) contours. It is worth noting on Figure 5.27 that the two-phase jet can be considered as quasi-steady for  $t > 4$  ms. Also, the authors would like to remind here that surface tension is not taken into account in the proposed RFM model and that future work should verify its effect on the numerical results of the subcritical T480 case. For the second case T560, n-hexane is injected at a supercritical liquid-like state into  $N_2$  which is at supercritical state as well. Although this supercritical condition, the shadowgraph + ELS image (Figure 5.26(b)) has revealed very rough borders indicating the presence of droplet clusters. This interesting phase change phenomena can be further discussed here using Figure 5.25(a). Indeed, the zoom inserted in this figure shows that the LES mixing temperature scatter plots for the T560 case has crossed the two-phase dome at high  $N_2$  mole fraction. This means that most of the droplets nucleus have appeared close to the jet periphery. This phase change can be seen in the numerical results of Figure 5.26(b) and in more detailed time evolution of the jet in Figure 5.28, in which very low liquid volume fraction is highlighted (see the palette where the value of gas volume fraction changes from around 0.9967 to unity).

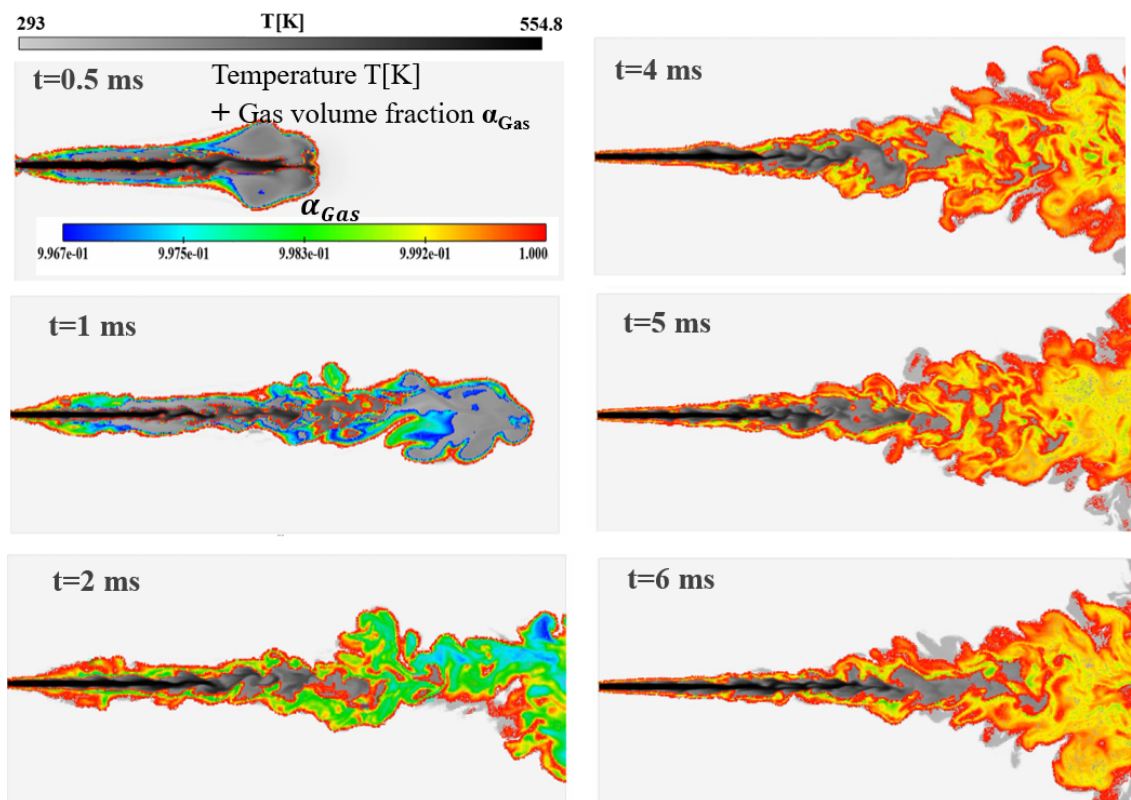


Figure 5.28: Temporal evolution of (temperature + gas volume fraction ( $\alpha_{Gas}$ )) contours using Sigma turbulence model for case 560 (see table 5.3).

In this case, the good qualitative validation of the appearance of liquid by condensation at the periphery of the jet could be considered as an a posteriori justification of the VLE assumption on which the proposed RFM model is based.

Finally, for case T600, Figure 5.25(a,b) demonstrates, the jet does not experience any phase change and two-phase regime. Hence, with respect to the mixture critical point, the jet undergoes a single phase mixing regime. The shadowgraph + ELS experiments have revealed this single-phase regime within the jet by showing no significant scattering signal, as shown in Figure 5.26(c). As shown in this figure, this single-phase (dense-gas) behavior within the jet has been also well predicted by the RFM model.

It is worth noting that the comparison between the simulation and the experiment has shown some differences regarding the jet penetration length and dispersion. This can be attributed to the experimental uncertainty of the velocity and unknown turbulence at the nozzle exit. In addition, there is some probability of uncertainty in the numerical simulation as well. However, the current validation has demonstrated that the RFM model can efficiently capture the main physics in various conditions.

#### 5.2.4.4 Analysis of droplet formation process for binary systems at supercritical regime

With the phase equilibrium model employed in this study, a detailed analysis of the droplet formation process becomes possible in the condition the metastability relaxation time is smaller than the CFD time step. Obviously, VLE assumption is not valid in case the metastability duration is much longer than the CFD time step. In this case, detailed models for nucleation and droplet growth under non-equilibrium condition are required [122].

Here, the case T560 is discussed based on Figure 5.29(a-d) in order to further illustrate the phase transition and droplet formation near to the jet border of an initially supercritical n-hexane fluid ( $T_{inj} > T_c$ ) due to the interaction with its surrounding supercritical nitrogen. More specifically, Figure 5.29 shows the contour plots of a) the temperature, b) the  $C_6H_{14}$  mass fraction in the mixture, c) the phase indicator PHI= 1, 2 which designates the gas state and the two-phase state, respectively, and finally d) the  $C_6H_{14}$  mass fraction in the liquid phase defined as follows: The mass fraction of each component (for a system with ( $k$ ) components), in any phase ( $p$ ), ( $Y_{k,p}$ ) is defined as the ratio of component ( $k$ ) density in the phase ( $p$ ) considered with respect to the phase density ( $\rho_p$ ), as  $Y_{k,p} = \frac{\alpha_p \rho_{k,p}}{\sum_k \alpha_p \rho_{k,p}}$ .

As the phase indicator shows in Figure 5.29(c), the periphery of the jet goes to two phase regions.

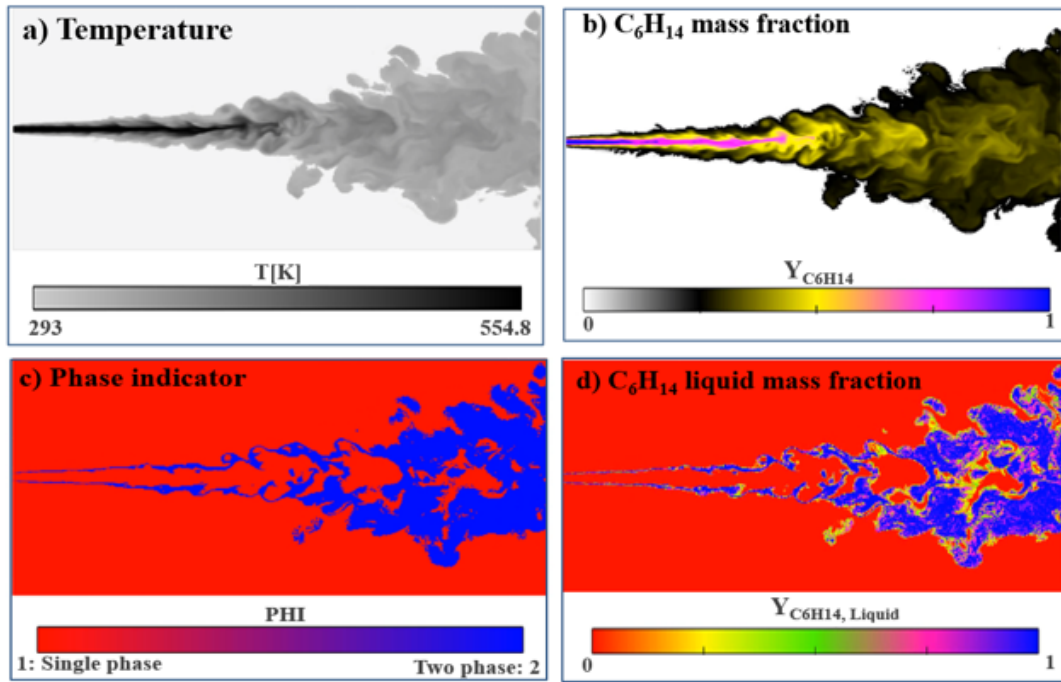


Figure 5.29: T560 case results: contour plot of (a) Temperature, (b)  $C_6H_{14}$  mass fraction, (c) Phase indicator in which PHI= 1, 2 denotes single phase and two-phase states, respectively, and (d)  $C_6H_{14}$  liquid mass fraction. This mass fraction ( $Y_{C_6H_{14},l}$ ) is defined as the ratio of  $C_6H_{14}$  density in the liquid phase (index  $l$ ) with respect to the liquid density ( $\rho_l$ ), as

$$Y_{C_6H_{14},l} = \alpha_l \rho_{C_6H_{14},l} / \rho_l.$$

This can also be seen in the mass fraction contour of  $C_6H_{14}$ , in Figure 5.29(b). In this figure, a small mass fraction of  $C_6H_{14}$  (black color) is present near the boundary of the jet at near room temperature (light gray color in the temperature contour in Figure 5.29(a)). More importantly, Figure 5.29(d) reveals the mass fraction of  $C_6H_{14}$  in the liquid phase formed by condensation, mostly near the jet periphery. It worth to mention that as  $\sum_k Y_{k,l} = 1$ , the mass fraction of  $N_2$  in the liquid phase formed by condensation is revealed to be very small in Figure 5.29(d).

#### 5.2.4.5 Turbulence modelling impacts on two phase jets

Turbulence is known to significantly enhance the mixing rate of species, momentum and energy. This convective process occurs at different length scales as it results from the occurrence of turbulent eddies with different characteristic sizes, in high Reynolds number flows. Currently, only the direct numerical simulation (DNS) method can handle turbulent flows, but only for single-phase gas flows. In general, if a simulation does not use a sufficiently refined grid (DNS), it cannot properly account for turbulent mixing effects. This is still not practical in most of industrial test cases. Thus, turbulence models are often employed to estimate the additional mixing due to turbulence. As Richard Feynman (the American theoretical physicist, Nobel Prize in Physics in 1965) mentioned: "Turbulence is the most important unsolved problem of classical physics",

hence developing a general turbulence model is still complicated due to highly unsteady and intricate interactions between various physical phenomena (turbulence, mixing, multi-phase flows, etc.) along with complex geometries and diverse boundary conditions. Traditionally, RANS (Reynolds-averaged Navier–Stokes equations) models [120] employ an effective turbulent viscosity to model the Reynolds stress term. Besides, in the past few years, Large-Eddy Simulation (LES) [118, 119] as a promising approach for turbulence modeling has been extensively used due to its unique potential to reproduce these unsteady and irregular phenomena. The main difference between LES and RANS models is how the fields are decomposed for modeling. For RANS approaches, the field is decomposed into an ensemble mean and a fluctuating component. However, LES resolves more of the turbulent spectrum by using a more refined grid in such a way that only the isotropic smallest eddies remain for an easier modelling of sub-grid scale. Hence, for LES approach, the field is decomposed into a resolved field and a sub-grid field, and numerous LES models have been developed to relate the turbulent stresses to a differential operator acting on the resolved velocity field, as Equations (5.1 - 5.3). However, recent studies still demonstrate that each approach has some cons and pros, and choosing the best global LES approach for turbulence modeling, especially for internal combustion engines, is a crucial issue due to appearance of various complex phenomena [123, 124]. The oldest and most commonly used approach is the one proposed by Smagorinsky [119]. This model, known as a zero-equation LES model, does not solve any additional transport equations for sub-grid scale. It relates the turbulent viscosity to the magnitude of the strain rate tensor and the filter (usually taken as the cell size). Besides, an other promising zero-equation sub-grid model, called the Sigma model, has been developed by Baya-Toda et al. [119]. This more recent model shows that it can be a better alternative to the Smagorinsky model. It constructs the turbulent viscosity from the singular values of the resolved velocity gradient tensor. Most of the performance study of Sigma model have been performed for combustion [123, 124], and not for two-phase flows. In addition, two-phase turbulence effects have largely been neglected in the current literature. Indeed, most of the current state of the art two-phase flow simulations still consider one-fluid turbulence modelling approach, i.e. assuming that the turbulent structures behave similarly to single-phase turbulence. In this study, the objective is to give some insight to two-phase turbulence modelling by analyzing the interaction between the turbulence and two-phase flows, especially when phase transition (evaporation, condensation) occurs. Generally, the turbulent viscosity in LES zero-equation models are defined as the following Equation 5.1.

$$\nu_{SGS} = (C_m \bar{\Delta})^2 \bar{D}_m \quad (5.1)$$

where  $C_m$  and  $D_m$  are the model ( $m$ ) specific constant, and differential operator of the model respectively.  $\bar{\Delta}$  is the filter width (i.e. the cell size in the context of LES with implicit filtering).  $D_m$  as the differential operator of the Smagorinsky and Sigma models are computed as the following Equations (5.2-5.3).

$$\bar{D}_{Smag} = \bar{S} = \sqrt{2\bar{S}_{ij}\bar{S}_{ij}}, \bar{S}_{ij} = 0.5\left(\frac{\partial\bar{u}_i}{\partial x_j} + \frac{\partial\bar{u}_j}{\partial x_i}\right) \quad (5.2)$$

$$\bar{D}_{Sigma} = \frac{\sigma_3(\sigma_1 - \sigma_2)(\sigma_2 - \sigma_3)}{\sigma_1^2} \quad (5.3)$$

The differential operator of the Smagorinsky model is based on the resolved characteristic rate of strain ( $\bar{S}_{ij}$ ). However, the Sigma model employs the singular values of the resolved velocity gradient tensor so that the singular values  $\sigma_i$  ( $\sigma_1 \geq \sigma_2 \geq \sigma_3$ ) are the square roots of the eigenvalues of the matrix  $\bar{S}_{ij} * \bar{S}_{ji}$  [119].

As a final comment on the turbulence modelling, it is worth to note that turbulent viscosity ( $\mu_{SGS}$ ) is known to be much greater than laminar one ( $\mu$ ) in single-phase turbulent flows. However, this is not always the case in turbulent two-phase flows, especially at the liquid-gas interface where the laminar viscosity experiences a high gradient. Another important point is that the rate of strain  $\bar{S}_{ij}$  in  $\bar{D}_m$  equations may vary significantly in the interface region due to a large phase transition. This is also may be the case due to non-linear property ( $C_p, D_T, \dots$ ) behaviors at supercritical state in the Widom line region. The latter two effects are somewhat included in the proposed RFM model through the tabulation of the VLE properties and the impulse effect of the phase change on the momentum. However, a more thorough fundamental study of the interaction between turbulence and EoS should be conducted in future work [125].

Figure 5.30 shows instantaneous contour plot of temperature, and density for case T480 at  $t=2.5$  ms using various turbulent models denoted as RANS, LES-Smagorinsky, and LES-Sigma models, respectively. Noteworthy, it does not make sense to compare ensemble averaged RANS results and instantaneous LES results. However, this Figure demonstrates the different behaviour between RANS and LES models. The liquid core (represented by the mixture density) is very short relatively to the LES results. This is due to the higher turbulent viscosity and kinetic energy (TKE) generated in the RANS simulation (see also Figure 5.31(a,c)).

The Sigma-LES model gives an initial spray cone angle that better matches the experimental image shown in Figure 5.26(a) than the LES-Smagorinsky model. Also, the liquid core obtained with Sigma-LES model is shorter than the one obtained by LES-Smagorinsky model. This demonstrates a higher evaporation rate obtained using the LES-Sigma model, and thus the

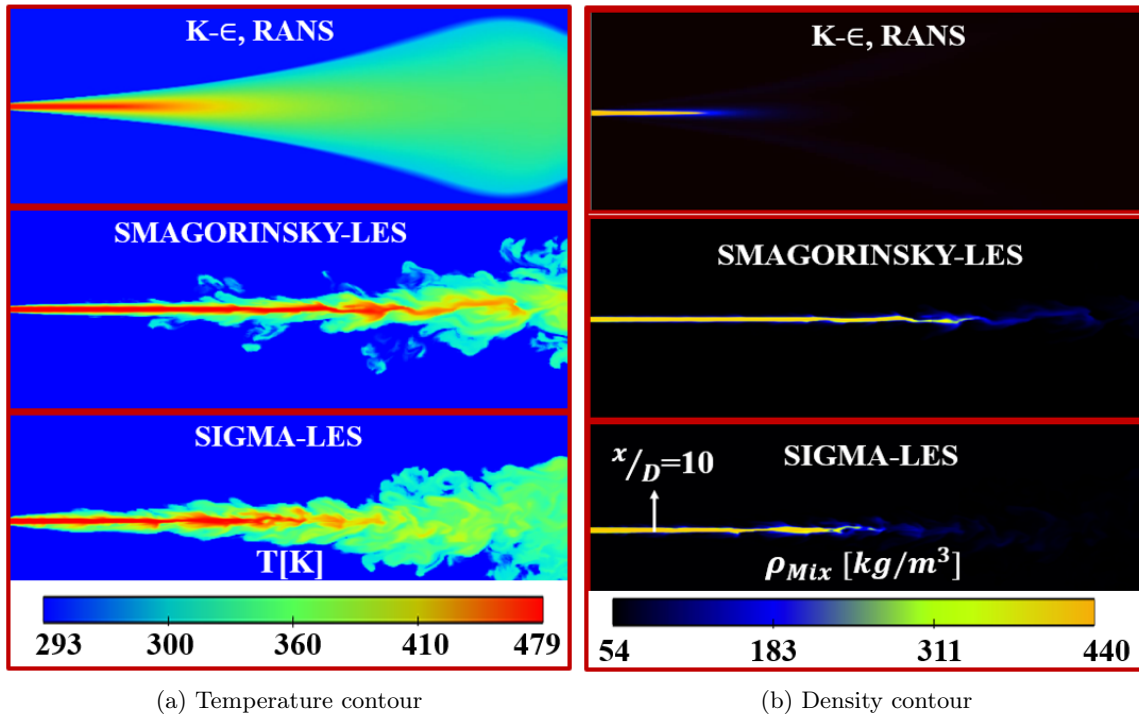


Figure 5.30: Impacts of turbulence modellings of the jet structure for various properties for two phase flows using  $(k - \epsilon)$  RANS, LES-Smagorinsky, and LES-Sigma models, respectively, from top to down, at  $t=2.5$  ms.

significant effect of turbulence modeling on such two-phase numerical results. However, more simulations should be performed in future work to assert the superiority of LES-Sigma in two-phase flows. To have a better insight, Figure 5.31(a-c) display a qualitative comparison of some turbulent properties profiles at  $X/D = 10$  (see the arrow in Figure 5.30(b)), as a) Turbulent viscosity ( $\mu_T$ ), b) Turbulent conductivity ( $\lambda_T$ ), and c) Turbulent kinetic energy (TKE) using the different turbulence models, respectively at  $t=2.5$  ms. Figure 5.31(a,b) demonstrates the huge values obtained with the RANS model relatively to the LES models. In addition, lower turbulent viscosity and conductivity levels are obtained using the Sigma model compared to the Smagorinsky model in the liquid-gas interface region. This lower turbulent viscosity is expected since Sigma model has been developed to avoid overestimating the SGS turbulence in shear layers, as also reported by [123]. Hence, this lower turbulent viscosity level has led to less dissipation of the turbulent energy, TKE, as shown in Figure 5.31(c).

Besides, some interesting points can be observed in Figure 5.32 in which is plotted dimensionless radial profiles of the density, density gradient, gas volume fraction and the turbulent conductivity, at  $X/D = 10$ . First, it is important to note in this figure that the extrema of the turbulent conductivity and density gradient almost coincide with the locus of the liquid-gas interface at  $\alpha_{Gas} = 0.5$ . This demonstrates the high coupling of turbulence with flow characteristics such as

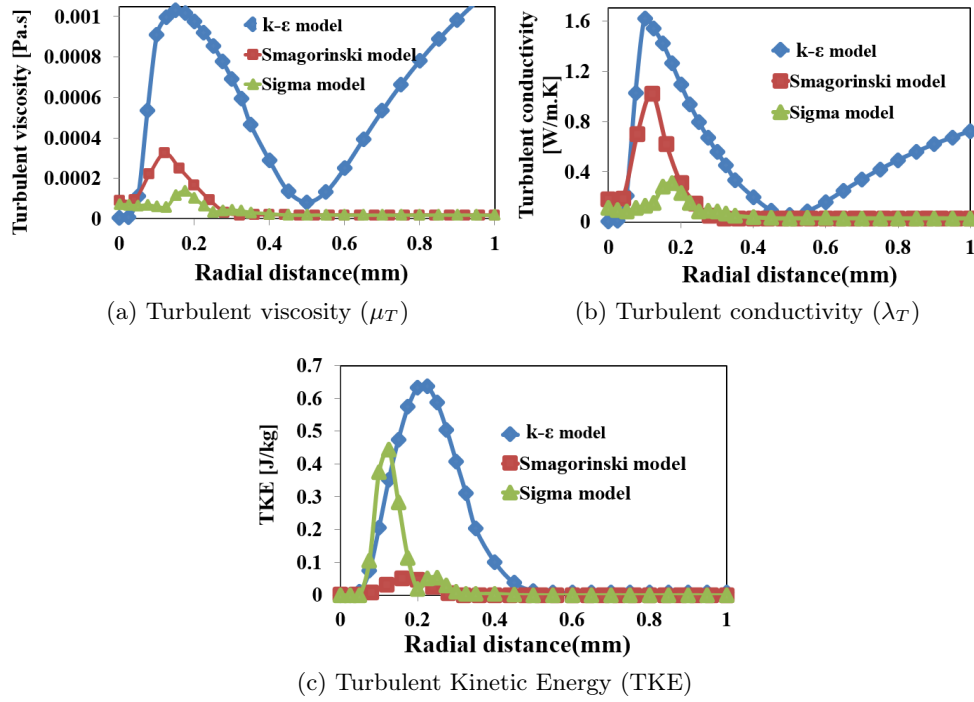


Figure 5.31: Impacts of turbulence modellings on different turbulent properties using different ( $k - \epsilon$ ) RANS, LES-Smagorinsky, and LES-Sigma models, respectively, from top to down, at  $t=2.5$  ms at  $X/D = 10$ . Due to the much higher values from the ( $k - \epsilon$ ) model for the different turbulent properties, they have been divided by 100, 100, and 20 for turbulent viscosity, TKE, and turbulent conductivity, respectively, to be in the same range as LES data.

density gradient. Indeed, it is well known that the density gradient in a two-phase flow plays a key role in turbulent two-phase flows and particularly on liquid atomization.

Generally, vorticity analysis can be used as an appropriate tool for the flow mixing analysis [126, 127]. the following Equation 5.4 gives the total derivative of vorticity  $\omega$  for compressible flows [126].

$$\frac{D\omega}{Dt} = -\omega(\nabla \cdot u) + (\omega \cdot \nabla)u + \frac{\nabla \rho * \nabla P}{\rho^2} - \nu \nabla^2 \omega \quad (5.4)$$

The first term on the right hand side of Equation 5.4 represents the expansion of the vorticity due to the compressibility.

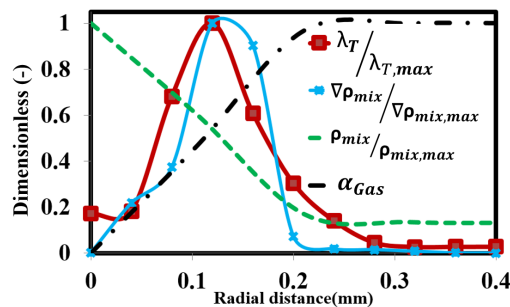


Figure 5.32: Impacts of density gradient on the turbulent properties, at  $t=2.5$  ms at  $X/D = 10$ , using LES-Sigma model.

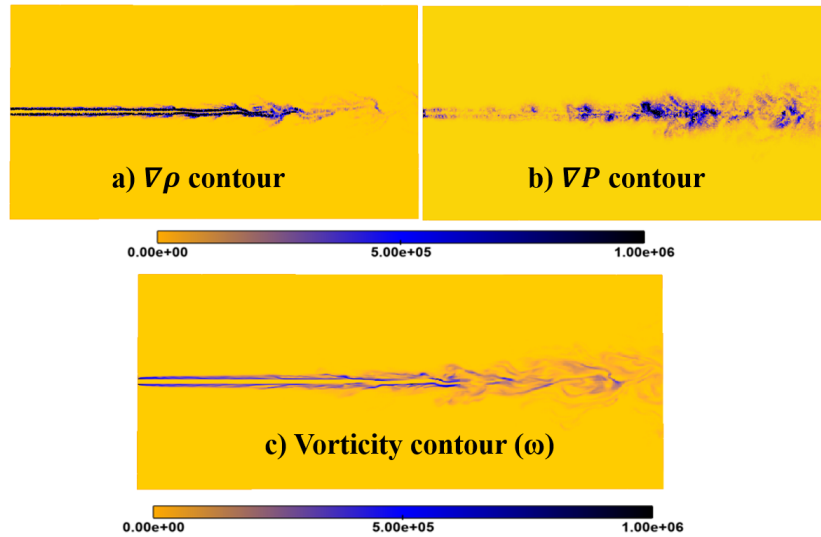


Figure 5.33: (a) Density gradient, (b) Pressure gradient and (c) Vorticity contours at the interface at  $t=2.5$  ms. The misalignment of spatial pressure and density gradients is at the origin of the baroclinic torque source term.

The second term, called vortex stretching term, is due to the enhancement of vorticity by stretching. The third term, called baroclinic torque, is due to the misalignment of spatial pressure and density gradients. Finally, the viscous diffusion last term expresses the vorticity change due to viscous dissipation. Figure 5.33(a,b) shows the appearance of a peak at density and pressure gradients contours at the interface, which leads to the formation of high vorticity in at the interface, as shown in Figure 5.33(c). This demonstrates that real fluid models are required to accurately compute density and pressure gradients and to simulate such turbulent injection flows, as recently reported by [107].

### 5.2.5 Quantitative validation

To quantitatively validate the tabulated RFM-LES results, the numerical results will be compared in this section with the recent experimental data from Baab et al. [31]. They performed quantitative sound speed measurements in jet mixing zones for different configurations with various mixtures at different conditions. The n-hexane case, which corresponds to "Case 1" in Baab et al. [31] is chosen for the comparison to our numerical results. The applied numerical setup is identical to the one used in the previous section. The experimental conditions, listed in Table 5.4, are very similar to the T600 case in Section 5.2.5, as shown in Table 5.3. One point is worth mentioning is that the nozzle exit temperature  $T_e = 627K$  and velocity  $u_e = 90m/s$  were estimated in that experimental study based on the assumption of an isentropic flow inside the injector [31].

In this study, another strategy has been adopted, where inflow turbulence fluctuations have been generated and superimposed on the inflow velocity profile using Fourier method, based on the proposals by [128]. This method has been used in order to generate correlated turbulent fluctuations over the mean inlet profile at the nozzle exit. Using synthetic turbulence at the computational domain inlet has shown significant effect on the spray development as demonstrated in [129, 130], when the in nozzle flow is not included in the simulation. As pointed out in [129, 130], this turbulent intensity ranges between 3 and 5% depending on the turbulence model. Hence, the injection boundary conditions in this study are based on the mean inlet velocity of 90 m/s and 5% turbulent intensity superimposed on the inflow velocity profile. In addition, n-hexane is injected with the estimated nozzle temperature of 627K to the chamber filled by  $N_2$  at  $T_{ch} = 296K$  and  $P_{ch} = 5MPa$ . With regard to the numerical setup, the same configuration as shown in Figure 5.24 is used with the base grid size set to  $(40\mu m)$  at the far-field of nozzle, and along with different levels of embedding to achieve a fine mesh resolution near the nozzle exit of  $(10\mu m)$ , corresponding to 26 cells in the nozzle diameter. Moreover, the time step is automatically controlled based on a maximum CFL number of 50 reaching a value in the range (10 ns-50ns).

Table 5.4: Operating conditions used for the current numerical study taken from Baab et al [31] experimental study. The nozzle exit temperature  $T_e$  was estimated based on the assumption of an isentropic flow inside the injector calculated by [31].

Injection fuel	Chamber gas	$P_{ch}[MPa]$	$T_{ch}[K]$	$T_{t,C_6H_{14}}[K]$	$T_{e,C_6H_{14}}[K]$
$C_6H_{14}$	$N_2$	5	296	630	627

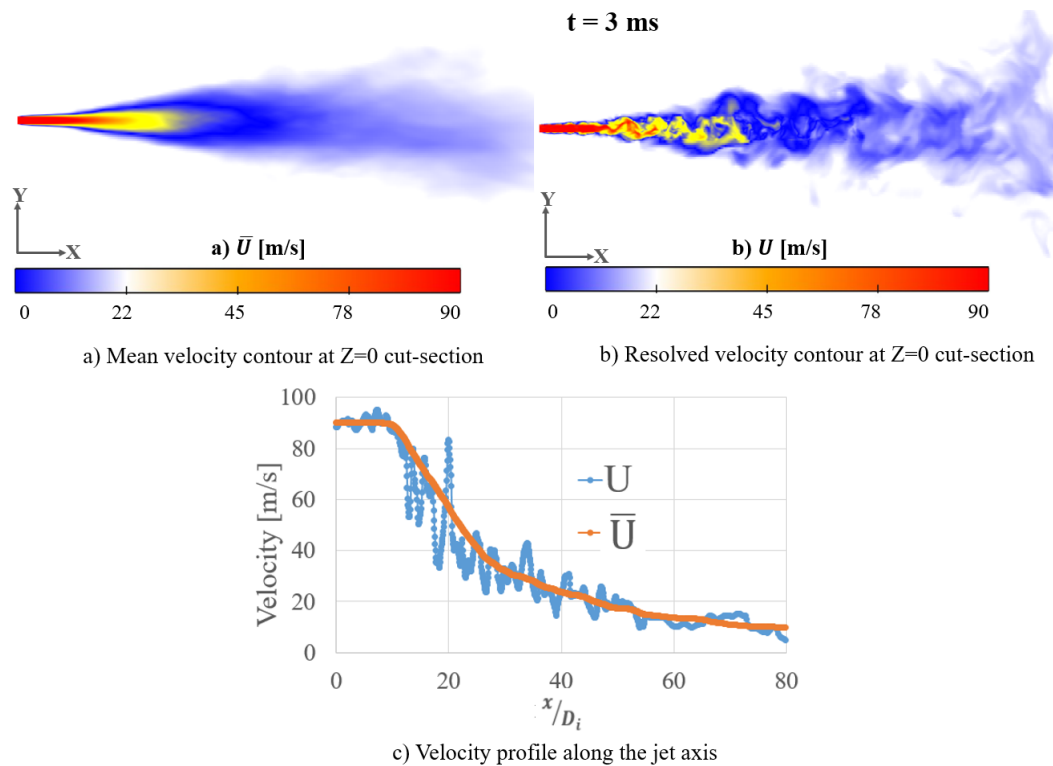


Figure 5.34: (a) Mean velocity field ( $\bar{U}$ ), (b) The resolved velocity ( $U$ ) at 3 ms, and (c) The velocity profile plotted along the jet axis where the resolved velocity is at 3 ms and the mean velocity is computed using the LES results in the time interval between 2 and 3 ms after the start of injection. For this case, a fluctuating boundary condition has been superimposed on the inflow velocity profile using Fourier method with 5% intensity.

Besides, the LES-Sigma model has been used for the turbulence modeling of this test case due to its performance, as shown in the previous section. Figure 5.34 demonstrates (a) The mean velocity contours computed using the LES results in the time interval between 2 and 3 ms after the start of injection, (b) The resolved velocity, in addition to (c) The velocity profile along the jet axis obtained with an inlet fluctuating boundary condition with 5% intensity. Unfortunately, no experimental velocity and turbulence data are available in this case. Therefore, these numerical results can be used as a reference for future work.

Figure 5.35 shows the Temperature- $N_2$  mole fraction diagram for the binary mixture of  $N_2 - C_6H_{14}$ , colored and mapped with the mixture sound speed, computed using the Wood formula [93] for the two-phase region at  $P = 5MPa$ , calculated by PR-EoS, along with the scatter plots (white points) locus of the mixing temperature obtained by the RFM-LES model. In this figure, we can observe the sound speed variations along the mixing temperature (white dots). This demonstrates that the flow in the current supercritical condition experiences relatively small sound speed variations. This could be seen more precisely in Figure 5.36(c) which depicts the instantaneous fully developed  $N_2 - C_6H_{14}$  LES results in terms of sound speed contour after  $t=3$  ms. Indeed, Figure 5.36 presents the instantaneous mixture sound speed at axial center-line and at ra-

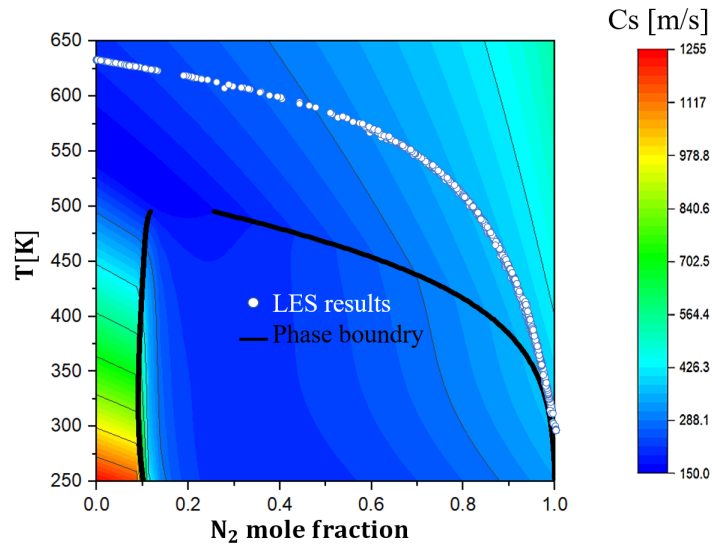


Figure 5.35: Temperature- $N_2$  mole fraction diagram for binary mixture of  $N_2 - C_6H_{14}$ , colored with the mixture sound speed, using Wood formula for two phase region [93] at  $P = 5$  MPa, using PR-EoS, along with the phase boundary (in black). The scatter plots (white points) show the locus of the mixing temperature obtained by the RFM-LES model for the case with  $T_e = 627K$  simulation.

dial direction at  $x/D_i = 35$ , extracted from the RFM-LES results. An intensely turbulent mixing process of n-hexane with the supercritical nitrogen ambient can be observed in Figure 5.36(a,b) in terms of the mixture temperature and the hexane mass fraction. The supercritical fuel jet with higher density ( $\rho \approx 115kg/m^3$ ) and temperature ( $T = 627K$ ) enters to the chamber filled with  $N_2$  with lower density ( $\rho \approx 58kg/m^3$ ) and temperature ( $T = 296K$ ), and then n-hexane jet gradually mixes with  $N_2$  inside the chamber. Moreover, as Figure 5.36(c) shows, the sound speed varies from  $C_{s,C_6H_{14}}(P_{ch}, T_e) = 197m/s$  at the exit of nozzle and  $C_{s,N_2}(P_{ch}, T_{ch}) = 360m/s$ . Finally, quantitative comparisons of the mixture sound speed with the experimental data from Baab et al. [31] are shown in Figure 5.37 along the axial and radial axis shown in 5.36(c). Ten numerical profiles shown as thin gray lines denotes the RFM-LES results in the time range of  $t=2-3$  ms. Furthermore, Figure 5.38(a) shows the instantaneous contours of the n-hexane mole fraction at  $Z=0$  cut section at  $t = 3ms$ . Besides, Figure 5.38 demonstrates the instantaneous contours of the n-hexane mole fraction and the validations of LES n-hexane mole fraction with the analytical self-similar solutions calculated by Gerber et al. [25] using REFPROP. Specifically, some instantaneous LES results on the jet axis, as shown in Figure 5.38(a), are shown (colorized with gray thin lines) in the range of  $t=2-3$  ms. Also, LES simulation results at  $t=3$  ms are highlighted. Overall, a good agreement are found in the sound speed as well as hexane mole fraction predicted results, compared to the reference data, which demonstrate that the RFM-LES solver is able to predict the mixing process of  $C_6H_{14}$  and  $N_2$  accurately.

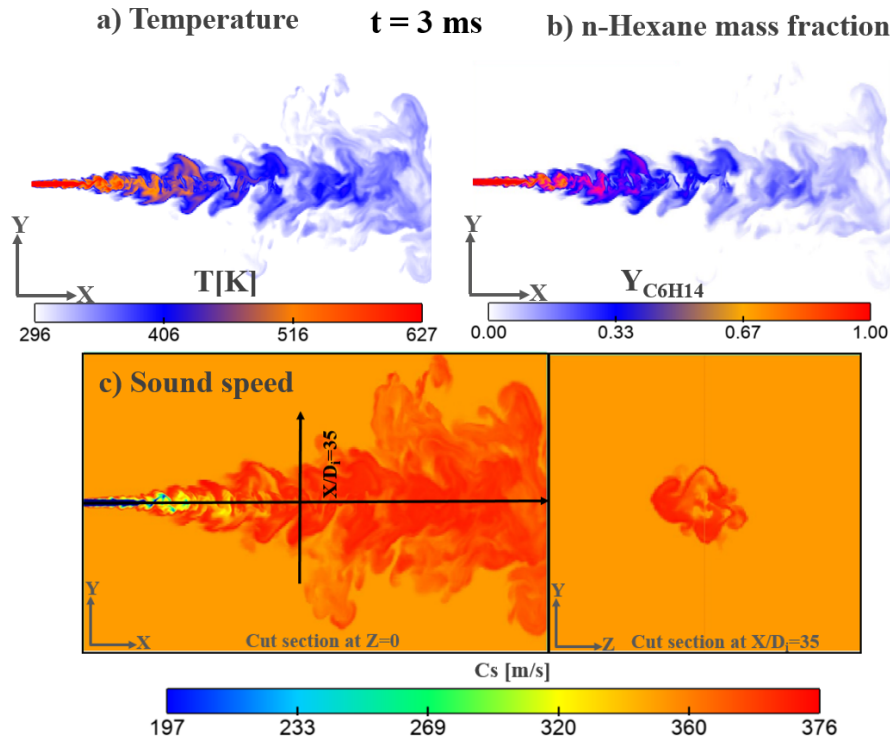


Figure 5.36: The top LES results at  $t = 3$  ms are: (a) Instantaneous contours of the mixture temperature, (b) n-hexane mass fraction at  $Z=0$  cut section. The bottom LES results (c) at  $t = 3$  ms are the mixture sound speed at  $z = 0$  (left), and at  $x/D_i = 35$  cut sections (right). The sound speed in the chamber, filled initially with the  $N_2$  at  $T_{ch} = 296K$ , is  $C_{s,ch} \approx 360m/s$  (orange color). At the nozzle exit where  $T_e = 627K$ , the sound speed is  $C_{s,exit} \approx 197m/s$  (blue color).

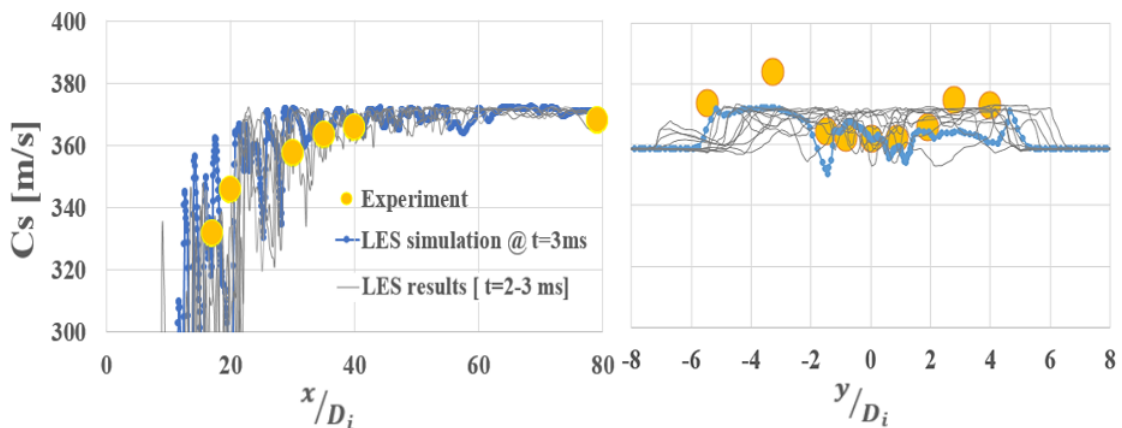


Figure 5.37: Validations of mixture sound speed with experimental data of Baab et al. [31], (a) Along the jet axis, and (b) At radial direction at  $x/D_i = 35$  determined and plotted at Figure 5.36. LES results colorized with gray thin line denotes the LES-sigma results for some instantaneous times in the range of  $t=2-3$  ms. LES simulation @  $t=3$  ms shows the variations of the mixture sound speed at  $t=3$  ms, as shown in Figure 5.36.

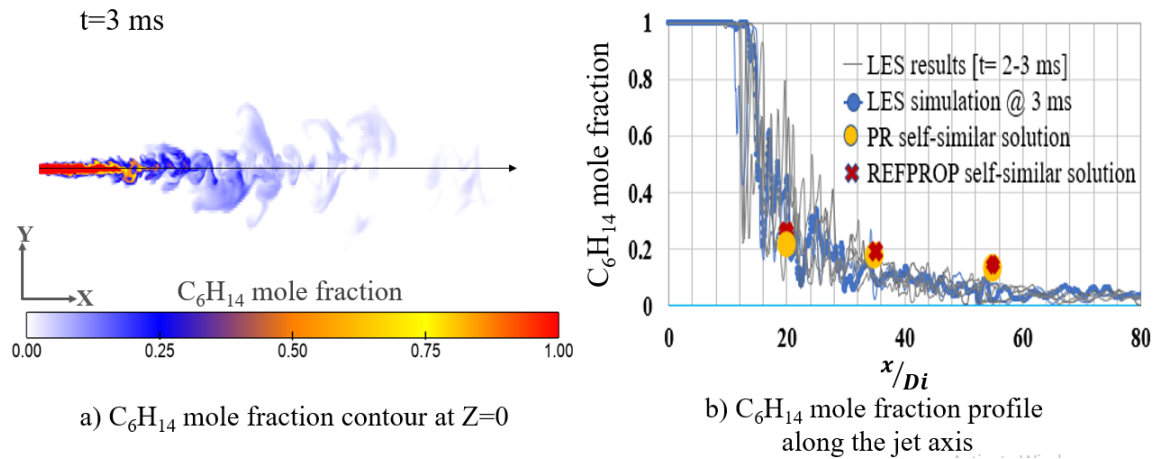


Figure 5.38: Instantaneous contours of (a) n-hexane mole fraction, at  $Z=0$  cut-section at  $t = 3ms$ , and (b) Validations of LES n-hexane mole fraction, along the jet axis, with the analytical self-similar solutions calculated by Gerber et al. [25]. They hired PR EoS, and REFPROP data to analytically calculate fuel mole fraction at different distances from the nozzle exit. LES results colorized with gray thin line denotes the LES-sigma results for some instantaneous times in the range of  $t=2-3$  ms. LES simulation @  $t=3$  ms, with blue color shows the variations of the n-hexane mole fraction, shown in contour plot in (a).

## 5.2.6 Conclusion

In this part, a fully compressible tabulated multi-component real-fluid (RFM) model has been developed in order to explore the interaction between phase separation and turbulent fluid dynamics in multi-species supercritical flow jets. More specifically, the converge CFD solver has been coupled to the IFPEN-Carnot thermodynamic library using a generalized tabulation method to gain computational efficiency and robustness. This modeling approach has been implemented in the CONVERGE solver for the simulation of the turbulent mixing of n-hexane injected in a chamber filled with nitrogen, considering phase separation processes (condensation) at high pressures conditions with the fluids initially at supercritical state. Hence, initially, n-hexane has been injected at three inflow temperatures in the same conditions as the experimental and numerical study of Traxinger et al. [30]. Besides, a more quantitative study has been performed using the experimental study of Baab et al. [31], which has the same setup configuration as [30]. The obtained numerical results have been shown and proved to be in good agreement with the experiments [30,31]. In addition, the RFM model was shown to be capable of simulating subcritical, transcritical and supercritical jets exhibiting phase separation and condensation processes. As a consequence, if the jet undergoes the subcritical state, with regard to the mixture critical point, it experiences the classical droplets formation process governed by the liquid atomization. In contrast, if n-hexane is injected at supercritical state in a colder nitrogen ambient, it may cross the two-phase dome, thus leading to local condensation and droplets formation mainly at

the periphery of the jet. It has been also shown that such condensation does not occur if the n-hexane is injected at a sufficiently high supercritical temperature.

In addition, comparisons between different turbulence models, including large eddy simulation models (LES Sigma and Smagorinsky) and a Reynolds-averaged Navier-Stokes model (RANS  $K - \epsilon$ ), have demonstrated the importance of a proper turbulence modeling, and the suitability of the LES-Sigma approach, in addition to accurate thermodynamic and transport properties, for these highly complex jet flows. Finally, compared to our previous studies [17, 22], the computational efficiency, accuracy, and robustness of this proposed tabulated RFM model as a remedy to the direct evaluation of costly phase equilibrium solver have been confirmed.

## Chapter 6

# Summary, conclusion, and future work

### Contents

---

<b>6.1</b>	<b>Summary and conclusions</b>	<b>132</b>
<b>6.2</b>	<b>Future work</b>	<b>136</b>
6.2.1	Cavitation simulation	136
6.2.2	Real fluid simulations by machine learning	137
<b>6.3</b>	<b>Sommaire et conclusions</b>	<b>139</b>

---

### 6.1 Summary and conclusions

This thesis is motivated by an exciting context seeking to contribute to the energy transition to carbon neutrality. For this purpose, a CFD model capable of predicting various real fluid jets mixing under subcritical, and supercritical conditions has been developed and validated in this thesis. This two-phase model is based on a diffuse interface method (DIM) considering phase equilibrium theory using different equations of state (EoS) to simulate simultaneously subcritical and supercritical flows as well as the transition between the two. The real fluid model (RFM) was coupled to the IFPEN-Carnot thermodynamic library using a generalized tabulation method to gain computational efficiency and robustness. To our knowledge, most of the available two-phase flow equilibrium solvers in the literature are proposed so that the thermodynamic state in each computational cell will be determined after solving for the mass, momentum, and energy equations [17, 22, 34, 35, 53, 83]. Therefore, one important achievement of this study is related to the strong coupling of the flow solver with the thermodynamic solver compared to conventional approaches. This thesis consists of six chapters, including some materials in 3 appendices.

After the background and motivation detailed in **Chapter 1**, **Chapter 2** was devoted to

explaining and reviewing the physical concepts and classical models available for single- and multi-component two-phase flows under different thermodynamic regimes such as subcritical, transcritical and supercritical. In addition, a literature review as well as thermodynamic and mathematical concepts have been presented in this chapter.

Then, the main contributions and discussions for developing a real fluid model (RFM) for simulating two-phase flows are presented in **Chapter 3** and **Chapter 4**.

More specifically, the governing equations, thermodynamic tabulation, and look-up methods using uniform tabulation are presented in **Chapter 3**. The modified SIMPLE and PISO algorithms for the RFM model are also detailed.

In **Chapter 4**, after a short review on the VLE tabulation approach, the difficulties of tabulating properties from the VLE algorithms are explained, and the reasons why grid-table refinement in the vicinity of the phase boundary are need has been discussed. Then, different studies have been presented for various tabulation refinement approaches including uniform and nonuniform refinements for single and multicomponent systems. These tabulation approaches have different table generation, searching, and interpolation procedures for which different algorithms have been developed. Thereby, the strengths and weaknesses of these different steps have been analyzed and identified. Some academic simulations have been performed in order to select the best tabulation method with low cost and memory requirements. It has been demonstrated that the CPU time of nonuniform approaches, like octree and quadtree, is very expensive compared to the uniform approach. It was also found that this high CPU time for the non-uniform tabulation approach can exceed the CPU time of the direct real fluid VLE evaluation in the CFD code, without tabulation, due mainly to the high searching step CPU time. Hence, although some researchers [88–92] have proposed nonuniform tabulation approaches, particularly for more refinement of the region close to the phase boundary, it will not be recommended for industrial applications. Therefore, a highly refined uniform table coupled to a shared memory strategy has been proposed for industrial applications (without combustion), which require only a few species, typically no more than three. Thus, using the RFM model for combustion is still among future challenges.

In **Chapter 5**, the developed RFM model was applied to the simulation of a series of academic and industrial tests, for 1-D, 2-D, and 3-D configurations, for validation. Different equations of state, namely PR and SRK have been used to primarily demonstrate the computational efficiency, accuracy, and robustness of the proposed RFM model coupled with the IFPEN-Carnot thermodynamic library. The different test cases are chosen so that they cover most of the thermodynamic regimes for different mixtures to quantify the effects of real fluid thermodynamics on multi-component systems with different physics. This work has been published in several papers, listed in page 2. More specifically, **Chapter 5** has summarized these papers, as follows:

**In section 5.1:**

1. The 1-D studies of the transcritical  $N_2$  shock tube test cases confirmed that the modified SIMPLE and PISO algorithms for the RFM model were in good agreement compared to the available data in the literature.
2. The LES studies of the cryogenic single-component case (liquid-like nitrogen injected into gaseous nitrogen) demonstrated its transcritical interface features by exhibiting the well known thermal shield, as a layer of sizeable isobaric heat capacity separating the liquid-like and the gas-like regions.
3. The LES study of classical cryogenic injection of liquid nitrogen injected coaxially with warm hydrogen jet showed some interesting thermodynamic phenomena, such as the condensation of  $H_2$  as well as cooling effects in the two-phase layer around the liquid core, which demonstrates the subcritical nature of the interface.
4. Another interesting observed phenomenon is related to the mixing of  $N_2$  and  $H_2$ , which led to locally increased mixture critical points. Therefore, due to the mixing process around the liquid core interface, some flow zones may move from the single-phase mixing regime to the two-phase regime, inducing condensation and evaporation.
5. The numerical results were finally compared with available experimental data [29] and published numerical studies [28], with a satisfactory agreement. Moreover, we confirmed the importance of using a powerful real fluid EoS. The current investigations illustrated that the SRK EoS had a better prediction of the fluid density compared to the PR EoS, corroborating the results reported by [28].

Besides, **in section 5.2:**

1. Different studies have been done in order to explore the interaction between phase sepa-

ration and turbulent fluid dynamics in multi-species supercritical flow jets. This has been done to simulate the turbulent mixing of n-hexane injected in a chamber filled with gaseous nitrogen, considering phase separation processes (condensation) at high-pressure conditions with the fluids initially at a supercritical state. The conditions are chosen so that they cover all the thermodynamic regimes for studying real-gas effects and phase separation for the multicomponent mixture.

2. The obtained numerical results have been shown and proved to be in good agreement with the experiments [30,31].
3. In addition, the RFM model was shown to be capable of simulating subcritical, transcritical, and supercritical jets exhibiting phase separation and condensation processes.
4. As a consequence, if the jet undergoes the subcritical state, with regard to the mixture critical point, it experiences the classical droplets formation process governed by the liquid atomization. In contrast, if n-hexane is injected at a supercritical state in a colder nitrogen ambient, it may cross the two-phase dome, thus leading to local condensation and droplets formation mainly at the periphery of the jet. It has also been shown that such condensation does not occur if the n-hexane is injected at a sufficiently high supercritical temperature.
5. In addition, comparisons between different turbulence models, including large eddy simulation models (LES Sigma and Smagorinsky) and a Reynolds-averaged Navier-Stokes model (RANS  $K - \epsilon$ ), have demonstrated the importance of a proper turbulence modeling and the suitability of the LES-Sigma approach, in addition to accurate thermodynamic and transport properties, for these highly complex jet flows.

Finally, compared to previous studies [17, 22, 27], the computational efficiency, accuracy, and robustness of the tabulated RFM model as a remedy to the direct evaluation of costly phase equilibrium solver were confirmed.

## 6.2 Future work

### 6.2.1 Cavitation simulation

In this thesis, the RFM model have been developed and validated mainly using transcritical turbulent jets [108, 131]. Another physical phenomenon that deserves to be studied using the RFM model is cavitation in high pressure injectors. As a final step of this thesis, a preliminary study of this phenomenon was therefore carried out to see if the RFM model is capable of performing such a simulation in the ECN Spray C injector [132], shown in Figure 6.1. The n-dodecane with the pressure and temperature of  $P_{inj} = 1500bar$ ,  $T_{inj} = 363K$  is injected into gaseous nitrogen, at a pressure, and temperature of  $P_{ch} = 60bar$ ,  $T_{ch} = 900K$ , as in table 6.1. The simulation has been done without needle movement, with fully opened needle, as shown in Figure 6.1. The first numerical results show the appearance of cavitation inside the orifice, as shown in figure 6.2 using gas volume fraction contour. As a result, the proposed RFM model can predict the first occurrence of cavitation at the sharp edge of the inlet. However, some as yet unresolved difficulties interrupted the simulation, which will be studied in future works.

Table 6.1: Injection and ambient conditions of ECN cavitation spray C

Injection fuel	Chamber gas	$P_{inj}[bar]$	$P_{ch}[bar]$	$T_{inj}[K]$	$T_{ch}[K]$
$C_{12}H_{26}$	$N_2$	1500	60	363	900

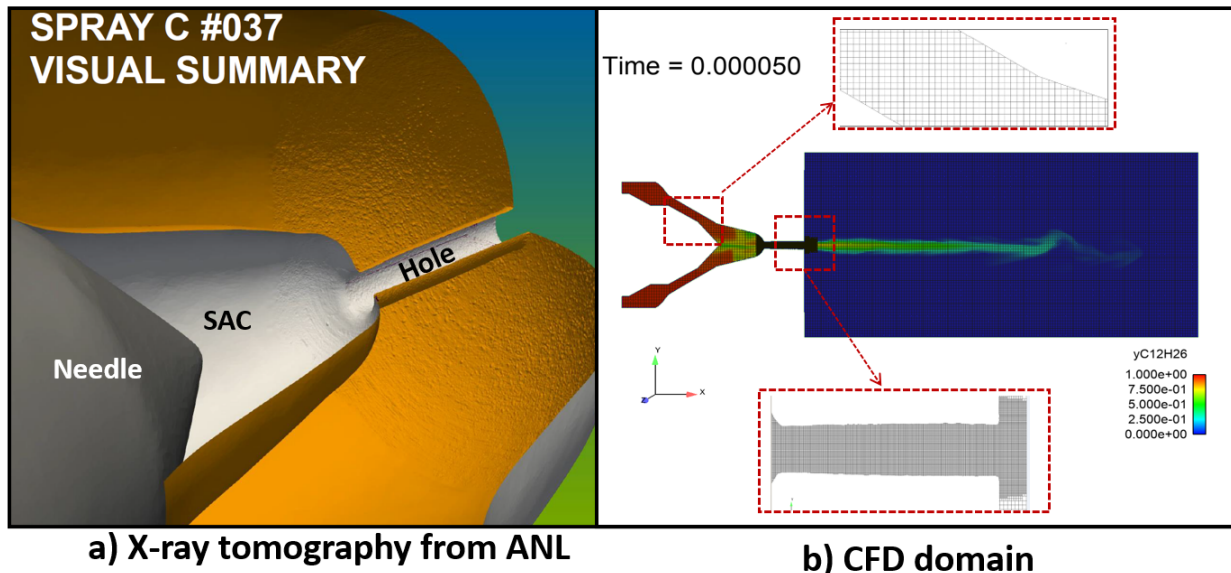


Figure 6.1: (a) X-ray tomography of a Spray C nozzle [132]; (b) Computational domain grids. Fixed embedding has been used to refine the grid in the nozzle orifice and the needle seat, as shown in the different inserts.

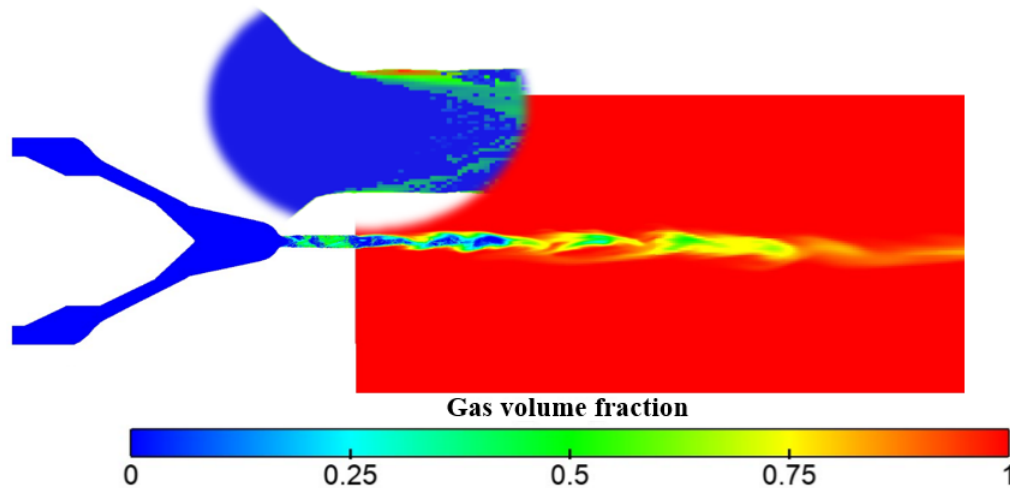


Figure 6.2: Illustration of cavitation appearance inside the orifice by gas volume fraction contour at a condition with no needle movement (fully open sac).

### 6.2.2 Real fluid simulations by machine learning

As discussed and explained in this thesis, the tabulation approach can lead to cumbersome tables and interpolations, or can lead to time-consuming simulation due to property search (especially for non-uniform tables). In addition, and more importantly, due to the exponential increase in memory with the number of chemical species, the tabulation approach can only be used to simulate flows with few species, typically no more than three. Therefore, an alternative to tabulation is needed in order to use the RFM model for combustion, for example.

In recent years, different researchers proposed the application of Machine Learning (ML) and Artificial Neural Networks (ANN) for tackling the complex issue of real fluid simulations using a larger number of chemical species. ANNs are recently being studied as a promising tool for CFD to accelerate modeling techniques. A variety of recent works demonstrate the capability of ANN in modeling various types of flows involving turbulence modeling, integrating combustion chemistry, multiphase flows for spray modelings, etc. [133–136]. Particularly, a comprehensive review and overview of past history, current developments, and emerging opportunities of ML for fluid mechanics for understanding, modeling, optimizing, and controlling fluid flows can be found in Brunton et al. [135]. Besides, various YouTube videos for CFD simulations in different applications collected by Prof. Brunton can be found in [137].

Meanwhile, a very recent study by Koukouvinis et al. [136] applied the ANN regression/fitting technique as an alternative to the tabulation of real fluid state equation which demonstrates a good prediction of real fluid thermodynamic properties for the simulation of ECN Spray A injection conditions.

Hence, the next studies will be assigned to:

- Implementation of the real fluid model using the ANN approach for CFD simulations.
- Continue the cavitation nozzle case modeling with a high-efficient model until the steady state. More explorations are essential to unravel the connections between cavitation and turbulence.
- Simulate a more realistic injection process with the consideration of needle movements.

## 6.3 Sommaire et conclusions

Cette thèse est motivée par un contexte passionnant cherchant à contribuer à la transition énergétique vers la neutralité carbone. Dans ce but, un modèle CFD capable de prédire différents jets de fluides réels se mélangeant dans des conditions sous-critiques et supercritiques a été développé et validé dans cette thèse. Ce modèle diphasique est basé sur une méthode d'interface diffuse (DIM) considérant la théorie de l'équilibre des phases en utilisant différentes équations d'état (EoS) pour simuler simultanément les écoulements sous-critiques et supercritiques ainsi que la transition entre les deux. Le modèle de fluide réel (RFM) a été couplé à la bibliothèque thermodynamique IFPEN-Carnot en utilisant une méthode de tabulation généralisée pour gagner en efficacité et en robustesse de calcul. À notre connaissance, la plupart des solveurs d'équilibre d'écoulement diphasique disponibles dans la littérature sont proposés de manière à ce que l'état thermodynamique dans chaque cellule de calcul soit déterminé après avoir résolu les équations de masse, de quantité de mouvement et d'énergie [17, 22, 34, 35, 53, 83]. Par conséquent, une réalisation importante de cette étude est liée au couplage fort du solveur d'écoulement avec le solveur thermodynamique par rapport aux approches conventionnelles. Cette thèse se compose de six chapitres, y compris certains matériaux dans 3 annexes.

Après le contexte et la motivation détaillés dans le **Chapitre 1**, le **Chapitre 2** a été consacré à l'explication et à la révision des concepts physiques et des modèles classiques disponibles pour les écoulements diphasiques à un ou plusieurs composants sous différents régimes thermodynamiques tels que sous-critique, transcritique et supercritique. En outre, une revue de la littérature ainsi que les concepts thermodynamiques et mathématiques ont été présentés dans ce chapitre.

Ensuite, les principales contributions et discussions pour le développement d'un modèle de fluide réel (RFM) pour la simulation d'écoulements diphasiques sont présentées dans les **chapitres 3 et 4**.

Plus précisément, les équations directrices, la tabulation thermodynamique et les méthodes de recherche utilisant la tabulation uniforme sont présentées dans le **Chapitre 3**. Les algorithmes SIMPLE et PISO modifiés pour le modèle RFM sont également détaillés.

Dans le **Chapitre 4**, après un bref rappel de l'approche de tabulation VLE, les difficultés de tabulation des propriétés à partir des algorithmes VLE sont expliquées, et les raisons pour lesquelles le raffinement des tables de grille à proximité de la frontière de phase est nécessaire ont été dis-

cutées. Ensuite, différentes études ont été présentées pour diverses approches de raffinement de la tabulation, y compris les raffinements uniformes et non uniformes pour les systèmes à un ou plusieurs composants. Ces approches de tabulation ont différentes procédures de génération de table, de recherche et d'interpolation pour lesquelles différents algorithmes ont été développés. Ainsi, les forces et les faiblesses de ces différentes étapes ont été analysées et identifiées. Des simulations académiques ont été réalisées afin de sélectionner la meilleure méthode de tabulation avec un faible coût et des besoins en mémoire réduits. Il a été démontré que le temps de calcul des approches non uniformes, comme l'octree et le quadtree, est très élevé par rapport à l'approche uniforme. Il a également été constaté que ce temps CPU élevé pour l'approche de tabulation non uniforme peut dépasser le temps CPU de l'évaluation directe de la VLE du fluide réel dans le code CFD, sans tabulation, principalement en raison du temps CPU élevé de l'étape de recherche. Par conséquent, bien que certains chercheurs [88–92] aient proposé des approches de tabulation non uniforme, notamment pour raffiner davantage la région proche de la limite de phase, elles ne sont pas recommandées pour les applications industrielles. Par conséquent, une table uniforme hautement raffinée couplée à une stratégie de mémoire partagée a été proposée pour les applications industrielles (sans combustion), qui ne nécessitent que quelques espèces, généralement pas plus de trois. Ainsi, l'utilisation du modèle RFM pour la combustion fait toujours partie des défis futurs.

Dans le **Chapitre 5**, le modèle RFM développé a été appliqué à la simulation d'une série de tests académiques et industriels, pour des configurations 1-D, 2-D et 3-D, à des fins de validation. Différentes équations d'état, à savoir PR et SRK, ont été utilisées pour démontrer principalement l'efficacité, la précision et la robustesse de calcul du modèle RFM proposé couplé à la bibliothèque thermodynamique IFPEN-Carnot. Les différents cas de test sont choisis de manière à couvrir la plupart des régimes thermodynamiques pour différents mélanges afin de quantifier les effets de la thermodynamique réelle des fluides sur des systèmes multi-composants avec différentes physiques. Ce travail a été publié dans plusieurs articles, listés dans la page 2. Plus précisément, le **Chapitre 5** a résumé ces articles, comme suit:

**Dans la section 5.1:**

1. Les études 1-D des cas d'essai de tubes à chocs transcritiques  $N_2$  ont confirmé que les algorithmes SIMPLE et PISO modifiés pour le modèle RFM étaient en bon accord par rapport aux données disponibles dans la littérature.

2. Les études LES du cas cryogénique à un seul composant (azote liquide injecté dans de l'azote gazeux) ont démontré ses caractéristiques d'interface transcritique en présentant le bouclier thermique bien connu, à savoir une couche de capacité thermique isobare importante séparant les régions liquide et gazeuse.
3. L'étude LES de l'injection cryogénique classique d'azote liquide injecté de manière coaxiale avec un jet d'hydrogène chaud a montré quelques phénomènes thermodynamiques intéressants, tels que la condensation de  $H_2$  ainsi que des effets de refroidissement dans la couche biphasée autour du noyau liquide, ce qui démontre la nature sous-critique de l'interface.
4. Un autre phénomène intéressant observé est lié au mélange de  $N_2$  et  $H_2$ , qui a conduit à une augmentation locale des points critiques du mélange. Par conséquent, en raison du processus de mélange autour de l'interface du noyau liquide, certaines zones d'écoulement peuvent passer du régime de mélange monophasique au régime biphasique, induisant condensation et évaporation.
5. Les résultats numériques ont finalement été comparés aux données expérimentales disponibles [29] et aux études numériques publiées [28], avec un accord satisfaisant. De plus, nous avons confirmé l'importance de l'utilisation d'un puissant EoS de fluide réel. Les études actuelles ont montré que l'EoS SRK avait une meilleure prédiction de la densité du fluide par rapport à l'EoS PR, ce qui corrobore les résultats rapportés par [28].

Par ailleurs, **dans la section 5.2:**

1. Différentes études ont été réalisées afin d'explorer l'interaction entre la séparation des phases et la dynamique turbulente des fluides dans les jets d'écoulement supercritiques multi-espèces. Ceci a été fait pour simuler le mélange turbulent de n-hexane injecté dans une chambre remplie d'azote gazeux, en considérant les processus de séparation de phase (condensation) à des conditions de haute pression avec les fluides initialement à un état supercritique. Les conditions sont choisies de manière à couvrir tous les régimes thermodynamiques permettant d'étudier les effets de gaz réel et la séparation de phase pour le mélange multicomposant.
2. Les résultats numériques obtenus ont été montrés et se sont avérés en bon accord avec les expériences [30, 31].
3. En outre, le modèle RFM s'est révélé capable de simuler des jets sous-critiques, transcritiques et supercritiques présentant des processus de séparation de phases et de condensa-

tion.

4. Conséquent, si le jet passe à l'état sous-critique, par rapport au point critique du mélange, il subit le processus classique de formation de gouttelettes régi par l'atomisation du liquide. En revanche, si le n-hexane est injecté à l'état supercritique dans un environnement d'azote plus froid, il peut traverser le dôme biphasé, ce qui entraîne une condensation locale et la formation de gouttelettes principalement à la périphérie du jet. Il a également été démontré qu'une telle condensation ne se produit pas si le n-hexane est injecté à une température supercritique suffisamment élevée.
5. En outre, des comparaisons entre différents modèles de turbulence, y compris des modèles de simulation de grands tourbillons (LES Sigma et Smagorinsky) et un modèle Navier-Stokes moyenné par Reynolds (RANS  $K-\epsilon$ ), ont démontré l'importance d'une modélisation correcte de la turbulence et l'adéquation de l'approche LES-Sigma, en plus des propriétés thermodynamiques et de transport précises, pour ces écoulements de jet très complexes.

Enfin, par rapport aux études précédentes [17, 22, 27], l'efficacité de calcul, la précision et la robustesse du modèle RFM tabulé comme remède à l'évaluation directe d'un solveur d'équilibre de phase coûteux ont été confirmées.

# Appendix

## Appendix A

# One dimensional validation of shock tube test case

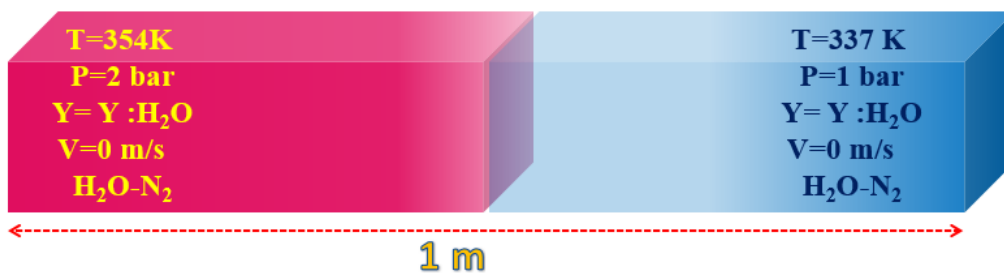


Figure A.1: Schematic representation of  $H_2O - N_2$  mixture along 1m long shock tube test case.

This examination is a classical 1D shock tube test case filled with the binary mixture of  $H_2O - N_2$  along 1m long tube, as shown in figure A.1. This investigates the accuracy of the presented numerical model using PISO and SIMPLE algorithm with available data in the literature [5,53]. The initial discontinuity is located at 0.5 m. The left side with 0.2 MPa is at a higher pressure than the right side considering 0.1 MPa. The temperatures on the left and right-hand sides are set as 354K and 337K, respectively. The computational mesh consists of 1000 cells running over a 1m long tube having four cells in its cross-section. Figure(A.2) and figure(A.3) show the variations of Pressure and Temperature, and velocity in different mass fractions of  $Y_{H_2O} = 0.3$ , and  $Y_{H_2O} = 0.98$ , respectively, along 1m long tube at  $t = 1ms$ . The obtained results using this tabulation approach as well are in good agreement with the available data in the literature [5,53].

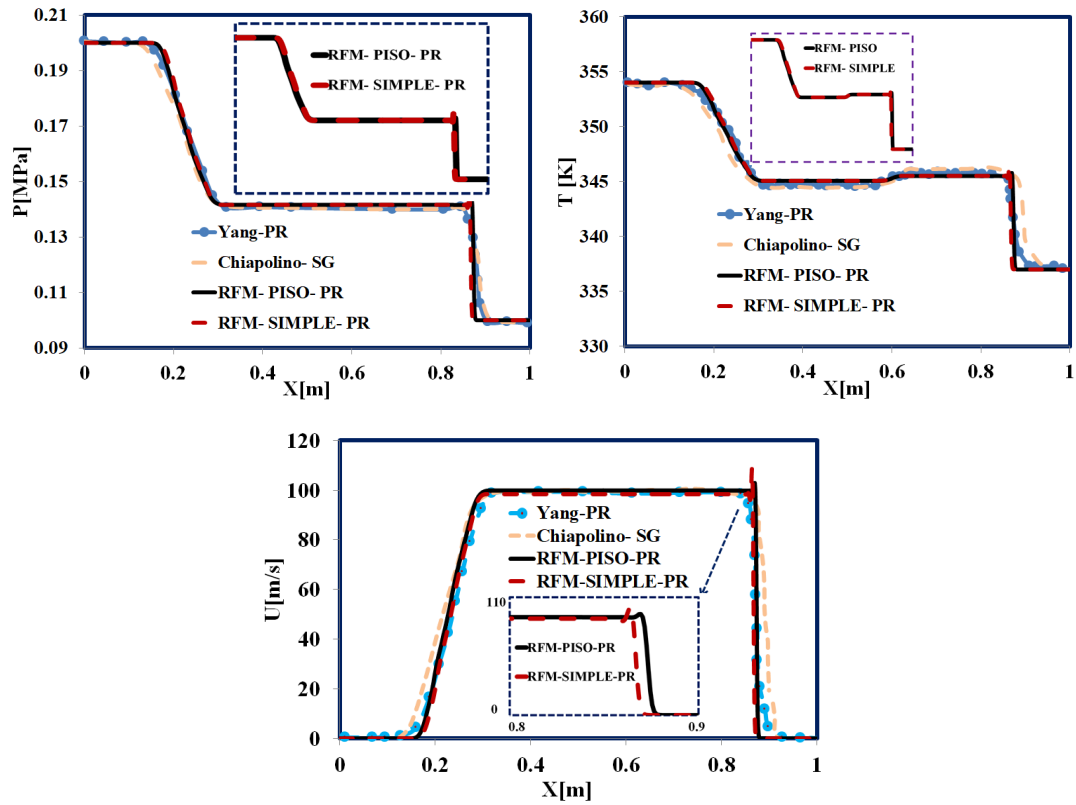


Figure A.2: Comparison between the presented numerical model using PISO, and SIMPLE algorithm with [5, 53] for  $Y_{H_2O} = 0.3$  for the binary mixture of  $H_2O - N_2$  along 1m long tube at  $t = 1ms$ .

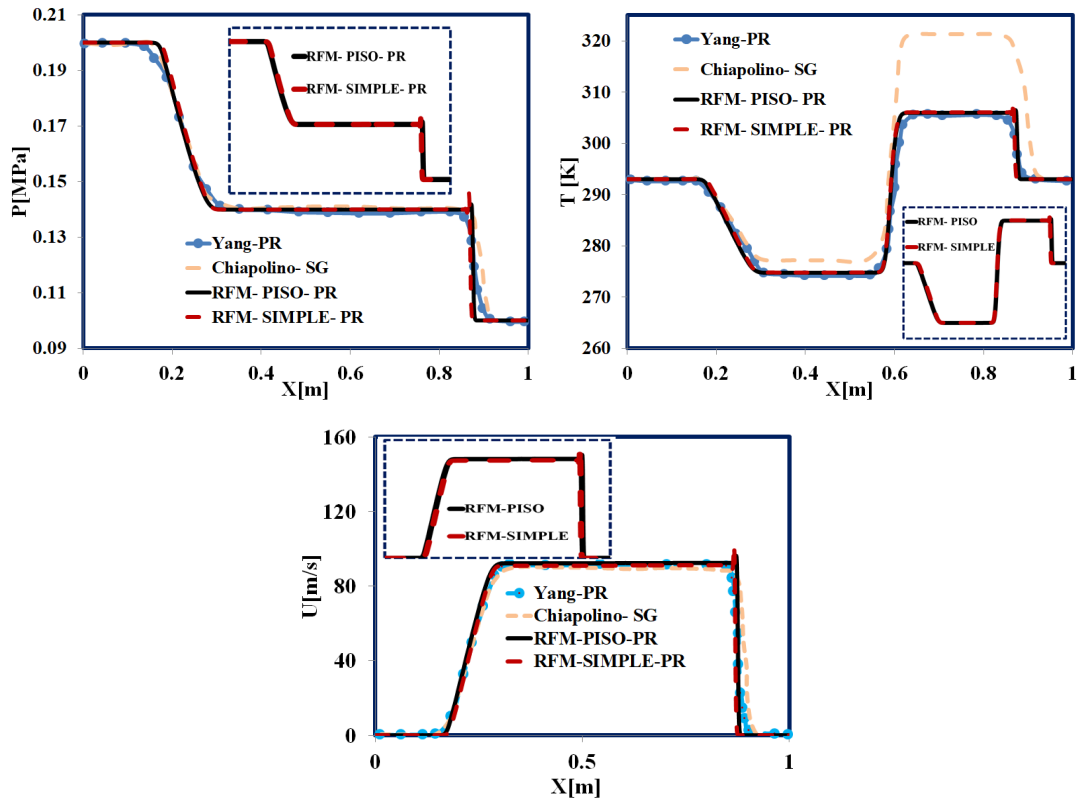


Figure A.3: Comparison between the presented numerical model using PISO, and SIMPLE algorithm with [5, 53] for  $Y_{H_2O} = 0.98$  for the binary mixture of  $H_2O - N_2$  along 1m long tube at  $t = 1ms$ .

## Appendix B

# Mixing layer study of Methane-Oxygen using different EOS

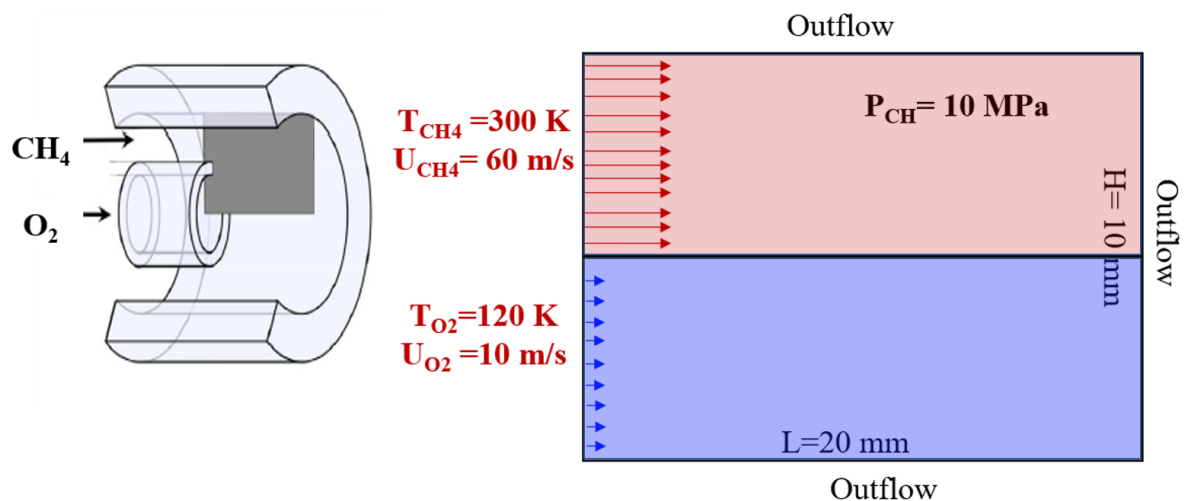


Figure B.1: Mixing layer configuration of methane-oxygen and computational domain. (left) Typical coaxial injector of a liquid rocket engine. (right) Computational domain dimensions and boundary conditions [109, 138].

Figure B.1 demonstrates the mixing layer configuration of methane-oxygen injector (left) and computational domain (right) same as [109, 138]. At the upper half of the inlet, methane flows in at  $60 \text{ m/s}$  and  $300 \text{ K}$ ; at the lower half of the inlet, LOX flows in at  $10 \text{ m/s}$  and  $120 \text{ K}$ . The pressure of  $10 \text{ MPa}$  is chosen the same as that in liquid rocket engines. Figure B.2 shows the comparison of instantaneous methane mass fraction (left) and Temperature (right) using different equations of state, at  $0.125 \text{ ms}$  ( half flow-through-time). Besides, figure B.3 exhibits the comparison of instantaneous sound speed (left) and isobaric heat capacity (right) using different equations of state, at  $0.125 \text{ ms}$ .  $C_{p,mix}$  has the maximum value at the interface.

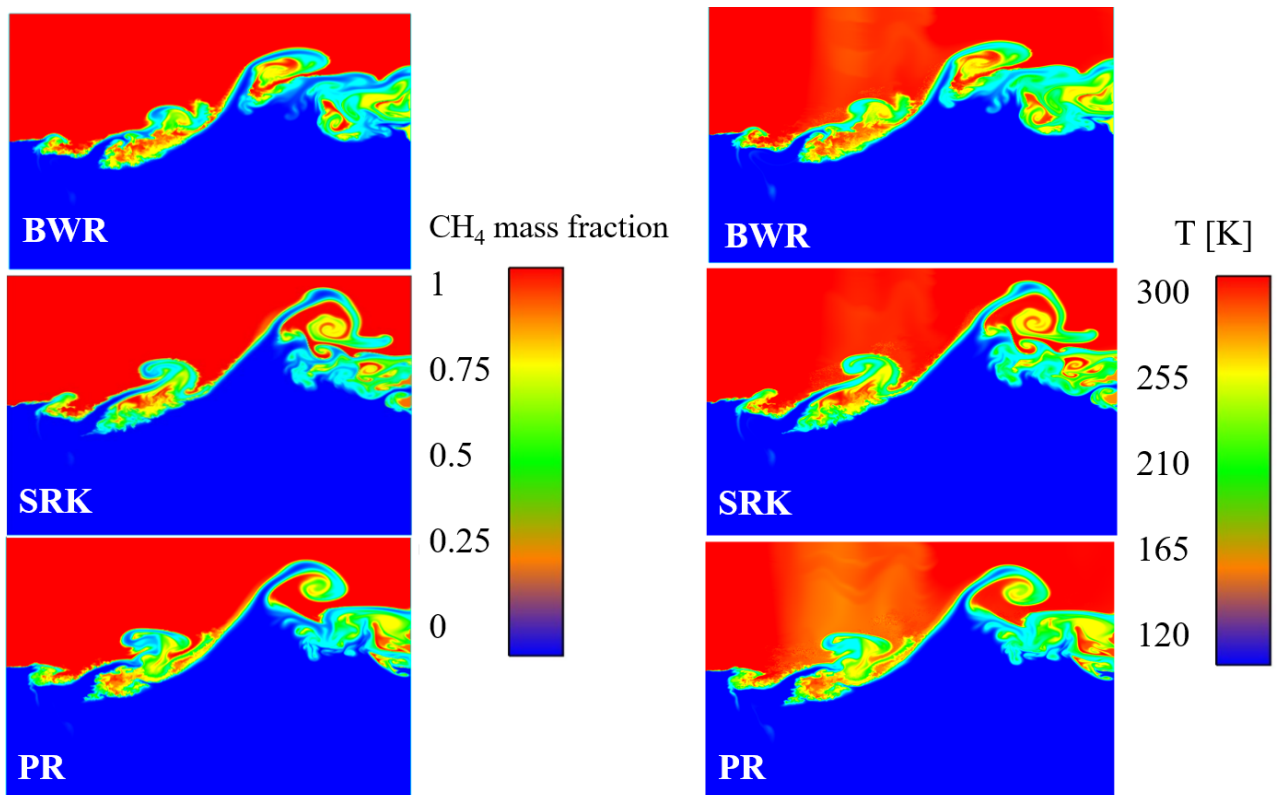


Figure B.2: Comparison of instantaneous methane mass fraction (left) and Temperature (right) using different equations of state, at 0.125 ms ( half flow-through-time).

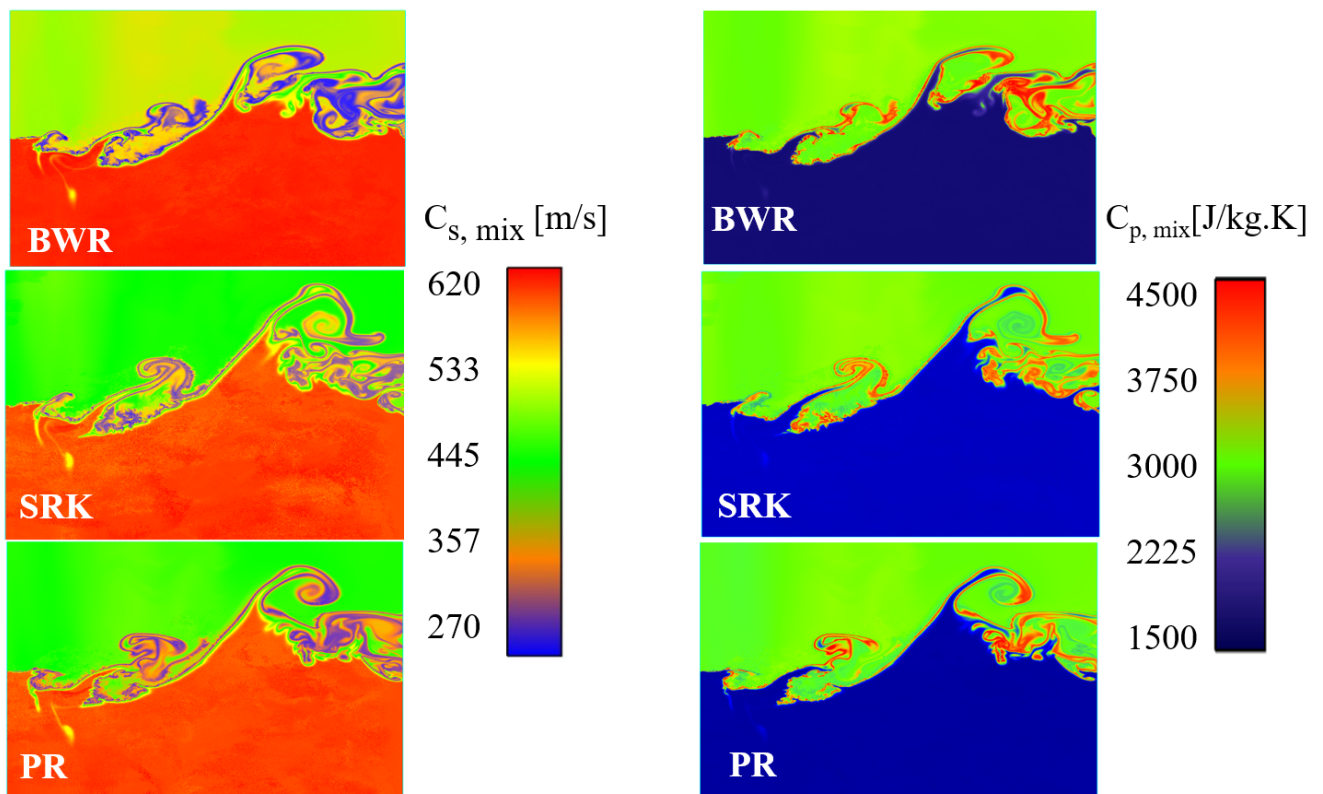


Figure B.3: Comparison of instantaneous sound speed (left) and isobaric heat capacity (right) using different equations of state, at 0.125 ms (half flow-through-time).  $C_{p,mix}$  has the maximum value at the interface.

## Appendix C

### Cavitation

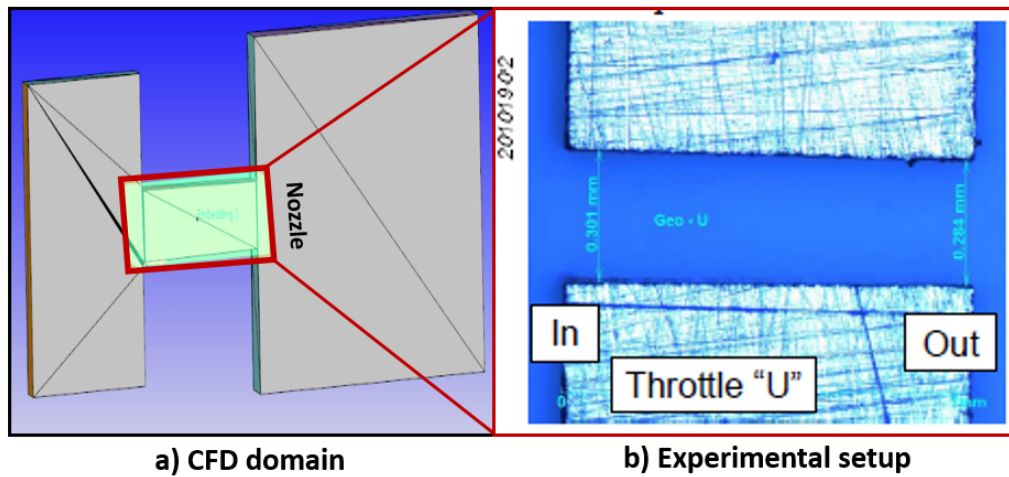


Figure C.1: (a) Schematic of a cavitation injector setup (geometry setup), (b) In addition with the experimental X-ray tomography of Winklhofer cavitation nozzle [139]

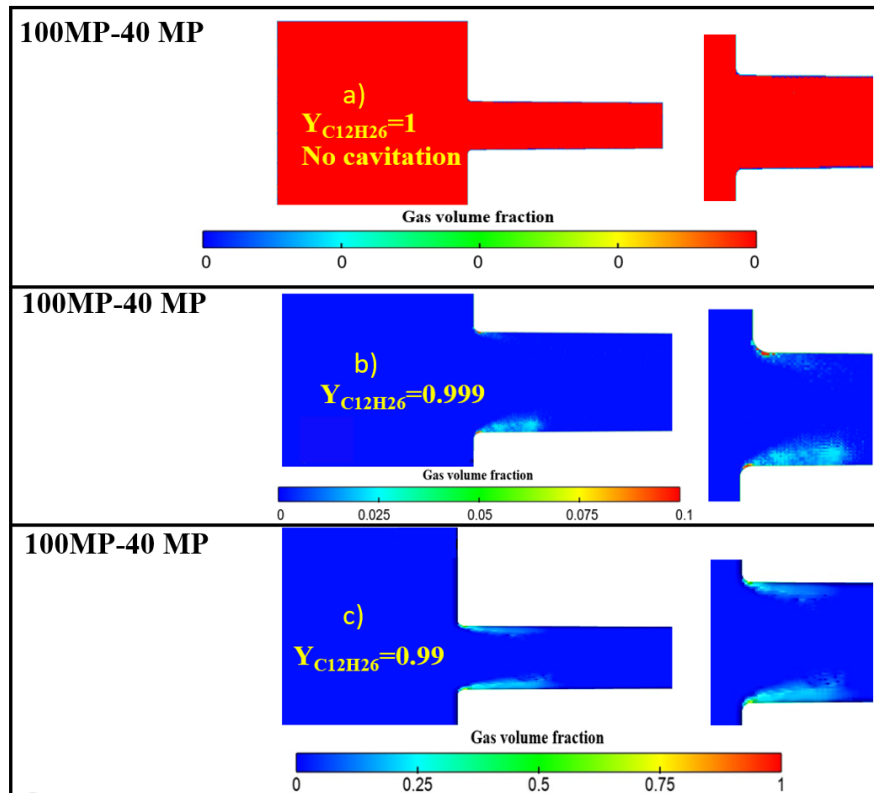


Figure C.2: Gas volume fraction contours for different percentages of nitrogen dissolved gas added to the n-dodecane fuel, as 0%  $N_2$  (a), 0.1%  $N_2$  (b), and 1%  $N_2$  (c). The cavitation intensity increases by adding more nitrogen dissolved gas due to the changing saturation pressure with  $N_2$  concentration, as thermodynamic demonstrates in figure 1.6.

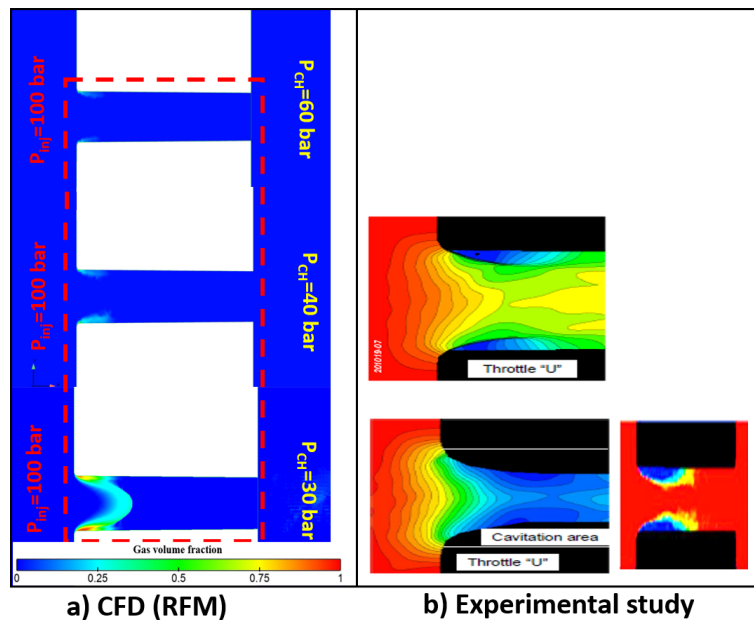


Figure C.3: Gas volume fraction contours for different chamber pressures (various pressure differences between the chamber and the injector), as  $\Delta P = 40MPa$ (a),  $\Delta P = 60MPa$ ,  $\Delta P = 70MPa$ , from top to down, respectively. The cavitation intensity enhances by increasing the pressure differences between the chamber and the injector. Besides, Figure (b) demonstrates the cavitation region experimentally studied by [139].

# Bibliography

- [1] National Centers for Environmental Information, <https://www.ncdc.noaa.gov/sotc/global/2021>
- [2] G. Kalghatgi , A.K. Agarwal, F. Leach, K. Senecal, (eds) Engines and Fuels for Future Transport. Energy, Environment, and Sustainability. Springer, Singapore, 2022. <https://doi.org/10.1007/978-981-16-8717-41>.
- [3] K. Senecal, F. Leach, Racing Toward Zero: The Untold Story of Driving Green, SAE International with a Product Code of R-501, 2021, ISBN of 978-1-4686-0146-6.
- [4] P. Domingo-Alvarez, High-pressure combustion large-eddy simulation for an a priori optical diagnostics validation. Thermics [physics.class-ph]. Normandie Université, 2019. English.2019.
- [5] S. Yang, Modeling of Diesel Injection in Subcritical and Supercritical Conditions, 2019. PhD dissertation, University of Paris-Saclay.
- [6] M. Pelletier, Diffuse interface models and adapted numerical schemes for the simulation of subcritical to supercritical flows. Other. Université Paris-Saclay, 2019. English. 2019SACLC059.
- [7] M. Pelletier, Th. Schmitt, S. Ducruix, A multifluid Taylor-Galerkin methodology for the simulation of compressible multicomponent separate two-phase flows from subcritical to supercritical states, Computers Fluids, Volume 206, 2020, 104588, <https://doi.org/10.1016/j.compfluid.2020.104588>.
- [8] A. P. Singh, A. Jain, and A. K. Agarwal. Fuel-Injection Strategy for PCCI Engine Fueled by Mineral Diesel and Biodiesel Blends, Energy and Fuels, 2017, 31 (8):8594–607. ACS Publications, <https://doi:10.1021/ACS.ENERGYFUELS.6B03393>.
- [9] Y. Takagi, H. Mori, Y. Mihara, N. Kawahara, E. Tomita, Improvement of thermal efficiency and reduction of NOx emissions by burning a controlled jet plume

- in high pressure direct-injection hydrogen engines. *Int J Hydrogen Energy* 2019, <https://doi.org/10.1016/j.ijhydene.2017.08.015>.
- [10] D.N. Cao, A.T. Hoang, H.Q. Luu, V.G. Bui, and T.T. Huong Tran, Effects of injection pressure on the NO<sub>x</sub> and PM emission control of diesel engine: A review under the aspect of PCCI combustion condition, *Energy Sources, Part A: Recovery, Utilization, and Environmental Effects*, 2020, DOI: 0.1080/15567036.2020.1754531
- [11] I. Stotz, G. Lamanna and B. Weigand, Fluid disintegration studies in a specialized shock tube, *EUCASS Proceedings Series – Advances in AeroSpace Sciences*, 2, 2011, 165-206, <https://doi.org/10.1051/eucass/201102165>.
- [12] R.N. Dahms, J.C. Oefelein, On the transition between two-phase and single-phase interface dynamics in multicomponent fluids at supercritical pressures, *Phys Fluids*, 25(9), 2013, pp.092103 -92127,10.1063/1.4820346. <https://doi.org/10.1063/1.4820346>
- [13] J. Manin, M. Bardi, L.M. Pickett, R.N. Dahms, J.C. Oefelein, Microscopic investigation of the atomization and mixing processes of diesel sprays injected into high pressure and temperature environments, *Fuel*, Volume 134, 2014, Pages 531-543, <https://doi.org/10.1016/j.fuel.2014.05.060>.
- [14] J. Cahn, J. Hilliard, Free energy of a nonuniform system. I. Interfacial free energy. *J. Chem. Phys.* 28, 258, 1958, <https://doi.org/10.1063/1.1744102>.
- [15] R. Saurel, C. Pantano, Diffuse-Interface Capturing Methods for Compressible Two-Phase Flows, *Annual Review of Fluid Mechanics*, 2018, 105-130, 10.1146, <https://doi.org/10.1146/annurev-fluid-122316-050109>.
- [16] W.A Sirignano, J.P. Delplanque, Transcritical vaporization of liquid fuels and propellants. *J Propul Power*, 15, 1999, pp. 806-902. <https://doi.org/10.2514/2.5513>.
- [17] S. Yang, P. Yi, and C. Habchi, Real-fluid injection modeling and LES simulation of the ECN Spray A injector using a fully compressible two-phase flow approach. *International Journal of Multiphase Flow*, 2020. 122: p. 103145. <https://doi.org/10.1016/j.ijmultiphaseflow.2019.103145>.
- [18] C. Crua, J. Manin, and L.M. Pickett, On the transcritical mixing of fuels at diesel engine conditions *Fuel*, 208, 2017, pp. 535-548. <https://doi.org/10.1016/j.fuel.2017.06.091>.

- [19] J. Bellan, Supercritical (and subcritical) fluid behavior and modeling: Drops, streams, shear and mixing layers, jets and sprays, 2000, Progress in Energy and Combustion Science, 26 (4-6):329–366. [https://doi.org/10.1016/S0360-1285\(00\)00008-3](https://doi.org/10.1016/S0360-1285(00)00008-3).
- [20] D.T. Banuti, Crossing the Widom-line—Supercritical pseudo-boiling. J. Supercrit. Fluids 2015, 98, 12–16. <https://doi.org/10.1016/j.supflu.2014.12.019>.
- [21] W.O. Mayer, A. Schik, M. Schaffler, and H. Tamura, Injection and mixing processes in high-pressure liquid oxygen/gaseous hydrogen rocket combustors. J Propul Power, 16, 2000, pp. 823-828. <https://doi.org/10.2514/2.5647>.
- [22] P. Yi, S. Yang, C. Habchi, and R. Lugo, A multicomponent real-fluid fully compressible four-equation model for two-phase flow with phase change, 2019. Phys. Fluids 31 (2), 026102. <https://doi.org/10.1063/1.5065781>.
- [23] B. Chehroudi, D. Talley, W. Mayer; R. Branam, J.J. Smith, A. Schik, and M. Oswald, Understanding injection into high pressure supercritical environments. Fifth international symposium on liquid space propulsion, long life combustion devices technology, NASA Marshall Spaceflight Center, Huntsville, 2003, pp. 27-30
- [24] L. Jofre, J. Urzay, Transcritical diffuse-interface hydrodynamics of propellants in high-pressure combustors of chemical propulsion systems, Progress in Energy and Combustion Science, 2021, Volume 82, 100877, <https://doi.org/10.1016/j.pecs.2020.100877>
- [25] V. Gerber, S. Baab, F.J. Förster, H. Mandler, B. Weigand, and G. Lamanna, Fluid injection with supercritical reservoir conditions: Overview on morphology and mixing, J. Supercrit. Fluids 169 (2021) 105097, <http://dx.doi.org/10.1016/j.supflu.2020.105097>.
- [26] D. J. Duke, <https://daniel-duke.net/media/> : Synchrotron X-ray Radiography of Nozzle Cavitation.
- [27] S. Yang, C. Habchi, Real-fluid phase transition in cavitation modeling considering dissolved non-condensable gas, 2020, Physics of Fluids 32(3): 032102. <https://doi.org/10.1063/1.5140981>.
- [28] J. Matheis, H. Müller, S. Hickel, and M. Pfitzner, Large-Eddy Simulation of Cryogenic Jet Injection at Supercritical Pressures, 2020, High-Pressure Flows for Propulsion Applications, Vol. 260. 531-570. <https://doi.org/10.2514/5.9781624105814.0531.0570>.

- [29] M. Oswald, A. Schik, M. Klar, and W. Mayer, "Investigation of coaxial LN<sub>2</sub>/GH<sub>2</sub>-injection at supercritical pressure by spontaneous Raman scattering, 1999, AIAA 1999-2887. 35th Joint Propulsion Conference and Exhibit.
- [30] C. Traxinger, M. Pfitzner, S. Baab, and G. Lamana, Experimental and numerical investigation of phase separation due to multicomponent mixing at high-pressure conditions, *Phys. Rev. Fluids* (2019), vol. 4, p. 074303, <https://doi.org/10.1103/PhysRevFluids.4.074303>.
- [31] S. Baab, C. Steinhausen, G. Lamanna, B. Weigand, and F.J. Förster, A quantitative speed of sound database for multi-component jet mixing at high pressure, *Fuel*, 2018, 233:918–925, <https://doi.org/10.1016/J.FUEL.2017.12.080>.
- [32] R.N. Dahms, J.C. Oefelein, On the transition between two-phase and single-phase interface dynamics in multicomponent fluids at supercritical pressures. *Phys. Fluids*, 2013, 25, 092103.
- [33] T. Andrews, The Bakerian lecture—On the continuity of the gaseous and liquid states of matter, 1869, *Philos. Trans. R. Soc. London* 159, 575, DOI:10.1098/rstl.1869.0021.
- [34] P.C. Ma, Y. Lv, and M. Ihme, An entropy-stable hybrid scheme for simulations of transcritical real-fluid flows. *Journal of Computational Physics*, 2017. 340: p. 330-357. <https://doi.org/10.1016/j.jcp.2017.03.022>
- [35] P.C Ma, H. Wu, D.T. Banuti, and M. Ihme, On the numerical behavior of diffuse-interface methods for transcritical real-fluids simulations, 2019, *Int. J. Multiph. Flow* 113, 231–249. <https://doi.org/10.1016/j.ijmultiphaseflow.2019.01.015>.
- [36] P.E. Lapenna, Thermodynamic Small Scales in Transcritical Turbulent Jets, 2021, AIAA journal, <https://doi.org/10.2514/1.J059664>.
- [37] A. Doehring, T. Kaller, S.J. Schmidt, and N.A. Adams Large-eddy simulation of turbulent channel flow at transcritical states, 2021, *International Journal of Heat and Fluid Flow*, Volume 89, 108781. <https://doi.org/10.1016/j.ijheatfluidflow.2021.108781>.
- [38] B.M. Ninge Gowda, F.N.Z. Rahantamialisoa, A. Pandal, H. Jasak, H.G. Im, and M. Battistoni, Numerical Modeling of Transcritical and Supercritical Fuel Injections Using a Multi-Component Two-Phase Flow Model, 2020, *Energies*, 13, 5676, <https://doi.org/10.3390/en13215676>.

- [39] V. Gerber, S. Baab, B. Weigand, and G. Lamanna, Enhanced Rayleigh scattering in supercritical fluid injection across the Widom line, *Atomization and Sprays*, Vol. 30, No. 12, 2020, pp. 881–893, DOI: 10.1615/AtomizSpr.2020035322.
- [40] K. Nishikawa, A.A. Arai, and T. Morita, Density fluctuation of supercritical fluids obtained from small-angle X-ray scattering experiment and thermodynamic calculation, *J. Supercrit. Fluids*, vol. 30, no. 3, pp. 249–257, 2004. <https://doi.org/10.1016/j.supflu.2003.09.003>.
- [41] P. Gallo, D. Corradini, and M. Rovere, Widom line and dynamical crossovers as routes to understand supercritical water, 2014, *Nat Commun* 5, 5806. <https://doi.org/10.1038/ncomms6806>.
- [42] L. Xu, P. Kumar, S. V. Buldyrev, S.-H. Chen, P. H. Poole, F. Sciortino, and H. E Stanley, Relation between the Widom line and the dynamic crossover in systems with a liquid–liquid phase transition, *Proceedings of the National Academy of Sciences* Nov, 2005, 102 (46), 16558–16562, <https://doi.org/10.1073/pnas.0507870102>
- [43] M. L. Michelsen, The isothermal flash problem, Part I. Phase split calculation, 1982, *Fluid Phase Equilib.*, vol. 9, pp. 1–19, [https://doi.org/10.1016/0378-3812\(82\)85002-4](https://doi.org/10.1016/0378-3812(82)85002-4).
- [44] D. Ayyappan, A. Vaidyanathan, C.K. Muthukumar, and K. Nandakumar, Transition of subcritical liquid jets in single and multicomponent systems, 2018, *Physics of Fluids* 30, 104106, <https://doi.org/10.1063/1.5045605>
- [45] W. Ning, R.D. Reitz, A.M. Lippert, and R. Diwakar, Development of a Next-generation Spray and Atomization Model Using an Eulerian- Lagrangian Methodology, 17th Int. Multidimens. Engine Model. User’s Gr. Meet., 2007.
- [46] S. Mirjalili, S. S. Jain, and M. Dodd, Interface-capturing methods for two-phase flows: An overview and recent developments. Center for Turbulence Research Annual Research Briefs, 2017, 117–135, <https://doddm.com/publications/2017-ctr-sm-sj-md.pdf> (accessed on 14 December 2021).
- [47] M. Baer, and J. Nunziato, A two-phase mixture theory for the deflagration-to-detonation transition (DDT) in reactive granular materials. *Int. J. Multiphase Flow*, 1986, 12:861–89, [https://doi.org/10.1016/0301-9322\(86\)90033-9](https://doi.org/10.1016/0301-9322(86)90033-9).
- [48] C. Pantano, R. Saurel, and T. Schmitt, An oscillation free shock-capturing method for compressible van der Waals supercritical fluid flows, 2017, *J. Comput. Phys.*, vol. 335, pp.

- 780–811, <https://doi.org/10.1016/j.jcp.2017.01.057>.
- [49] C. W. Hirt, and B. D. Nichols, Volume of fluid (vof) method for the dynamics of free boundaries, *Journal of Computational Physics*, 1981, 39, 201-225, [https://doi.org/10.1016/0021-9991\(81\)90145-5](https://doi.org/10.1016/0021-9991(81)90145-5).
- [50] R. Scardovelli, and S. Zaleski, Analytical relations connecting linear interfaces and volume fractions in rectangular grids, *Journal of Computational Physics*, 2000, 164, 228-237, <https://doi.org/10.1006/jcph.2000.6567>.
- [51] M.N. Mastrone, E.A. Hartono, V. Chernoray, and F. Concli, Oil distribution and churning losses of gearboxes: experimental and numerical analysis, 2020, *Tribol Int*, 151, p. 106496, [doi:10.1016/j.triboint.2020.106496](https://doi.org/10.1016/j.triboint.2020.106496).
- [52] Q. Peng; L. Gui, and Z. Fan, Numerical and experimental investigation of splashing oil flow in a hypoid gearbox, 2018, *Engineering Applications of Computational Fluid Mechanics*, 12(1), 324–333. [doi:10.1080/19942060.2018.1432506](https://doi.org/10.1080/19942060.2018.1432506)
- [53] A. Chiapolino, P. Boivin, and R. Saurel, A simple phase transition relaxation solver for liquid-vapor flows, 2017, *International Journal for Numerical Methods in Fluids*, 83(7):583–605. ISSN 02712091, <https://doi.org/10.1002/fld.4282>.
- [54] A. Zein, M. Hantke, and G. Warnecke, Modeling phase transition for compressible two-phase flows applied to metastable liquids, 2010, *J. Comput. Phys.*, vol. 229, no. 8, pp. 2964–2998, <https://doi.org/10.1016/j.jcp.2009.12.026>.
- [55] S. Mirjalili, C. B. Ivey, A. Mani, Comparison between the diffuse interface and volume of fluid methods for simulating two-phase flows, *International Journal of Multiphase Flow*, 2019, 116, 221-238, <https://doi.org/10.1016/j.ijmultiphaseflow.2019.04.019>.
- [56] V. Boniou, T. Schmitt, and A. Vié. Comparison of interface capturing methods for the simulation of two-phase flow in a unified low-Mach framework. 2021. [fhal-03241460](https://arxiv.org/abs/2106.01864), <https://arxiv.org/abs/2106.01864>.
- [57] S. Osher, and R.P. Fedkiw, Level set methods: an overview and some recent results, *Journal of Computational physics* 2001, 169(2), 463-502, <https://doi.org/10.1006/jcph.2000.6636>.
- [58] J.A. Sethian, and P. Smereka, Level set methods for fluid interfaces, *Annual Review of Fluid Mechanics*, 2003, 35(1), 341-372, [DOI:10.1146/ANNUREV.FLUID.35.101101.161105](https://doi.org/10.1146/ANNUREV.FLUID.35.101101.161105).

- [59] O. Desjardins, V. Moureau, and H. Pitsch, An accurate conservative level set/ghost fluid method for simulating turbulent atomization, *J. Comput. Phys.*, 2008, 227, 8395-8416, <https://doi.org/10.1016/j.jcp.2008.05.027>.
- [60] A. Umemura, J. Shinjo, Detailed SGS atomization model and its implementation to two-phase flow LES, *Combustion and Flame*, 2018, Volume 195, Pages 232-252, ISSN 0010-2180, <https://doi.org/10.1016/j.combustflame.2018.01.026>.
- [61] J.P. Legier, T. Poinsot, and D. Veynante, Dynamically thickened flame LES model for premixed and non-premixed turbulent combustion, 2000, Proceedings of the Summer Program, Center for Turbulence Research, <https://web.stanford.edu/group/ctr/ctrsp00/poinsot.pdf>.
- [62] B.M. Devassy, C. Habchi, and E. Daniel, Atomization Modelling of Liquid Jets Using a Two-Surface-Density Approach, 2015, *At. Sprays*, vol. 25, no. 1, pp. 47–80, DOI: 10.1615/AtomizSpr.2014011350.
- [63] K.J. Richards, P.K. Senecal, and E. Pomraning, CONVERGE 3.0, Convergent Science, Madison, WI, 2021, <https://convergecf.com>.
- [64] D.-Y Peng, and D. B. Robinson, A new two-constant equation of state, 1976, *Ind. Eng. Chem. Fundam.* 15, 59–64, DOI:10.1021/I160057A011.
- [65] G. Soave, Equilibrium constants from a modified redlichkwong equation of state, 1972, *Chemical Engineering Science*, 27(6): 1197–1203, [https://doi.org/10.1016/0009-2509\(72\)80096-4](https://doi.org/10.1016/0009-2509(72)80096-4).
- [66] P. Linstrom; and W. Mallard, The NIST Chemistry WebBook: A Chemical Data Resource on the Internet, *Journal of Chemical and Engineering Data*, 2001, vol. 46, no. 5, pp. 1059–1063.
- [67] D. Banuti, and K. Hannemann, Efficient multiphase rocket propellant injection model with high quality equation of state. 2014, In Proceedings of of the 4th Space Propulsion Conference.
- [68] T.H. Chung, M. Ajlan, L.L. Lee, and K.E. Starling, Generalized multi-parameter correlation for non-polar and polar fluid transport properties, 1988, *Industrial Engineering Chemistry Research*, 27(4): 671–679, DOI: 10.1021/IE00076A024.
- [69] Y. Bartosiewicz, and J.-M. Seynhaeve, Delayed Equilibrium Model (DEM) of Flashing Choked Flows Relevant to LOCA and Implementation in System Codes, *MultScienTechn*

- 25(2-4):117–131, 2013, DOI:10.1615/MultScienTechn.v25.i2-4.50.
- [70] S. Saha, and J. J. Carroll, The isoenergetic-isochoric flash, 1997, *Fluid Phase Equilib.*, vol. 138, pp. 23–41, [https://doi.org/10.1016/S0378-3812\(97\)00151-9](https://doi.org/10.1016/S0378-3812(97)00151-9).
- [71] J.C. De Hemptinne, J.M Ledanois, P. Mougin, and A. Barreau, *Select Thermodynamic Models for Process Simulation Editions Technip*, Paris, 2012. ISBN: 9781621986843 1621986845.
- [72] G. Jacobsohn, C. Mohapatra, R. Grover, and D. Duke, et al., Comparison of Turbulence Modeling Methods for Evaluating GDI Sprays with Transient Needle Motion, SAE Technical Paper 2019-01-0271, 2019, <https://doi.org/10.4271/2019-01-0271>.
- [73] S. K. Rachakonda, A. Paydarfar, and D. P. Schmidt, Prediction of spray collapse in multi-hole gasoline direct-injection fuel injectors, 2019, *International Journal of Engine Research*, 20(1), pp. 18–33. doi: 10.1177/1468087418819527.
- [74] K. Saha, S. Quan, M. Battistoni, S. Som, et al., Coupled Eulerian Internal Nozzle Flow and Lagrangian Spray Simulations for GDI Systems, SAE Technical Paper 2017-01-0834, 2017, <https://doi.org/10.4271/2017-01-0834>
- [75] Z. Bilicki, and J. Kestin, Physical Aspects of the Relaxation Model in Two-Phase Flow, *Proceedings of the Royal Society of London A*, 428(1875), 379-397, 1990. <https://doi.org/10.1098/rspa.1990.0040>.
- [76] J. D. Van der Waals, The equation of state for gases and liquids: Nobel Lecture, December 12, 1910". Nobel Lectures, Physics 1901–1921. Amsterdam: Elsevier Publishing Company. 1967. pp. 254–265. Archived from the original on 10 April 2020.
- [77] P. Ma, Modeling of turbulent mixing and combustion at transcritical conditions, 2018. PhD dissertation, Stanford University.
- [78] P. Yi, S. Jafari, S. Yang, and C. Habchi, Numerical analysis of subcritical evaporation and transcritical mixing of droplet using a tabulated multicomponent vapor-liquid equilibrium model, 2019, ILASS–Europe 2019, 29th Conference on Liquid Atomization and Spray Systems.
- [79] P. Sagaut, *Large-Eddy Simulation for Incompressible Flows*, 3rd edn. Scientific Computation, 2005, Springer, Berlin Heidelberg New York.

- [80] M. L. Michelsen, The isothermal flash problem, Part II. Phase split calculation, 1982, *Fluid Phase Equilib.*, vol. 9, pp. 21–40, [https://doi.org/10.1016/0378-3812\(82\)85002-4](https://doi.org/10.1016/0378-3812(82)85002-4).
- [81] C. Ware, W. Knight, and D. Wells, Memory intensive statistical algorithms for multi-beam bathymetric data, 1991, *Computers Geosciences*, vol. 17, no. 7, pp. 985–993, DOI: 10.1016/0098-3004(91)90093-S.
- [82] W. B. Streett, and J. C. G Calado; Liquid-vapour equilibrium for hydrogen+ nitrogen at temperatures from 63 to 110 k and pressures to 57 mpa. 1978, *The Journal of Chemical Thermodynamics*, 10(11):10891100, [https://doi.org/10.1016/0021-9614\(78\)90083-6](https://doi.org/10.1016/0021-9614(78)90083-6).
- [83] B. Boyd, D. Jarrahbashi, A diffuse-interface method for reducing spurious pressure oscillations in multicomponent transcritical flow simulations, 2021, *Computers and Fluids*, doi: <https://doi.org/10.1016/j.compfluid.2021.104924>.
- [84] R.I. Issa, A.D. Gosman, and A.P Watkins, The Computation of Compressible and Incompressible Recirculating Flows by a Non-Iterative Implicit Scheme, 1986, *Journal of Computational Physics*, 62, 66-82, [https://doi.org/10.1016/0021-9991\(86\)90100-2](https://doi.org/10.1016/0021-9991(86)90100-2).
- [85] S.V. Patankar, *Numerical Heat Transfer and Fluid Flow*, 1980, Hemisphere Publishing Corporation, New York – London. McGraw Hill Book Company, New York 1980. 1. Aufl., 197 S., 76 Abb., geb., DM 71,90.
- [86] P. Koukouvinis, A. Vidal-Roncero, C. Rodriguez, M. Gavaises; , and L. Pickett, High pressure/high temperature multiphase simulations of dodecane injection to nitrogen: application on ECN Spray – a, 2020, *Fuel*, 275, <https://doi.org/10.1016/j.fuel.2020.117871>.
- [87] S. Brown, L. Peristeras, S. Martynov, R.T.J. Porter, H. Mahgerefteh, I. Nikolaidis, G. Boulougouris, D. Tsangaris, ; and I. Economou, Thermodynamic interpolation for the simulation of two-phase flow of non-ideal mixtures, 2016, *Comput. Chem. Eng.*, 95, pp. 49-57, <https://doi.org/10.1016/j.compchemeng.2016.09.005>.
- [88] AR. Azimian, J. Arriagada, and M. Assadi, Generation of steam tables using artificial neural networks, 2004, *Heat Transfer Engineering*, vol. 25, no. 2, pp. 41-51, <https://doi.org/10.1080/01457630490276132>.
- [89] M. De Lorenzo, P. Lafon, M. Di Matteo, M. Pelanti, J. M. Seynhaeve, and Y. Bartosiewicz, Homogeneous two-phase flow models and accurate steam-water table look-up method for

- fast transient simulations, 2017, *International Journal of Multiphase Flow*, 95 :199219, <https://doi.org/10.1016/j.ijmultiphaseflow.2017.06.001>.
- [90] Y. Fang, M. De Lorenzo, Ph. Lafon, S. Poncet, and Y. Bartosiewicz, An Accurate and Efficient Look-up Table Equation of State for Two-phase Compressible Flow Simulations of Carbon Dioxide, 2018, *Industrial Engineering Chemistry Research*, <https://doi.org/10.1021/acs.iecr.8b00507>.
- [91] F. Foll, T. Hitz, C. Muller, C.-D. Munz, and M. Dumbser, On the use of tabulated equations of state for multi-phase simulations in the homogeneous equilibrium limit, 2019, *Shock Waves* 29 769–793. doi:10.1007/s00193-019-00896-1.
- [92] S. Praneeth, and J.-P. Hickey, Uncertainty quantification of tabulated supercritical thermodynamics for compressible Navier–Stokes solvers, 2018, <https://arxiv.org/abs/1801.06562>.
- [93] A. B. Wood, *A Textbook of Sound*. Third Edition. Bell, London, 1955. 610 pp. Illustrated. 42s.,” *J. R. Aeronaut. Soc.*, 2016, doi:10.1017/S0368393100130998.
- [94] A. V. AHO, J. E. HOPCROFT, and J. D. ULLMAN, *Data Structures Algorithms*. Addison-Wesley, Reading, MA, 1983.
- [95] M. A. Weiss, *Data Structures and Algorithm Analysis in C++*, Pearson Education. ISBN 978-81-317-1474-4, 2009.
- [96] C. Burstedde, L.C. Wilcox, and O. Ghattas p4est: scalable algorithms for parallel adaptive mesh refinement on forests of octrees *SIAM, J. Sci. Comput.*, 33 (2011), pp. 1103-1133
- [97] Y. Zeng, A. Xuan, J. Blaschke, L. Shen, A parallel cell-centered adaptive level set framework for efficient simulation of two-phase flows with subcycling and non-subcycling, *Journal of Computational Physics*, Volume 448, 2022, 110740, <https://doi.org/10.1016/j.jcp.2021.110740>.
- [98] D. Fuster, A. Bagué, T. Boeck, L. Le Moyne, A. Leboissetier, S. Popinet, P. Ray, R. Scardovelli, S. Zaleski, Simulation of primary atomization with an octree adaptive mesh refinement and VOF method, *International Journal of Multiphase Flow*, Volume 35, Issue 6, 2009, Pages 550-565, <https://doi.org/10.1016/j.ijmultiphaseflow.2009.02.014>.
- [99] H. Samet, J. Sankaranarayanan, and M. Auerbach. Indexing methods for moving object databases: games and other applications. In *SIGMOD*, pages 169–180, 2013, <https://doi.org/10.1145/2463676.2465332>.

- [100] A. S. Mohammed, Ş E. Amrahov, F. V. Çelebi, Interpolated binary search: An efficient hybrid search algorithm on ordered datasets, *Engineering Science and Technology, an International Journal*, Volume 24, Issue 5, 2021, Pages 1072-1079, <https://doi.org/10.1016/j.jestch.2021.02.009>.
- [101] J. Bohbot, N. Gillet, and A. Velghe, IFP Energies Nouvelles IFPEN, System and method for predicting a physical and/or chemical phenomenon by means of a shared memory segment. U.S., 2019, Patent Application 16/275,765.
- [102] J. Matheis, S. Hickel, Multi-component vapor-liquid equilibrium model for LES and application to ECN spray A. In: *Studying turbulence using numerical simulation databases - XVI – Proceedings of the 2016 Summer Program*. Center for Turbulence Research, Stanford University. 2016; pp. 25-34
- [103] B. Ningegowda, F. Rahantamialisoa, J. Zembi, A. Pandal, et al., Large Eddy Simulations of Supercritical and Transcritical Jet Flows Using Real Fluid Thermophysical Properties, *SAE Technical Paper 2020-01-1153*, 2020, <https://doi.org/10.4271/2020-01-1153>.
- [104] C. Rodriguez, P. Koukouvinis, M. Gavaises, Simulation of supercritical diesel jets using the PC-SAFT EoS, *The Journal of Supercritical Fluids*, Volume 145, 2019, Pages 48-65, <https://doi.org/10.1016/j.supflu.2018.11.003>.
- [105] H. Zhu, M. Battistoni, B. Ningegowda, F.N.Z. Rahantamialisoa, Z. Yue, H. Wang, M. Yao, Thermodynamic modeling of trans/supercritical fuel sprays in internal combustion engines based on a generalized cubic equation of state, *Fuel*, Volume 307, 2022, 121894, ISSN 0016-2361, <https://doi.org/10.1016/j.fuel.2021.121894>.
- [106] G. Lacaze, T. Schmitt, A. Ruiz, J.C. Oefelein, Comparison of energy, pressure-and enthalpy-based approaches for modeling supercritical flows, 2019 *Comput.Fluids* 181 35–56, <http://dx.doi.org/10.1016/j.compfluid.2019.01.002>
- [107] A. Poormahmood, and M. Farshchi, Numerical study of the mixing dynamics of trans- and supercritical coaxial jets, 2020, *Physics of Fluids* 32, 125105, <https://doi.org/10.1063/5.0030183>.
- [108] S. Jafari, H. Gaballa, C. Habchi, and J.C De Hemptinne, Towards understanding the structure of subcritical and transcritical liquid-gas interfaces using a tabulated real fluid modeling approach, *J. Energies*, 2021, <https://doi.org/10.3390/en14185621>.

- [109] G. Lacaze, T. Schmitt, A. Ruiz, J.C. Oefelein Comparison of energy-pressure- and enthalpy-based approaches for modeling supercritical flows, *Comput. Fluids*, 181 (2019), pp. 35-56, <https://doi.org/10.1016/j.compfluid.2019.01.002>.
- [110] G. Eliosa-Jimenez, G. Silva-Oliver, F. Garcia-Sanchez, A. de Ita de la Torre, High-pressure vapor-liquid equilibria in the nitrogen + n-hexane system, *J. Chem. Eng.*, 2007, Data 52, 395(404), <https://doi.org/10.1021/je060341d>.
- [111] G.G. Simeoni, T. Bryk, F.A. Gorelli, M. Krisch, G. Ruocco, M. Santoro, T.Scopigno, The Widom line as the crossover between liquid-like and gas-like behaviour in supercritical fluids, *Nature Phys* 6, 503–507, 2010, <https://doi.org/10.1038/nphys1683>
- [112] F. Gorelli, M. Santoro, T. Scopigno, M. Krisch, G. Ruocco, Liquid like behavior of supercritical fluids, *Phys. Rev. Lett.* 97 (24), 2006, <https://doi.org/10.1103/physrevlett.97.245702>
- [113] F. A. Gorelli, T. Bryk, M. Krisch, G. Ruocco, M. Santoro, T. Scopigno, Dynamics and Thermodynamics beyond the critical point, *Scientific Report Vol. 3* (2013) 1203, <https://doi.org/10.1038/srep01203>.
- [114] A. Romei, G. Persico, Computational fluid-dynamic modelling of two-phase compressible flows of carbon dioxide in supercritical conditions (2021), *Applied Thermal Engineering*, Volume 190, 116816, ISSN 1359-4311, <https://doi.org/10.1016/j.applthermaleng.2021.116816>.
- [115] A. Roy, C. Joly, and C. Segal, Disintegrating supercritical jets in a subcritical environment, *J. FluidMech* (2013), 717, 193, <https://doi.org/10.1017/jfm.2012.566>
- [116] L. Qiu, and R. D. Reitz, Simulation of supercritical fuel injection with condensation, *Int J Heat Mass Transf* (2014), pp. 1070-1086, <https://doi.org/10.1016/j.ijheatmasstransfer.2014.08.081>.
- [117] P. Tudisco, and S. Menon, Numerical investigations of phase-separation during multi-component mixing at super-critical conditions, *Flow Turbulence Combust* (2019), pp. 693–724, <https://doi.org/10.1007/s10494-019-00101-4>.
- [118] F. Nicoud, H.B. Toda, O. Cabrit, S. Bose, and J. Lee, Using singular values to build a subgrid-scale model for large eddy simulations, *Phys. Fluids* (2011), 23(8), 085106, <https://doi.org/10.1063/1.3623274>.

- [119] P. Sagaut, *Large-Eddy Simulation for Incompressible Flows*, 3rd edn. Scientific Computation, 2005, Springer, Berlin Heidelberg New York, ISBN: 978-3-642-06580-4.
- [120] Z. Han, and R.D. Reitz, Turbulence Modeling of Internal Combustion Engines Using RNG k-e Models, *Combustion Science and Technology* (1995), 106(4-6), 267-295, <https://doi.org/10.1080/00102209508907782>.
- [121] L. Qiu, and R.D. Reitz, An investigation of thermodynamic states during high-pressure fuel injection using equilibrium thermodynamics, *J. Multiphas. Flow* (2015), Volume 72, Pages 24-38, <https://doi.org/10.1016/j.ijmultiphaseflow.2015.01.011>
- [122] X. Luo, B. Prast, M.E.H. van Dongen, H.W.M. Hoeijmakers, J. Yang: On phase transition in compressible flows: modelling and validation, *J. Fluid Mech.* (2006), 548, 403–430
- [123] A. Misdariis, A. Robert, O. Vermorel, S. Richard, T. Poinsot, Numerical methods and turbulence modeling for LES of piston engines: impact on flow motion and combustion, *Oil Gas Sci Technol IFP* (2013), 69(1), pp. 83-105, <https://doi.org/10.2516/ogst/2013121>.
- [124] M. Rieth, F. Proch, O. Stein, M. Pettit, A. Kempf. Comparison of the sigma and Smagorinsky les models for grid generated turbulence and a channel flow. *Computers and Fluids* (2014); 99(Supplement C):172–81, <https://doi.org/10.1016/j.compfluid.2014.04.018>.
- [125] A. Poormahmood, M. Mahdi Salehi, and M. Farshchi , "A methodology for modeling the interaction between turbulence and non-linearity of the equation of state", *Physics of Fluids* 34, 015106 (2022) <https://doi.org/10.1063/5.0076099>
- [126] P. Chassaing, R. A. Antonia, F. Anselmet, L. Joly, and S. Sarkar, *Variable Density Fluid Turbulence*, 1st ed. Springer(2002), <https://doi.org/10.1007/978-94-017-0075-7>.
- [127] M.M. Rogers, and R. D. Moser, The three-dimensional evolution of a plane mixing layer: The Kelvin-Helmholtz rollup, *Journal of Fluid Mechanics* (2017), 243, 183-226. <https://doi.org/10.1017/S0022112092002696>.
- [128] L. Davidson, and M. Billson, Hybrid LES-RANS using synthesized turbulent fluctuations for forcing in the interface region, *International Journal of Heat and Fluid Flow*, 27, 1028-1042, 2006. DOI: 10.1016/j.ijheatfluidflow.2006.02.025.
- [129] J.M. Desantes, J.M. García-Oliver, J.M. Pastor, I. Olmeda, A. Pandal, B. Naud, LES Eulerian diffuse-interface modeling of fuel dense sprays near- and far-

- field, *International Journal of Multiphase Flow*, 2020, 103272, ISSN 0301-9322, <https://doi.org/10.1016/j.ijmultiphaseflow.2020.103>.
- [130] J.M. Desantes, J.M. García-Oliver, J.M. Pastor, A. Pandal, B Naud, K. Matusik, D. Duke, A. Kastengren, C. Powell, D.P. Schmidt, Modelling and validation of near-field Diesel spray CFD simulations based on the  $\gamma$ -model. In: *Proceedings of the 28th European Conference on Liquid Atomization and Spray Systems*, September 6–8, Valencia, Spain, 2017, doi: 10.4995/ILASS2017.2017.4715.
- [131] S. Jafari, H. Gaballa, C. Habchi, J.Ch. de Hemptinne, and P. Mougine, Exploring the interaction between phase separation and turbulent fluid dynamics in multi-species supercritical flow jets using a tabulated real-fluid model, *J. Supercrit. Fluids*, 2022, <https://doi.org/10.1016/j.supflu.2022.105557>.
- [132] ECN, Engine Combustion Network. URL <http://www.sandia.gov/ecn/>
- [133] OI. Abiodun, A. Jantan, AE. Omolara, KV. Dada, NA. Mohamed and H. Arshad, State-of-the-art in artificial neural network applications: a survey. *Heliyon* 2018; 4(11): e00938.
- [134] A. Ansari, S. Boosari and S. Mohaghegh, Successful implementation of artificial intelligence and machine learning in multiphase flow smart proxy modeling: two case studies of gas-liquid and gas-solid CFD models. *J Pet Environ Biotechnol* 2020; 101(1): 1–8.
- [135] SL. Brunton, B. Noack and P. Koumoutsakos, Machine learning for fluid mechanics. *Annu Rev Fluid Mech* 2020; 52(1): 477–508, DOI: 10.1146/annurev-fluid-010719-060214
- [136] P. Koukouvinis, C. Rodriguez, J. Hwang, I. Karathanassis, M. Gavaises, L. Pickett, Machine Learning and transcritical sprays: A demonstration study of their potential in ECN Spray-A. *International Journal of Engine Research*. May 2021. doi:10.1177/14680874211020292.
- [137] <https://www.youtube.com/c/Eigensteve>
- [138] S. Yang, Y. Li, X. Wang, U. Unnikrishnan, V. Yang, W. Sun, Comparison of tabulation and correlated dynamic evaluation of real fluid properties for supercritical mixing, in: *53rd AIAA/SAE/ASEE Joint Propulsion Conference*, Atlanta, GA, 2017.
- [139] E. Winklhofer, E. Kull, E. Kelz, and A. Morozov, “Comprehensive hydraulic and flow field documentation in model throttle experiments under cavitation conditions,” in *Proceedings of the ILASS-Europe conference*, Zurich, 2001, pp. 574–579.